The University of
Nottingham

Mechanical Properties of Laser Beam Welded Ti6Al4V

By

Yu Fan, BEng, MSc

Thesis Submitted to the University of Nottingham for the degree of Doctor of Philosophy

January 2010

Declaration

I declare that this work has not already been accepted for any degree, and is not currently submitted in candidature for any degree other than the degree of Doctor of Philosophy of Nottingham University.

Yu Fan (BEng, MSc)

Abstract

Many items of medical, aeronautical, electronic and military equipment exposed to corrosive conditions, or required to have extreme performance characteristics, are sealed hermetically into micro packages. Laser beam welded (LBW) Ti6Al4V alloy has been adopted in anti-corrosion micro packages for the impeller of a left ventricular assistance device (LVAD). Thin and narrow welds were required for such medical equipment. A wide variety of laser types can be applied in sealing micro packages, which include traditional lasers (CO_2, Diode and Nd:YAG) to the newest laser types (fibre). Compared with other LBW types, continuous wave fibre laser welds are well known for exhibiting narrow weld zones, low distortion, lower heat input and high efficiency. However, in this work significant porosity was found in the continuous wave fibre laser welds due to the high traverse speeds and high associated solidification rates. The largest distortion and melting area was found in the continuous wave diode laser welds due to the high heat generation. A pulsed Nd:YAG welding was suggested as the hermetic laser welding technique for sealing the micro packages, since it is a good-balance between low porosity, less distortion and a narrow weld zone.

The microstructures of Ti6Al4V were complex and strongly affected the mechanical properties. These structures include: α' martensite, metastable β, Widmanstätten, bimodal, lamellar and equiaxed microstructure. Bimodal and Widmanstätten structures exhibit a good-balance between strength and ductility. The microstructure of laser beam welded Ti6Al4V was primarily α' martensite, which showed the lowest ductility but not significantly high strength. A heat treatment at 950°C followed by furnace cooling can transform the microstructure in the weld from α' martensite structure into Widmanstätten structure.

The fatigue fracture behaviour of laser beam welded thin sheet Ti6Al4V was examined in this project as the lifetime of the LVAD impeller has been seen to be limited by fatigue cracking. Grain size, phase content, stress ratio and frequency are all affected fatigue fracture behaviour. A transformed Widmanstätten structure in the weld gave the highest fatigue fracture life. A time of 8 hours heat treatment gave the highest fatigue fracture life due to a good-balance between the grain size and phase content; the existence of metastable β limits the crack propagation as well.

The geometries, distortion and porosity of the welds were variable and depended on the types of the laser used for the welding process. These factors significantly affected the local stress levels during the tensile testing and fatigue testing. FEA was used to understand and evaluate these influences. By simulation in FEA, the maximum stress locations were observed to be strongly dependent on the specifics of the cross-sectional geometries of the welds. For the pulsed Nd:YAG weld in the fatigue testing, the FEA-derived modified local stress amplitudes exhibited a increase of about 40% compared to the nominal applied stress.

Acknowledgement

It is my great pleasure to have this opportunity to express my respect and gratitude to people who have helped me during my studies and my life at the University of Nottingham.

I would like to express my most sincere thanks to Professor Geoff Tansley, and be heartily thankful to Professor Philip Shipway, whose encouragement, supervision and support throughout this research.

I would like to acknowledge the help, guidance and financial assistance given to me by the University of Nottingham, Timet UK Ltd. and Microkerf Ltd.

I would like to acknowledge Mr. Keith Dinsdale, Dr. Janet Folkes, Dr. Kenny Ding, Dr. Deng Zhang, Dr. Wei Sun, Dr. John Yellup, Mr. Graham Malkinson, Mr. Stuart Branston, Mr. Tom Buss, Dr. Nigel Neate, Dr. Yan Wang, Mr. Jiayuan He and Mr. Mark Daine for their helps on day-to-day basis. Without their constant helps and keen interests, it would have been impossible for me to carry out a whole project of this magnitude in a very smooth manner and well in time.

I would also like to express my thanks to the friends for support and help in my life. They are: Miss. Carole Wu, Mr. Ruipu Wang, Ms. Lan Guo, Dr. David Lo, Dr. Dingshan Zhuang, Ms. Lois Johnson, Dr. Yan Zhang, Mr. Jie Xu, Dr. Zhijian Wang, Mr. Haigang Zhang.

Finally, the unconditional love, support and care of my parents, Mr. Gang Fan and Ms. Yulan Zhao, have been unsurpassed at all times; for this I am eternally indebted.

Contents

List of Figures

List of Tables

Glossary

b.c.c.:	body centered cubic
BSE:	Back Scattered Electron
CW:	Continue Wave
DLW:	Diode Laser Weld
EBW:	Electron Beam Welding
EDX:	Energy Dispersive X-Ray
FEA:	Finite Element Analysis
FLW:	Fibre Laser Weld
FZ:	Fusion Zone
h.c.p.:	hexagonal close-packed
HAZ:	Heat-affected Zone
LBW:	Laser Beam Welding
LVAD:	Left Ventricular Assistant Device
Micro-CT:	X-ray Microtomograph
Nd:YAG:	Neodymium-doped yttrium aluminium garnet
N_F:	Crack propagation
N_I:	Crack Initiation
PM:	Parent Material
RT:	Room Temperature
SE:	Secondary Electron
SEM:	Scanning Electron Microscopy
Ti6Al4V:	Ti-6wt%Al-4wt%V
TIG:	Tungsten Inert Gas
WB:	Width of Bottom Surface
WT:	Width of Top Surface

CHAPTER 1

Chapter 1 Introduction

Micro packaging is being applied more and more widely in the electronics, telecom, medical device and aircraft industry [1]. Some of the micro packages need to be hermetically welded in order to protect fragile components inside from outside service conditions. For example, a Left Ventricular Assistant Device (LVAD) has been designed to help heart failure patients. There is one moving part - a hydrodynamically suspended impeller (Figure 1.1); the impeller is exposed to human blood corrosion conditions [2]. The electronic and magnetic devices inside the impeller are fragile components, which need to be sealed hermetically [3].

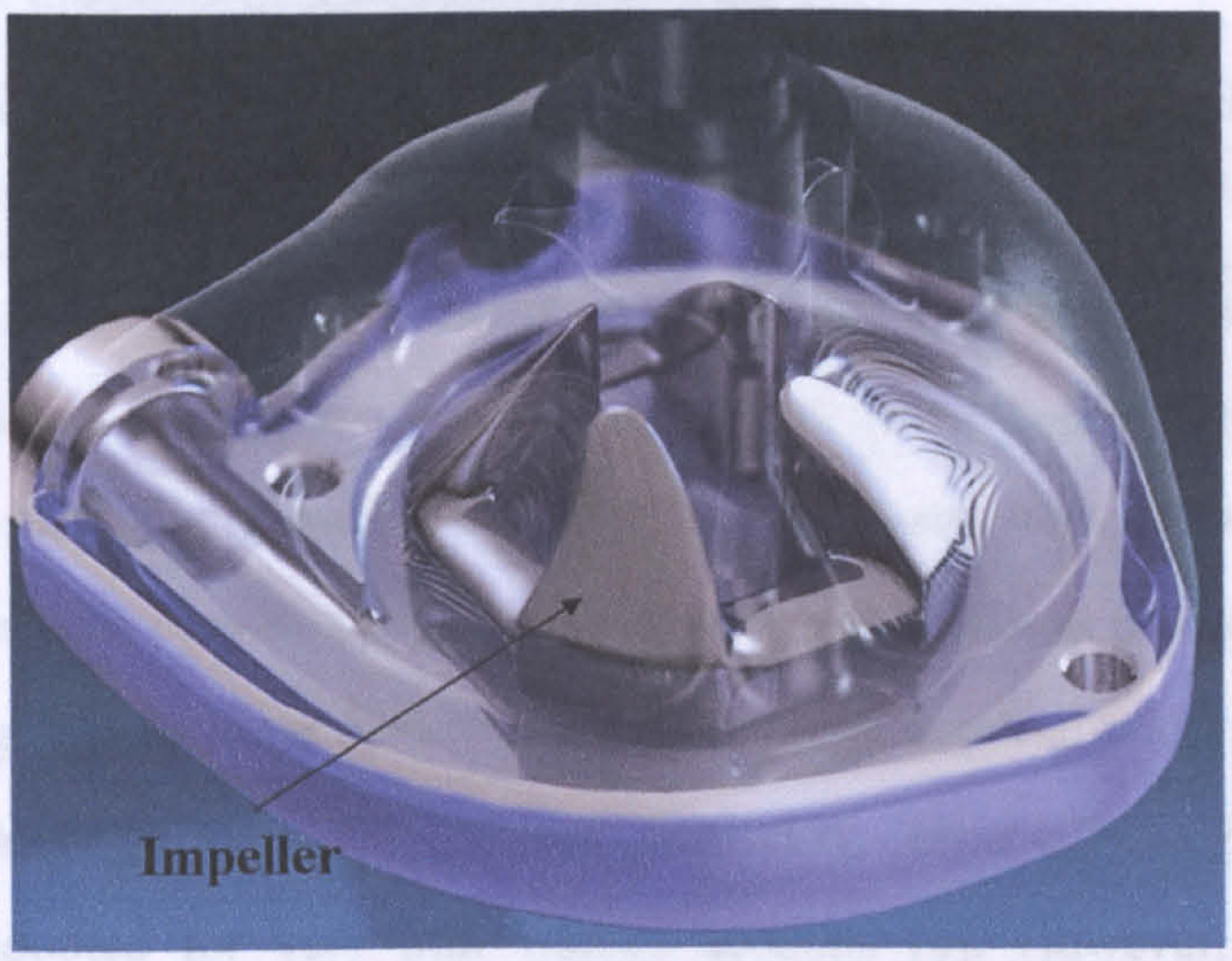

Figure 1.1 The hydrodynamically suspended impeller in the LVAD

There are quite a lot of welding techniques which are applied for sealing hermetically in thin metal systems, such as Electron Beam Welding (EBW), Tungsten Inert Gas (TIG), Resistance Welding and Laser Beam Welding (LBW). However, micro package welding requires smaller and smaller joining areas. For example, the wall thickness of the shell of impeller in LVAD is usually very thin – typically around 0.5 mm. These dimensions make manufacturing difficult leaving a possibility of weld cracking or leakage due to geometrical stress-raisers which occur through inadequate weld penetration, poor machining, poor weld parameters or poor weld geometry design. Figure 1.2 shows a typical micro package applied for the impeller in an LVAD.

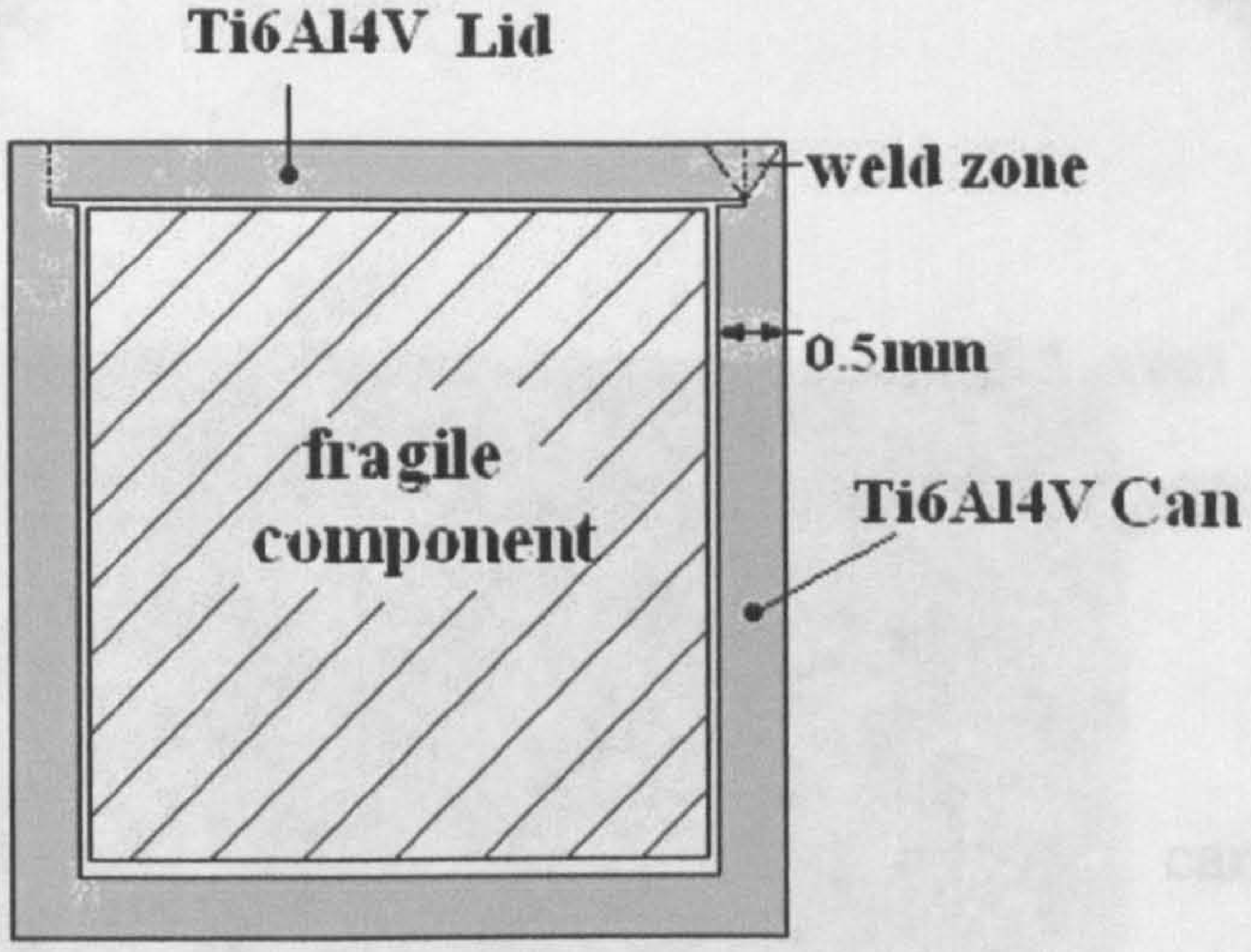

Figure 1.2 A typical micro package in impeller of LVAD

Laser welding of such thin sheet requires a small focal spot, good laser beam quality and fast travel speed, since too much heat generation can cause distortion for thin sheet weld or, more significantly damage of the component which is being sealed [4, 5]. A laser beam can provide a high power density and results in producing a keyhole during welding. The keyhole feature provides the high depth-to-width ratio. Because of high production rates and process flexibility, especially, LBW has been successfully adopted for very thin welded sections [6]. However, the predicted lifetime of the impeller is 5-10 years due to micro-cracking. The potential micro-cracking is from cyclic loading due to the blood pressure which may cause crack initiation and then crack propagation due to fatigue. (Figure 1.3)

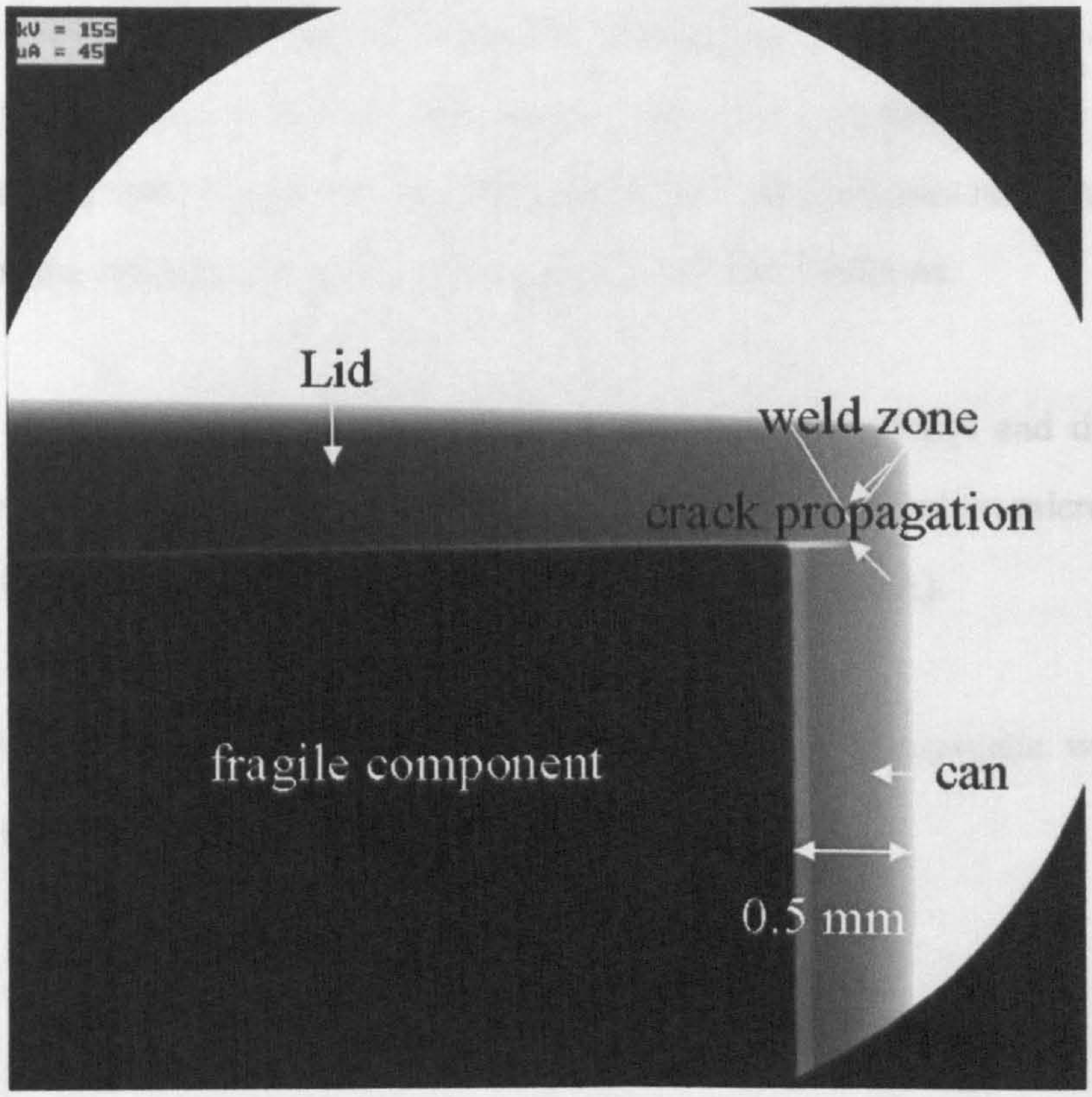

Figure 1.3 X-ray microtomograph (Micro-CT) image of crack propagation (red arrow area) in micro packaging of impeller

The material adopted for the lid and can of the micro package in the impeller of LVAD is Ti-6wt%Al-4wt%V (Ti6Al4V) alloy. Ti6Al4V alloy is widely used in the medical device industry for its desirable properties： strength to weight ratio, corrosion resistance, biocompatibility and processability (casting, deformation, powder metallurgy, machinability, welding etc.) [7-10]. The alloy can be heat treated to obtain various microstructures. The shape and distribution of alpha (α), beta (β) and martensite α′ control some of the critical mechanical properties of the material (such as fatigue behaviour). Equiaxed microstructures, small grain sizes and low α phase content confer benefits on fatigue life behaviour of Ti6Al4V alloy. In contrast, martensite α′, coarse grains and higher α phase content reduce the fatigue life.

The metallurgy of LBW Ti6Al4V is complex. The fusion zone (FZ) and associated heat-affected zone (HAZ) are generally very narrow and result in a high depth-to-width ratio (aspect ratio), which is one primary advantage of laser welding compared with the other welding processes. Martensite α′with a coarse grain structure primarily exists in the FZ due to high cooling rates from above the β-transus temperature; this area can be the weakest part under cyclic loading service conditions.

The aim of this project is to understand the mechanical properties and the fatigue behaviour of laser beam welded thin sheet of Ti6Al4V alloy based on microstructure modification, geometry control and Finite Element Analysis (FEA).

During the work, three types of lasers will be applied for hermetic welding of Ti6Al4V alloy, namely Nd:YAG, diode and fibre lasers.

References:

[1] K.F.Kleine, W.J.Fox, K.G.Watkins. Micro Welding with Pulsed Single Mode Fiber Lasers. Proceedings of the 23rd international congress on applications of laser and electro-optics; 4-7 October 2004; San Francisco California: Laser institute of American; 4-7 October 2004.

[2] G.D.Tansley, S.Vidakovic, J.Reizes. Fluid Dynamic Characteristics of the VentrAssist Rotary Blood Pump. *Artificial Organs*. 2000; 24(6):483-7.

[3] G.D.Tansley, M.Cook, N.Zhang, M.Chung, J.Woodard, J.Reizes. Complete passive suspension of the VentrAssist rotary blood pump. 4-8 December, 2000; University of Technology, Sydney; 4-8 December, 2000. p. 809 - 13.

[4] Y.Okamoto, A.Gillner, A.Olowinsky. Fine micro-welding of thin metal sheet by high speed laser scanning. In: Photonic materials d, and applications II editor. Proc of SPIE; 2007; Maspalomas, Gran Canaria, Spain; 2007. p. 65930D 1-10.

[5] A.Salminen, A.Jansson, V.Kujanpaa. Effect of welding parameters on high power diode laser welding of thin sheet. In: SPIE Po, editor. High-Power Diode Laser Technology and Applications; 2003; p. 106-15.

[6] J.Du, J.Longobardi, W.P.Latham, A.Kar. Weld strength and process controllability for laser welding of thin sheet metals. *Journal of laser applications*. 2000; 12(6):239-44.

[7] L.W.Tsay, C.Y.Tsay. The effect of microstructures on the fatigue crack growth in Ti6Al4V laser welds. *Int J Fatigue*. 1997; 19(10):713-20.

[8] F.J.Gil, M.P.Ginebra, J.M.Manero, J.A.Planell. Formation of alpha-Widmanstätten structure: effect of grain size and cooling rate on the Widmanstätten morphologies and on the mechanical properties in Ti6Al4V alloy. *Journal of Alloy and compounds*. 2001; 329:142-52.

[9] F.Caiazzo, F.Curcio, G.Daurelio, F.Memola Capece Minutolo. Ti6Al4V sheets lap and butt joints carried by CO2 Laser: mechanical and morphological characterization. *Journal of Materials Processing Technology*. 2004; 149:546-52.

[10] I.J.Polmear. Light Alloys: from traditional alloy to nanocrystals. 4th ed: Butterworth-Heinemann 2006.

CHAPTER 2

Chapter 2 Literature Review: Laser Beam Welding

Certain micro packaged components need to be hermetically sealed. For example, the corrodible micro package components in LVAD need to be prevented from entering human blood. Of the several sealing weld technologies which have been fully developed, laser beam welding (LBW) was selected for this application. A basic understanding of LBW and the control of quality for continuous wave (CW) and pulsed weld are detailed in this chapter.

2.1 Suitability of LBW

Laser is an acronym of Light Amplification by Stimulated Emission of Radiation, a process first invented in 1958 by Charles Townes and Arthur Schawlow of Bell Laboratories. 'Laser beam welding (LBW) is a fusion welding process that results in joining of materials by the interaction of a concentrated, coherent beam of light and the material surface.' [1] This interaction creates sufficient elevations in temperature to melt the material and form a joint from the molten material from the two components being welded [1]. There are several other techniques available for sealing micro packages, such as Electron Beam Welding (EBW), Tungsten Inert Gas (TIG) and Resistance Welding [2-5]. However, all of these welding techniques have limitations when applied to sealing micro packages. In TIG welding, a wider weld zone and more heat generation may damage the components inside the package and cause serious distortion. In resistance welding, there are too many restrictions on weld joint shape and material properties; for example resistance welding can be used only for materials with reasonably high electrical resistance and for a lap weld joint geometry. Electron Beam Welding can create narrow, deep penetration welding with the 'keyhole' (the explanation of keyhole mode welding is discussed in Section 2.3) mechanism which is quite similar to LBW. However, EBW cannot be adopted for a micro package which has magnetic component inside, since the magnetic component will causes the deflection of the electron-beam during the welding process. LBW allows the manufacture of precision welded joints with a high depth-to-width ratio and a high welding speed due to 'keyhole mode welding'.

Table 2.1 The advantages and disadvantages of the LBW process [1, 6, 7]

Advantages of Laser Beam welding
1. Deep narrow welds • The laser beam weld produces narrow fusion zones and heat-affected zones. • Single pass weld penetration has reached depth of 15mm thickness on steel. [6] • Extremely narrow welds have been produced successfully, especially in fibre laser welding.
2. Low heat input • Low heat input results in low thermal distortion, which can eliminate the need for preparation of V joint. • Welds can be made in micro package applications with heat sensitive components inside, such as electronic circuits and magnet devices.
3. High production rates and process flexibility • Welding speeds are high, traverse speeds of up to 500 mm/s are possible [1]. • Laser welding machines are operated automatically or by robots. • Welds can be made without additional fillet materials at narrow gaps between two components. • Dissimilar materials and component thicknesses can be welded.
Disadvantages of Laser Beam Welding
1. Extremely high cooling rate and traverse speed may induce defects, such as hot cracking, porosity. 2. Thin section welds have a high requirement on Jigs and sample edge preparation. 3. The depth of beam focus is small, so the work surface needs to be accurately maintained to achieve the required power density. 4. Vaporization of some alloying elements can occur due to high temperature from high power density. 5. The costs of equipment and operating are high 6. Safety protection is required, to prevent eye damage and skin burns from the laser beam.

LBW has certain limitations as outlined in previous work [1, 6, 7]; however, deep narrow welds, low heat input and high production rates meet the requirement of hermetical sealing of micro packaged components where avoidance of thermal damage to the component being sealed is paramount.

2.2 Laser types

The lasers used in welding can be divided into different types by the wide variety of lasing gain medium types available such as gas (He-Ne and carbon dioxide), solid state (neodymium-doped yttrium aluminium garnet; Nd:$Y_3Al_5O_{12}$), semiconductor (diode lasers) etc. In the following section, Nd:YAG lasers, diode lasers and fibre lasers are discussed. All these three laser types were adopted in the laser welding experimental work.

2.2.1 Nd:YAG laser

Nd:YAG lasers are the most common type of solid-state laser used for welding [8]. They can produce either pulsed or continuous wave output power. At present, Nd:YAG lasers are mostly used in the pulsed mode for welding. It is 'a mature process with a proven record of producing high-quality welds for many diverse joining applications' [1]. The wavelength of Nd:YAG laser is about 1.06 μm [9]. A single head pulsed Nd:YAG laser typically has average power levels of approximately 500 W [1].

2.2.2 Diode laser

A diode laser uses a semiconductor similar to that found in a light-emitting diode as the gain medium. Diode lasers have been used for some time, but their low power and poor beam quality has restricted their use [10, 11]. The advantages of diode lasers include lower cost, smaller volume and higher efficiency. The applications of diode lasers have been mainly in telecommunications as they are easily modulated and easily coupled light sources for fibre optic communication.

2.2.3 Fibre laser

The fibre laser is the most recently developed solid state laser technology, and is well known for high speed, high beam quality and small volume. In recent years, since the size of components has become smaller, the welding of thin sheet has been required.

Some welding applications require a focus spot diameter of the order of 25 μm and pulse energy levels as low as 10 mJ [7]. The combination of micro beam and high speed laser scanning has advantages for thin metal sheet welding. Therefore, the pulsed Nd:YAG laser [12] has been the most widely adopted for micro-welding for thin metal sheet; however, the fibre laser has the attributes required for such welding and may have advantages in this area.

2.3 Keyhole mode welding versus conduction mode welding

Keyhole mode welding occurs as the power density increases. The molten zone penetrates fully through the material to be joined, and a relatively narrow weld is then created (Figure 2.1(a)). When power density is low, the energy of the laser is predominantly conducted through the material. As the temperature of the material is increased, it melts and forms a wide and shallow weldpool (Figure 2.1(b)) which is called conduction mode welding.

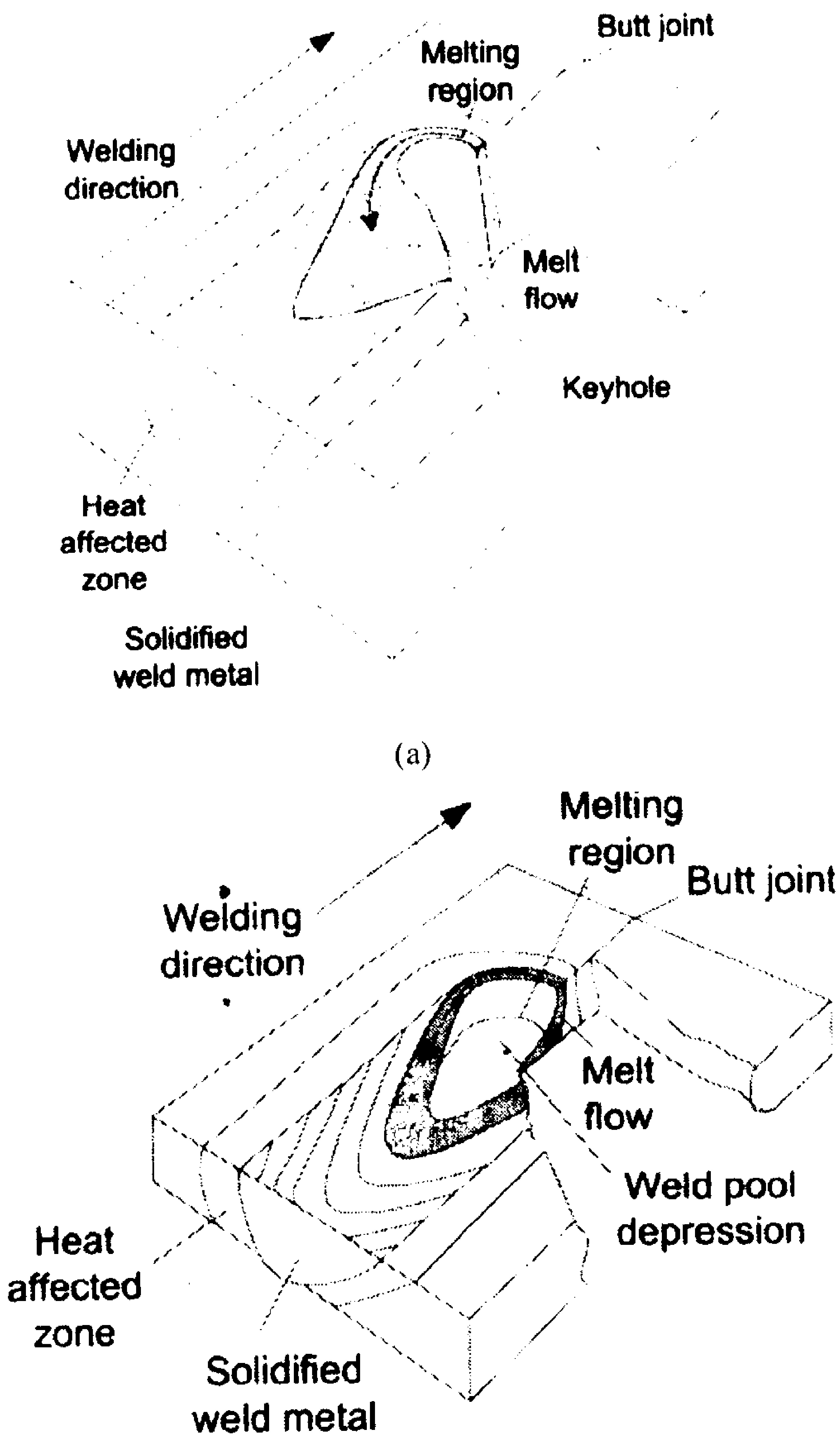

Figure 2.1 Diagram of Keyhole mode welding and conduction mode welding[13]

The conduction mode weldpool is stable, 'as vaporisation of the materials is negligible'[13]. The limitations of conduction mode welding include: 1) it cannot be used for thick material welding; 2) too much heat generation could produce a wider weld zone and serious distortion. The benefits of keyhole welding include:

- deep penetration
- high production rates
- reduced heat input
- reduced distortion, residual stress.

2.4 Continuous wave laser versus pulsed

The output laser beam from welding lasers is either a continuous wave beam or a pulsed power beam. As the name implies, a continuous wave (CW) laser produces a laser beam with a relatively constant output power over time. When a CW laser is used for welding, the beam establishes a steady molten weld pool which is traversed along the weld path. The liquid metal weld pool that is created by CW lasers is more stable than that for pulsed lasers and, therefore, metal spatter is less of a problem [1].

Pulsed laser welds are characterized by an extremely fast cooling rate, minimum heat-affected zone, and low total heat input to the work [14]. Due to spatter, weld penetration is usually limited to relatively thin sections (<2 mm) [1]. Pulsed lasers excel in thin-section applications because of their unique ability to produce extremely high powers for very short periods of time and to precisely control pulse energy.

2.5 Laser beam welding process parameters

Several researchers describe the process of LBW for CW and pulsed lasers [15-18]. For laser welding, the weld characteristics are controlled by the combination of the following parameters:

2.5.1 Control of parameters in CW laser beam welding

The main parameters for CW Laser Beam Welding include: power (***P***), traverse speed (***V***), focused spot size (***D***), power density or irradiance (***I***), and linear heat input (***E'***)

Power (*P*): is the rate of energy flow from the radiation source.

Traverse Speed (*V*) is the linear traverse speed by which the weld joint moves relative to the beam.

Focused Spot Size (*D*). The diameter of the focused laser beam at the workpiece surface is commonly known as the spot size.

Power Density or Irradiance (*I*). The laser beam power per unit area at the surface is commonly known as the beam power density or irradiance. Power density, is given by the equation 2.1:

$$I = \frac{P}{A}$$ **Equation 2.1**

where, A is the area of the focused laser beam at the workpiece surface.

Linear Heat Input (*E'*). The ability of the laser beam to melt a volume of material depends on the energy delivered per unit length of weld and it is commonly referred to as the linear heat input [1]. Linear heat input (J/m) is calculated by dividing the laser power by the linear traverse speed as shown below:

$$E' = \frac{P}{V}.$$ **Equation 2.2**

In CW Laser Beam Welding, penetration is determined most strongly by the laser power density but it also influenced by traverse speed. If spot size is unaltered, then to increase the weld penetration the power must be increased independently. The work of Caiazzo et al. [15] illustrated the melting depth versus laser power level for different traverse speeds of a CW CO_2 laser (Figure 2.2). If the laser power is already at the maximum, there are two ways to increase penetration; 1) decrease the spot size to increase the power density, 2) reduce the traverse speed since this will increase the melting depth (Figure 2.3).

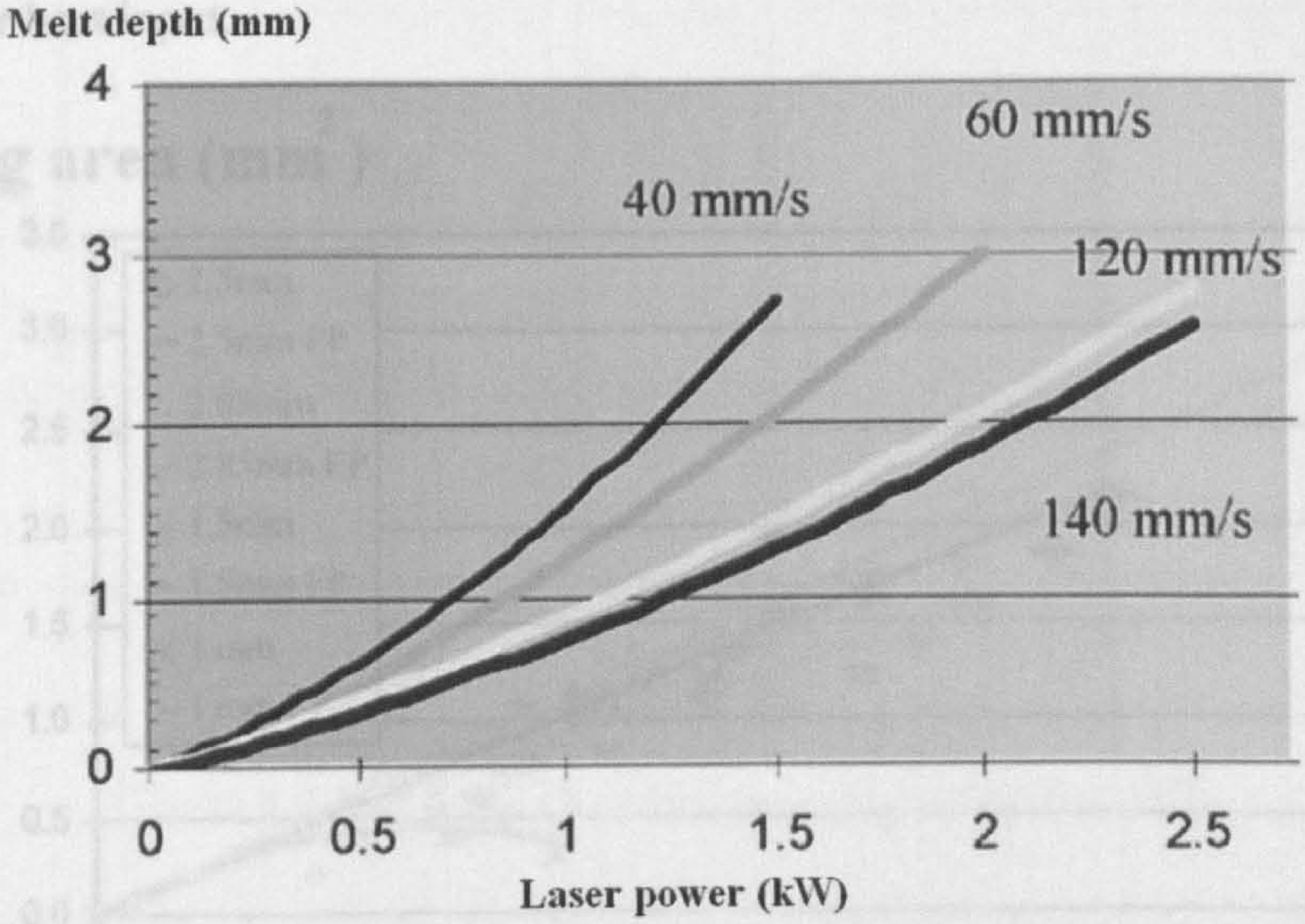

Figure 2.2 Melt depth laser power level for different traverse speed values, CO_2 laser weld in Ti6Al4V [15]

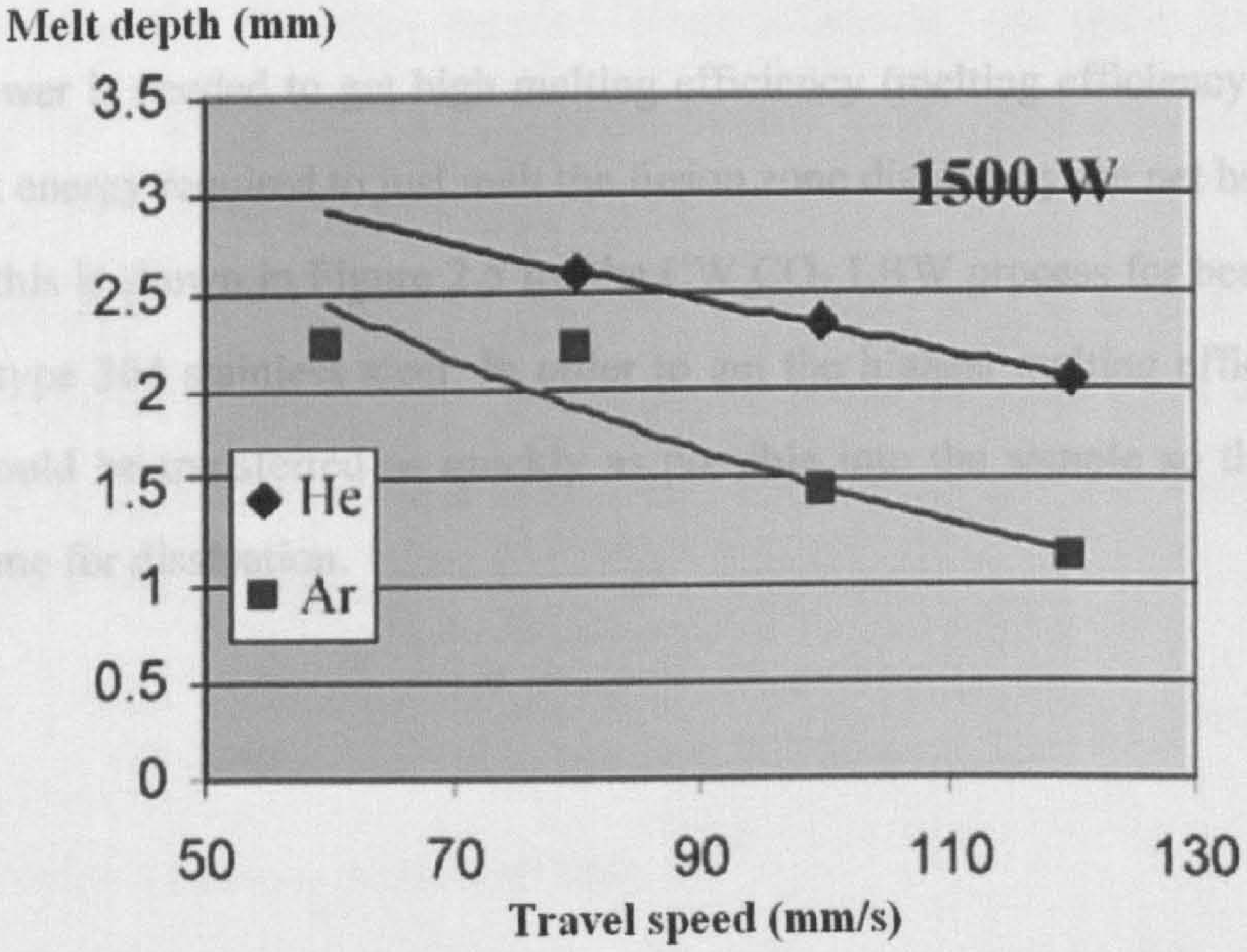

Figure 2.3 Melt depth versus traverse speed for He and Ar covering gas at 1500W power level, CO_2 laser weld in Ti6Al4V [15]

Equation 2.2 indicates that when the power is increased or the traverse speed is reduced, then the linear heat input will increase. Figure 2.4 shows that, no matter what material thickness from 1.0 to 2.85 mm or whether penetration is partial or full, the melting area (i.e. cross sectional area of the molten zone) tends to increase linearly with linear heat input.

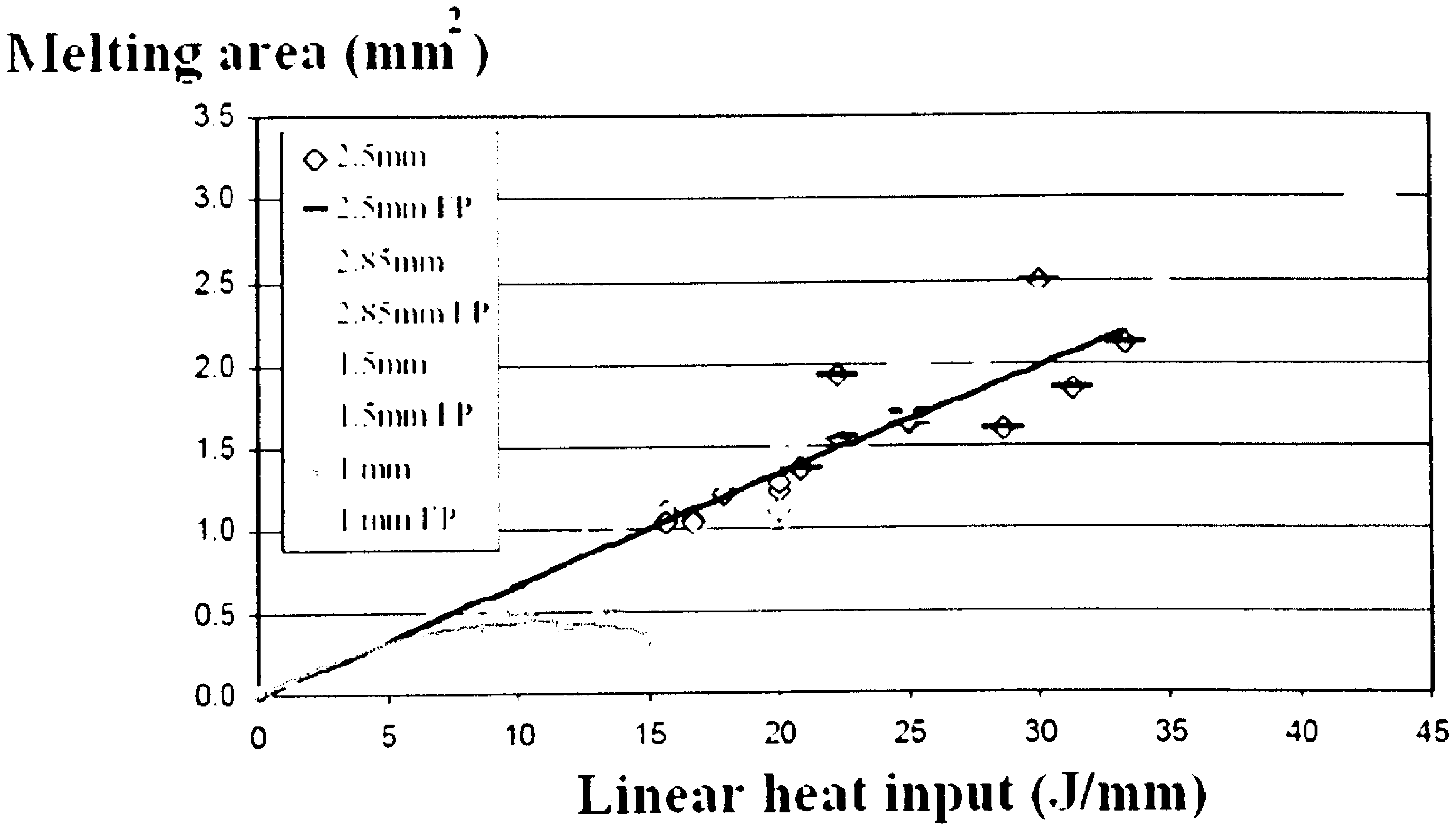

Figure 2.4 Melting area versus Linear heat input [15]

A high power is needed to get high melting efficiency (melting efficiency is defined as the heat energy required to just melt the fusion zone divided by the net heat input to the part); this is shown in Figure 2.5 for the CW CO_2 LBW process for bead-on-plate welds on type 304 stainless steel. In order to get the highest melting efficiency, the energy should be transferred as quickly as possible into the sample so that there is reduced time for dissipation.

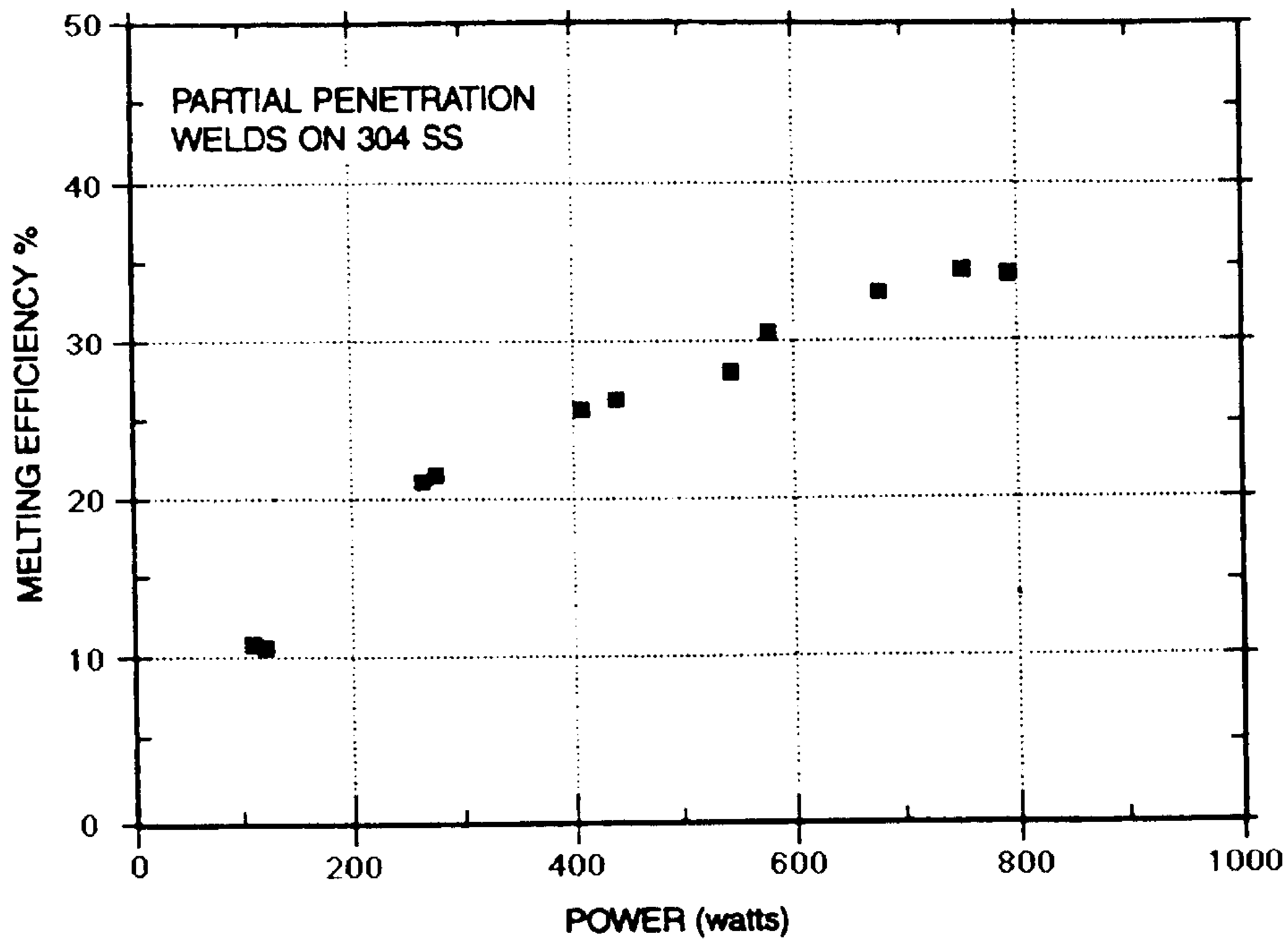

Figure 2.5 Melting efficiency versus laser power [19]

2.5.2 Control of Parameters in Pulsed Lasers

Pulse Energy (*E*). The melted volume of a fusion zone produced by an individual laser pulse is determined by the pulse energy.

Pulse Duration (t_p). The time duration of an individual laser pulse is sometimes called the pulse length, pulse width, or pulse-on-time. Pulse duration for laser welding typically ranges from about 0.250 to 20.0 ms [1].

Pulse Frequency (*f*). The rate of laser pulsation in pulses per second (Hz) is an important variable in pulsed LBW. Pulse frequency and traverse speed will control the amount of pulse overlap in a seam weld. Pulse frequency also determines the average power. Pulse frequency (*f*) can be determined by:

$$f = \frac{1}{(t_p + t_0)}$$ **Equation 2.3**

where t_p is pulse on time, t_o is pulse off time.

Pulse Overlap. It is the amount (usually expressed as a percentage of the diameter of the melted zone) by which the diameter of the melted area created by one pulse overlaps that created by the preceding pulse (Figure 2.6). It depends on many factors including the pulse energy, pulse frequency, traverse speed, and material properties.

Peak Power (P_p). The high powers that are achieved during the short duration laser pulse are described by the peak power. The peak power can be determined by dividing the pulse energy by the pulse duration (t_p) as shown below:

$$P_p = \frac{E}{t_p}$$ **Equation 2.4**

Average Power (P_A). The pulsed laser beam power that is the summation of all the laser pulses averaged over time is commonly known as the average power. It is roughly equivalent to the power (P) given above for a continuous wave laser and it is an indicator of the processing capabilities of a pulsed laser. The average power can be determined from the product of the pulse frequency and the pulse energy as follows:

$$P_A = f \times E$$ **Equation 2.5**

Power Density or Irradiance (I). The power density for pulsed LBW is, in effect, the same as described before in CW and pulsed LBW, except that it is calculated from the peak power instead of the average power. It is calculated as follows:

$$I = \frac{P_p}{A}$$ **Equation 2.6**

One significant difference and advantage of pulsed LBW is that it does not have to use very high traverse speeds to obtain a high melting efficiency. Peak powers during the very short duration laser pulse are extremely high, so the melting efficiencies are also very high. Traverse speed is usually only adjusted to achieve the required pulse overlap. The melting zone size (depth and width) for pulsed laser welding is determined by the pulse energy. In order to increase the melting zone size, a longer pulse duration is normally selected rather than an increase in peak power since a peak power which is too high could cause excessive vaporization and spatter.

The depth of penetration is determined primarily by the peak power density. For a fixed spot size, the peak power density is controlled by the peak power. As peak power is the ratio of the pulse energy to the pulse duration, the penetration can be increased by either increasing pulse energy or decreasing the pulse duration. Average power is not a good indicator of weld penetration because it is possible to have two welding process with the same average power but very different pulse energies. Kuo and Jeng [14] used a pulsed Nd:YAG laser system, operated at the same mean laser source power of 1.7 kW; by changing the ratio of high power-low power laser delivery, they changed progressively from a pulsed wave (PW) mode to a continuous wave (CW) mode. They indicated that ΔP (the difference between peak power and base power) level determined the depth-to-width ratio. In Figure 2.6 for stainless steel (SUS 304L), it can be seen that if traverse speed is kept uniform, the highest ΔP caused the biggest D/W (depth-to-width), which implies that peak power is the key to controlling penetration depth.

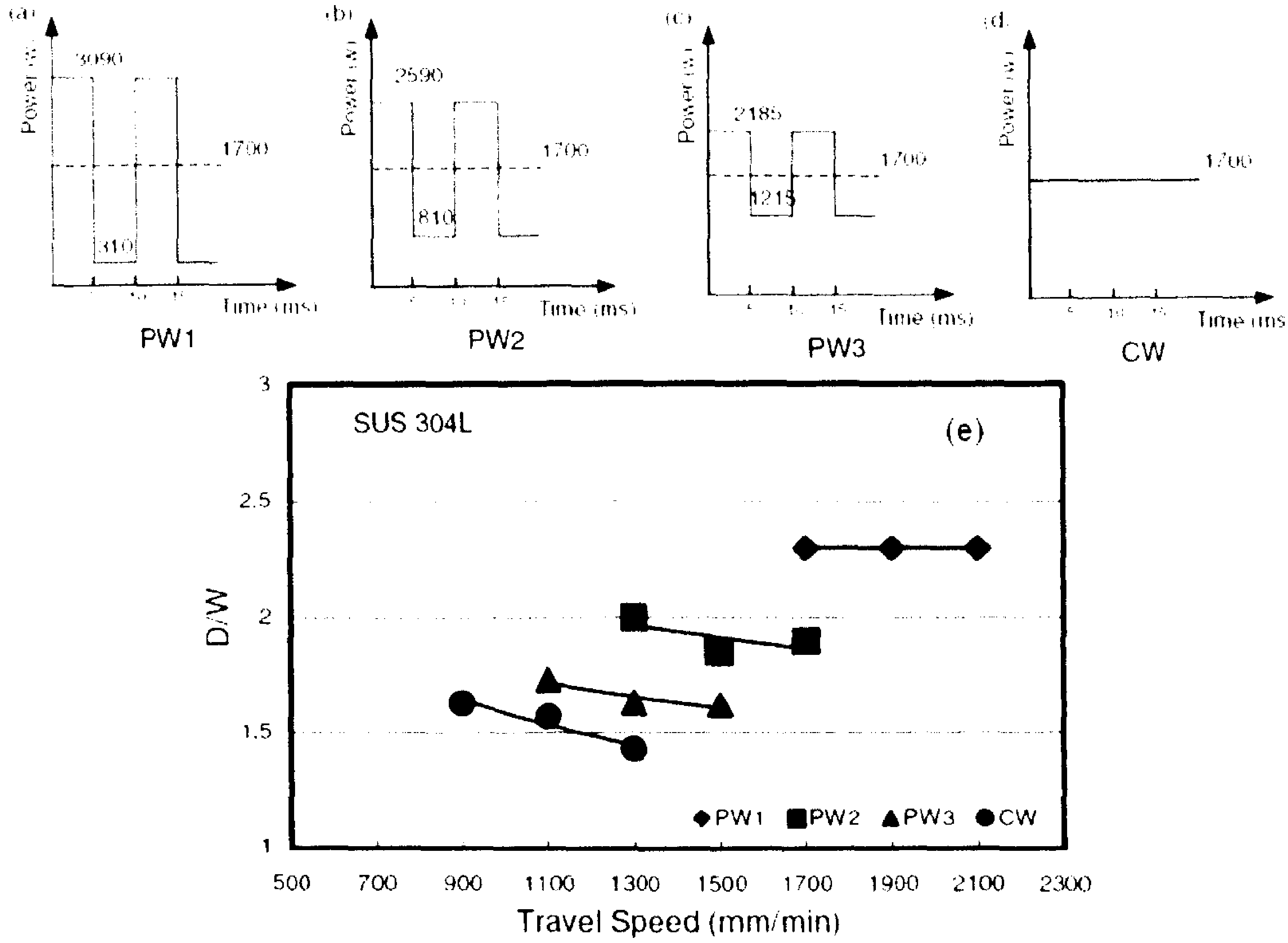

Figure 2.6 a) PW1; b) PW2; c) PW3; d) CW; e) Depth-to-width (D/W) curves for bead-on-plate welds as function of ΔP level and traverse speed [14]

Pulse frequency is normally used to increase the overall welding speed. Traverse speed is used to obtain the required pulse overlap. Pulse overlap is an important factor in hermetic welding. Proper pulse overlap is chosen by examining the melted spot diameter at the chosen pulse energy, traverse speed, and frequency, then assessing the overlap. The American Welding Society [1] recommends 'an overlap of 70 to 80 percent' to ensure constant weld penetration at the weld root and hermetically sealed joints. This is illustrated in Figure 2.7.

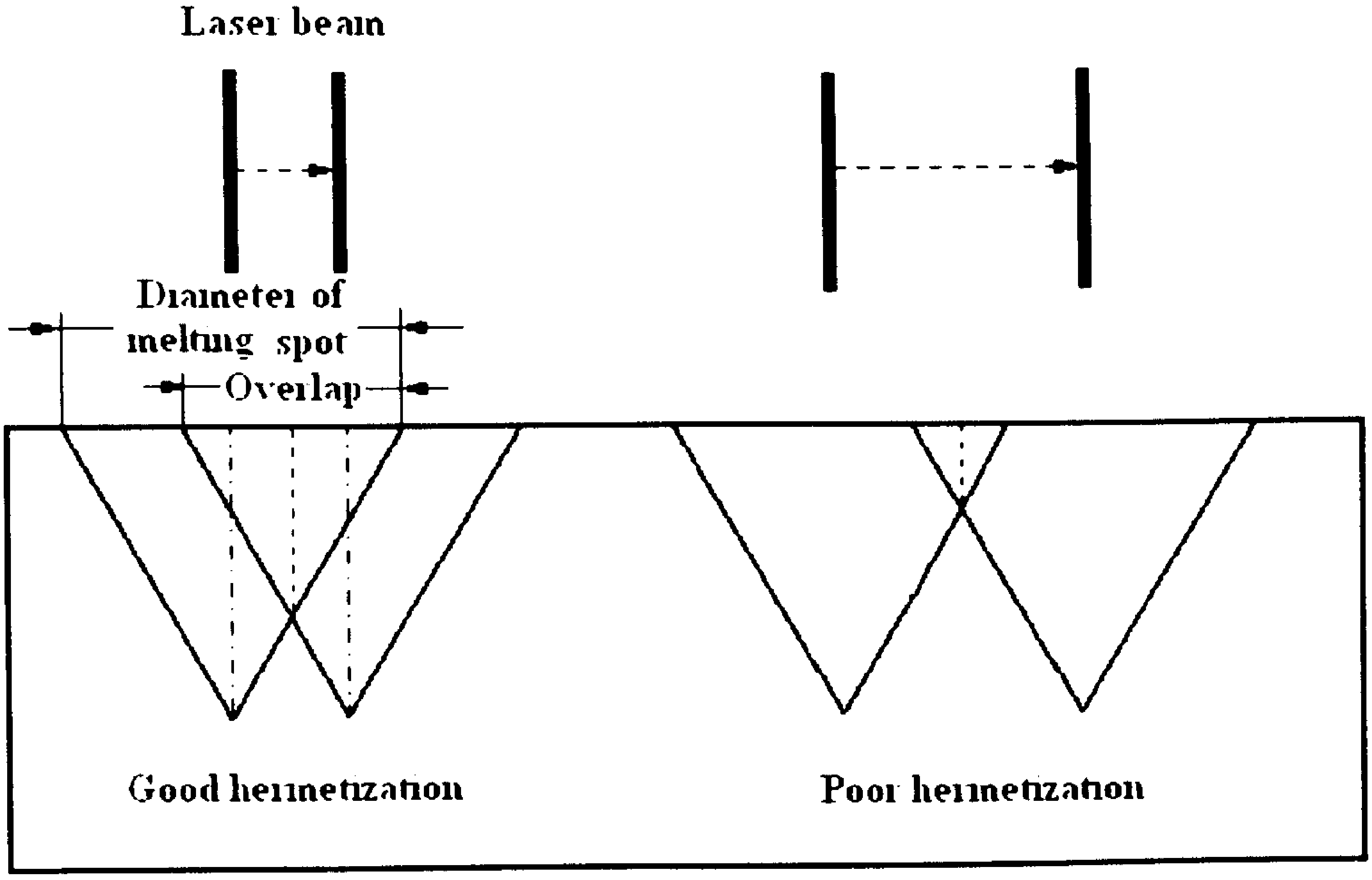

Figure 2.7 Schematic diagram of overlap and hermetization

Figure 2.8 is a development for thin-section pulsed Nd:YAG LBW. It can be used as a guideline for weld development of stainless steel, titanium and aluminium. The top and bottom axes are used to choose traverse speed and pulse frequency. Then the right axis is used to determine the pulse energy and control the penetration (left axis). The curves generated by energy and pulse frequency are average power values.

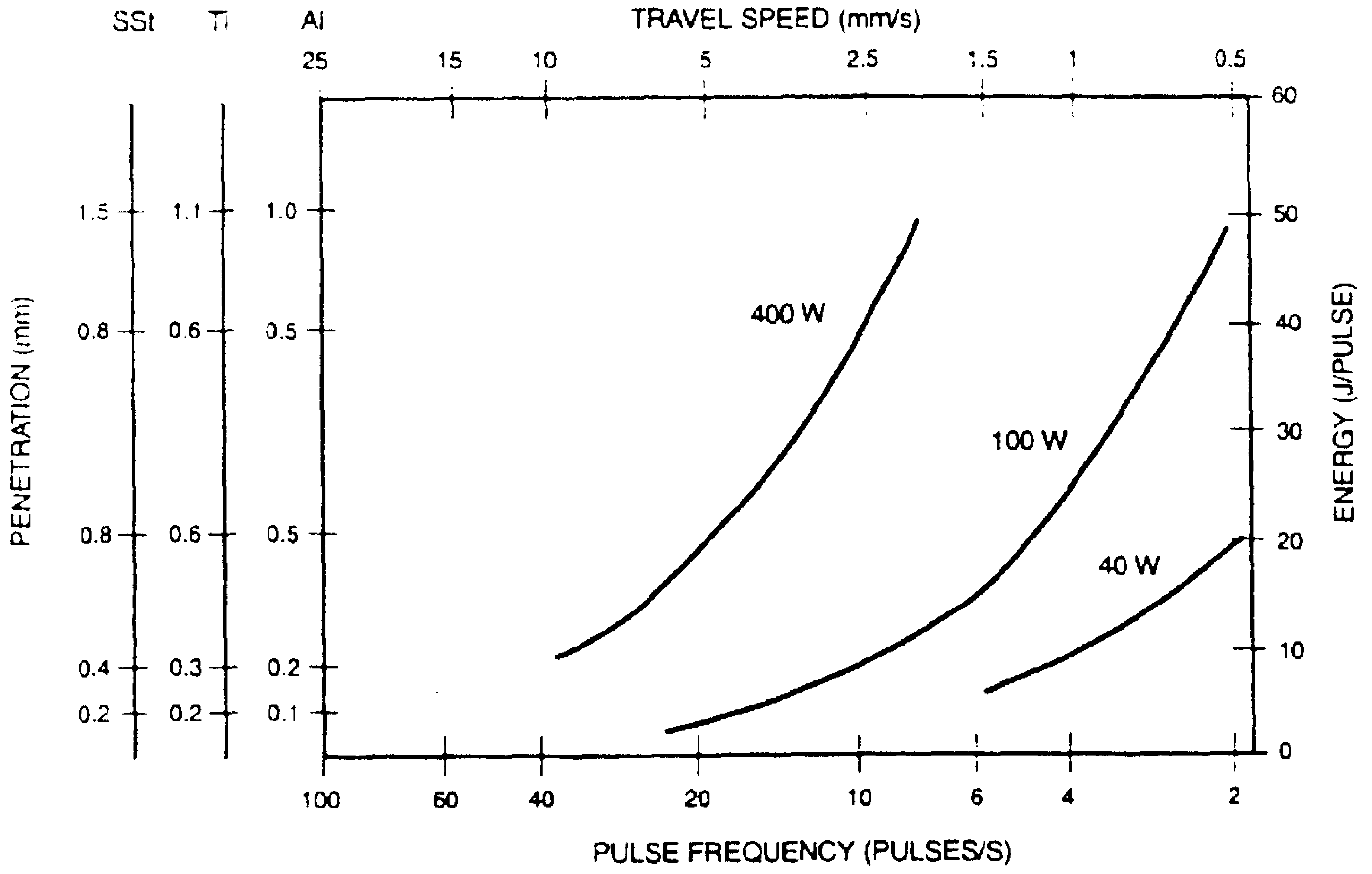

Figure 2.8 Dependence of penetration in three metals on the operating conditions for Nd:YAG pulsed lasers with three average power values [1]

2.6 Summary

Compared with other sealing welding methods, the laser beam welding process is suitable for micro package hermetic sealing. The Nd:YAG laser is the most developed technique for such application. The diode laser is perhaps not suitable for micro package welding due to poor beam quality. The fibre laser is the newest type of laser which can create very thin weld zones. Keyhole mode welding and pulsed laser welding create thin weld zones compared with conduction mode welding and continuous wave laser welding. There are more parameters which can be used to control the welding process in pulsed laser welding rather than in continuous wave laser welding. However, the melting pool in keyhole mode welding and pulsed laser welding is less stable than in continuous wave welding or conduction mode welding.

References:

[1] American Welding Society. Recommended Practices for Laser Beam Welding, Cutting, and Drilling: ANSI/AWS 1998.

[2] J.Oh. N.J.Kim, S.Lee and E.W.Lee. Correlation of fatigue properties and microstructure in investment cast Ti-6Al-4V welds. *Materials Science and Engineering*. 2003; A340:232-42.

[3] Y.Qi. J.Deng, Q.Hong, L.Zeng. Electron beam welding, laser beam welding and gas tungsten arc welding of titanium sheet. *Materials Science and Engineering*. 2000; A280:177-81.

[4] Z.Sun and R.Karppi. The application of electron beam welding for the joining of dissimilar metals: an overview. *Journal of Materials Processing Technology*. 1996; 59(3):257-67.

[5] D.Stavrov and H.E.N.Bersee. Resistance welding of thermoplastic composites-an overview. Composites Part A. *Applied Science and Manufacturing*. 2005; 36(1):39-54.

[6] C.Dawes. Laser welding: a practical guide. Jaico Publishing House 1994.

[7] K.F.Kleine, W.J.Fox, K.G.Watkins. Micro Welding with Pulsed Single Mode Fiber Lasers. Proceedings of the 23rd international congress on applications of laser and electro-optics; 4-7 October 2004; San Francisco California: Laser institute of American; 4-7 October 2004.

[8] S.E.Anthony. Lasers. University Science Books 1986.

[9] L.Q.Zhu, J.C.Niu, S.L.Zhu, Z.J.Xue. Application of Modern Laser Engineering. 1st ed. Beijing: National Defense Industry Press 2008.

[10] K.Maeda, M.Kumagai and K.Namba. Application of diode laser to welding of aluminium alloys. *Welding international*. 2003; 17(11):860-3.

[11] C.A.Walsh, H.K.D.H.Bhadeshia, A.Lau, B.Matthias, R.Oesterlein and J. Drechsel. Characteristics of High-Power Diode-Laser Welds for Industrial Assembly. *Journal of Laser Applications*. 2003; 15(2):68-76.

[12] Y.Okamoto, A.Gillner and A.Olowinsky. Fine micro-welding of thin metal sheet by high speed laser scanning. In: Photonic materials d, and applications II editor. Proc of SPIE; 2007; Maspalomas, Gran Canaria, Spain; 2007. p. 65930D 1-10.

[13] A.B.Short. Gas tungsten arc welding α+β Titanium alloy: a review. *Material Science and Technology*. 2009; 25:309-24.

[14] T.Y.Kuo and S.L.Jeng. Porosity reduction in Nd-YAG laser welding of stainless steel and inconel alloy by using a pulsed wave. *Journal of physics D: applied physics*. 2005; 38:722-8.

[15] F.Caiazzo, F.Curcio, G.Daurelio and F.Memola Capece Minutolo. Ti6Al4V sheets lap and butt joints carried by CO2 Laser: mechanical and morphological characterization. *Journal of Materials Processing Technology*. 2004; 149:546-52.

[16] L.Zhang, S.L.Gobbi, I.Norris, S.Zototovsky and K.H.Richter. Laser welding techniques for titanium alloy sheet. *Journal of materials processing technology*. 1997; 65:203-8.

[17] S.H.Wang, M.D.Wei, L.W.Tsay. Tensile properties of LBW welds in Ti-6Al-4V alloy at evaluated temperatures below 450°C. *Materials Letters*. 2003; 57(12):1815-23.

[18] T.Chai and C.K.Chou. Mechanical properties of laser-welded cast titanium joints under different conditions. *Journal of prosthetic dentistry*. 1998:477-83.

[19] P.W.Fuerschbach and G.A.Knorovsky. A study of Melting Efficiency in Plasma Arc and Gas Tunsgten Arc Welding. *Welding Journal*. 1991; 70(10):287s-197s.

CHAPTER 3

Chapter 3 Literature Review: Structure and Properties of Titanium and Titanium Alloys

Ti6Al4V alloy is widely used in the aerospace and medical device industries for its desirable properties: strength to weight ratio, corrosion resistance, biocompatibility and processability (casting, deformation, powder metallurgy, machinability, welding, brazing, etc.) [1-4]. Previous researchers have indicated that the mechanical properties (strength and toughness) of Ti6Al4V alloy are quite sensitive to microstructure [2, 5, 6]. The microstructures are controlled by heat treatment generally at temperatures in the dual α-β phase region [7, 8]. A basic understanding of Ti6Al4V and its microstructure, mechanical properties and fatigue properties are presented in this chapter.

3.1 α&β phases in Ti6Al4V

Titanium exists in two crystalline states: a low-temperature alpha (α) phase (hexagonal close-packed (h.c.p.) crystal structure), and a high-temperature beta (β) phase (body centered cubic (b.c.c.) crystal structure) (Figure 3.1). The allotropic transformation occurs at 882.5 °C [4] in nominally pure titanium.

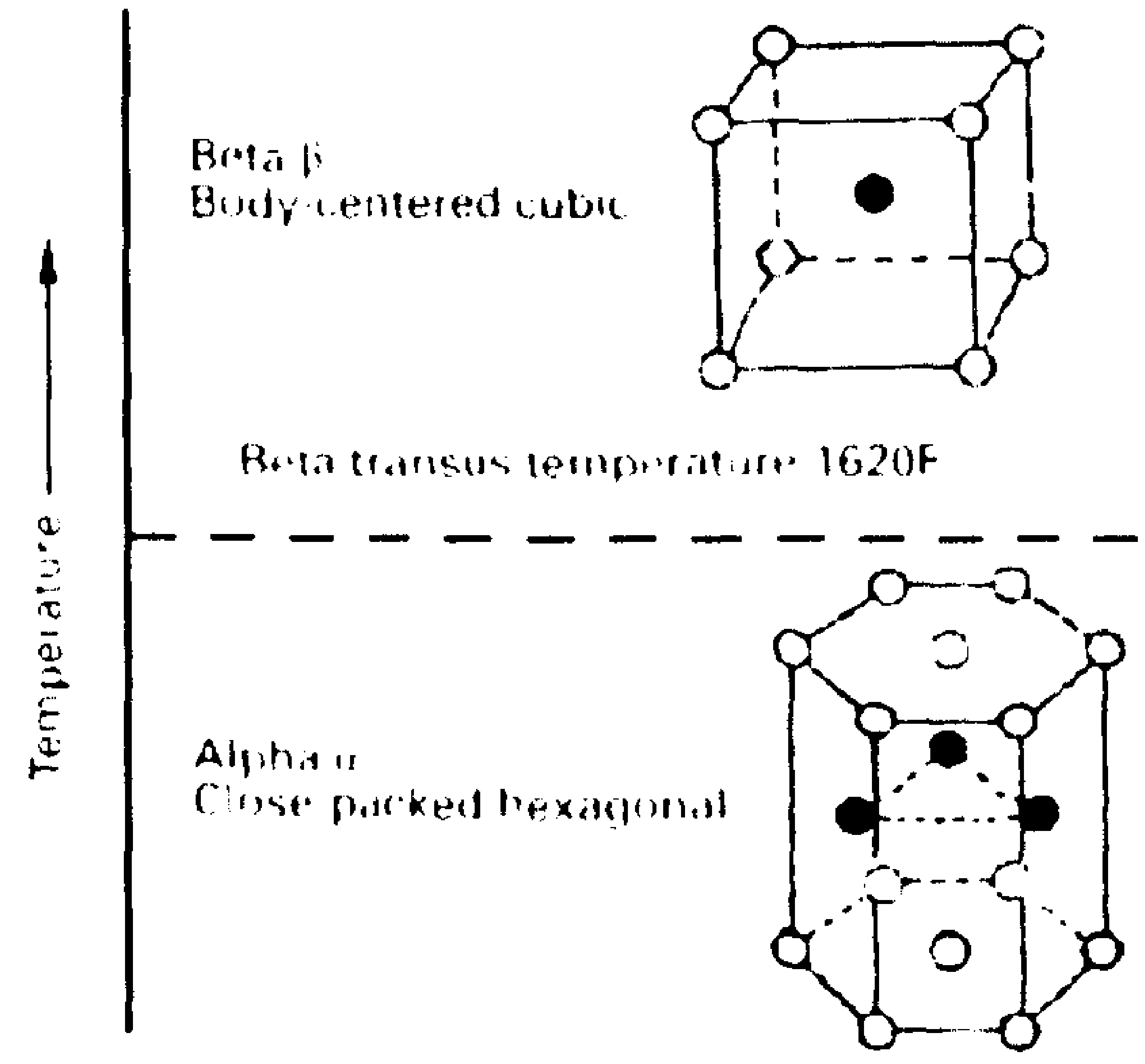

Figure 3.1 Crystal structure of hcp α and bcc β phase[9]

Alloying of titanium is dominated by the ability of elements to stabilize either of the α- or the β- phases. Generally, titanium alloys are classified into three main groups: α, α+β and β. α+β alloys are the most widely used of the titanium alloy [2, 5, 6]. Most of α+β alloys contain 4-6% β-stabilizing elements and are quenched from β or α+β phase fields. Among the α+β alloys, Ti-6Al-4V is the most popular titanium alloy, so that more than 50% of all titanium alloys in use today are of this composition [9]. Other commonly used α+β alloys include Ti-6Al-6V-2Sn, Ti-6Al-2Sn-4Zr-6Mo, Ti-6Al-2Sn-2Zr-2Mo-2Cr-0.25Si and Ti-5Al-2Sn-2Zr-4Mo-4Cr.

Table 3.1 summarizes the main properties of α, α+β and β titanium alloys. Table 3.2 shows a qualitative comparision of characteristics of titanium alloy which include Ti6Al4V. As can be seen, α alloys show higher ductility but lower strength. On the other hand, β alloys exhibit higher strength but lower ductility and poor weldability. In contrast, α+β alloy (Ti6Al4V) shows a good balance of strength and ductility.

Table 3.1 Mechanical properties of three types titanium alloys [9]

Alloy	Chemical composition [wt.%]	T_β [°C]	Hardness [HV]	E [GPa]	YS [MPa]	TS [MPa]	%El
α-alloy							
High purity Ti	99.98 Ti	882	100	100-145	145	235	50
α+β alloy							
Ti-6-4	Ti-6Al-4V	995	300-400	110-140	800-1100	900-1200	13-16
β-alloy							
SP 700	Ti-4.5Al-3V-2Mo-2Fe	900	300-500	110	900	960	8-20

*** T_β - Beta transus temperature; E – Young's Modulus; YS – Yield stress; TS – Tensile stress; El - Elongation**

Table 3.2 Qualitative comparision of characteristics of α, α+β and β Ti alloy [9]

	α	α+β	β
Strength	-	+	++
Ductility	++	+	--
Weldability	++	+	-

***+ stands for high, - stands for low**

3.2 Microstructure of Ti6Al4V

3.2.1 Lamellar versus equiaxed microstructure

The microstructure of titanium alloys are generally described by the size and arrangement of the α and β phases. The two extreme cases of phase arrangements are the lamellar microstructure (with a greater α/β surface area and more oriented colonies) (Figure 3.2 (a)), which is generated upon cooling from the β phase field, and the equiaxed microstructure (uniform structure composed of α-grains and grain boundaries of β [4]) (Figure 3.2 (b)), which is result of a recrystallization and globularization process [9].

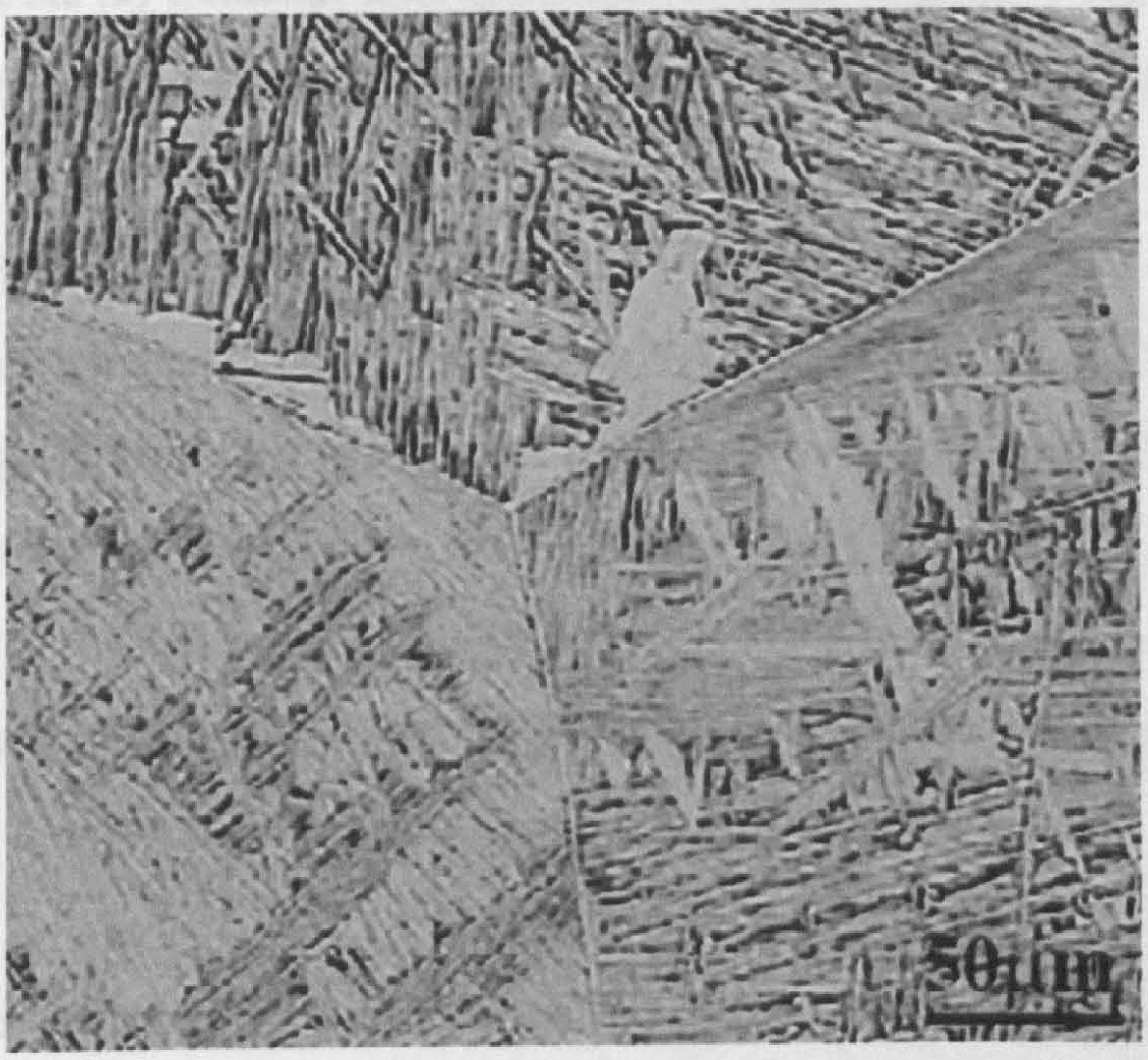

(a)

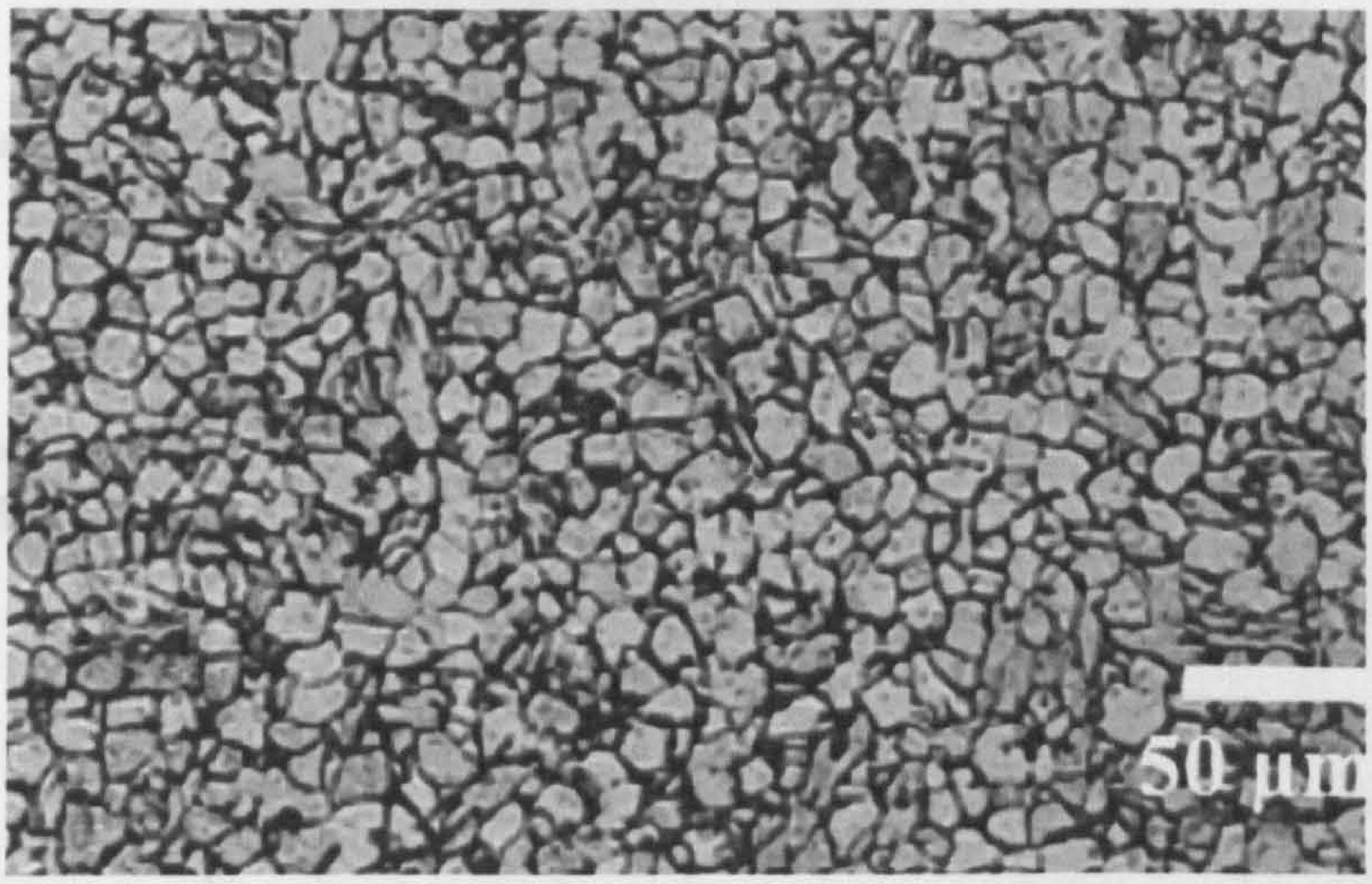

(b)

Figure 3.2 (a) Lamellar microstructure of Ti6Al4V [10] (b) Equiaxed microstructure of Ti6Al4V from heat treatment at 950°C for 4 hours [11]

Figure 3.3 shows the β-transus temperature of Ti6Al4V. The β-transus, T_β is a boundary line between β phase and α+β phase fields in the equilibrium phase diagram. Only the single β phase field exists above β-transus line. The β-transus temperature of Ti-6Al-4V is 980°C [8]. Lamellar microstructures result from simple cooling from temperatures above the β-transus temperature [9]. Once the temperature falls below the transus temperature, α nucleates (light region) at grain boundaries and grows as lamellae into the prior β grain (dark region) [10].

The equiaxed microstructure is always from refinement globularization during annealing. Generally, the annealing process for Ti6Al4V is conducted in the temperature range of 850-950°C [11], for several hours, followed by furnace cooling or air cooling.

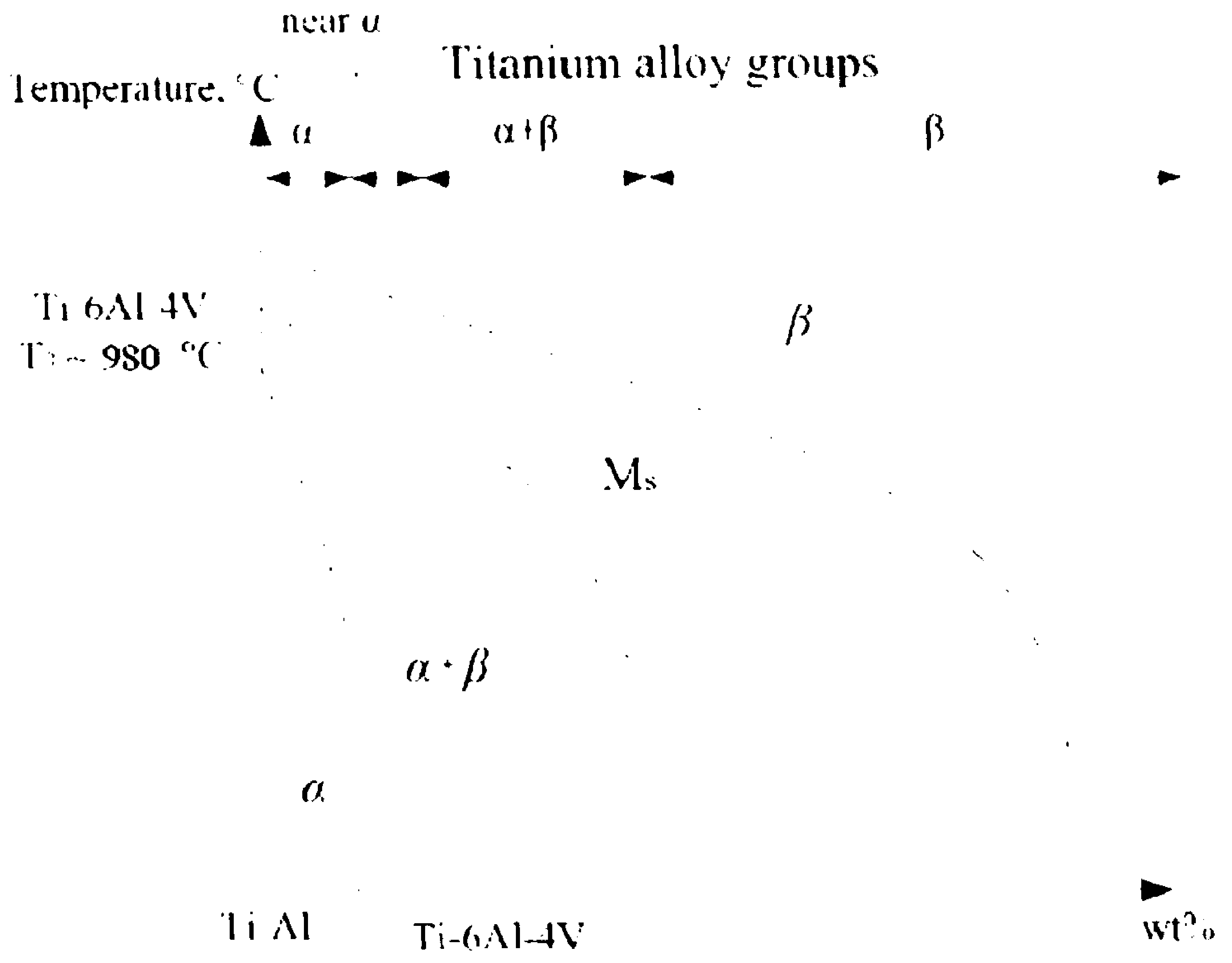

Figure 3.3 Schematic section of the ternary phase equilibrium diagram [12]
***MS: martensite start temperature, X axis stands for Vanadium content by weight percentage**

3.2.2 The effect of heat treatment on microstructure

The temperature and cooling rate during the heat treatment are two big factors which affect the microstructure of Ti6Al4V. There is a wide body of literature which describes these influences [2, 6, 10, 12, 13]. Figure 3.4 and Table 3.3 show typical microstructure development at 800, 950, and 1050°C for water cooling and air cooling heat treatment.

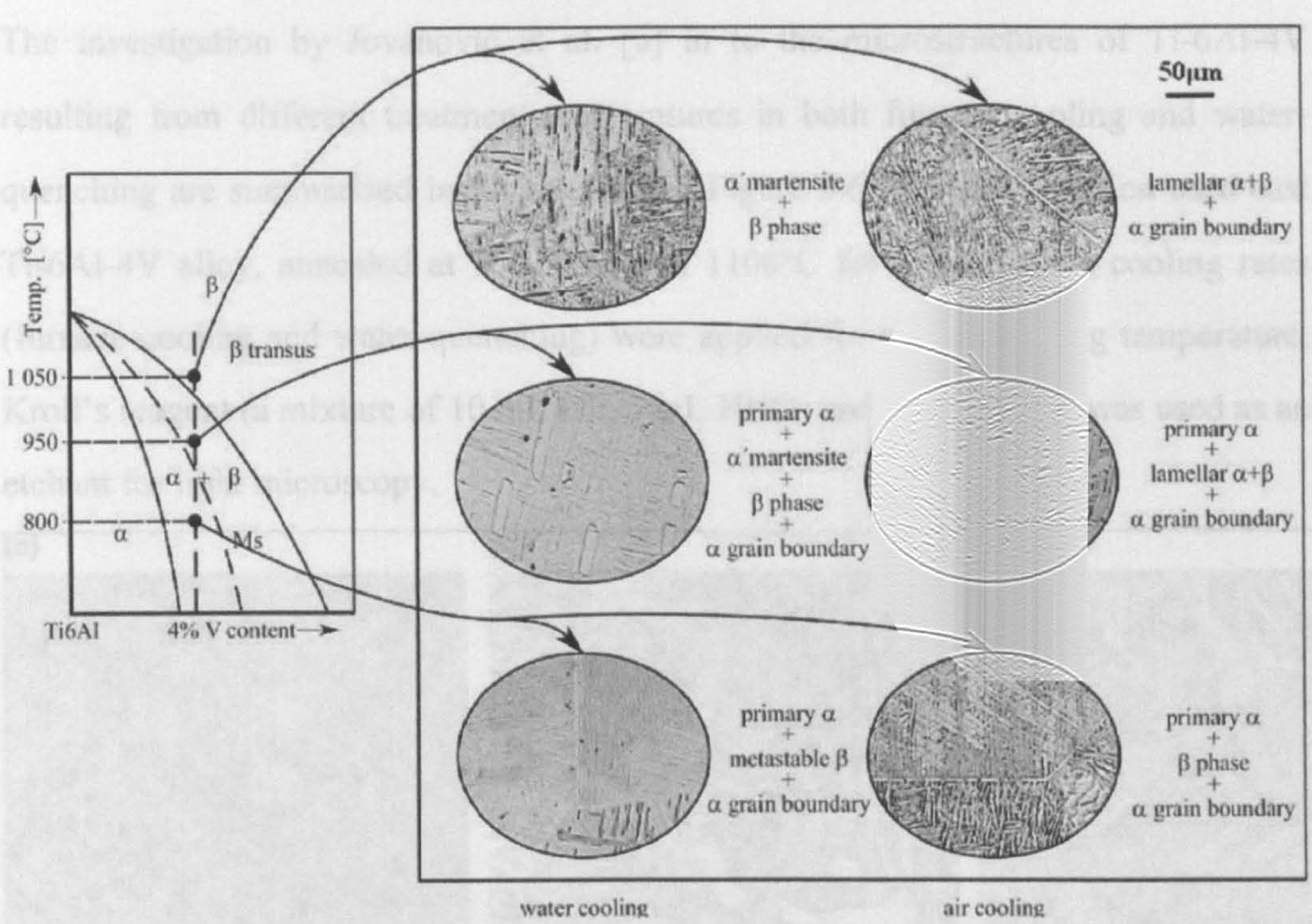

Figure 3.4 The microstructure developed at different heat treatment and cooling rate of Ti6Al4V [10]

Table 3.3 Evolution of microstructure in Figure 3.4

	Water cooling	**Air cooling**
1050°C	Rapid cooling rate from 1050°C leads to acicular α’ martensite structure. β phase can be between martensitic laths.	Slower cooling rate at 1050°C leads to the typical lamellar α+β structure with grain boundary α in the prior β grains.
950°C	A microstructure rapidly cooled from 950°C includes acicular α’ martensite and primary α.	A microstructure more slowly cooled from 950°C consists of a lamellar mixture of α+β phase, primary α and grain boundary α.
800°C	A metastable β phase with primary α and grain boundary α occurs with a fast cooling rate.	At slower cooling rate, β phase is observed instead of metastable β phase. The grain boundary α phase and primary α are observed with both water and air cooling from 800°C

The investigation by Jovanović et al. [6] in to the microstructures of Ti-6Al-4V resulting from different treatment temperatures in both furnace-cooling and water-quenching are summarized in Figure 3.5 and Figure 3.6. The investigation used cast Ti-6Al-4V alloy, annealed at 900, 950, and 1100°C for 1 hour. Two cooling rates (furnace-cooling and water-quenching) were applied for each annealing temperature. Kroll's reagent (a mixture of 10 mL HF, 5 mL HNO_3 and 85 mL H_2O) was used as an etchant for light microscopy.

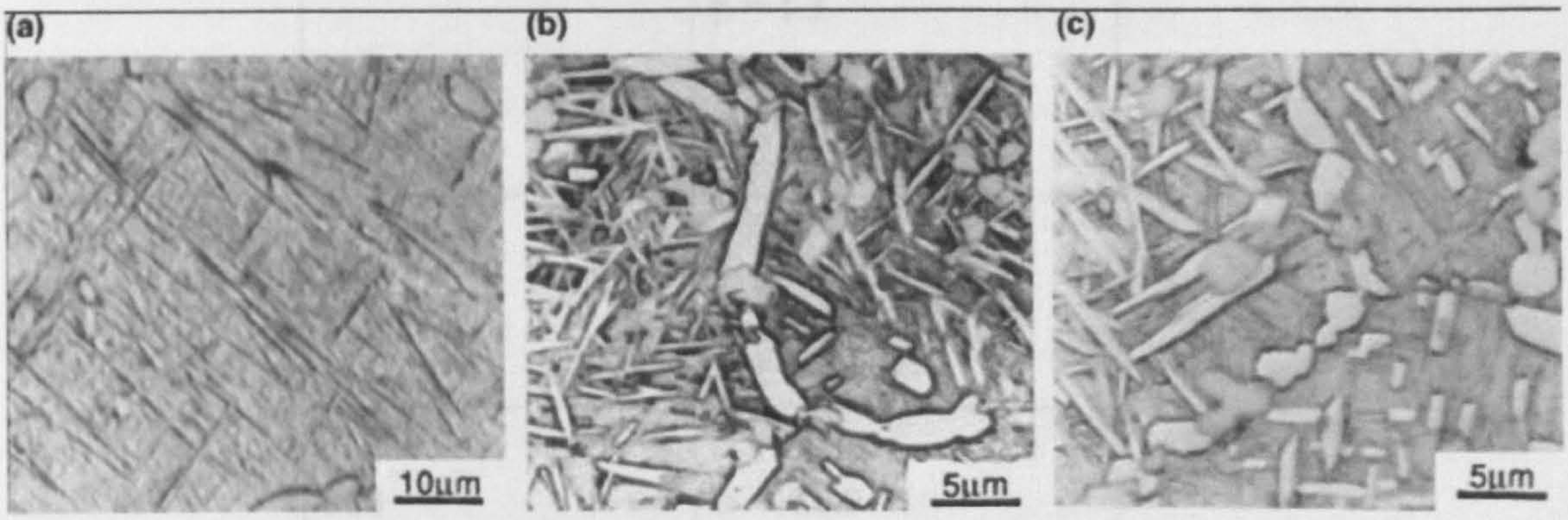

Figure 3.5 Microstructure upon water-quenching from: (a) 1100°C; (b) 950°C; (c) 900°C [6]

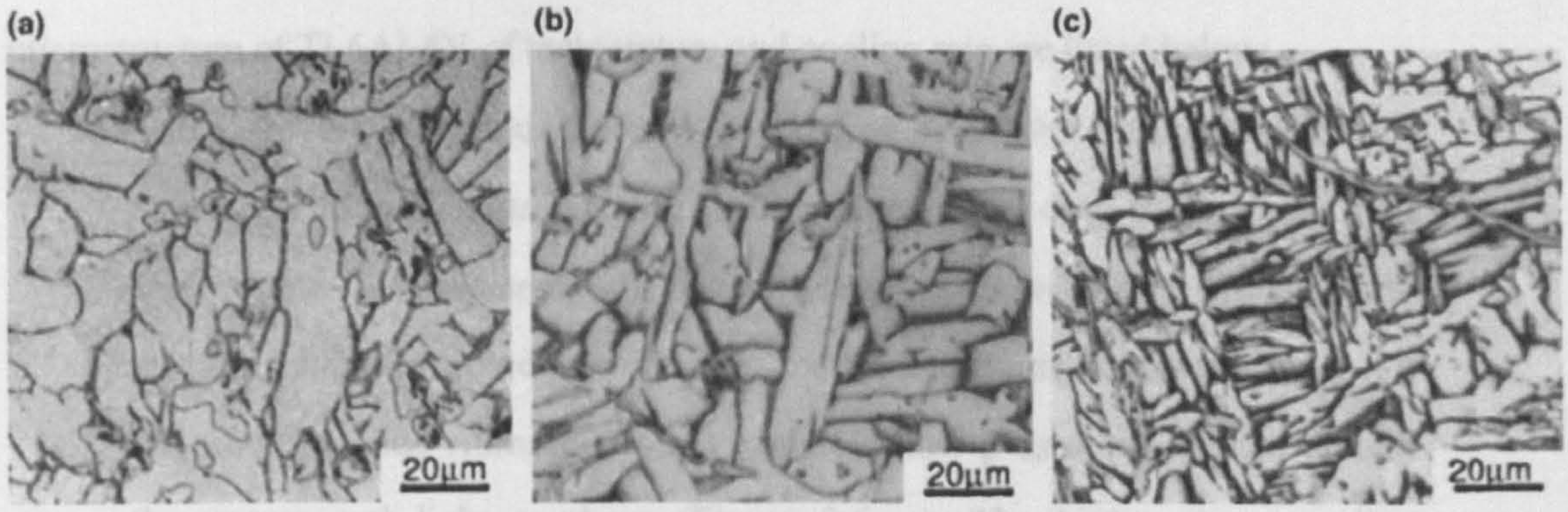

Figure 3.6 Microstructure upon furnace-cooling from: (a) 1100°C; (b) 950°C; (c) 900°C [6]

The cooling rate significantly influences the grain size. The slower the cooling rate is, the coarser the grain size will be, which has been shown by Jovanović's work (Figure 3.5a and Figure 3.6a). Rapid quenching leads to a martensitic transformation of β which causes a very fine needle-like microstructure (Figure 3.5a). Unlike ferrous martensites, titanium martensite is 'not significantly stronger or more brittle' [14] than its parent phase, and hardening effect for titanium alloy martensite is only moderate. Table 3.4 shows the volume fractions of the various phases as presented by Jovanović [6].

Table 3.4 volume fraction (%) of phase present as a function of heat-treatment for Ti6Al4V [6]

T (°C)	Water-quenching
1100	β = 1.3 α′= 98.7
950	α = 42.2 α′ ~ 50 - 57.8 β ~ 8
900	α = 63.1 α′ ~ 26.9 β ~ 10

Summarizing the research of Jovanović et al. on the effects of heat treatment on the microstructure of Ti-6Al-4V of temperature and cooling rate are listed below:

1. There are two possible products as cooling from the β-phase which are martensite α′ and metastable β. The martensite α′ only exists with high cooling rate (water-quenching). Higher temperatures within the β phase field result in a higher volume fraction of α′ and lower volume fraction of β.
2. All slowly cooled (furnace-cooled) samples show β as a small seam around the coarse and light α phase (Figure 3.6a-c). The higher the annealing temperature is, the larger the thickness of the α phase is (Figure 3.6a-c)

The microstructures developed at different heat treatment and cooling rate of Ti6Al4V from Pinke et al. [10] and Jovanović et al. [6] shows some differences except in that from water-quenching above β transus temperature. The reason is that the Ti6Al4V parent materials they used were different as shown in Figure 3.7.

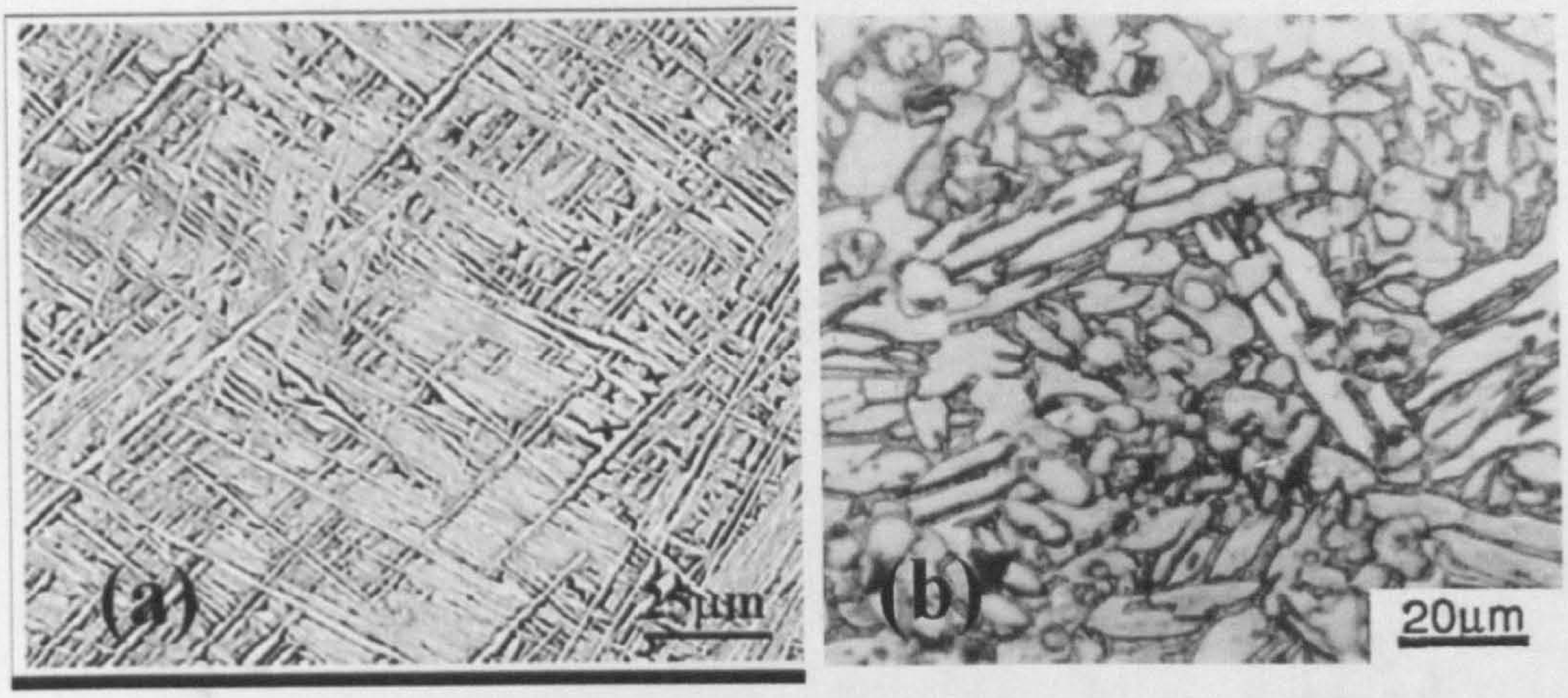

Figure 3.7 The parent materials used by (a) Pinke et al.'s precision cast Ti6Al4V (b) Jovanović et al.'s investment cast Ti6Al4V [6, 10]

Besides the temperature and cooling rate, heat treatment time will also affect the grain size. Figure 3.8 shows grain size results from Ti6Al4V cylindrical rods (13 mm in diameter by 11 cm in length) heat treated at 1050, 1100, 1150 and 1200°C, for 5, 10, 15, 20, 30, 60 and 120 minutes by Gil et al. [2].

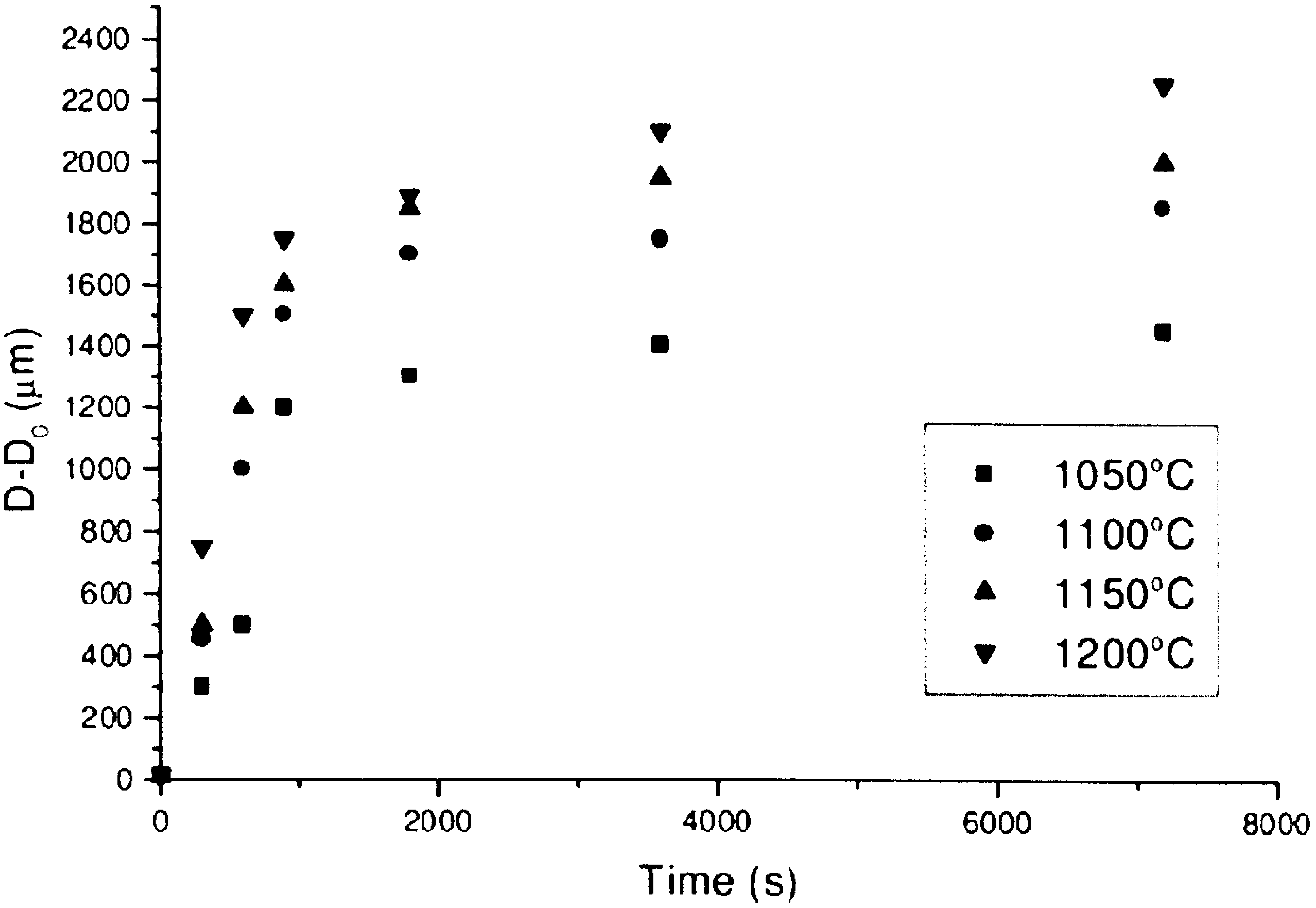

Figure 3.8 Increase of the grain diameter in relation to temperature and duration of heat treatment of Ti6Al4V. D is the grain size at a certain time, D_0 is the initial grain size [2]

3.2.3 Widmanstätten structure in Ti6Al4V

During the heat treatment, a structure named the Widmanstätten structure may be found in Ti6Al4V. As a classical structure in Ti6Al4V from heat treatment, Widmanstätten structure is discussed especially here. The original Widmanstätten patterns, named after Count Alois von Beckh Widmanstätten, were unique structures of long nickel-iron crystals, found in the octahedrite iron meteorites. The Widmanstätten structure in Ti6Al4V is observed when materials are cooled at a critical rate from extremely high temperature. Figure 3.9 shows the microstructure development due to cooling rate. At low cooling rate (between 410°Cs^{-1} and 20°Cs^{-1}), massive α-plates (α_m) grow from the grain boundary and α colonies are formed. When the cooling rate is below 20°Cs^{-1}, α colonies change into basket weave structure (Widmanstätten). Ahmed [15] indicated, for a heat treatment at 1050°C for 30 min, Widmanstätten is formed when cooling rate is below 20°Cs^{-1}.

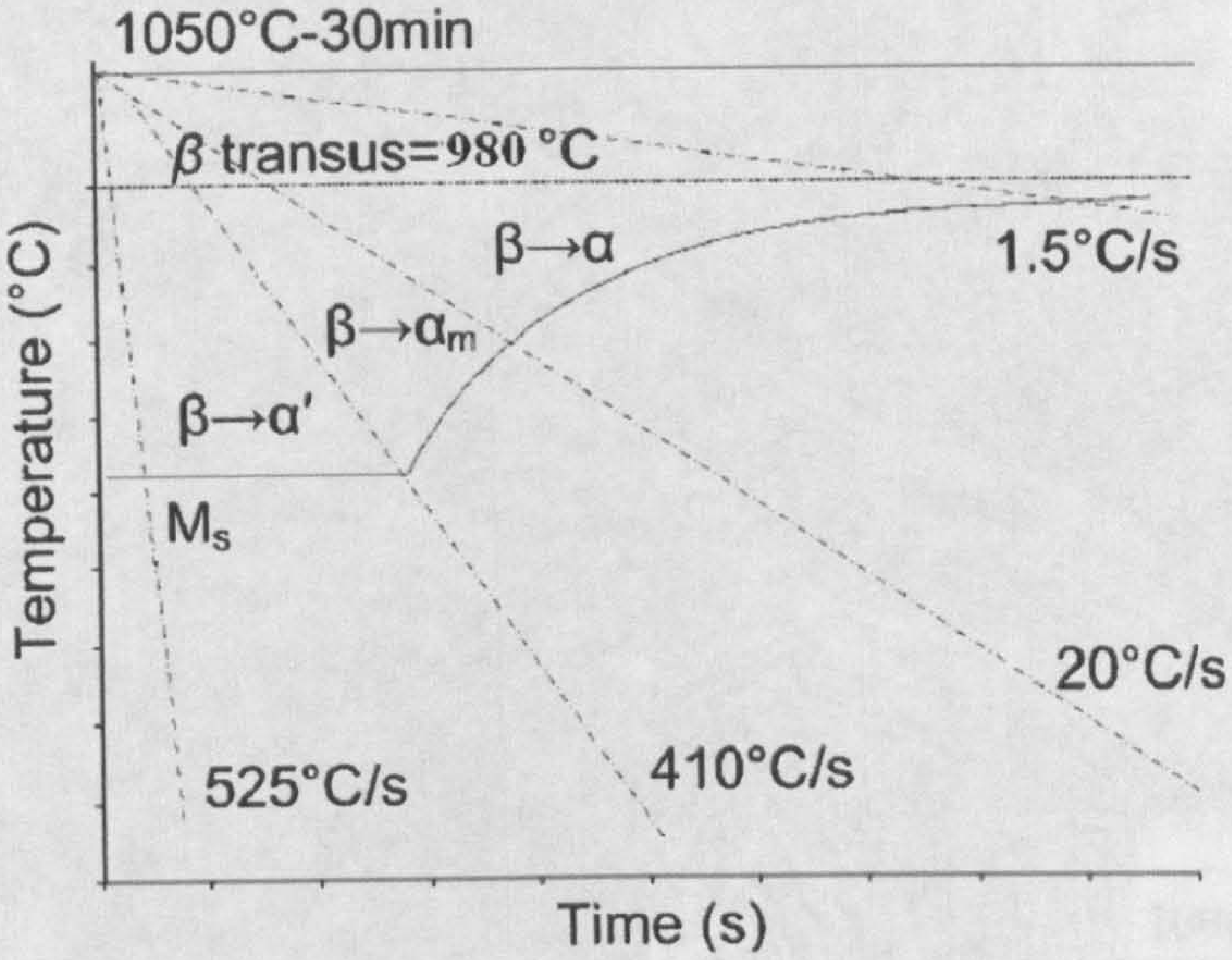

Figure 3.9 Schematic continuous cooling transformation diagrams for Ti6Al4V [15]

The influence of the cooling rate on the α colony plate sizes can be observed in Figures 3.10-3.12 for 0.23, 0.81 and 3.40°Cs^{-1} cooling rates from 1100°C, respectively. The width of Widmanstätten plates tend to be thicker as the cooling rate decreases. The reduced cooling rates allow greater diffusion distances which generate coarser α colony plates [2].

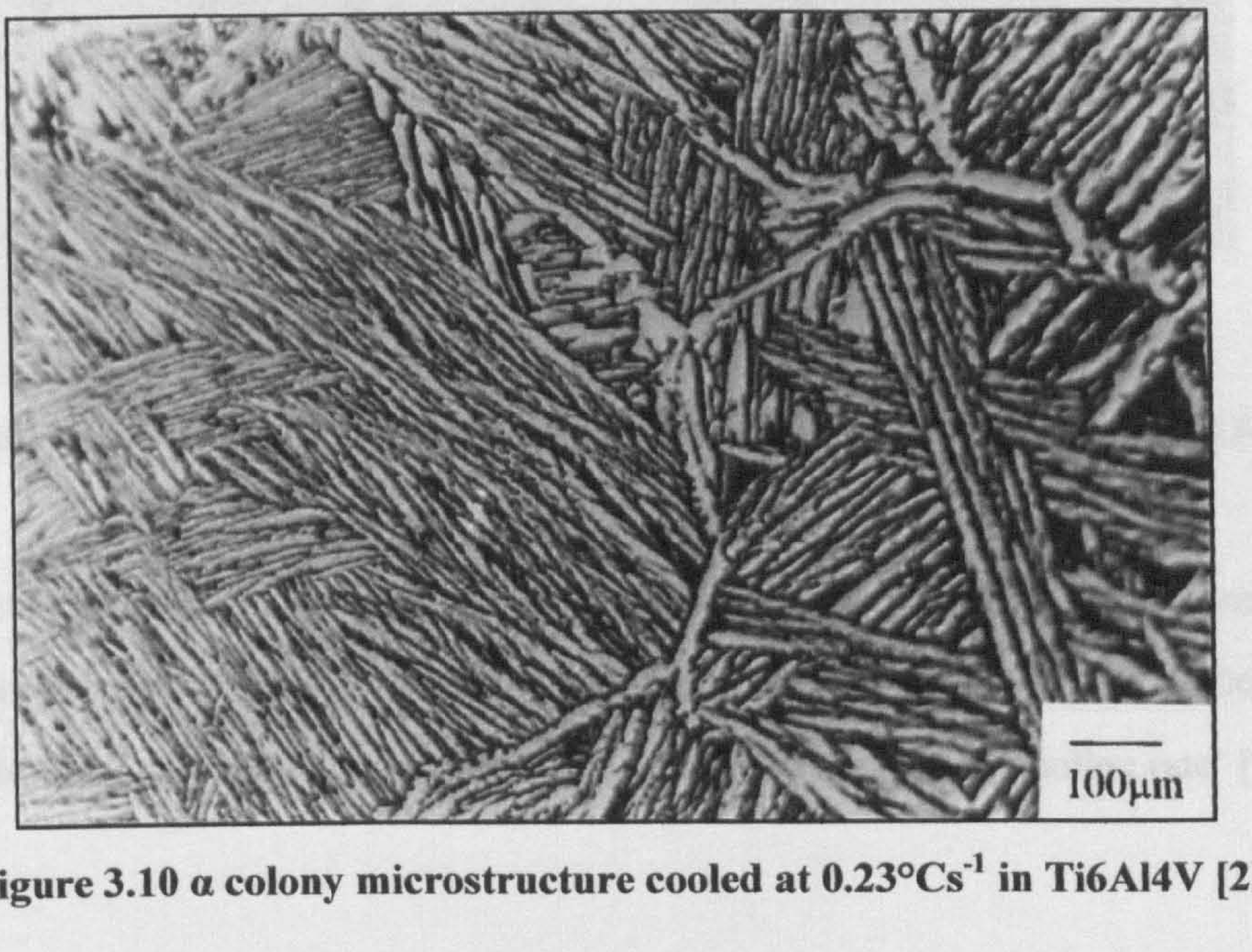

Figure 3.10 α colony microstructure cooled at 0.23°Cs^{-1} in Ti6Al4V [2]

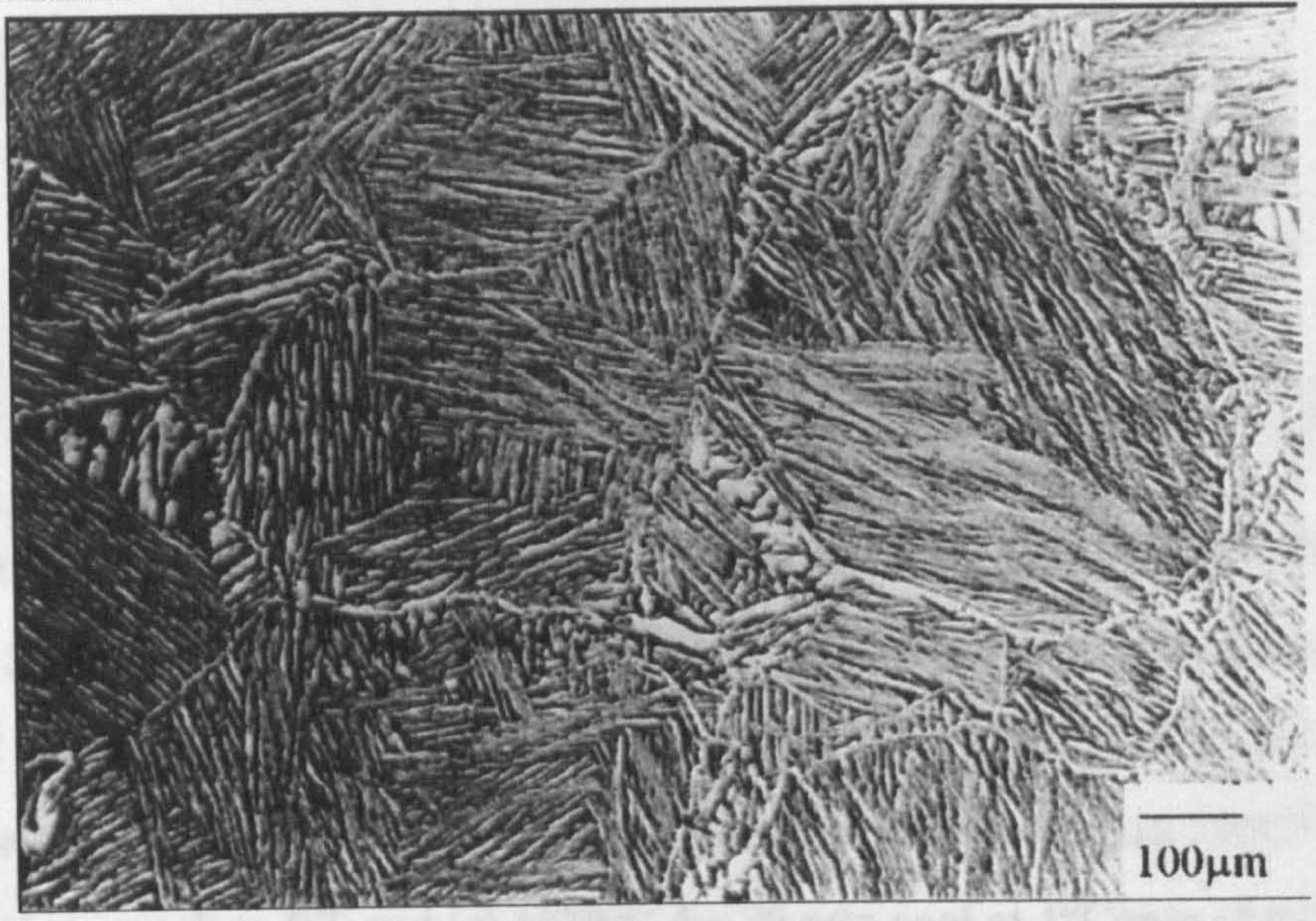

Figure 3.11 α colony microstructure cooled at 0.81°Cs^{-1} in Ti6Al4V [2]

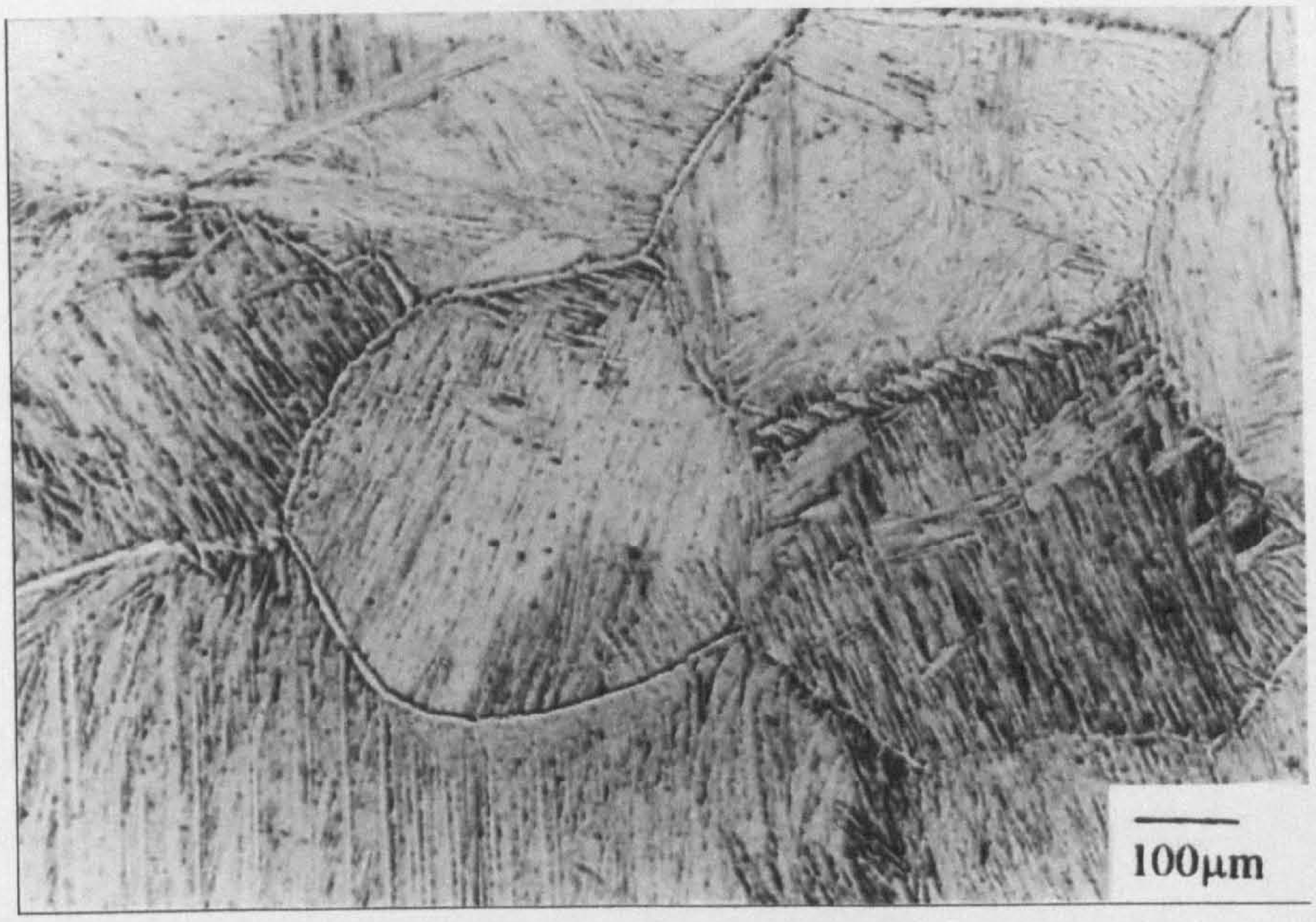

Figure 3.12 α colony microstructure cooled at 3.40°Cs^{-1} in Ti6Al4V [2]

Similar results from Shademan et al. [8] also showed that the size of colony increases with decreasing cooling rate (Figure 3.13). They stated that this is 'due to the lower nucleation rate and higher growth rate associated with the slower cooling rate' [8].

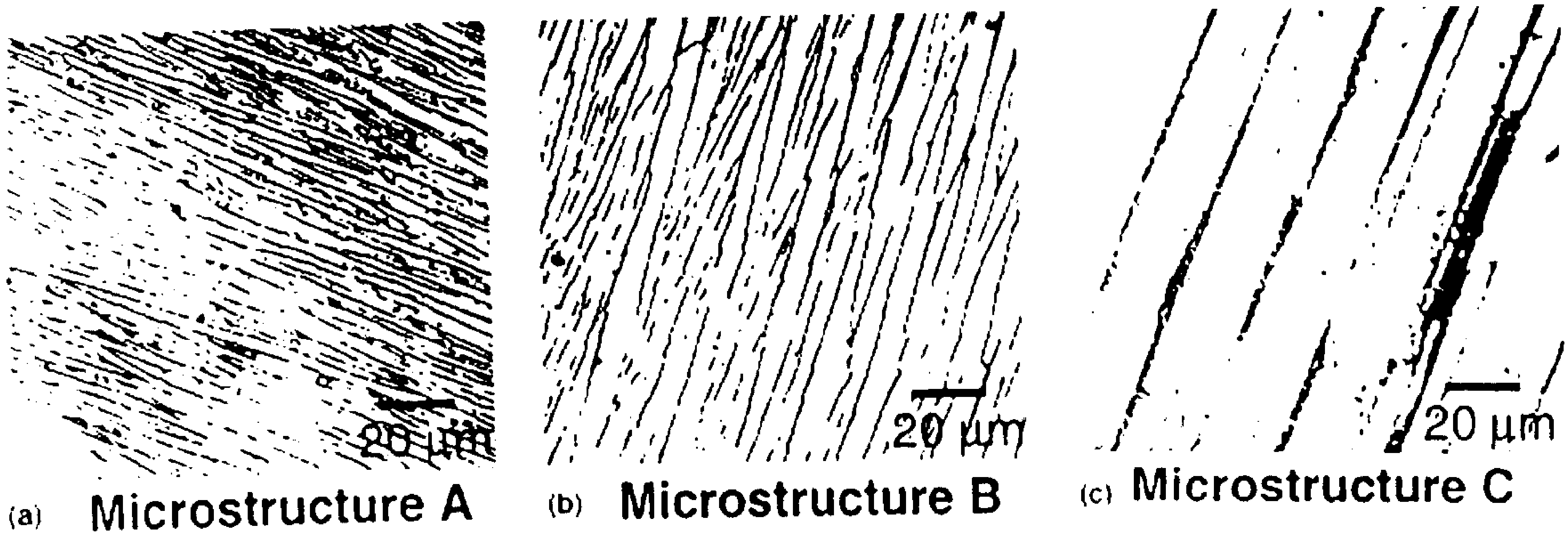

(a) Microstructure A (b) Microstructure B (c) Microstructure C

Figure 3.13 Microstructural modifications in Ti6Al4V after heat treatments. (a) 1070°C for 30 min cool at 25 °C/min (0.42°Cs^{-1}) to 400 °C/Ar quench to Room Temperature (RT), (b) 1070°C for 30 min cool at 3 °C/min (0.05°Cs^{-1}) to 400 °C/Ar quench to RT and (c) 1070°C for 30 min cool at 1°C/min (0.02°Cs^{-1}) to 400°C/Ar quench to RT. [8]

3.3 The effect of microstructure on mechanical properties of Ti6Al4V

The mechanical properties of Ti6Al4V are strongly affected by the grain size and microstructure. The comparison of characteristics of Ti6Al4V as a function of the various microstructures is summarized in Table 3.5:

Table 3.5 Qualitative comparison of influence of microstructure on characteristics of titanium alloys [9]

Fine	Coarse	Property	Lamellar	Equiaxed
+	-	Strength	-	+
+	-	Ductility	-	+
+	-	Fatigue crack initiation resistance	-	+
-	+	Fatigue crack propagation resistance	+	-

***+ stands for good, - stands for bad**

The effect of grain size on yield strength is described by the well-known Hall-Petch equation:

$$\sigma_y = \sigma_o + \frac{K}{\sqrt{d}}$$ **Equation 3.1**

where k is the strengthening coefficient (a constant unique to each material), σ_o is the starting stress for dislocation movement (or the resistance of the lattice to dislocation motion), d is the grain diameter, and σ_y is the yield stress.

Sirilar and Srichandr's [11] research showed that with an increase of grain size from 8 to 20 μm, the tensile strength and yield strength slightly dropped off. At the same time, the different grain types can affect the tensile properties (Figure 3.14).

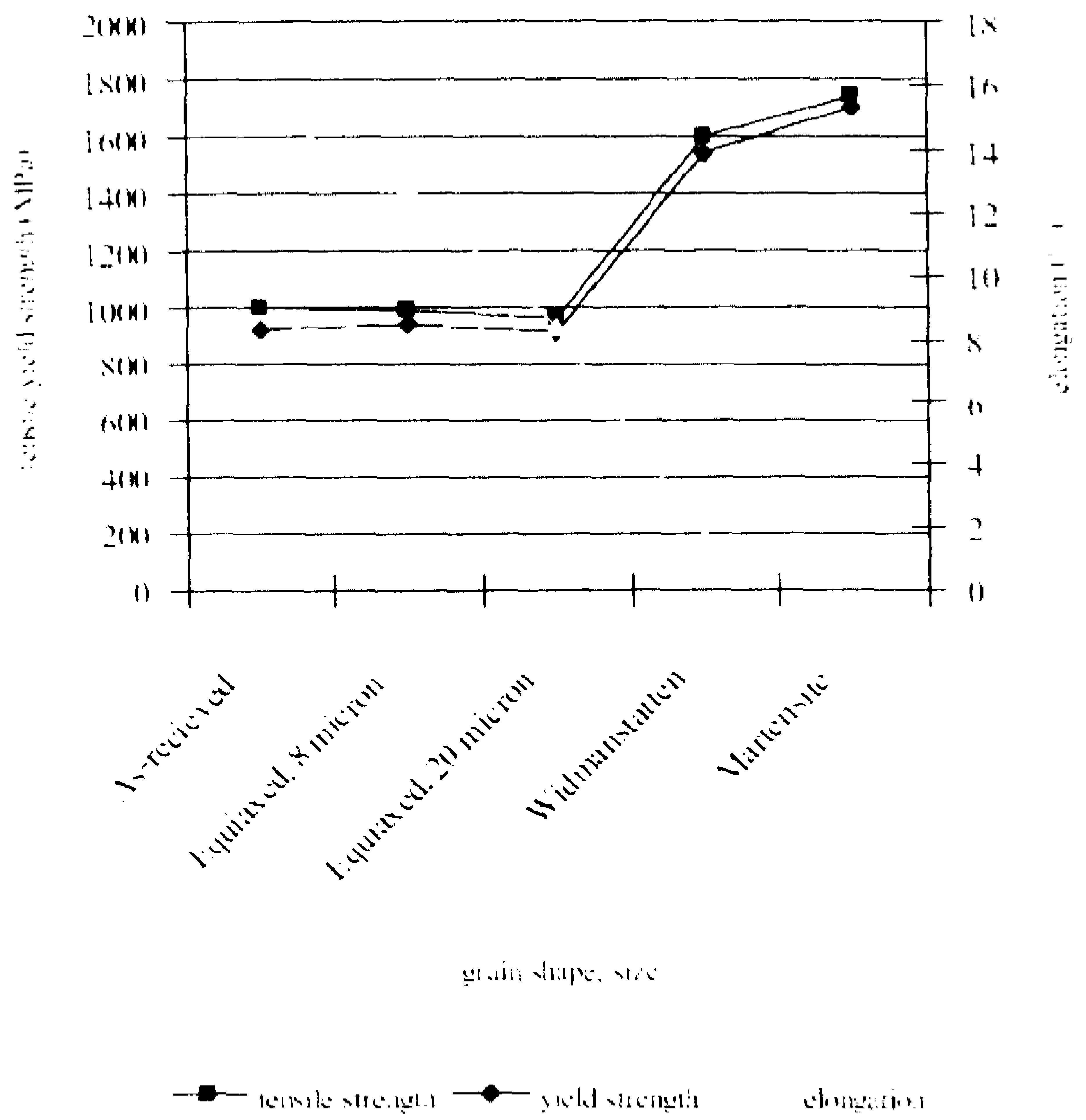

Figure 3.14 Tensile properties of Ti6Al4V effected by different types of microstructure and grain size [11]

Jovanović et al. [6] have investigated the hardness, tensile strength, and elongation to failure of Ti-6Al-4V which was heat treated at different temperatures and with different cooling rates (Figure 3.15 and Figure 3.16).

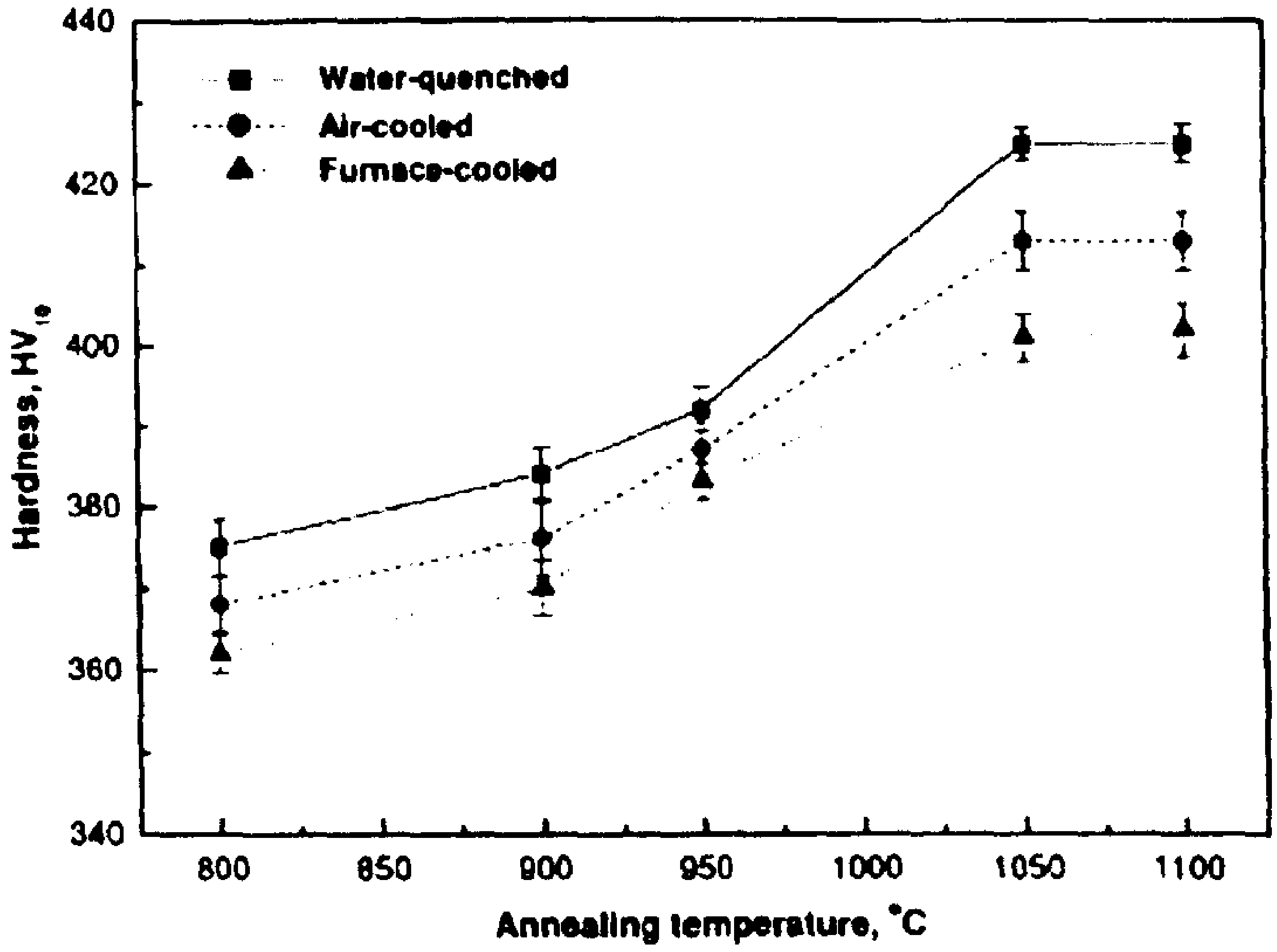

Figure 3.15 The effect of different annealing temperatures and cooling rates on hardness of Ti6Al4V [6]

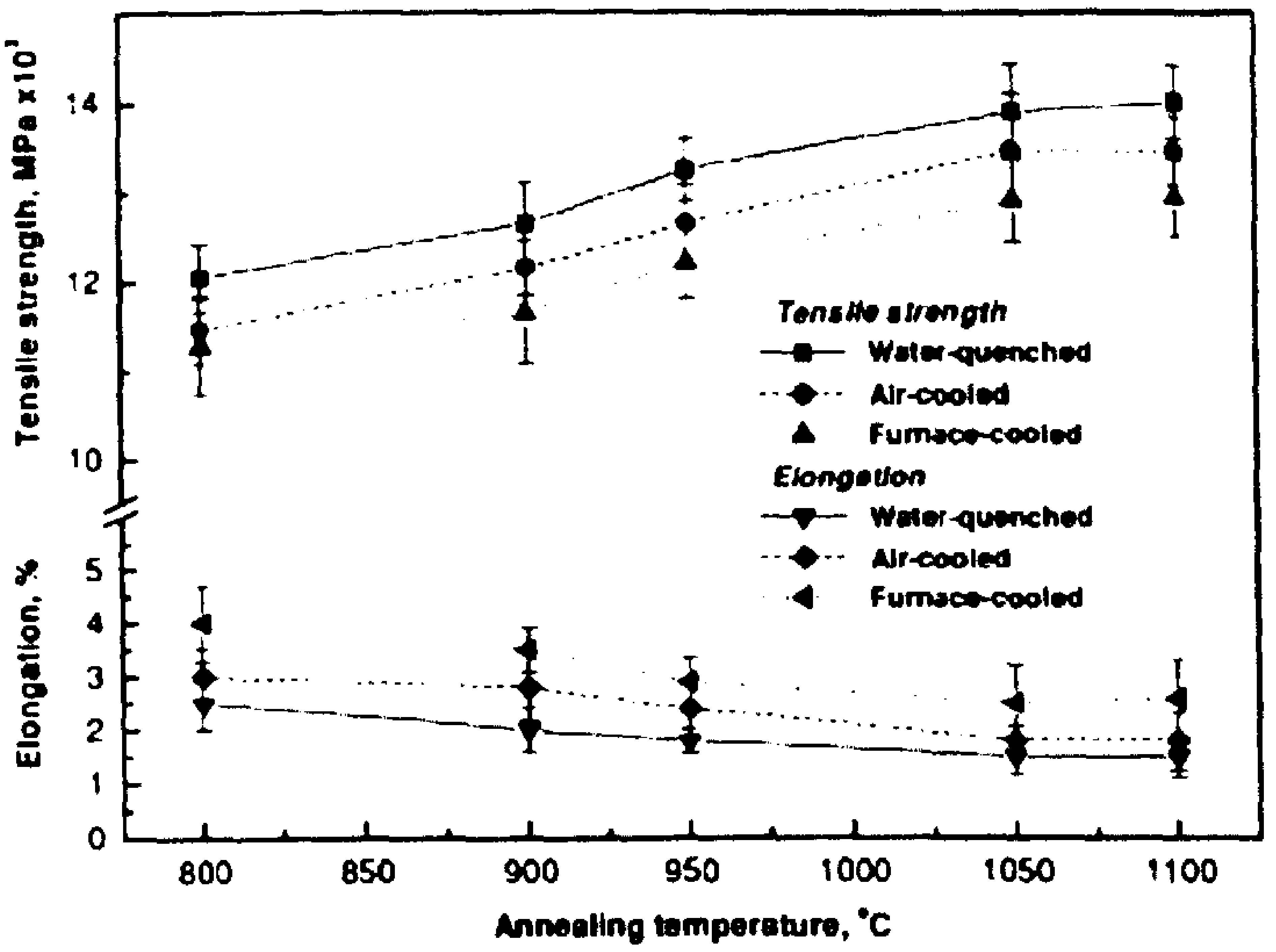

Figure 3.16 The effect of different annealing temperatures and cooling rates on tensile strength and elongation of Ti6Al4V [6]

As the cooling rate increased, both the hardness and tensile strength increased. On the other hand, elongation decreased with the increase of cooling rate. These results form an increase in metastable β with cooling rate, which itself is strong but exhibits poor ductility. The higher the temperature of heat treatment for all cooling rates, the higher the value of hardness and tensile strength and, the lower the value of elongation will be. For rapid cooling rates (water-quenched), higher temperature means more metastable β (Table 3.4). For slow cooling rate (air-cooled and furnace-cooled), higher temperature results in the formation of large grains which exhibit poor ductility (Table 3.5). The reason that the strength is higher is that higher temperature results in more metastable β which confers high strength, although large grains result in low strength. This implies phase content dominates the mechanical properties of Ti6Al4V rather than grain size. In addition, the highest value of hardness and tensile strength accompanied the lowest elongation for α′ martensite.

Figures 3.17 and 3.18 show the resulting mechanical properties at room temperature for each cooling rate (v) in terms of tensile strength, yield stress and ductility. From 0.23°Cs^{-1} to 1.5°Cs^{-1}, the yield stress and ductility are very sensitive to cooling rate. Then, the properties change little between 1.5°Cs^{-1} and 3.5°Cs^{-1}, whereupon the strength levels increase sharply as the transformation moves from forming Widmanstätten to martensite. The cooling rate for forming Widmanstätten structures here is very different from Ahmed's [15] results. The explanation is perhaps found in the sample size. In Ahmed's research, the sample was 31.8 mm diameter bar; in Gil's research, the sample was 13 mm in diameter.

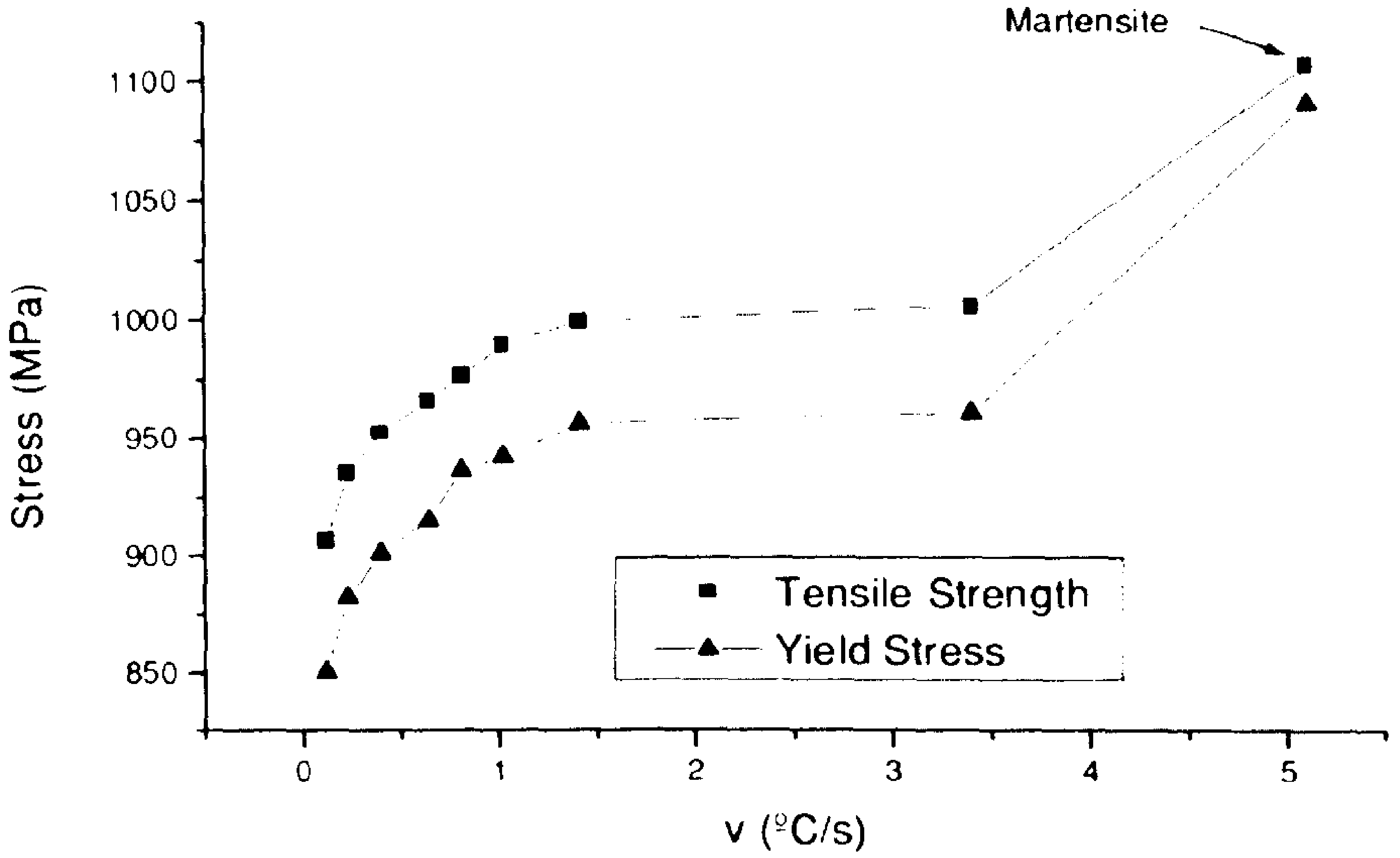

Figure 3.17 The influence of cooling rate on mechanical strength and yield stress for Ti6Al4V [2]

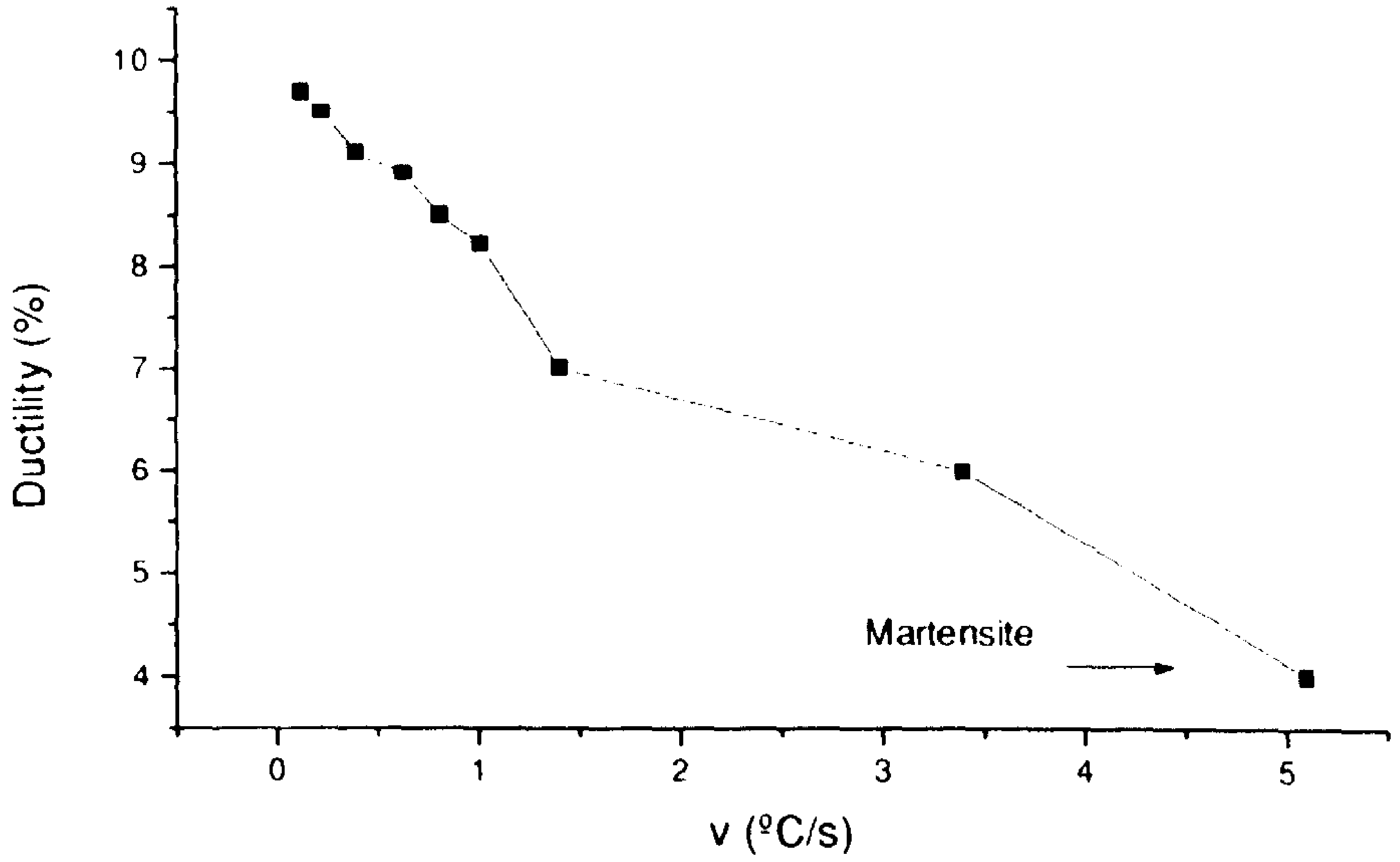

Figure 3.18 The influence of cooling rate on ductility for Ti6Al4V [2]

3.4 Fatigue behaviour of Ti6Al4V

The term 'fatigue' relates to the initiation and growth of cracks (normally in metallic materials) due to the repeated application of mechanical stresses or strains and any associated changes in mechanical properties [16]. Most welded micro package components are subjected to cyclic loading, and fatigue and fracture eventually occur. The fatigue behaviour can be divided into crack initiation (N_I) and crack propagation (N_F) stages. A previous investigation has indicated that for the fatigue life of titanium alloy for high stress or strain amplitudes, the crack initiation life may only be a very small fraction of the propagation life, i.e. $N_I / N_F = 0.01$ [9]. The combination of crack initiation and crack propagation is called the fatigue life (N_f).

To summarize a body of previous research [8, 9, 12, 16-21], the fatigue behaviour of titanium alloys is primarily affected by the stress level, grain size, microstructure (lamellar and equiaxed) and phase content. The stress ratio and other factors (e.g. temperature, surface treatment) can also affect the fatigue behaviour. However, fatigue behaviour, sometimes is quite unpredictable [18]. Fracture of a micro package from propagation occurs under high frequency, cyclic loading, where the crack initiation originates from small defects. In the following section, a description of fatigue life, S-N curve and some influential factors (microstructure, phase content and stress ratio) on fatigue behaviour are discussed.

3.4.1 S-N curve

Curves relating stress range with the number of cycles (S/N curves) are used to describe the endurance limits of the materials including titanium alloys [16]. Figure 3.19 shows a sinusoidal cycle which is a stress-time function which is repeated periodically. The stress values are from a tensile fatigue test in which the force acting on a known sample cross-section area are measured, whilst a strain values are from the displacement on the sample parallel area (the gauge) which is measured with a strain gauge. The loading style can be a repeated axial, bending or torsional load, applied on the sample parallel area.

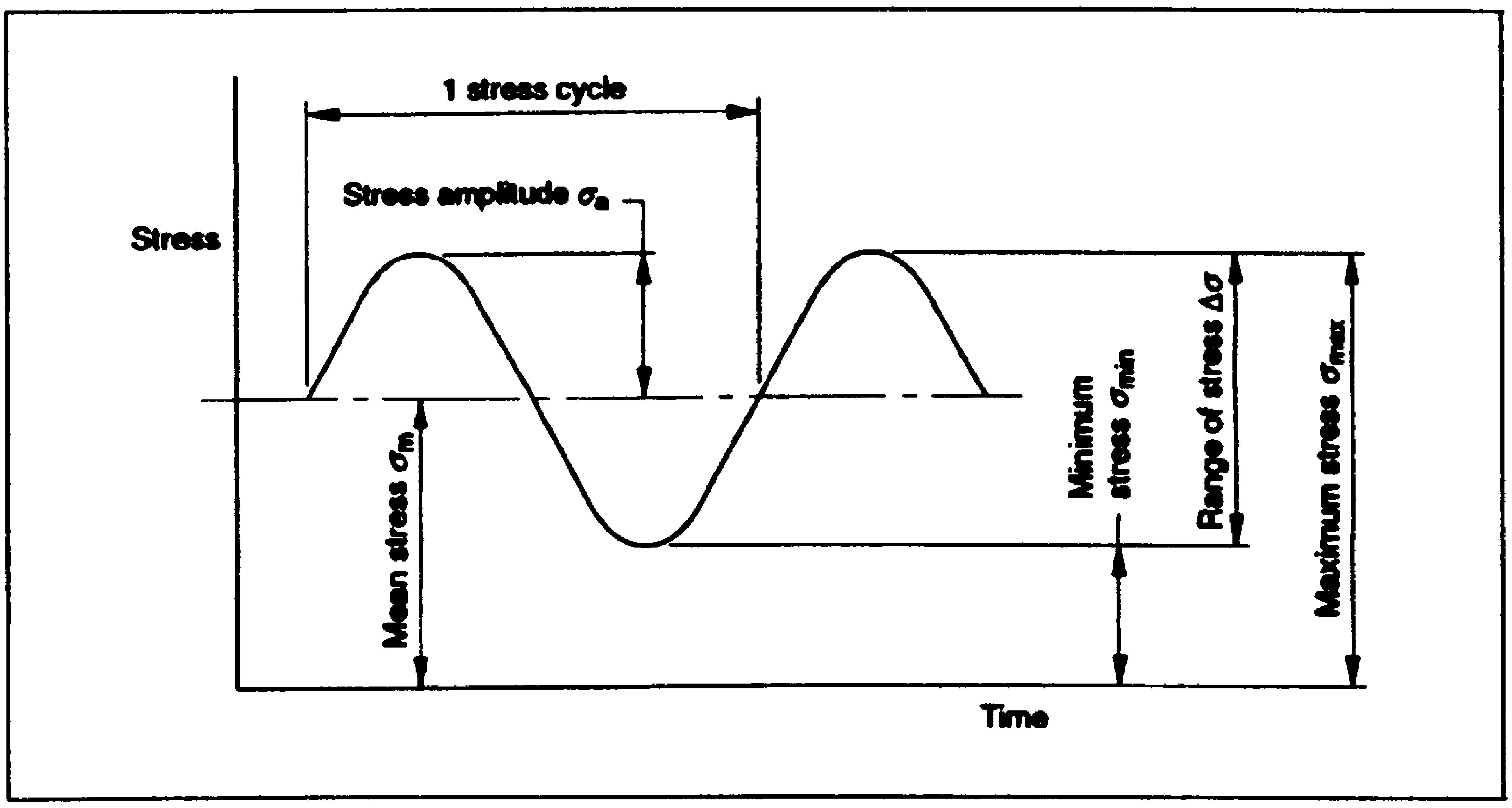

Figure 3.19 A typical fatigue stress cycles [16]

The main parameters for a fatigue stress cycle include: stress (*σ or S*), maximum stress (σ_{max}), minimum stress (σ_{min}), mean stress (σ_m), stress amplitude (σ_a), range of stress ($\Delta\sigma$), stress ratio (R), number of stress cycles (n), frequency of cycles (f) and endurance or fatigue life (N).

Stress (σ *or S*): the force applied on the original cross-section area.

Maximum stress (σ_{max}): the highest algebraic value of stress in the stress cycle.

Minimum stress (σ_{min}): the lowest algebraic value of stress in the stress cycle.

Mean stress (σ_m): Half of the algebraic sum of the maximum and minimum stresses.

Stress amplitude (σ_a): Half of the algebraic difference between the maximum and minimum stresses.

Range of stress (Δ_σ): The algebraic difference between the maximum and minimum stresses.

Stress ratio (R): the algebraic ratio of the minimum stress to the maximum stress in one cycle.

Number of stress cycles (n): the number of cycles applied.

Frequency of cycles (f): the number of cycles applied per second.

Endurance or fatigue life (N): the number of stress cycles to failure.

Figure 3.20 shows three fatigue stress cycles with different stress ratio values. R is greater than unity for fluctuating compression; R is less than zero for reversed cycles; R is between zero and unity for fluctuating tension.

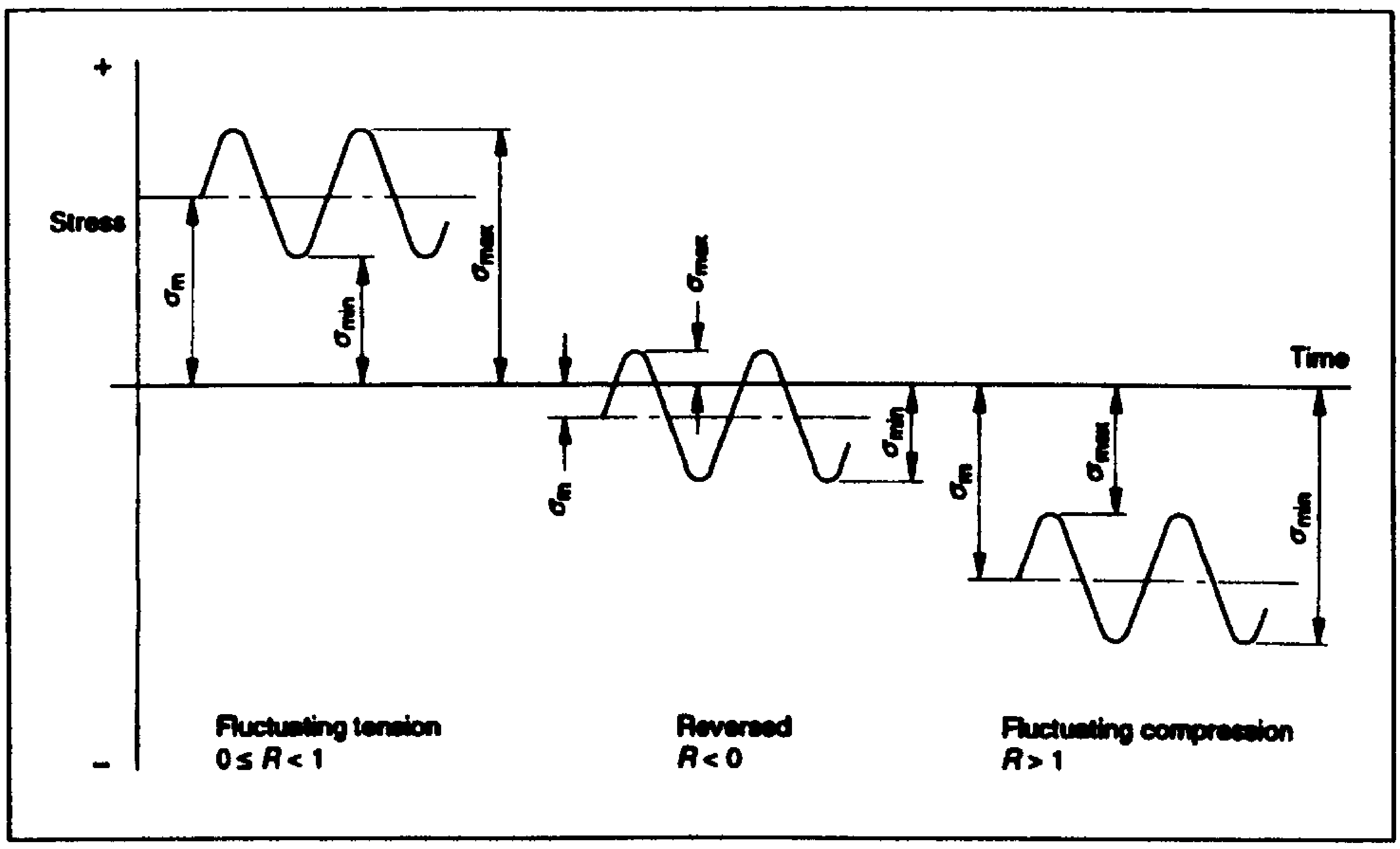

Figure 3.20 The type of stress cycle with algebraic notation [16]

The most popular graphical presentation for fatigue behaviour is the S-N curve. Its construction involves plotting the number of cycles to failure as the abscissa and the stress amplitude as the ordinate. An example is shown in Figure 3.21:

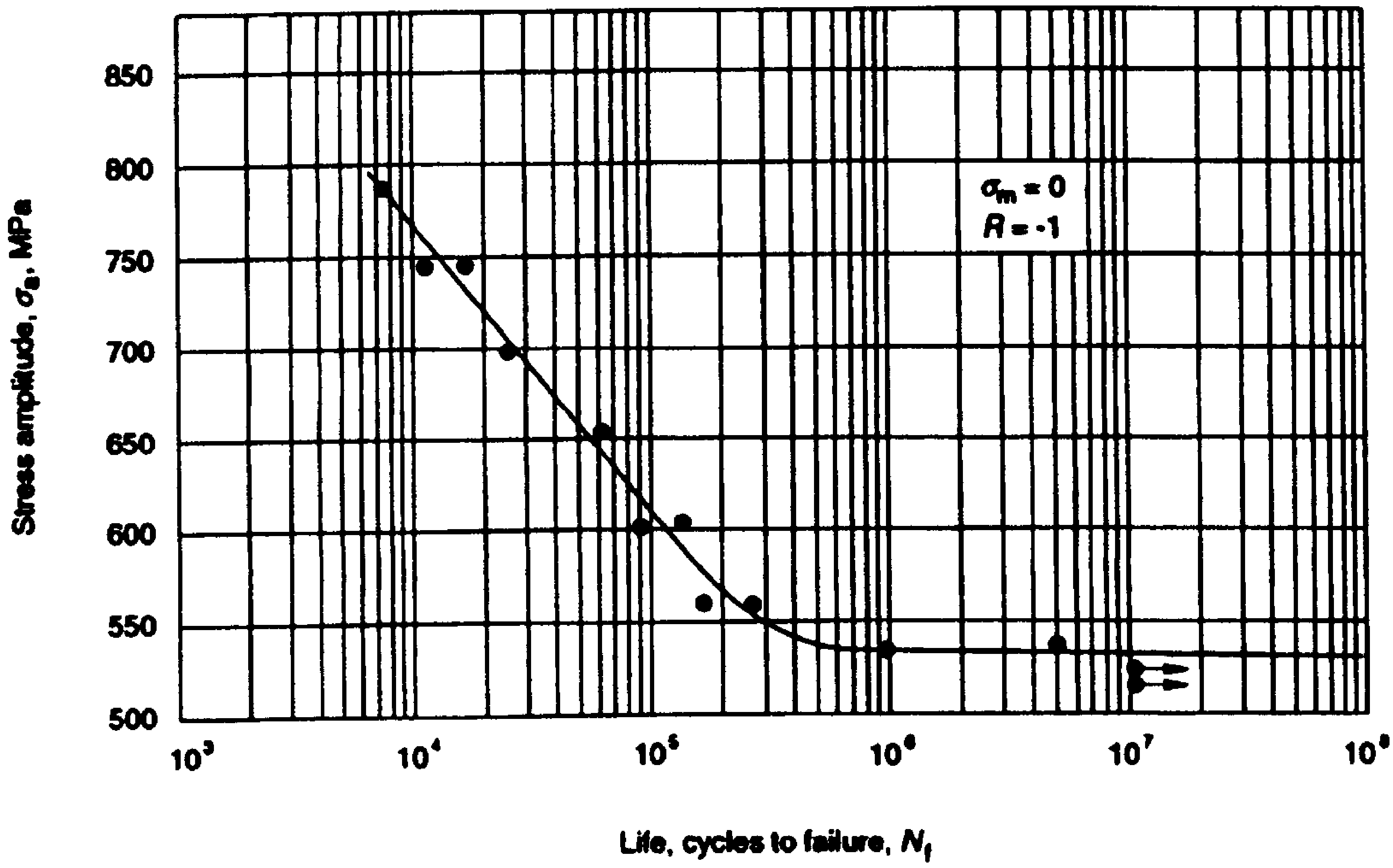

Figure 3.21 A typical S-N curve for fracture fatigue behaviour [16]

The graphical representation of the S-N curve contains all the test results, and clearly indicates the results from tests which were terminated prior to failure.

3.4.2 The effects of microstructure on fatigue behaviour in Ti-6Al-4V

Table 3.5 showed the effects of microstructure on initial crack resistance and propagation resistance in Ti6Al4V. As mentioned in section 3.3, equiaxed structure and fine grain size provide better fatigue initiation resistance but poorer propagation resistance. In this section, these are discussed further.

Leyens [9] reports that in a low stress, high cycle loading regime, fatigue cracks initiated preferentially at 'α/β interfaces and grain boundaries' [9]. As shown in Figure 3.22, the fatigue strength of a lamellar microstructure with a lath width about 12 μm (approximately 480 MPa) is lower than that of equiaxed microstructures with a grain size about 12 μm (approximately 560 MPa). Even with a smaller width lamellar microstructure (0.5 μm), the fatigue strength (approximately 675 MPa) is lower than that of an equiaxed microstructures with a grain size about 2 μm (approximately 720

MPa). Hence, equiaxed microstructures exhibit longer fatigue lives than lamellar microstructures. The reason is that, lamellar microstructures exhibit a greater α/β surface area and more oriented colonies, so that 'slip is easily transmitted from one plate to another in lamellar microstructures, because of the crystallographic relation between the α and β phases' [9].

Figure 3.22 also shows the high cycle fatigue behaviour of these microstructures at different grain sizes or width of lamellar colonies. When the α lamellae width is reduced from 12 to 0.5 μm, the fatigue strength increases from 480 to 675 MPa (Figure 6.22a). When the grain size is reduced from 12 to 2 μm in equiaxed microstructures, the fatigue strength increases from 560 to 720 MPa (Figure 6.22b).

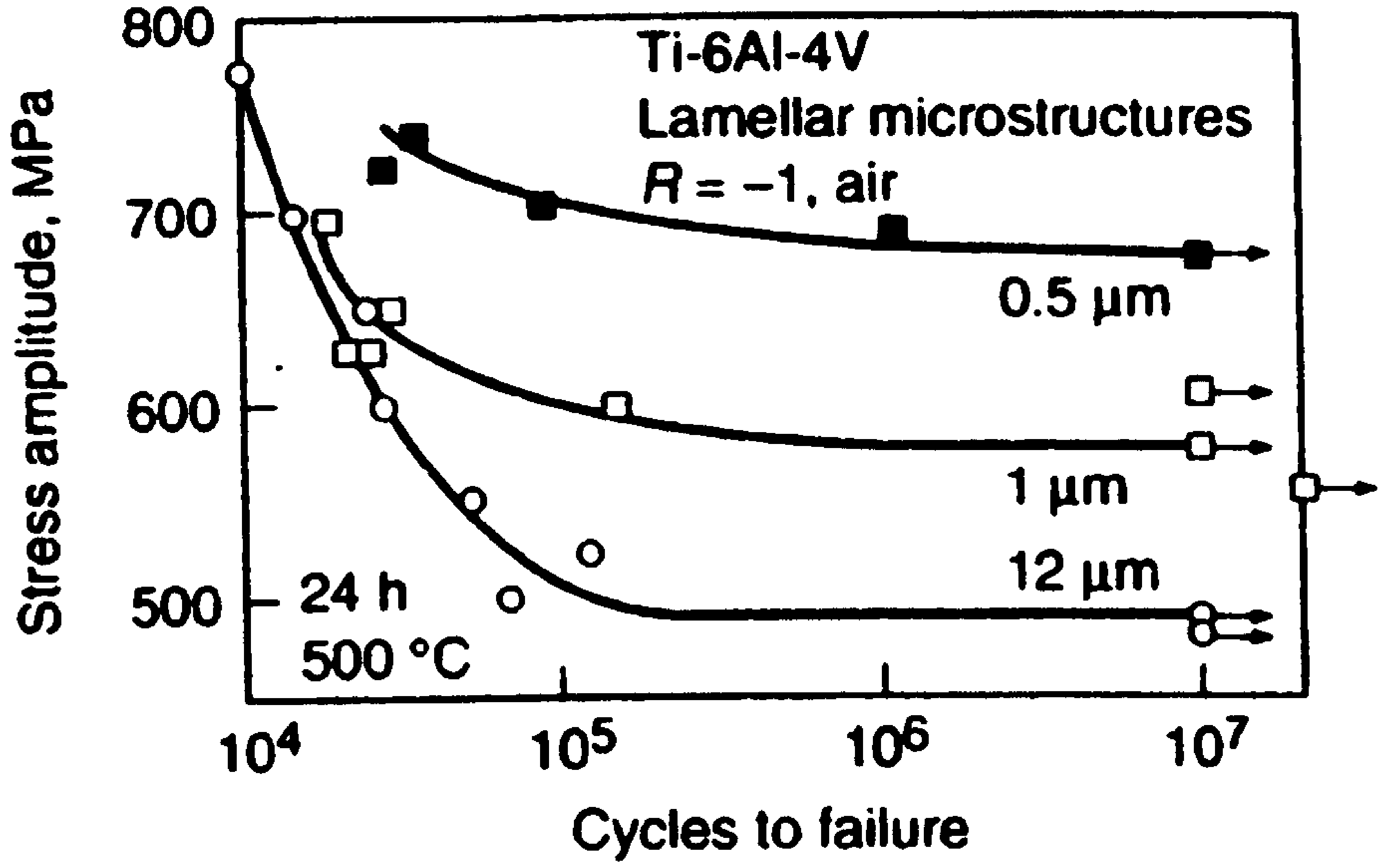

(a)

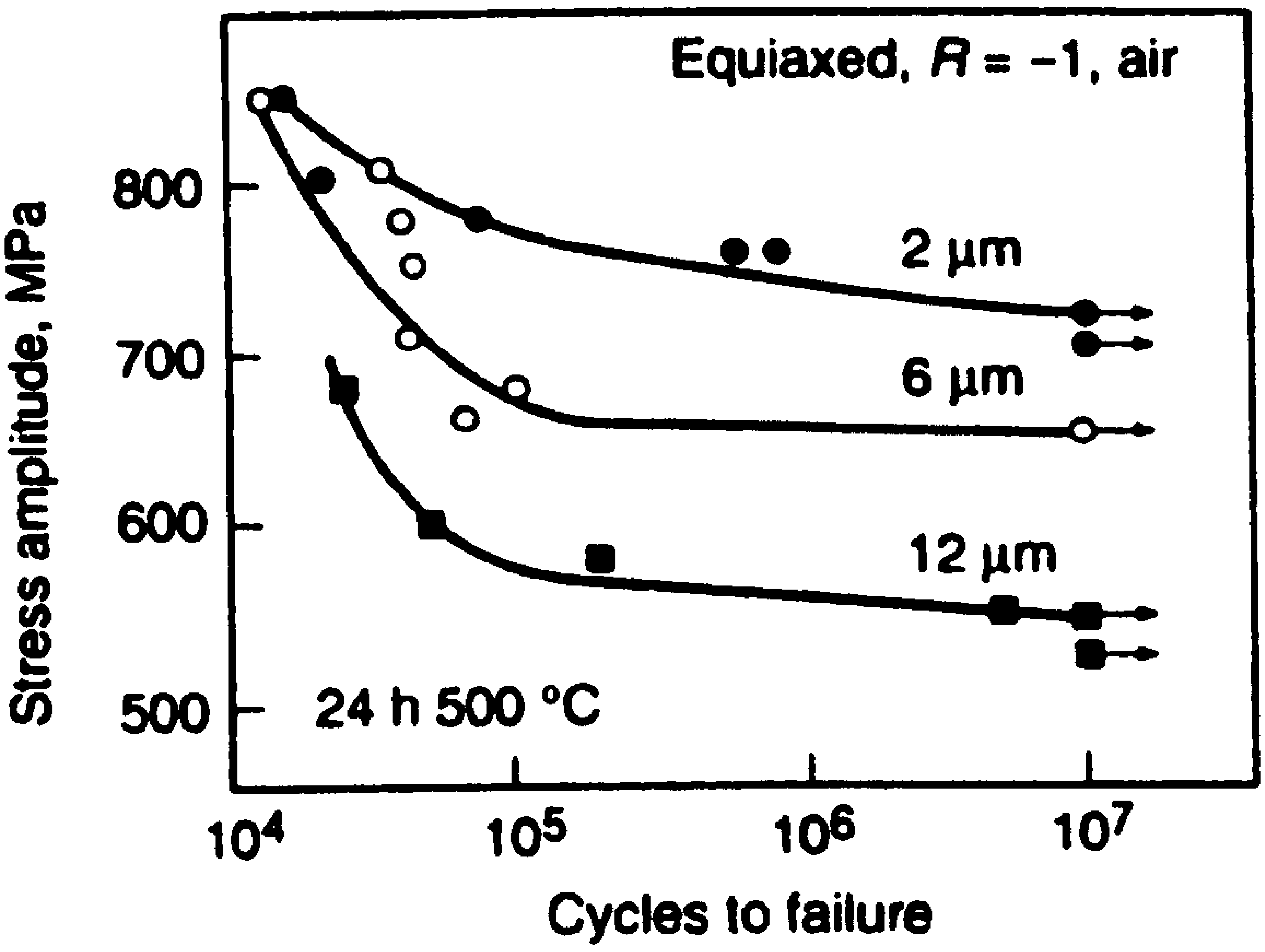

(b)

Figure 3.22 High cycle fatigue behaviour (R=-1) of Ti-6Al-4V: a) Influence of lamella width (lamellar microstructure); b) Influence of α grain size (equiaxed microstructure) [9]

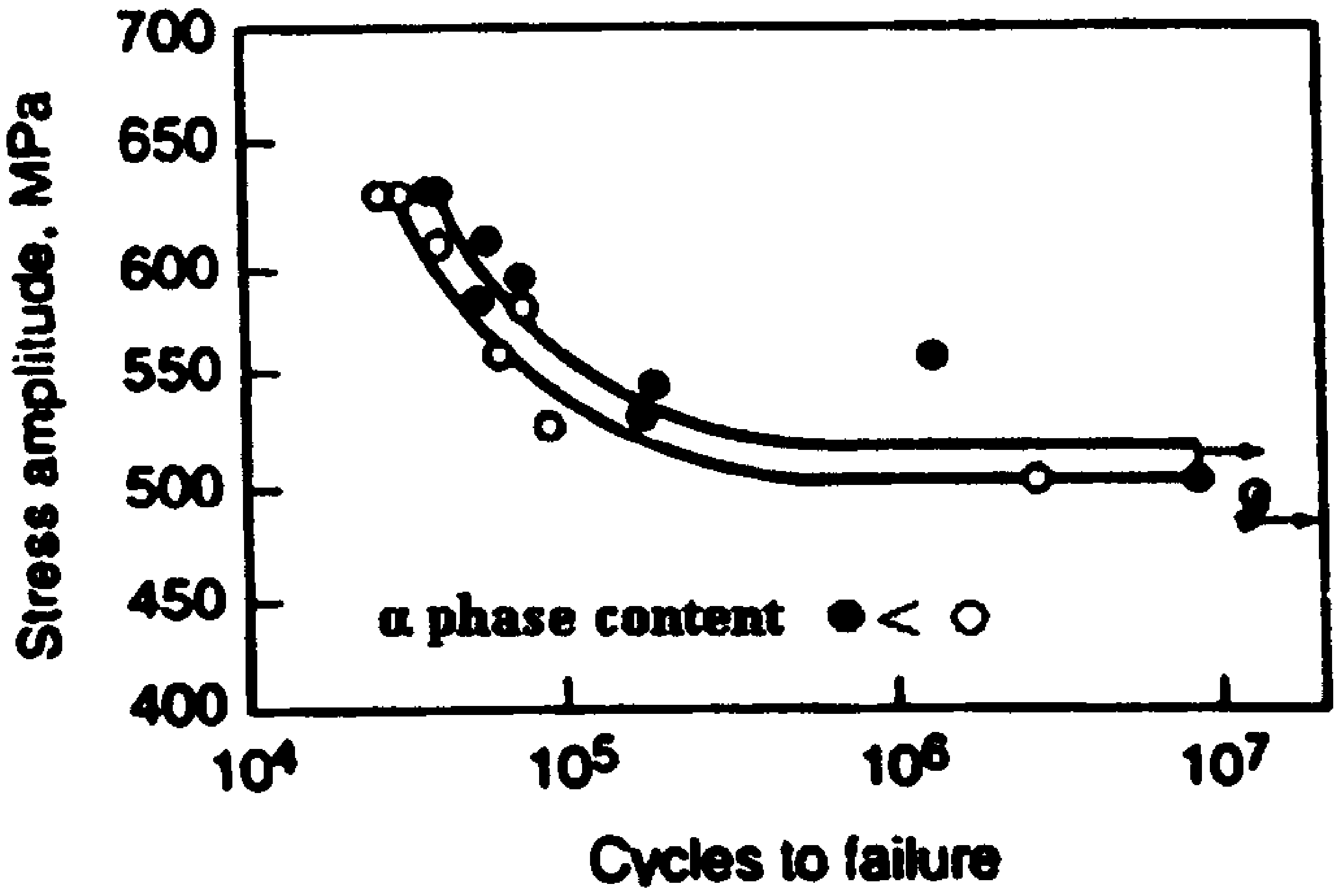

Figure 3.23 Effect of α content on S-N curve (R=-1) in TIMETAL 1100 [22]

Besides microstructure types and grain size, phase content plays an important role in fatigue life behaviour. Previous research [22] reports aging of TIMETAL 1100 ($Ti6Al2.7Sn4Zr0.4Mo0.4Si$, a near-alpha Titanium alloy) at 650°C to get two alloys with different α phase contents. The resulting S-N curves are given in Figure 3.23. Decreasing the α phase content extends the fatigue life in both low-cycle fatigue and high-cycle fatigue. They suggested that primary α can act as 'large single grains which are easy for microcracks to propagate through' [23].

There is another kind of structure named a bimodal microstructure which is considered as a combination of lamellar and equiaxed structures as shown in Figure 3.24(a). Bimodal microstructures exhibit a well-balanced fatigue properties profile [9], since they combine the advantages of both lamellar (higher fatigue crack propagation resistance) and equiaxed (higher fatigue crack initiation resistance) structures.

Results from Zuo et al.'s [24] research work on the effect of bimodal and Widmanstätten structures on fatigue behaviour of $Ti6Al4V$ are shown in figure 3.24. They indicated that the alloy with a bimodal structure has slightly higher fatigue strength than that with Widmanstätten structure.

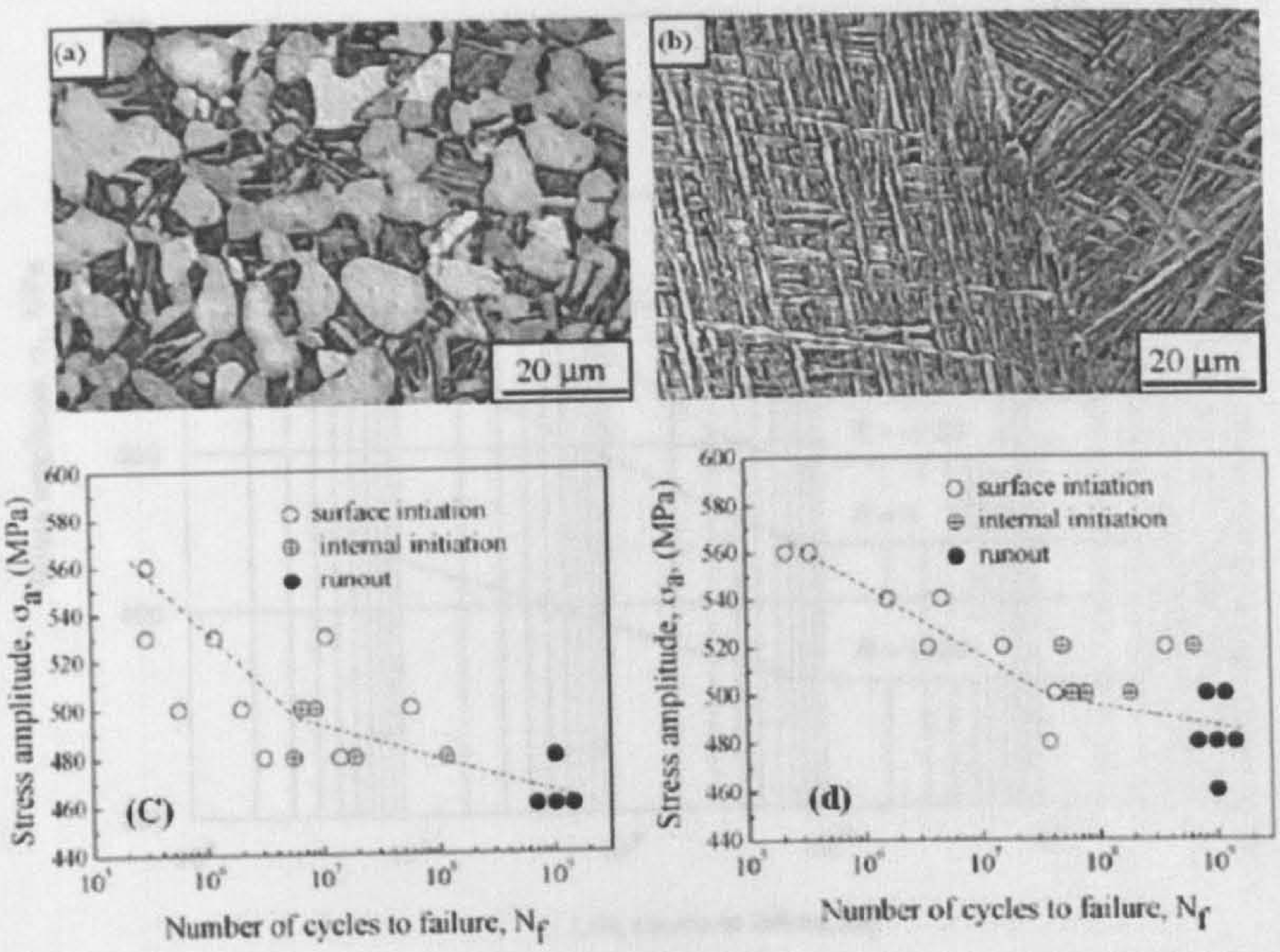

Figure 3.24 Comparison of fatigue behaviours of bimodal microstructure and Widmanstätten structures in Ti6Al4V (a) bimodal microstructure (b) Widmanstätten structures microstructure (c) S-N curve of bimodal structures (d) S-N curve of Widmanstätten structures [24]

3.4.3 The effects of stress ratio on fatigue behaviour in Ti-6Al-4V

Figure 3.25 shows the typical effect of stress ratios on fatigue life in the form of a S-N curve.

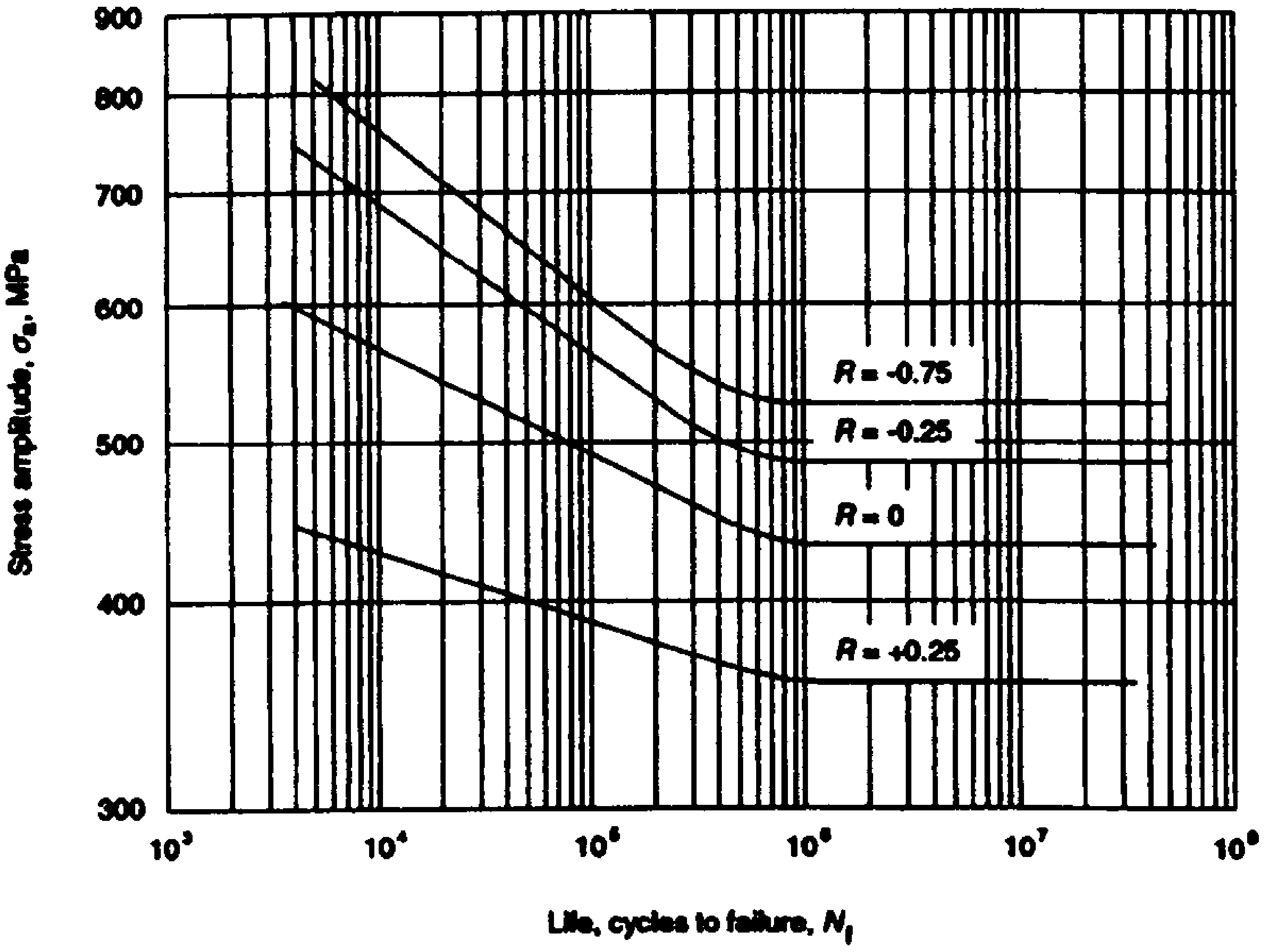

Figure 3.25 General S-N curves corresponding to particular stress ratios [16]

As can be seen in Figure 3.25, as the stress ratio increases, fatigue strength of a given stress amplitude decreases. McEvily et al.'s [17] work verifies the conclusion above (Figure 3.25). Figure 3.26 shows an S-N curve under different stress ratios. The reason is that when the stress ratio R values are increased, the mean stress values increase as well. As shown in Figure 3.27, when the mean stress value is increased, the stress amplitude at a certain fatigue strength (normally consider as 10^7 cycles) drops off. It needs to be noted that in McEvily et al.'s study that, 10^8 cycles was defined as the fatigue strength rather than 10^7 cycles.

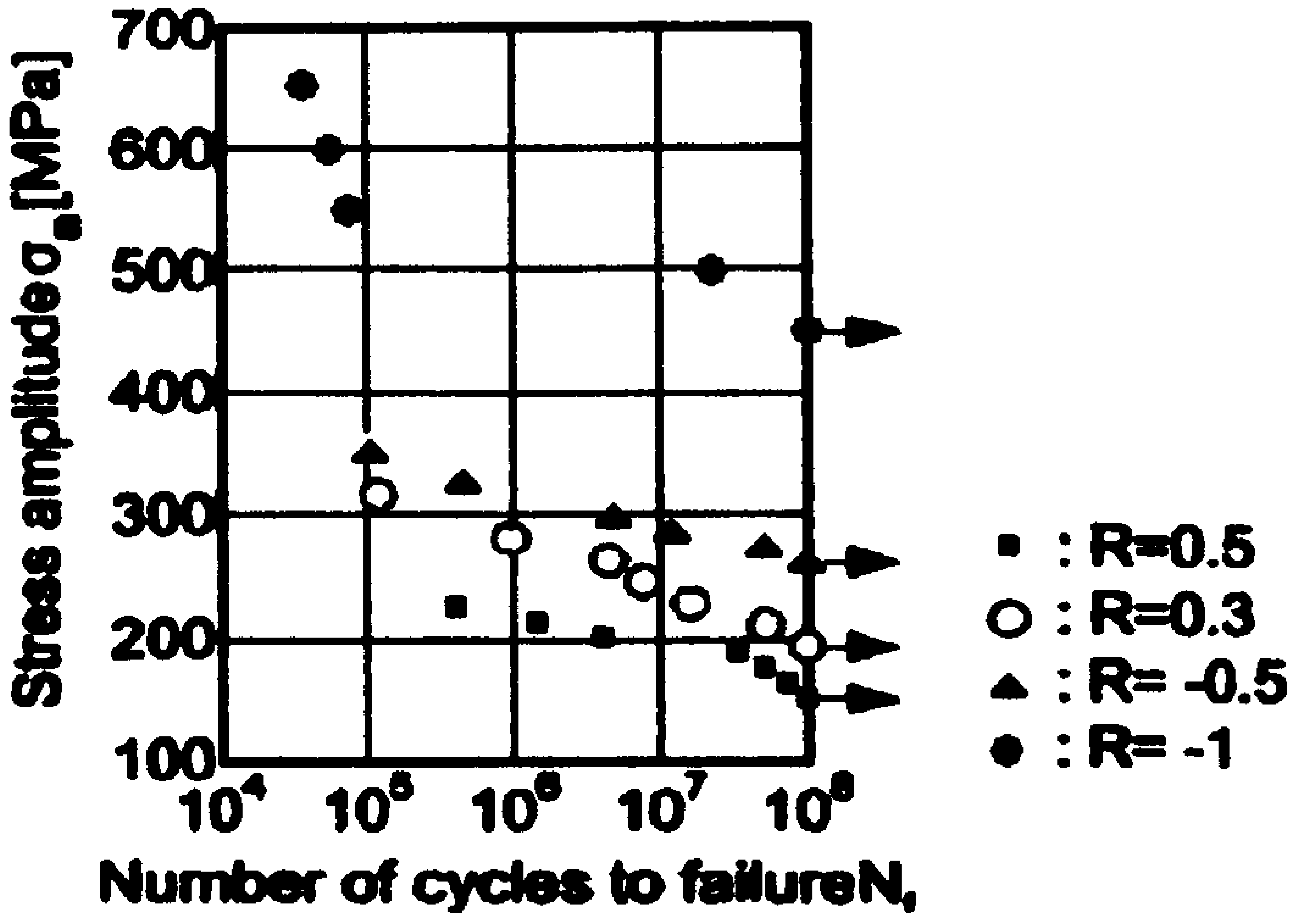

Figure 3.26 S-N curve at different ratios for Ti6Al4V [17]

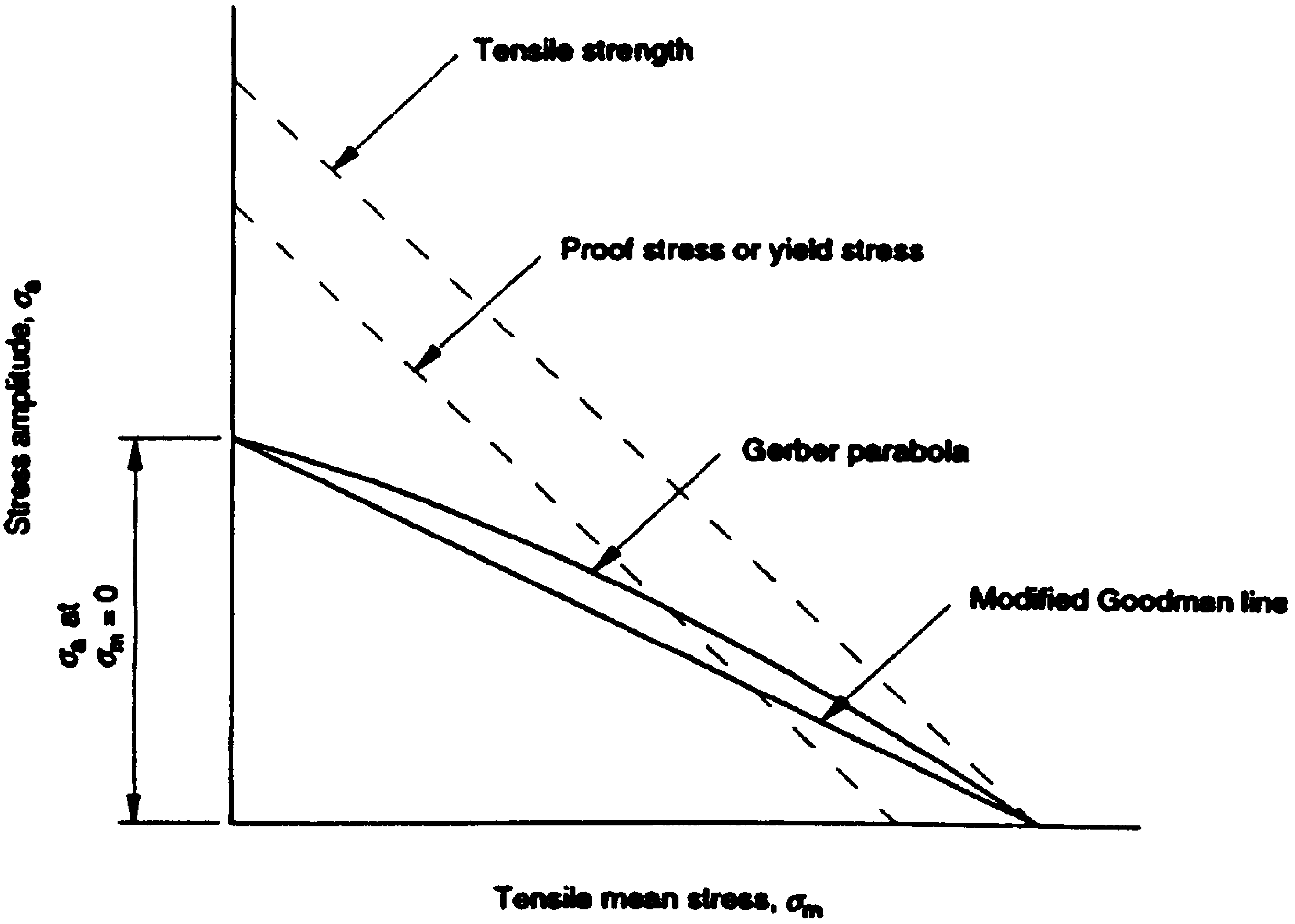

Figure 3.27 Relationships between the level of mean stress and stress amplitude resulting in fatigue strength [25]

3.5 Summary

1. Martensite α′ is transformed from β phase at fast cooling rate and above martensitic transformation temperature, which results in a material with a high strength and low ductility. The higher the temperature, the more β phase, and the bigger the grain size is. The longer the heat treatment time, the bigger the grain size is. Lamellar and Widmanstätten structures result from slow cooling rate. The equiaxed microstructure is always from refinement globularization during annealing

2. The strength (tensile yield stress) of Ti6Al4V ranks from high to low are respectively: Martensite structure, lamellar structure, Widmanstätten structure, equiaxed structure. The ductility (elongation) of Ti6Al4V ranks from high to low are respectively: equiaxed structure, Widmanstätten structure, lamellar structure and Martensite structure.

3. Fatigue crack behaviour is the combination of fatigue crack initiation and fatigue crack propagation, which is affected by grain size, stress ratio and phase content. Fine grain size shows better fatigue crack initiation resistance; coarse grain size shows better fatigue crack propagation resistance. Previous research indicates that, less α phase content and exquiaxed microstructure results in a higher fatigue life. As the stress ratio increases, fatigue strength decreases. In addition, high strength and high ductility results in long crack initiation life but short crack propagation lives.

References:

[1] L.W.Tsay and C.Y.Tsay. The effect of microstructures on the fatigue crack growth in Ti6Al4V laser welds. *Int J Fatigue*. 1997; 19(10):713-20.

[2] F.J.Gil, M.P.Ginebra, J.M.Manero and J.A.Planell. Formation of α-Widmanstätten structure: effect of grain size and cooling rate on the Widmanstätten morphologies and on the mechanical properties in Ti6Al4V alloy. *Journal of Alloy and compounds*. 2001; 329:142-52.

[3] F.Caiazzo, F.Curcio, G.Daurelio and F.Memola Capece Minutolo. Ti6Al4V sheets lap and butt joints carried by CO2 Laser: mechanical and morphological characterization. *Journal of Materials Processing Technology*. 2004; 149:546-52.

[4] I.J.Polmear. Light Alloys: from traditional alloy to nanocrystals. 4th ed: Butterworth-Heinemann 2006.

[5] M.Žitňanský and L.Čaplovič. Effect of the thermomechanical treatment on the structure of titanium alloy Ti6Al4V. *Journal of Materials Processing Technology*. 2004; 157-158:643-9.

[6] M.T.Jovanović, S.Tadić, S.Zec, Z.Mišković and I.Bobić. The effect of annealing temperatures and cooling rates on microstructure and mechanical properties of investment cast Ti-6Al-4V alloy. *Materials and design*. 2006; 27:192-9.

[7] D.Hardie and S.Ouyang. Effect of microstructure and heat treatment on fracture behaviour of smooth and precracked tensile specimens of Ti6Al4V. *Materials Science and Technology*. 1999; 15:1049-57.

[8] S.Shademan, V.Sinha, A.B.O.Soboyejo and W.O.Soboyejo. An investigation of effects of microstructure and stress ratio on fatigue crack growth in Ti-6Al-4V with colony α/β microstructures. *Mechanics of materials*. 2003; 36:161-75.

[9] C.Leyens and M.Peter. Titanium and titanium alloy: fundamentals and applications: WILEY-VCH GmbH & Co. KGaA 2003.

[10] P.Pinke, L.Čaplovič and T.Kovács. The influence of heat treatment on the microstructure of the casted Ti6Al4V Titanium alloy. *Materials World*. 2007; 2:1-6.

[11] P. Sirilar PS. Grain refinement of α/β phase Ti6Al4V alloy by thermomechanical treatment. King Mongkut's University of Technology Thonburi, Bangkok, 2006.

[12] J.O.Peter and G.Lütjering. Comparison of the fatigue and fracture of α + β and β titanium alloys. *Metall Mater Trans.* 2001; 32A:2805-18.

[13] A.B.Short. Gas tungsten arc welding α+β Titanium alloy: a review. *Material Science and Technology.* 2009; 25:309-24.

[14] American Welding Society. Recommended Practices for Laser Beam Welding, Cutting, and Drilling: ANSI/AWS 1998.

[15] T.Ahmed and H.J.Rack. Phase transformations during cooling in alpha+beta titanium alloys. *Materials Science and Engineering A.* 1998; 243(1-2):206-11.

[16] British Standard. 3518-1:Methods of fatigue testing. 1993.

[17] A.J.McEvily, T.Nakamura, H.Oguma, K.Yamashita, H.Matsunaga and M.Endo. On the mechanism of very high cycle fatigue in Ti-6Al-4V. *Scripta Materialia.* 2008; 59(11):1207-9.

[18] Z.Chu, J.Yu, X.Sun, H.Guan and Z.Hu. High cycle fatigue behavior of a directionally solidified Ni-base superalloy DZ951. *Materials Science and Engineering: A.* 2008; 496(1-2):355-61.

[19] L.W.Tsay, Y.P.Shan, Y.H.Chao and W.Y.Shu. The influence of porosity on the fatigue crack growth behavior of Ti-6Al-4V laser welds. *Materials Science.* 2006; 41:7498-505.

[20] Y.Y.Jiang, F.Ding and M.L.Feng. An approach for fatigue life prediction. 2005 Jul 17-21; Denver, CO: Asme-Amer Soc Mechanical Eng; 2005. p. 182-9.

[21] J.Oh, N.J.Kim, S.Lee and E.W.Lee. Correlation of fatigue properties and microstructure in investment cast Ti-6Al-4V welds. *Materials Science and Engineering.* 2003; A340:232-42.

[22] ASM Handbook. Volume 19 - Fatigue and fracture. 1996.

[23] A.Berg, J.Kiese and L.Wagner. In light-weight alloys for aerospace applications III. 1995.

[24] J.H.Zuo, Z.G.Wang and E.H.Han. Effect of microstructure on ultra-high cycle fatigue behavior of Ti-6Al-4V. *Materials Science and Engineering: A.* 2008; 473(1-2):147-52.

[25] S.Suresh. Fatigue of materials. 2nd ed: Cambridge university press 1998.

CHAPTER 4

Chapter 4 Literature Review: Laser Beam Welded Ti6Al4V and Defects in Laser Beam Welded Structures

As outlined in Chapter 3, the mechanical properties (including the fatigue behaviour) of Ti6Al4V are affected significantly by structure, grain size and phase content. The main feature of laser welding which separates it from other welding techniques is high depth-to-width ratio [1, 2]. As such, the narrow weld zone and high production rate can cause some defects which reduce the performance of the welded structures. In this chapter, the features of laser beam welded Ti6Al4V are discussed, and specifically, two main defect types (porosity and distortion) are presented.

4.1 Laser beam weld microstructure

The weld zone in laser beam welding is melted and resolided metal resulting from a process lasting only a short period of time. Hence the fusion zone (FZ) has properties similar to those resulting from a water quench process from a high temperature. The fatigue behaviour of martensite α' is generally seen as poor since the titanium martensite is not significantly stronger than the parent phase [1].

4.1.1 Microstructure of laser beam welded Ti6Al4V

Figure 4.1 shows a symmetrical cross section of laser beam welded Ti6Al4V from the work of Wang et al. [3]. The welds were made with a Rofin-Sinar RS 850 5 kW CO_2 laser for bead-on-plate welding. The laser power was 2500 W, the travel speed was 1500 mm/min and the shielding gas was He.

The macrograph in Figure 4.1a demonstrates the growth direction of the dendritic grains controlled by the heat flow direction during solidification. The weldment of LBW Ti6Al4V shows a narrow fusion zone around 2 mm wide with an even smaller

HAZ of around 0.5 mm. The enlarged micrograph (figure 4.1b) shows the microstructural transformations from the FZ to Parent material (PM) through the heat affected zone (HAZ). The microstructure of the HAZ as shown in figures 4.1c and 4.1d include a mixture of martensite α′, acicular α, and primary α. Wang et al. indicate that 'this kind of structure corresponds to a specimen quenched from a temperature below the beta transus' [3]. However, it is hard to determine the range of temperatures from which the cooling has occurred. Figure 4.1e shows martensite α′ transformed from the β phase, which is very similar to that observed in titanium alloy following water quenching from 1100°C (as shown in Figure 3.5a by Jovanović et al. [4]).

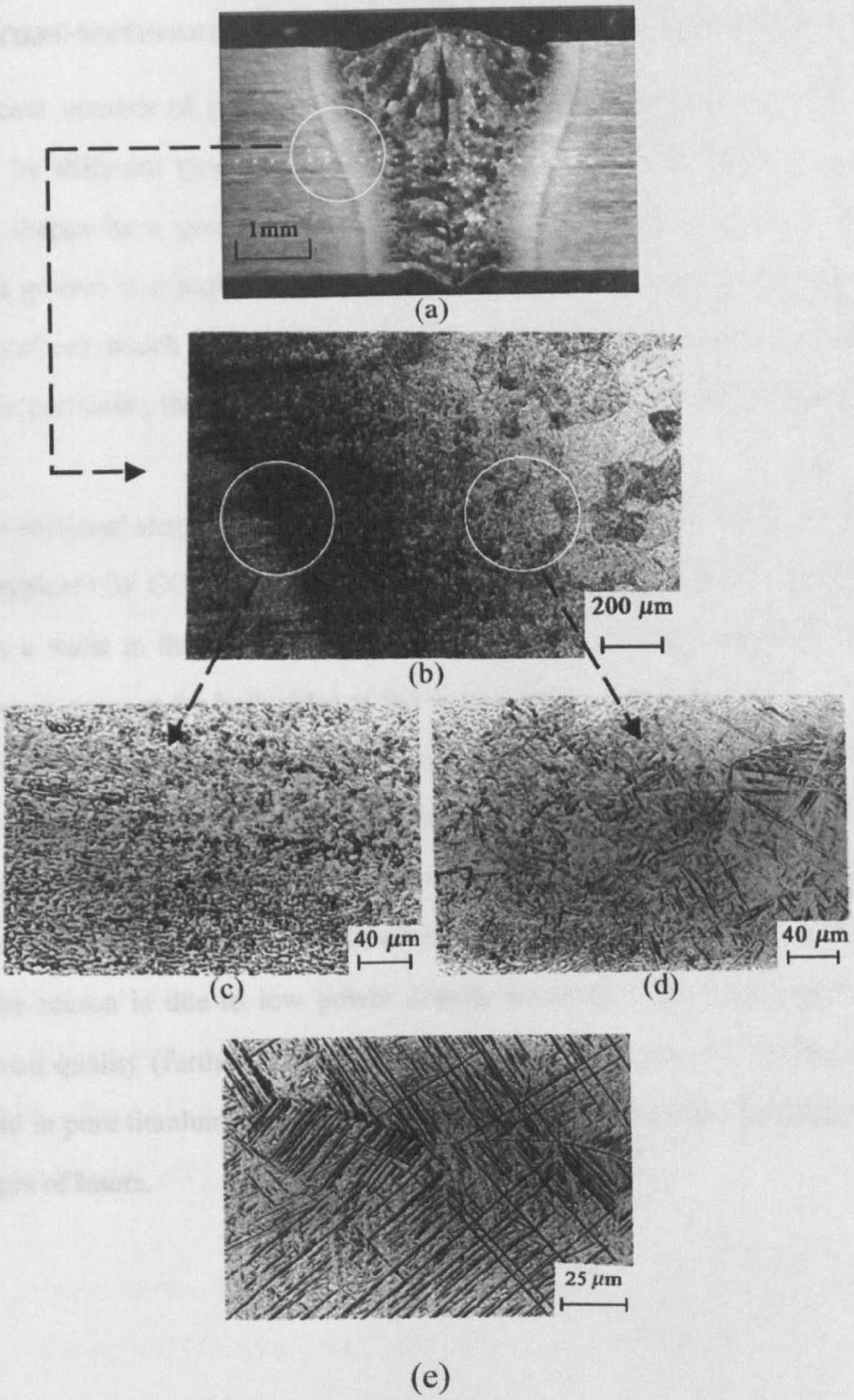

Figure 4.1 Microstructure of laser beam welded Ti6Al4V (a) macrograph of LBW Ti6Al4V. (b) Enlarged micrograph of both the boundary of (right) the fusion zone (FZ)/the heat affected zone (HAZ) and the boundary of (left) the HAZ/parent material (PM). (c) Microstructure of the boundary of the HAZ/PM. (d) Microstructure of the boundary of the FZ/ the HAZ. (e) Microstructure of the FZ [3]

4.1.2 Cross-sectional shape of continuous wave and pulsed LBW

A significant number of research papers report on the cross-sectional weld shapes produced by different types of lasers and technologies [5-10]. Most of the cross-sectional shapes have grooves (figure 4.2 a-d) at certain points across the cross-section (a groove is a region where the surface sits below that of the original pre-welded surface) which decrease the strength of the joint. In welds, in thin-plate material in particular, the effect of distortion on the strength is even more significant.

The cross-sectional shape of a LBW is sensitive to the type of laser used. Figure 4.2 (a) shows a typical CW CO_2 laser bead-on-plate fully penetrated weld in Ti6Al4V. There always is a waist in the weld zone which is generated by the well-known keyhole. Four grooves occur at the both sides of the weld centreline near the HAZ in figure 4.2 (a) and figure 4.2 (d). Figure 4.2 (b) shows a typical pulsed Nd:YAG Laser Beam Weld in commercially pure titanium. In this case, the groove in pulsed LBW appears at the weld centreline. Figure 4.2 (c) shows a typical diode laser weld in a low carbon steel. The ratio between the top width of the weld to the bottom width of the weld is large. The reason is due to low power density resulting from bigger spot size and lower beam quality (further discussion is in chapter 7). Figure 4.2 (e) shows a fibre laser weld in pure titanium, which generate very narrow weld zone compared with the other types of lasers.

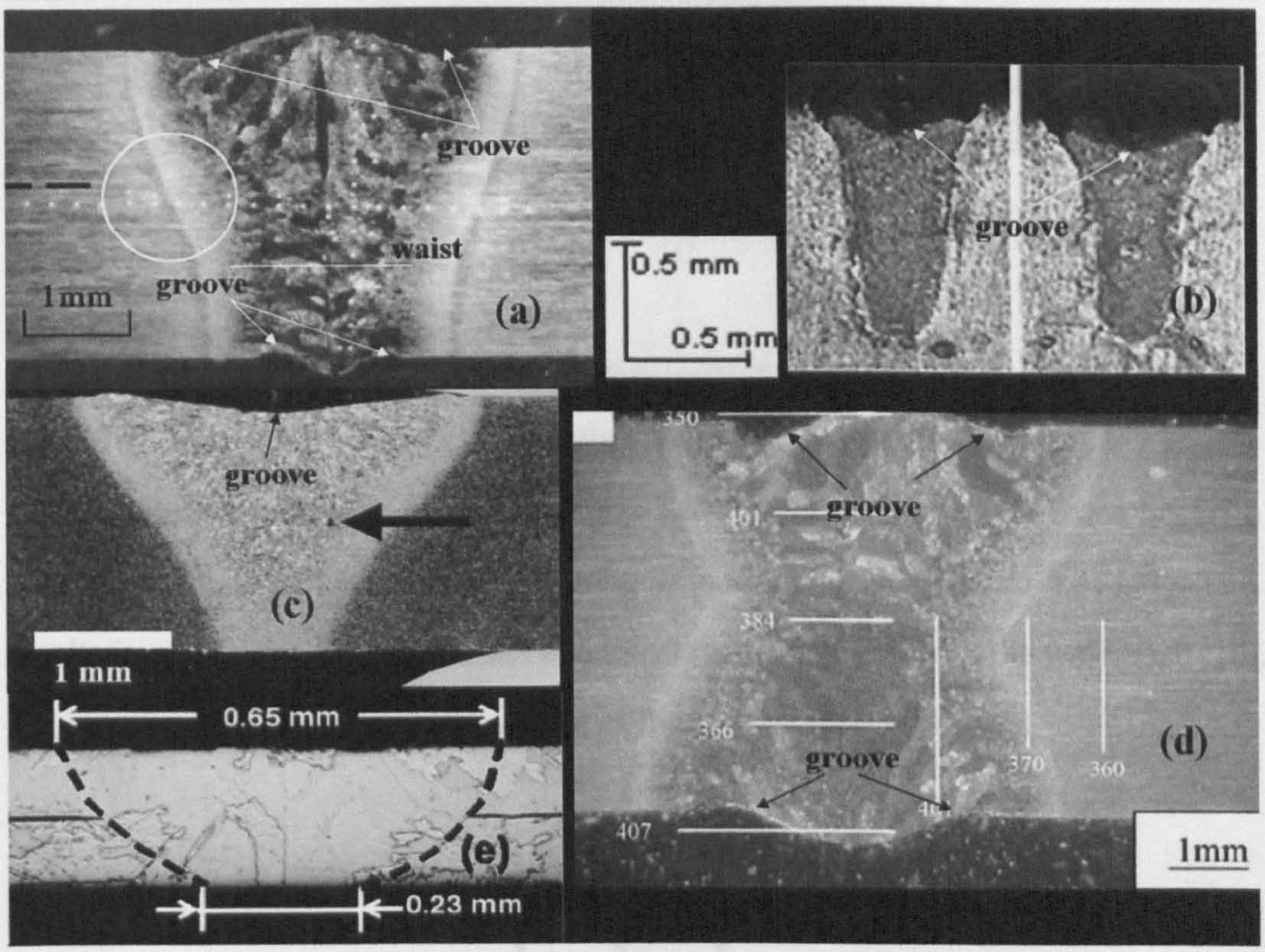

Figure 4.2 Cross-sectional shape in different types of laser welding process: a) Continue wave (CW) CO_2 laser weld in Ti6Al4V, power 2500 W, speed 1500 mmmin^{-1} [3]; b) Pulsed Nd:YAG weld in commercial pure titanium, power 1600 W [11], pulse duration 2ms; c) Diode laser weld in low carbon steel, power 2260 W, welding time 0.18s [6]; d) CW CO2 laser weld in Ti6Al4V, power 2000 W, speed 1200 mmmin^{-1} [5]; e) CW fibre laser weld in pure titanium, power 47 W, speed 600 mmmin^{-1} [10]

The mechanism for the formation of the groove in CW laser welding is shown in figure 4.3. During a CW keyhole weld, the molten material has to travel a longer way to the fill the keyhole. 'In this way, the melt will have more time to cool down and hence more material can solidify' before the two melt flows reach the keyhole (figure 4.3 II) [12]. The shape of these solidified layers on each side of the weld was the first part of the groove formation. When the two flows come together and solidify, the cross-sectional shape with grooves is generated as shown in figure 4.3 III.

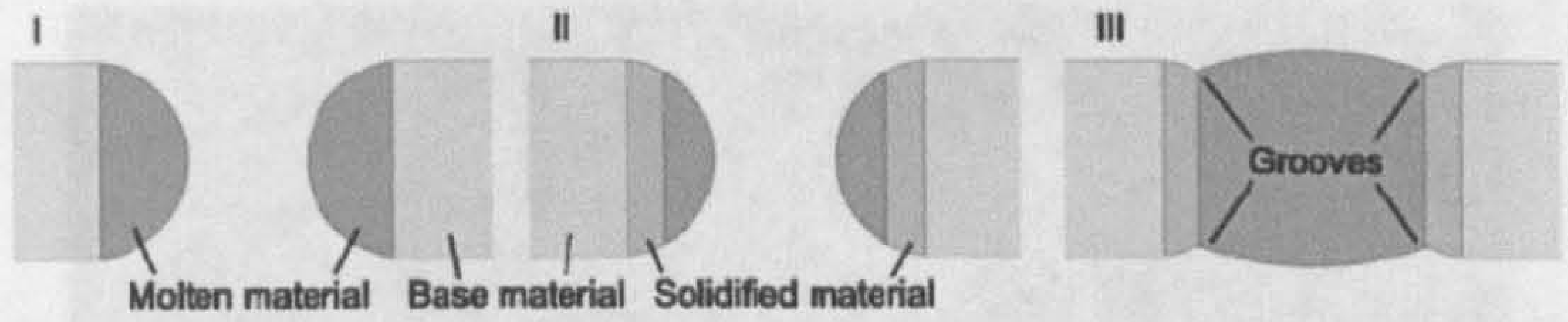

Figure.4.3 Schematic drawing of formation of the grooves [12]

The groove in pulsed Nd:YAG LBW tends to appear at the centre area of the weld bead. The reason is that in pulsed welding, high peak power density forms a vapour from the keyhole. Under such high temperatures generated by the laser beam, a plasma zone was generated from shielding gas or vapour gas (figure 4.4) [13]. This results in rapid material evaporation and thus loss of material from the weld zone [14]. This results in the formation of a groove of the centre of the weld bead.

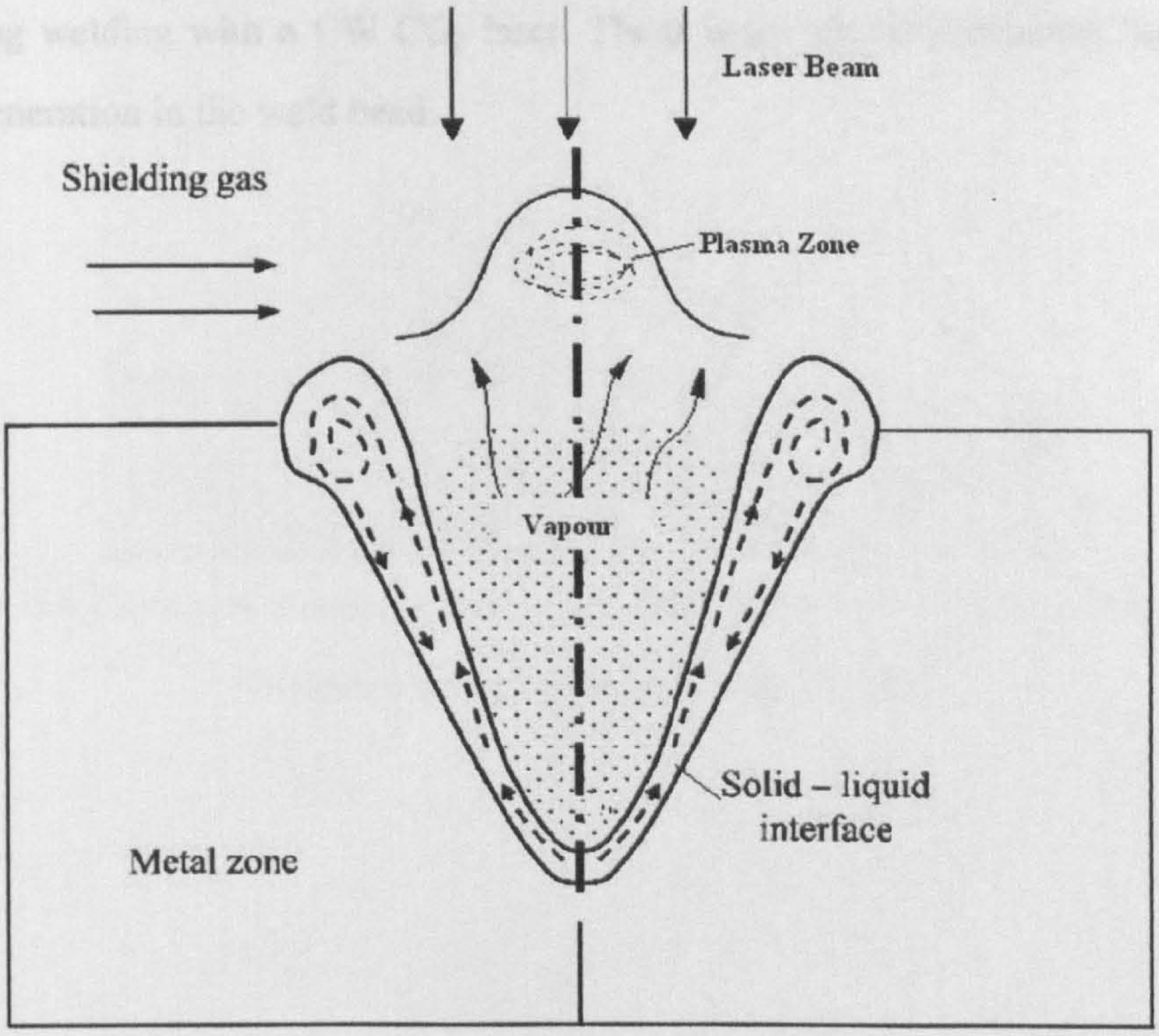

Figure.4.4 Schematic drawing of a pulsed laser welding process, modified from [13, 14]

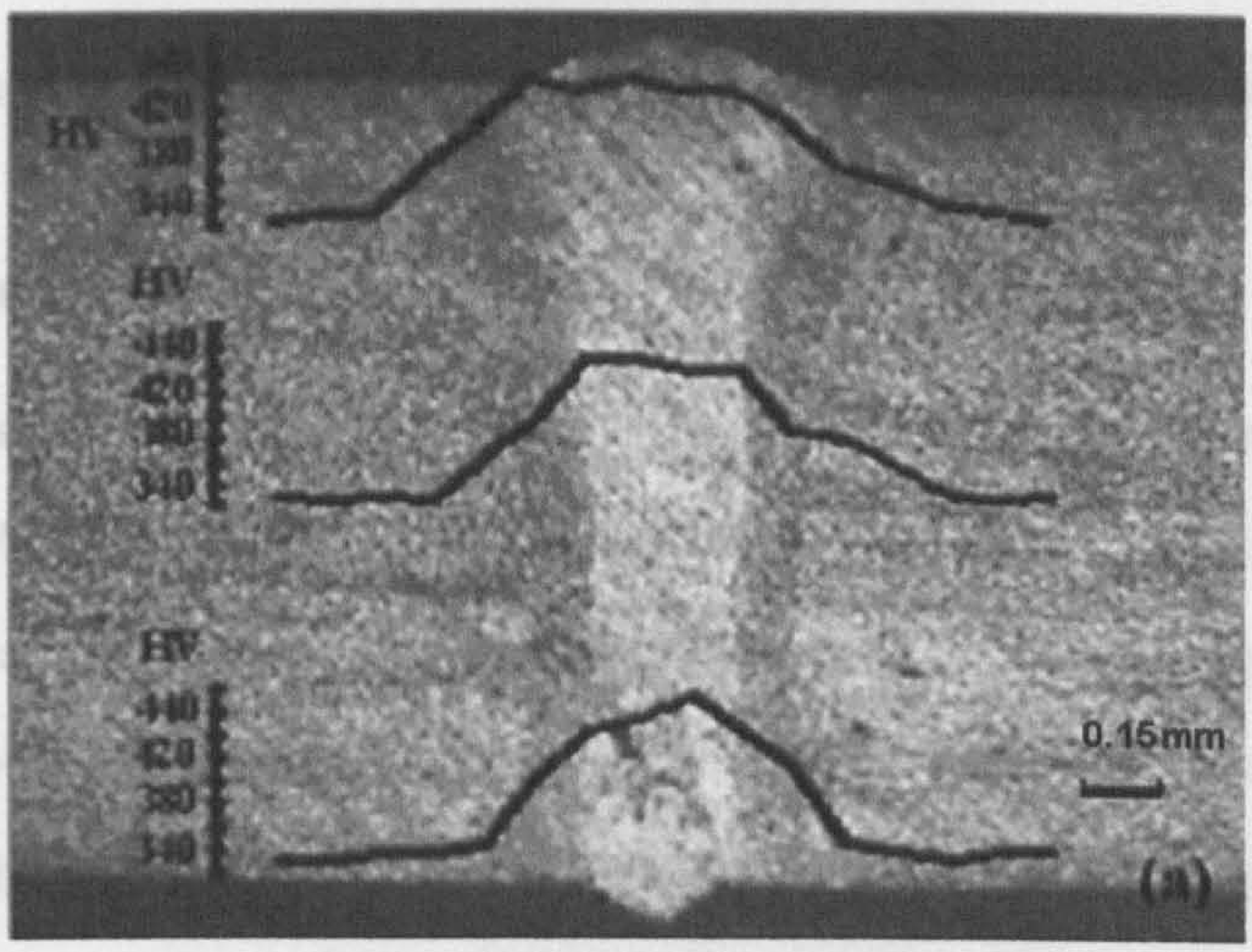

Figure 4.5 Cross sectional shape of CW CO_2 laser [15]

Figure 4.5 shows an example of another type of cross-sectional shape of weld bead, following welding with a CW CO_2 laser. There is no groove formation, but instead bulge generation in the weld bead.

4.2 Mechanical properties of welded titanium alloy

4.2.1 Hardness

As shown in chapter 3, hardness is quite sensitive to microstructure and heat treatment. In LBW Ti6Al4V, the variation in hardness observed across the weld is consistent with the observed changes in microstructure. Figures 4.6 and 4.7 highlight hardness values of Ti6Al4V from previous research work [3, 15-17]. The hardness of the FZ and HAZ were higher than those of the PM. The FZ exhibited the highest hardness as martensite α′ which had formed from the β phase (figure 4.1e) under the high cooling rates in this area. The hardness dropped quickly with position from the FZ to PM as the microstructure changed from martensite α′ to equiaxed α/β phase.

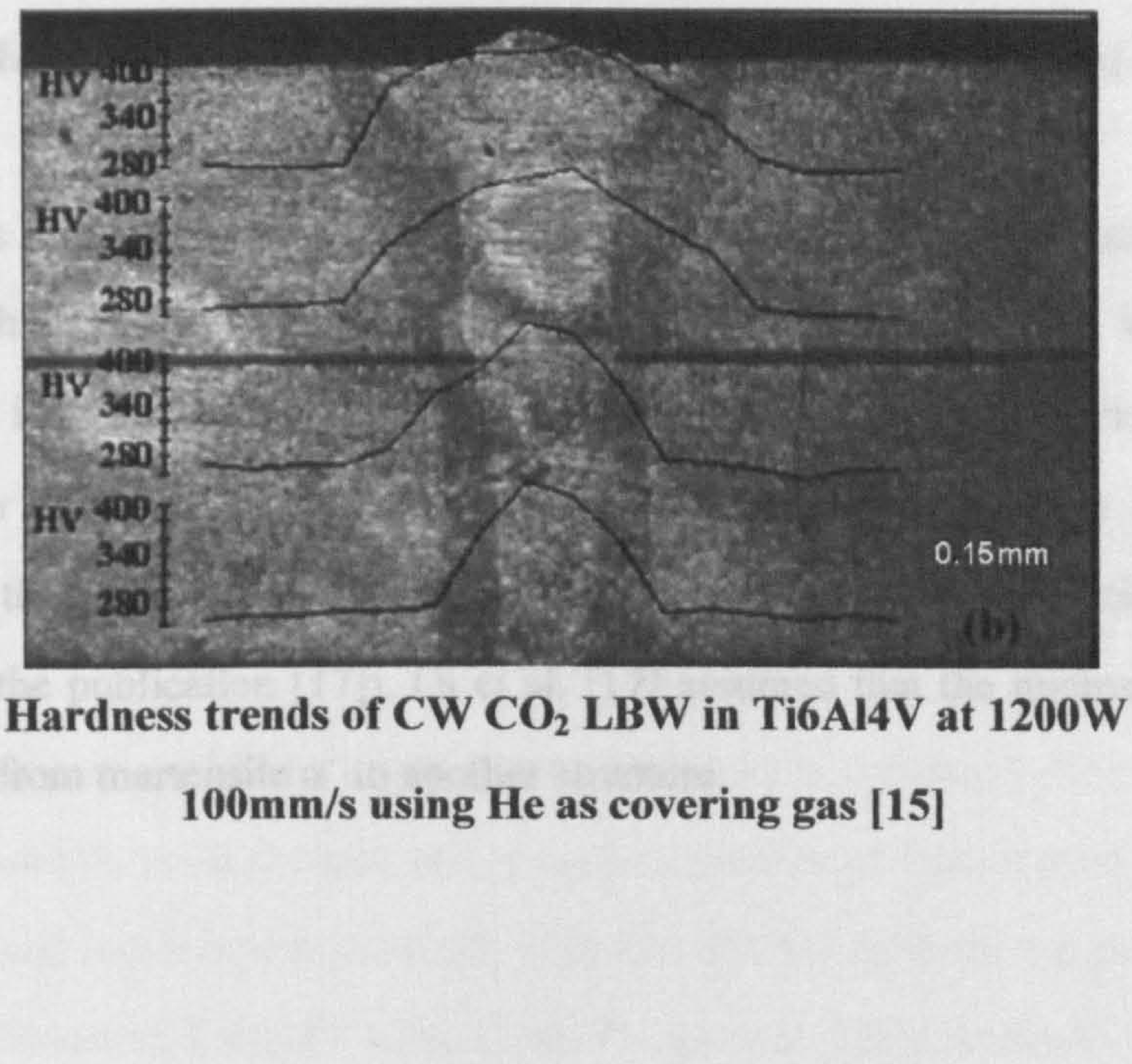

Figure 4.6 Hardness trends of CW CO_2 LBW in Ti6Al4V at 1200W and WS = 100mm/s using He as covering gas [15]

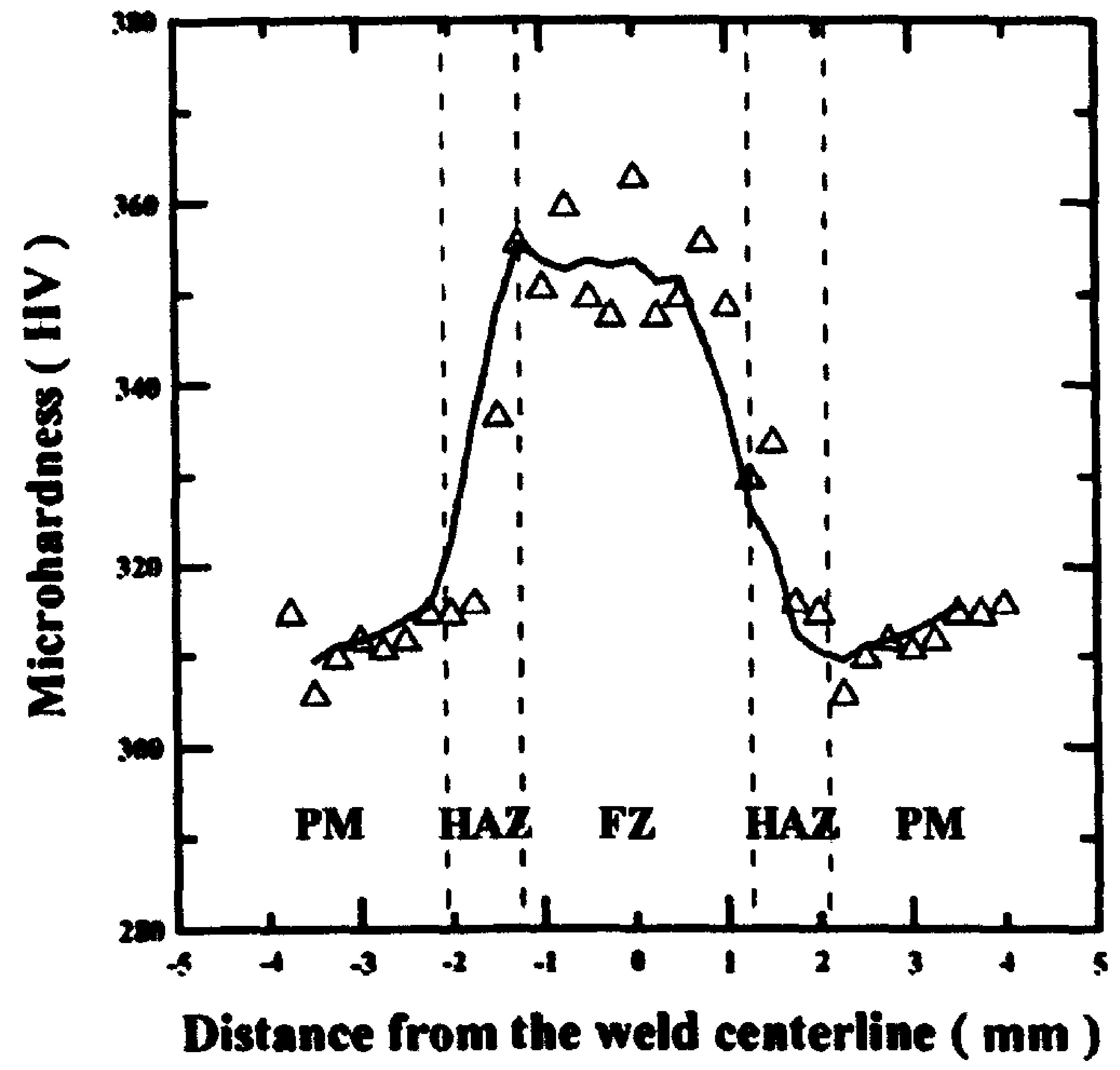

Figure 4.7 Hardness trends of CW CO_2 LBW in Ti6Al4V (3.3mm) at 2500W and WS = 25mm/s using He as covering gas [3]

The hardness of a weldment in Ti6Al4V can be modified by heat treatment. Figure 4.8 shows that the lowest hardness (150 $kgmm^{-2}$) in Laser Beam Welded pure titanium was is in the HAZ and the highest hardness (375 $kgmm^{-2}$) in the FZ was 1.5 times greater than that in the HAZ. After annealing, the hardness significantly decreased in the FZ to a value of only 225 $kgmm^{-2}$ (the annealing conditions were not indicated in the publication [17]). Qi et al. [17] assumed that the microstructure was transformed from martensite α' to another structure.

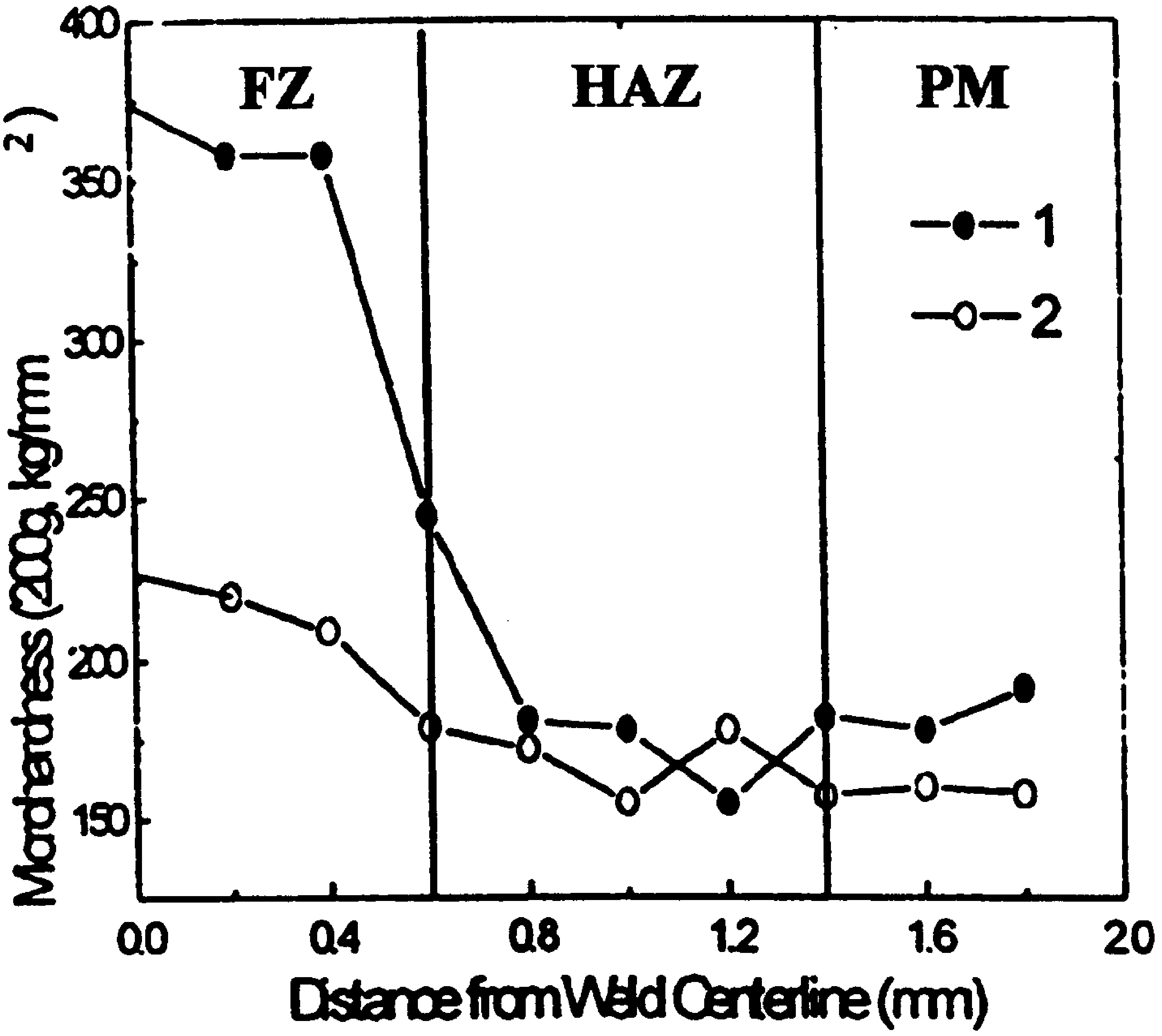

Figure 4.8 Heat treatment effect on the hardness of CO_2-LBW Titanium Sheet (1, welded state, 2, welded and then annealed state) [17]

4.2.2 Tensile properties and fatigue behaviour of welded Ti6Al4V

The tensile properties of PM Ti6Al4V were described in Chapter 3. Figure 4.9 shows the tensile strength, yield strength and elongation conducted from tensile tests at room temperature and low-temperature (150, 300, and 450°C) for both the parent material and the weldment of Ti6Al4V alloy from Wang et al. [3]'s research. The ultimate tensile strength of the weldment is very similar to that of the PM indicating that the FZ and HAZ are not the strength-limiting structures in the weldment. However, it is noted that the elongation to failure of the weldment is always lower than that of the PM. As the martensite α′ in the weld shows poor ductility.

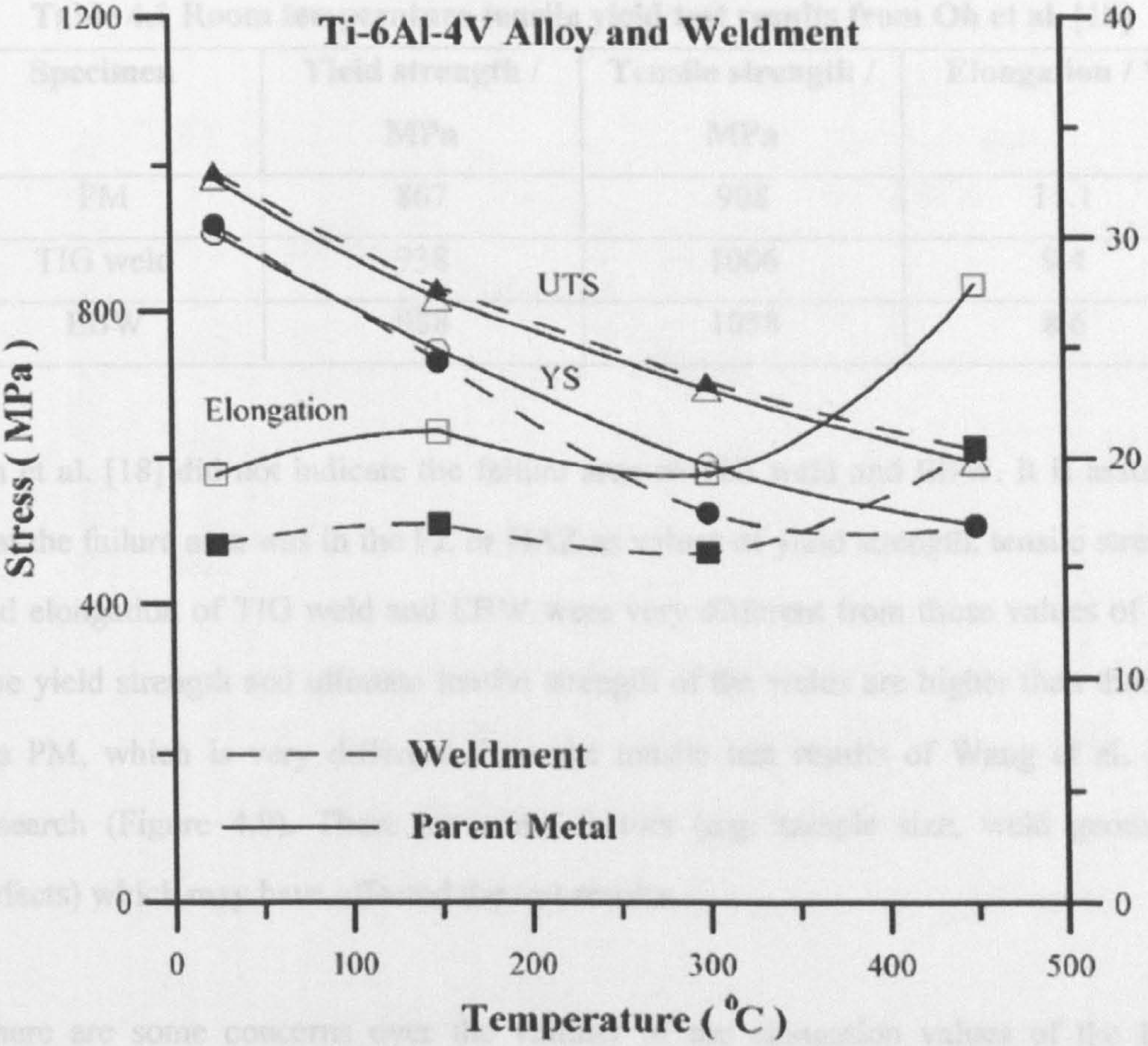

Figure 4.9 Tensile stress and elongation of CW CO_2 LBW as a function of temperature for both the parent metal and weldment in Ti6Al4V [3]

Oh et al.[18] conducted research on the high-cycle fatigue properties of welded Ti6Al4V alloy with both the Tungsten Inert Gas (TIG) and the Electron Beam (EB) welding process. Both LBW and EBW share the feature of high power densities in narrowly focused beams, and the resultant appearance of these types of welds are sometimes quite similar [17]. The tensile properties of PM, TIG welded and EBW Ti6Al4V are shown in table 4.1:

Table 4.1 Room temperature tensile yield test results from Oh et al. [18]

Specimen	Yield strength / MPa	Tensile strength / MPa	Elongation / %
PM	867	908	11.1
TIG weld	938	1006	9.4
EBW	988	1058	8.6

Oh et al. [18] did not indicate the failure area of TIG weld and EBW. It is assumed that the failure area was in the FZ or HAZ as values of yield strength, tensile strength and elongation of TIG weld and EBW were very different from those values of PM. The yield strength and ultimate tensile strength of the welds are higher than those of the PM, which is very different from the tensile test results of Wang et al. [3]'s research (Figure 4.9). There are some factors (e.g. sample size, weld geometry, defects) which may have affected the test results.

There are some concerns over the validity of the elongation values of the EBW samples, since the FZ and HAZ of EBW are always narrow and brittle and the sample size (13×30×6mm) is not big enough. EB weld samples may fail before plastic deformation as Oh et al. [18] indicated that micropores in the weld were the issue limiting the strength of welded Ti6Al4V. In addition, Oh et al. [18] conducted works on the fatigue behaviour of welded Ti6Al4V. Figure 4.10 shows the high-cycle fatigue test results. The fatigue life of TIG welded Ti6Al4V was observed to be higher than that of PM. The explanation is that the Ti6Al4V was transformed from a lamellar structure into 'a basket-weave structure after welding and annealing' [18] (figure 4.11a-b). The EBW Ti6Al4V has higher yield strength than the other materials, but the lowest fatigue life of all. The reason is that the size of 'α platelets, α grain boundary and prior β grains' [18] was the smallest in the EBW samples because of the fast cooling rates following welding, thus, EBW Ti6Al4V has highest yield and tensile strength. However, coarse micropores (figure 4.11c) were observed in EBW which reduced the resistance to fatigue crack initiation.

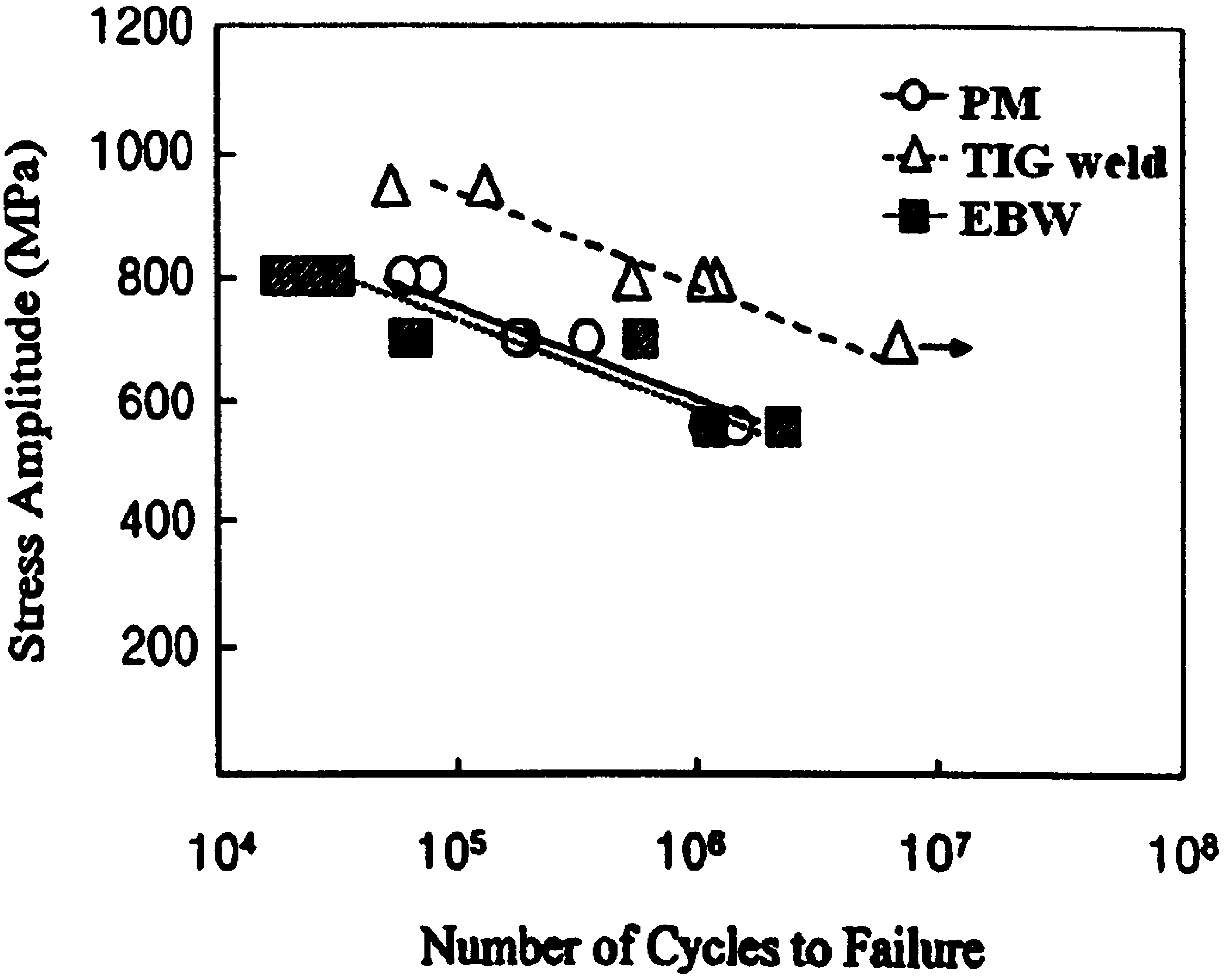

Figure 4.10 S-N curves of PM, TIG weld, and EBW Ti6Al4V [18]

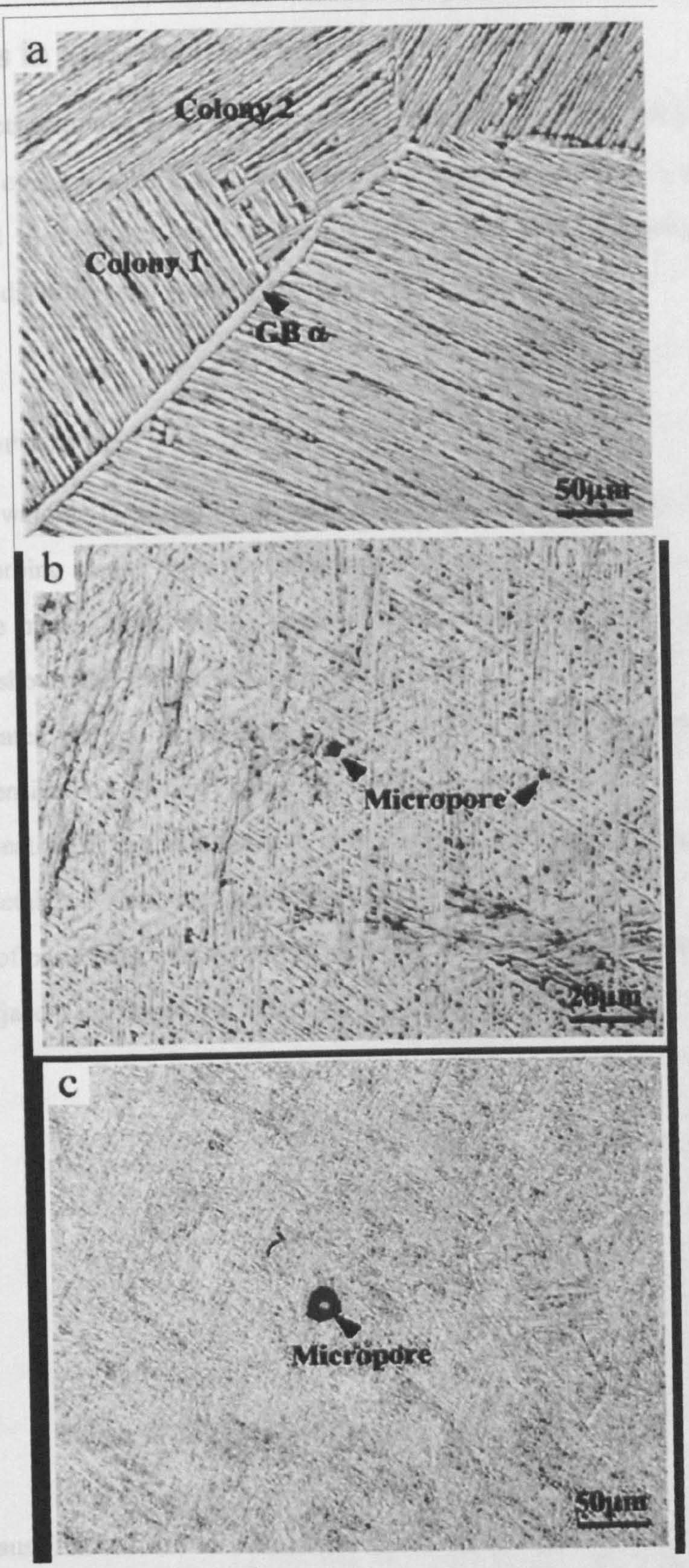

Figure 4.11 Light Micrographs of structures observed in Ti6Al4V of (a) PM, (b) FZ of TIG weld (c) FZ of EB weld [18]

4.3 Defects in laser beam welds

Welding defects following laser beam welding include cracks, incomplete penetration, weld colour (contamination), pits, distortion and porosity. Distortion and porosity were detected in the laser beam welds in this project. The formation, effect and prevention of distortion and porosity are discussed in this section.

4.3.1 Distortion

Distortion in welding is caused by warping of the joint plate caused by heat from the laser. The warping results from the expansion and contraction of the weld metal and adjacent base metal during the heating and cooling cycle of the welding process. Figure 4.12 shows the reason for distortion occurring in a weld. If a metal bar is uniformly heated with no restraining, it will expand in all direction and return to its original dimensions on cooling (figure 4.12 (a)). If restrained as shown in figure 4.12 (b), during heating, it can expand only in the vertical direction. During cooling, the deformed metal bar contracts uniformly (figure 4.12 (c)). This is a simplified explanation of basic reason of distortion in weld if considering metal bar to be melted metal and adjacent restrained bar to be non-melted metal.

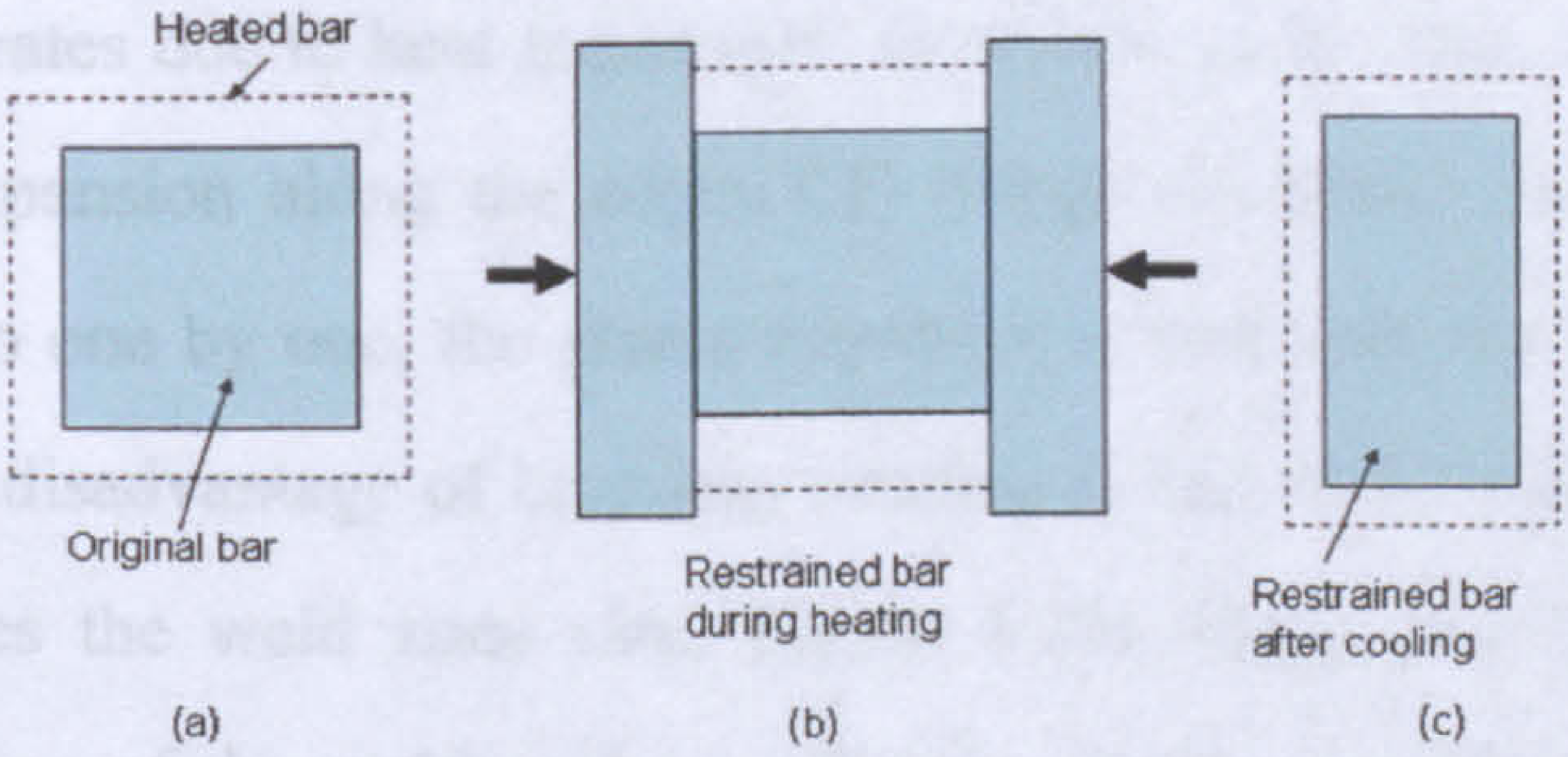

Figure 4.12 Reason of distortion in a welding [19]

The main cause for concern associated with weld distortion is that the weld geometry changes, so that the strength of weld is often reduced. The factors affecting distortion were identified in Lightfoot et al.'s study to be plate thickness, heat input, travel speed [20], edge preparation and material properties [21]. These factors can be divided into three types. The first type was plate thickness and material properties which are fixed for a given material. The second type was welding parameters which include heat input and travel speed. The third type was weld design (edge preparation).

Distortion cannot be prevented, but it can be controlled. Better control of welding variables can minimize distortion; these include using high speed welding, using a low heat input welding process, using intermittent welds, using a backstep technique and balancing heat about the plate's neutral axis [20]. To use high traverse speed is to minimize welding time, and thus affect the heat input and shrinkage. As shown in figure 4.12, shrinkage is the big issue in distortion. Another way to minimize weld distortion is to use intermittent rather than continuous welds (figure 4.13 a), as an intermittent weld can balance residual stresses if the position of the weld bead alternates. However, intermittent welding cannot be applied to give hermeticity from the welding process. The backstep welding technique is a very commonly used way to reduce the distortion. In the backstep welding technique (figure 4.13 b), the welding direction is from left to right, but each bead segment is deposited from right to left. During the welding process, when each bead segment is placed, the point B temporarily separates due to heat expansion. However, as the heat moves from point A to point C, expansion along the edges CD brings the plates back together. With repeated backstep one by one, the plates expand less and less due to the restraint of prior welds. The disadvantage of backstep welding is that it decreases the production rate and increases the weld zone size. Figure 4.13c shows one design method to minimize distortion of the weldment by balancing welds around the neutral axis to offset one shrinkage force with another.

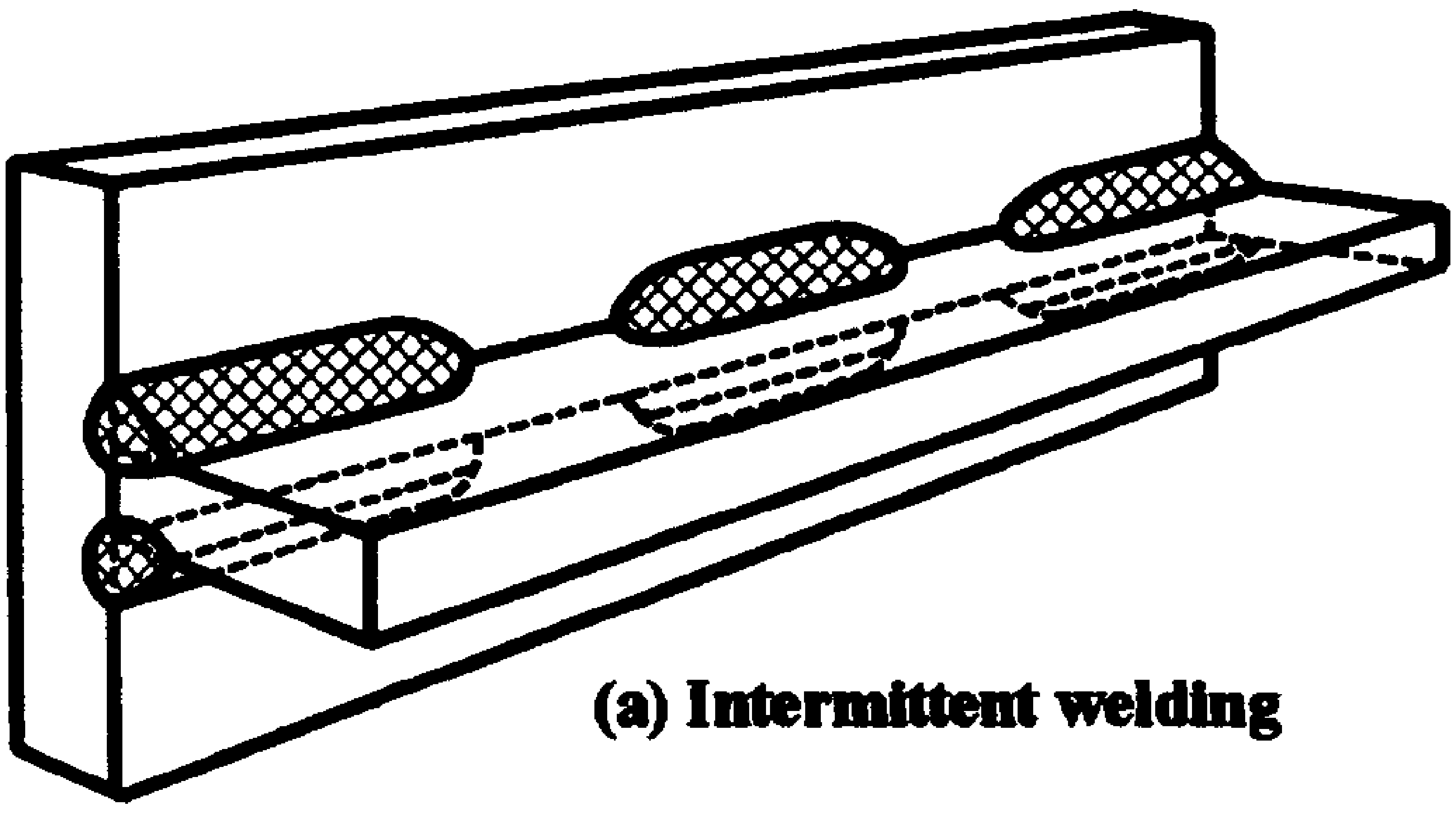

(a) Intermittent welding

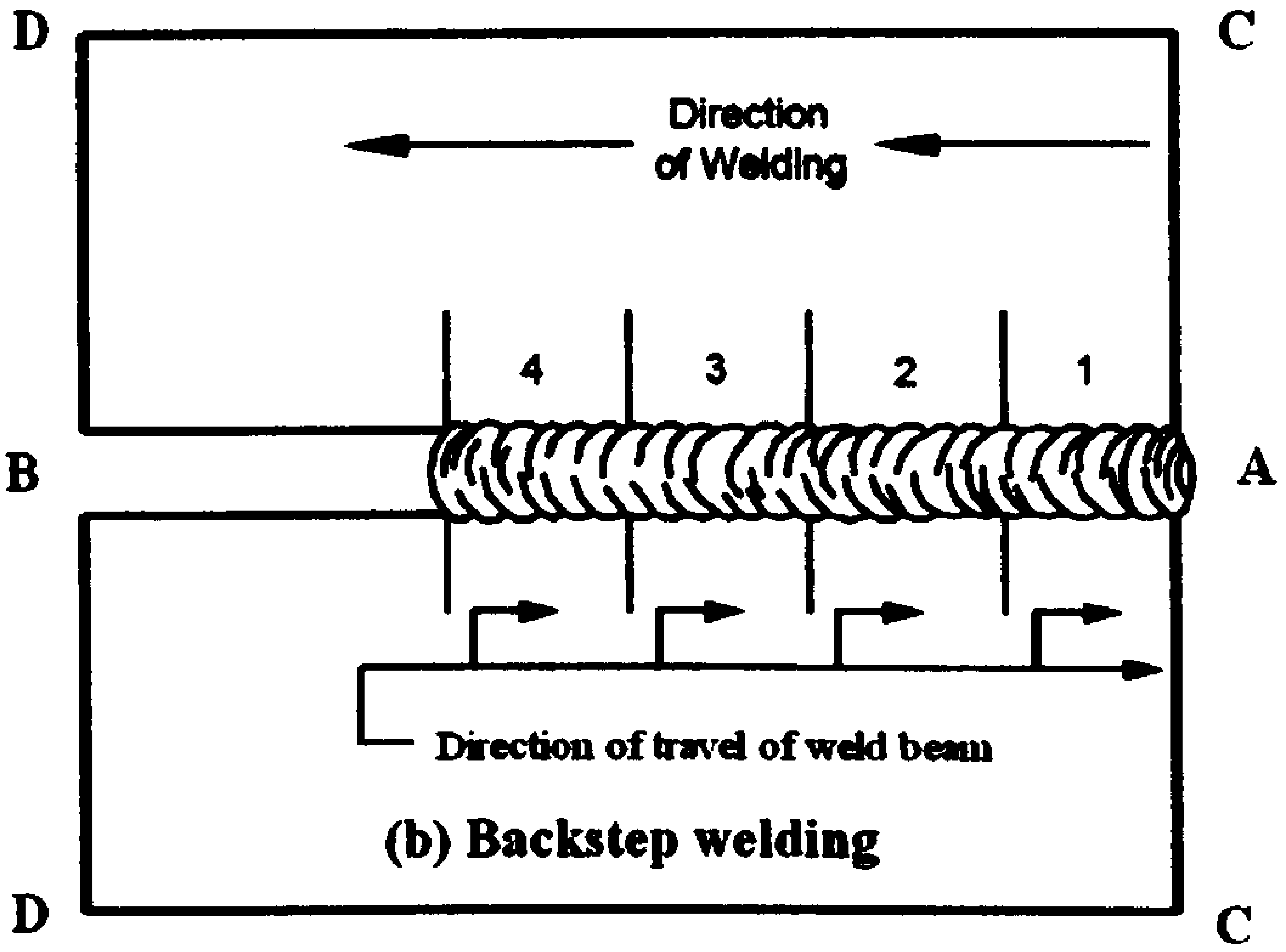

(b) Backstep welding

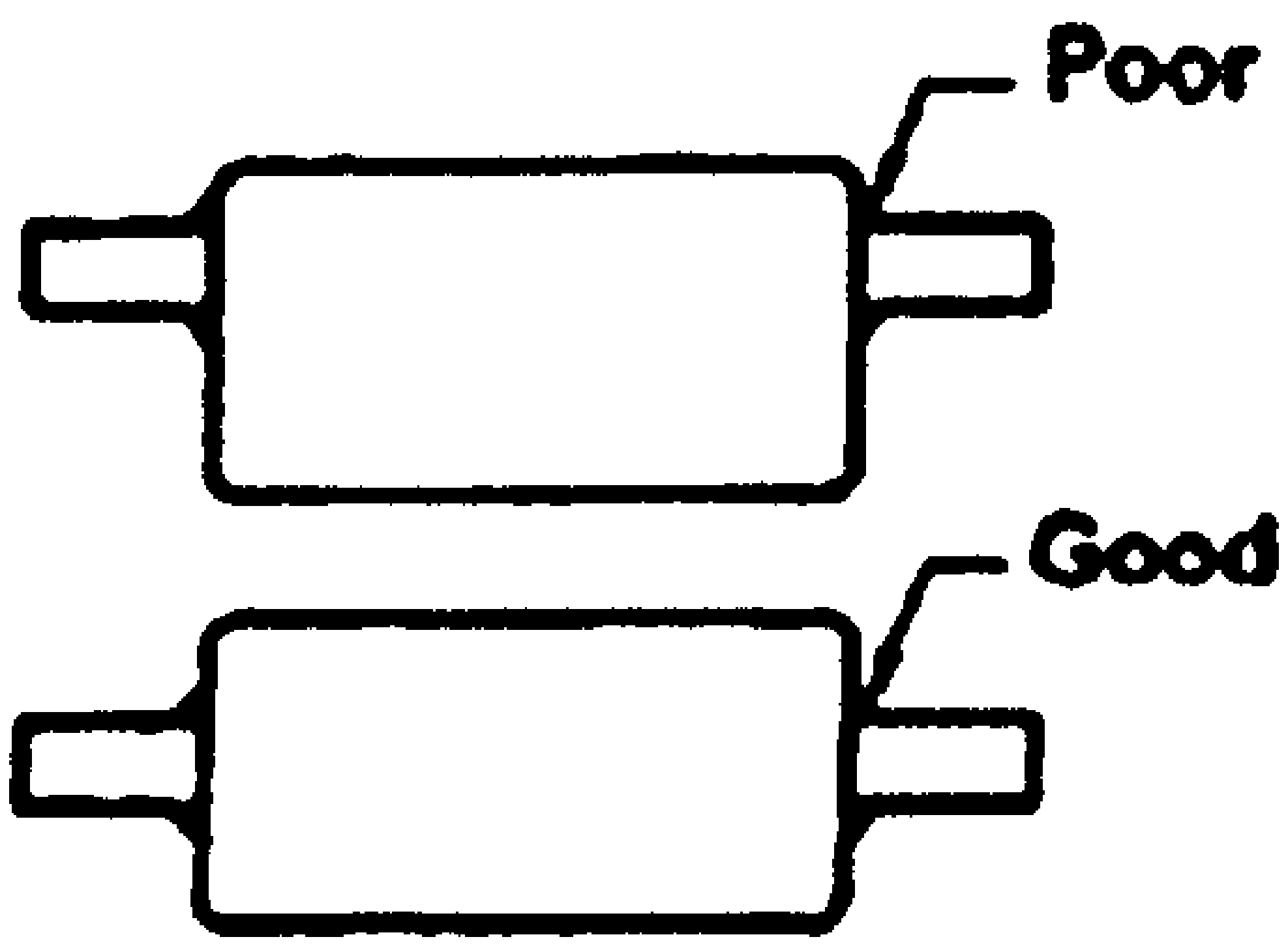

(c) Balancing welds around neutral axis

Figure 4.13 Welding techniques utilised to minimize the distortion [19, 20]

Edge preparation and assembly can be designed in anticipation of the shrinkage force, thus, minimizing the distortion as well. Figure 4.14 shows designs which take the shrinkage into account.

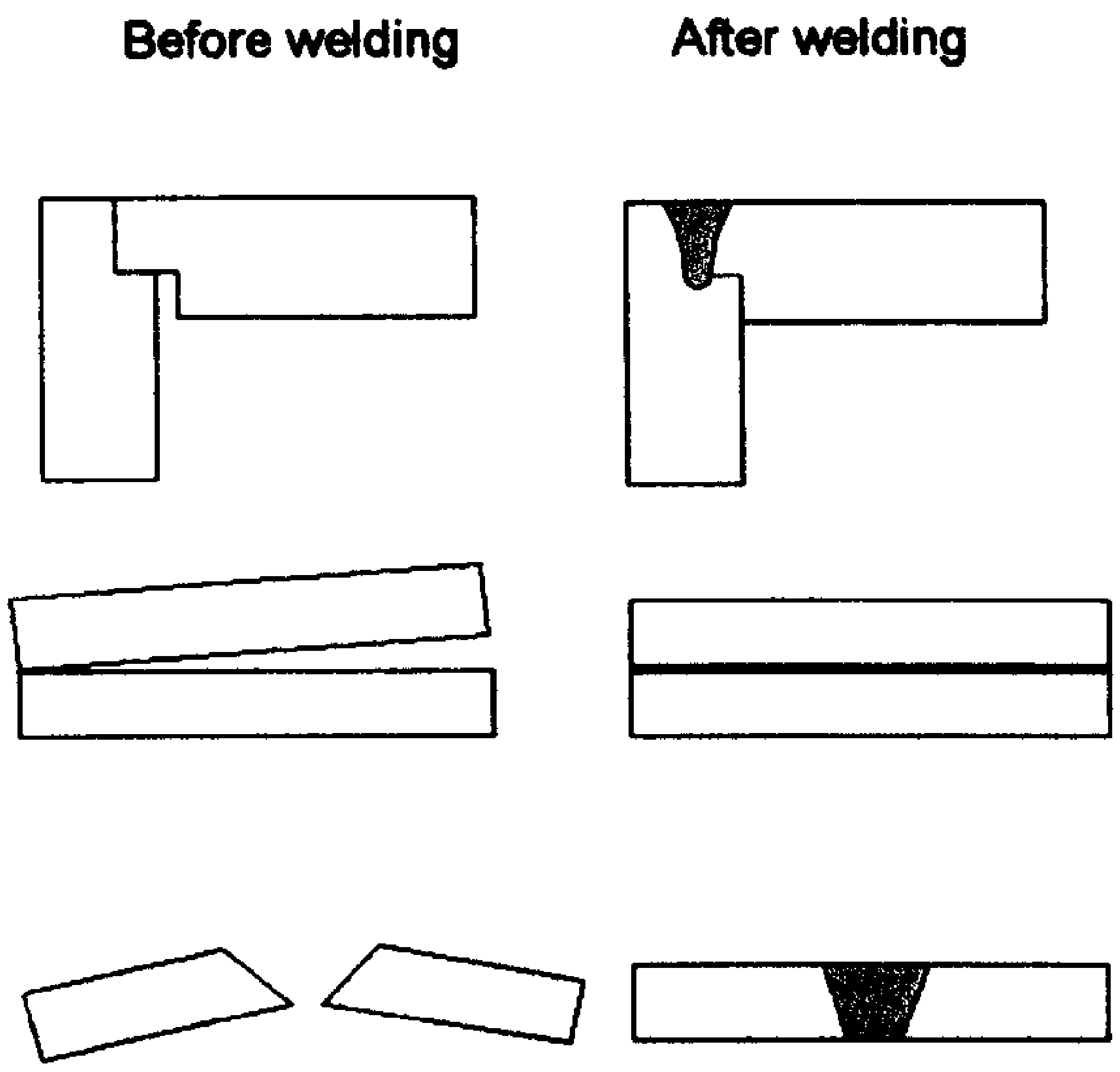

Figure 4.14 Edges preparation and assembly to minimize the distortion following welding [1, 20]

There are some other ways to reduce distortion, such as preheating the samples, peening and stress relieving heat treatment.

4.3.2 Porosity

Porosity can be a significant defect in welds prepared by laser beam welding. Statistical analysis of defects in laser beam welded titanium alloy has shown that pores accounted for 43 to 56% of the total number of defects [22]. Porosity can significantly affect the strength and the reliability of welded joints, being most deleterious under fatigue loading. This reduction in fatigue resistance is associated both with the geometrical stress concentration associated with the pores and also with changes in material ductility in this region [22]. Previous research indicates that under high power densities, there is rapid vapour formation from the base of the keyhole, along with melt flow and the formation of solid-liquid zones as the metal melt-front expands. Under such conditions, pores can be formed and trapped in the melt during the solidification period [13]. In the laser welding processes, it has been proposed that the tendency to form a porous weld is associated with the liquid metal solidification rate and the speed at which the molten metal back-fills the keyhole. It is clear that the backfilling speed decreases and the solidification rate increases as the keyhole depth-to-width ratio increases, and as such, narrow keyholes are more prone to retention of porosity than wide welds [14]. It has also been observed that the plasma formation during the weld process may affect pore formation, and that since the plasma dynamics are controlled in part by the choice of the shielding gas, then the porosity can be thus controlled also [23].

Whilst porosity is observed in both continuous wave and pulsed laser welds, the work of Kuo and Jeng [24] indicated that pulsed laser welding of both stainless steel and a nickel alloy resulted in lower porosity compared with comparable CW laser welding (figure 4.15 and figure 4.16). They postulated that laser pulsing agitates the molten pool and promotes a periodic molten metal flow, which causes bubbles to float to the surface, hence decreasing weld porosity. Conversely, in the CW mode, there is no pulsing, and hence more bubbles remain in the weld pool during solidification. Moreover, they argued that the effect of the use of a pulsed laser on porosity was much more significant for the nickel alloy than for the stainless steel, and that this was related to the higher viscosity of the nickel alloy when molten.

People have already proposed several methods to prevent porosity formation. The first method [25] involved welding in a vacuum. However, the inflexibility and high cost mean that welding in a vacuum environment is not suitable for most industrial situations. The second method is to use a particular kind of shielding gas (e.g. N_2 and CO_2) which can be dissolved in the molten metal. The limitation of the application is that it is only suitable for certain welding cases in which the shielding gas 'matches' the weld metal (304S has high solubility of N_2 due to a high Cr content) with no negative chemical reactions; use of nitrogen is unsuitable in titanium welding as nitrogen is very reactive with titanium alloy [1]. The last methods can be summarized as the control of parameters during welding, which include travel speed, power, spot size, shielding gas flow rate. In pulsed LBW, more parameters were controllable, such as pulse duration, peak power and base power, wave shape. Zhou and Tsai's [14] research indicated that formation of porosity in pulsed LBW is caused by two competing factors: solidification rate of the molten metal and the backfilling speed of the molten metal during the keyhole collapse process. 'Porosity will be formed in the final weld if the solidification rate of the molten metal exceeds the backfilling speed of the molten metal during the keyhole collapse and solidification processes' [14]. Hence, once the backfilling speed has been identified, a reduction in the solidification rate of the molten metal can decrease the porosity. The increase of the peak power density increased the melting area which thus reduced the solidification rate of the molten area. This could be another explanation of the observation reported in Kuo and Jeng's [24] work.

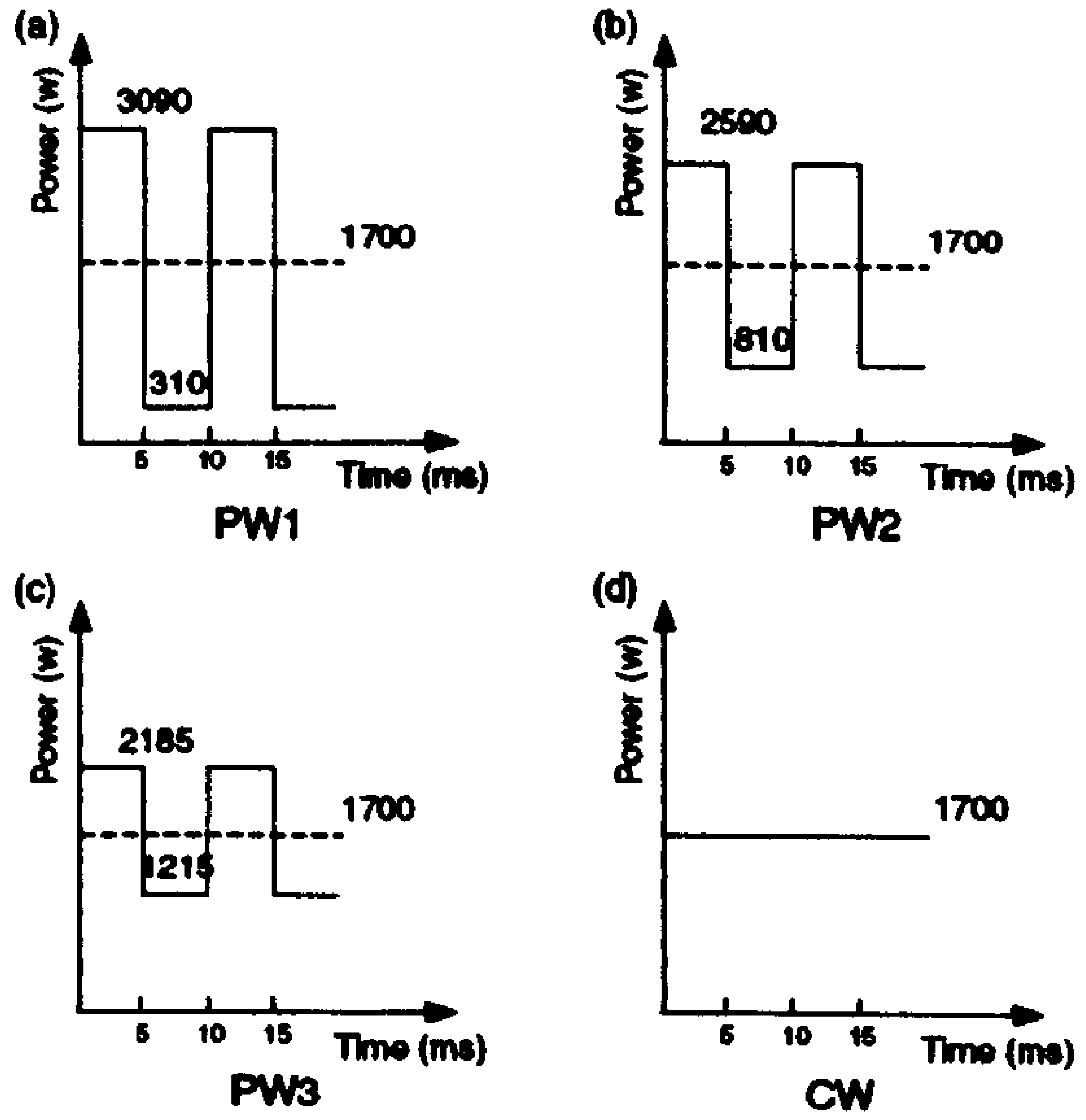

Figure 4.15 Laser power output modes and ΔP level: (a) PW1, (b) PW2, (c) PW3, and (d) CW [24]

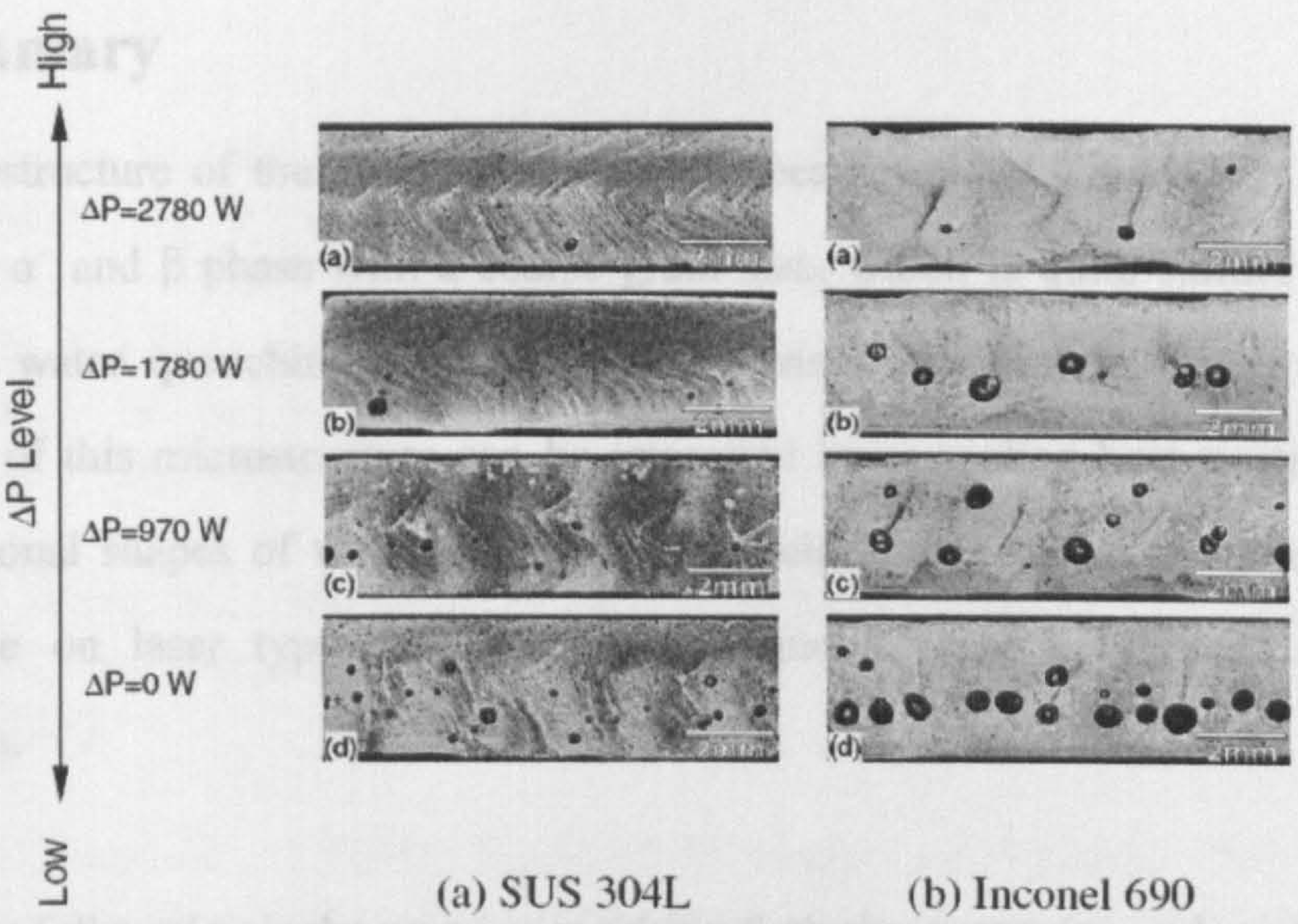

(a) SUS 304L (b) Inconel 690

Figure 4.16 Porosity in longitudinal sections of butt-welded samples in two metals (as indicated): (a) PW1, (b) PW2, (c) PW3, and (d) CW (see Figure 4.15) [24]

4.4 Summary

The microstructure of the fusion zone in laser beam welded Ti6Al4V is primarily martensite α' and β phase with a coarse grain size, which is quite similar with that formed in water quenching process above β-transus temperature. The mechanical properties of this microstructure can be improved by annealing heat treatment. The cross-sectional shapes of welds in laser beam welded titanium alloy have a strong dependence on laser type, weld mode (continuous wave or pulsed) and edge preparation.

The origin of distortion is the warping resulting from the expansion and contraction of the weld metal and adjacent parent metal. Parameter control, edge preparation and special welding techniques can be used to minimize weld distortion. The origin of porosity is that the bubbles cannot come out when the upper melt material rapidly fills in the melting area and solidifies. The source of the bubbles is primarily from evaporation of the liquid during welding. Parameter control, welding in a vacuum and using dissolved shielding gas can be used to minimize porosity. Pulsed LBW with high peak power and short duration exhibits less porosity than continuous wave LBW.

References:

[1] American Welding Society. Recommended Practices for Laser Beam Welding, Cutting, and Drilling: ANSI/AWS 1998.

[2] J.Oh, N.J.Kim, S.Lee and E.W.Lee. Correlation of fatigue properties and microstructure in investment cast Ti-6Al-4V welds. *Materials Science and Engineering A*. 2003; 340(1-2):232-42.

[3] S.H.Wang, M.D.Wei and L.W.Tsay. Tensile properties of LBW welds in Ti-6Al-4V alloy at evaluated temperatures below 450°C. *Materials Letters*. 2003; 57(12):1815-23.

[4] M.T.Jovanović, S.Tadić, S.Zec, Z.Mišković and I.Bobić. The effect of annealing temperatures and cooling rates on microstructure and mechanical properties of investment cast Ti-6Al-4V alloy. *Materials and design*. 2006; 27:192-9.

[5] L.W.Tsay, Y.P.Shan, Y.H.Chao, and W.Y.Shu. The influence of porosity on the fatigue crack growth behavior of Ti-6Al-4V laser welds. *Materials Science*. 2006; 41:7498-505.

[6] C.A.Walsh, H.K.D.H.Bhadeshia, A.Lau, B.Matthias, R.Oesterlein and J. Drechsel. Characteristics of High-Power Diode-Laser Welds for Industrial Assembly. *Journal of Laser Applications*. 2003; 15(2):68-76.

[7] Y. Okamoto, A.Gillner and A.Olowinsky. Fine micro-welding of thin metal sheet by high speed laser scanning. In: Photonic materials d, and applications II editor. Proc of SPIE; 2007; Maspalomas, Gran Canaria, Spain; 2007. p. 65930D 1-10.

[8] A.Salminen A.Jansson and V.Kujanpaa. Effect of welding parameters on high power diode laser welding of thin sheet. In: SPIE Po, editor. High-Power Diode Laser Technology and Applications; 2003; Mark S. Zediker; 2003. p. 106-15.

[9] A.I.Koruk and I.Hrivnak. High power laser welding application of thin sheets and assessment of weld bead properties. In: SPIE Po, editor. High-Power Lasers in Manufacturing; 2000.

[10] Y.Kawahito, T.Ohnishi and S.Katayama. In-process monitoring and feedback control for stable production of full-penetration weld in continuous wave fibre laser welding. *Journal of physics D: applied physics*. 2009; 42(8):085501.

[11] Y.Kawahotp, M.Kito, S.Katayama. In-process monitoring and adaptive control for gap in micro butt welding with pulsed YAG laser. *Journal of Physics D: Applied Physics*. 2007; 40:2972-8.

[12] B.J.Aalderink, D.F.de.Lange, R.G.K.M.Aarts and J.Meijer. Keyhole shapes during laser welding of thin metal sheets. *J Phys D: Appl Phys.* 2007; 40:5388-93.

[13] N.Kumar, S.Dash, A.K.Tyagi and B.Raj. Hydrodynamical phenomena during laser welding. *Science Tech Welding Joining*. 2007; 12:540.

[14] J.Zhou and H.Tsai. Porosity formation and prevention in pulsed laser welding. *ASME*. 2007; 129:1014-24.

[15] F.Caiazzo, F.Curcio, G.Daurelio and F.Memola Capece Minutolo. Ti6Al4V sheets lap and butt joints carried by CO2 Laser: mechanical and morphological characterization. *Journal of Materials Processing Technology*. 2004; 149:546-52.

[16] ASTM Standard. Standard specification for titanium-6aluminum-4vanadium surgical implants. UNS 54406; F1108-02.

[17] Y.Qi, J.Deng, Q.Hong and L.Zeng. Electron beam welding, laser beam welding and gas tungsten arc welding of titanium sheet. *Materials Science and Engineering*. 2000; A280:177-81.

[18] J.Oh, N.J.Kim and S.Lee. High-cycle fatigue properties of investment cast Ti-6Al-4V alloy welds. *Journal of Materials Science Letters*. 2001; 20:2183-7.

[19] W.Galvery and F.M.Marlow. Welding Essentials:Question and Answers. 1st ed: Industrial Press Inc. 2001.

[20] C.L.Tsai, S.C.Park and W.T.Cheng. Welding distortion of a thin-plate panel structure. *Welding journal*. 1999; 78:157s-65s.

[21] M.P.Lightfoot, N.A.McPherson, K.Woods and G.J.Bruce. Artificial neural networks as an aid to steel plate distortion reduction. *Journal of materials processing technology*. 2006; 172:238-42.

[22] V.I.Murav'ev. Problems of pore formation in welded joints of titanium alloys. *Metal Science and Heat Treatment*. 2005; 47:282-8.

[23] N.Seto, S.Katayam and A.Matsunawa. High-speed simultaneous observation of plasma and keyhole behaviour during the high power CO2 laser welding: effect of shielding gas on porosity formation. *Journal of laser applications*. 2000; 12(6):245-50.

[24] T.Y.Kuo and S.L.Jeng. Porosity reduction in Nd:YAG laser welding of stainless steel and inconel alloy by using a pulsed wave. *Journal of physics D: applied physics*. 2005; 38:722-8.

[25] S.Katayama, Y.Kobayashi, N.Seto, M.Mizutani and A.Matsunawa. Effect of vacuum on penetration and defects in laser welding. *Journal of Laser Applications.* 2001; 13(5):182-91.

CHAPTER 5

Chapter 5 Experimental Procedures

In this chapter, the preparation of the Ti6Al4V weld part is introduced. Three types of weld (pulsed Nd:YAG laser weld, continuous wave diode-pumped laser weld and continuous wave fibre laser weld) were employed to enable comparison of the quality and properties of the weld microstructures, geometries and properties. Microstructure was assessed through optical microscopy and SEM; geometry was assessed through microscopy methods and profilometry; mechanical properties were assessed through hardness testing, tensile failure testing and tensile fatigue testing. In order to understand the influence of microstructure on mechanical properties and fatigue behaviour, heat treatment was used for phase transformation of the as-welded structure and structure modification. Finite Element Analysis (FEA) was employed to aid understanding of the influence of weld geometry on stress level, so that the tensile fatigue behaviour of the welded components could be understood and properly evaluated.

5.1 Materials and weld process

The material used in this study was 0.7 mm thick sheet Ti6Al4V alloy[1]. Following rolling, the sheet was heat treated at 850°C for 8 hours followed by 750°C for 30mins and then a furnace cooled to room temperature. The measured composition was provided by the supplier of the sheet and is shown in Table5.1.

Table 5.1 Measured chemical composition of Ti6Al4V sheet (wt %)

Ti	Al	V	C	Fe	O	N	H	Y
Bal.	6.5	4.0	0.006	0.17	0.156	0.007	0.0005	<0.005

As-received sheet material was cut in to samples used in testing; the size of these samples was 60 mm × 25 mm × 0.7 mm as shown in Figure 5.1. The edges of each sample were machined using a vertical milling cutter to ensure 90° angle between top

---

[1] Provide by Timet UK Limited, Off Brookvale Road, P O box 704Whiten, Birmingham, B6 7UR

surface and weld interface; the air gap required between the two abutting faces was less than 0.005 mm.

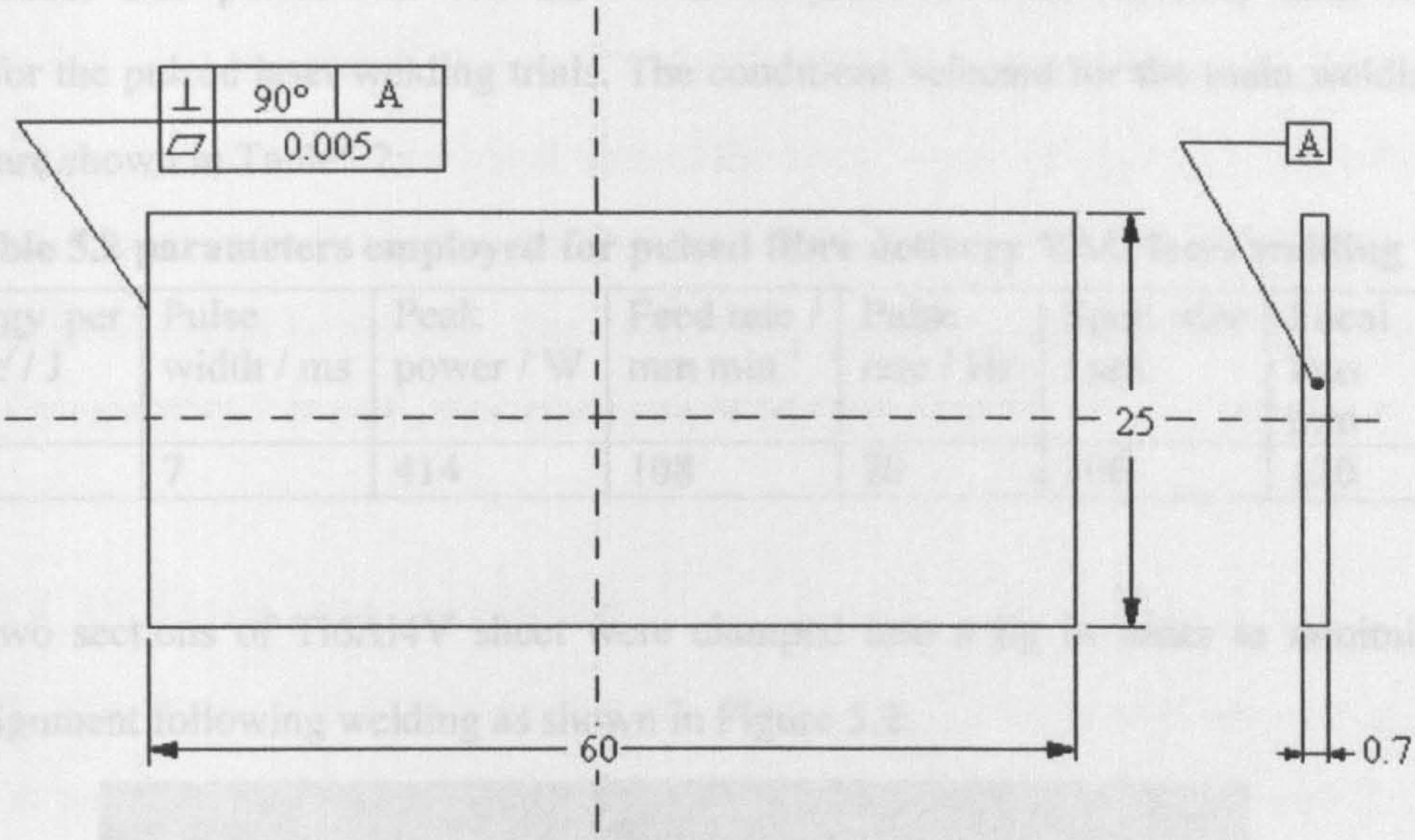

Figure 5.1 Laser Beam Welding samples

5.1.1 Initial weld trials

For each laser type, a bead-on-plate and penetration step was made to achieve the desired weld penetration (100% penetration) and acceptable visual appearance. During the bead-on-plate process, a start point for one of the key input laser parameters was selected. The selection of these parameter starting points and the main key parameters was based upon historical knowledge of welding of similar materials with similar weld joint configuration. For each weld-run, the selected starting key parameter was held constant as the others were varied. These variations provided different results for penetration depth. At the end, suitable welding parameters for each of the laser types were gained to identify sets of conditions under which full penetration could be achieved robustly and reproducibly for the lowest incident energy per unit length. Also, there was a requirement that no pits, holes, cracks and contamination (pure colour) could be observed upon visual inspection.

5.1.2 Pulsed fibre delivery Nd:YAG laser welding

A JK702H GSI[2] pulsed Nd:YAG laser with 400µm fibre beam delivery laser was used for the pulsed laser welding trials. The conditions selected for the main welding trials are shown in Table5.2:

Table 5.2 parameters employed for pulsed fibre delivery YAG laser welding

Energy per pulse / J	Pulse width / ms	Peak power / W	Feed rate / mm min^{-1}	Pulse rate / Hz	Spot size / µm	Focal lens / mm
2.9	7	414	108	20	300	120

The two sections of Ti6Al4V sheet were clamped into a jig in order to minimise misalignment following welding as shown in Figure 5.2.

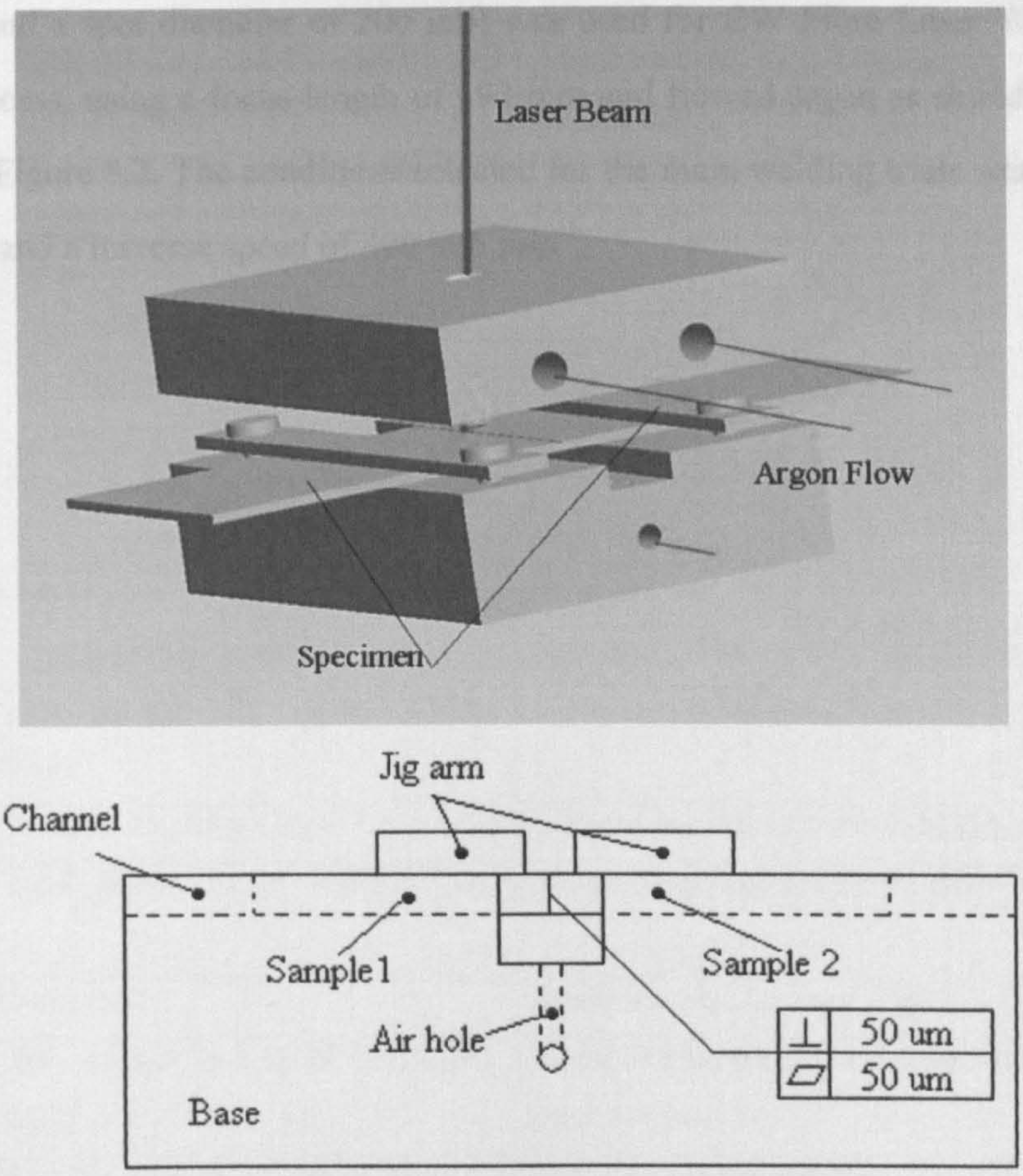

Figure 5.2 Image and sketch of Jig used in the LBW process

---

[2] CSI Lumonics, Cosford Lane, Swift Valley Rugby, Warwickshire, CV21 1QN, UK

5.1.3 CW diode laser welding

A ROFIN DL 025 Industrial Diode Laser[3] with a large rectangular spot size of 6 mm × 2 mm was used for CW Diode Laser Weld (CW-DLW) process. Argon was used as the shielding gas; this was contained around the weld by use of a polymer bag which was sealed around the specimen table and weld head. The maximum power is 2500 W and the focus length is 100 mm. The conditions selected for the main welding trials were a power of 650 W and a traverse speed of 300 mm min^{-1}.

5.1.4 CW fibre laser welding

A TLR-2000 Series CW Ytterbium 200 μm Fibre Laser[4] (with a maximum power of 2000 W and a spot diameter of 200 μm) was used for CW Fibre Laser Weld (CW-FLW) process, using a focus length of 192 mm and flowed argon as shielding gas as shown in Figure 5.2. The conditions selected for the main welding trials were a power of 600 W and a traverse speed of 400 mm min^{-1}.

---

[3] Rofin-Sinar, York Way, Willerby, Kingston upon Hull, UK, HU10 6HD

[4] IPG Photonics, 50 Old Webster Road, Oxford, MA 01540, USA

5.2 Microstructure analysis

5.2.1 Sample preparation

Samples for microstructural analysis were mounted in conductive hot-mounting resin. The samples were ground with 240 mesh silicon carbide papers (to remove any oxide layer) followed by 400, 800, 1200 mesh silicon carbide papers, and finally polished using a porous neoprene polishing disc to a mirror finish. Different compositions of microetchants are suitable in different applications for titanium alloy metallography. Table 5.3 shows different etchants used for different purposes in the examination of titanium and titanium alloys [1]. The composition of etching solution used in this study was a mixture of 2 ml HF and 5 ml HNO_3 acids in water (Kroll's reagent).

Table 5.3 Etchants for examination of titanium and titanium alloys [1]

Etchant	**Comments**
Macroetchants	
50 mL HCL, 50 mL H_2O	General-purpose etch for α+β alloys
30 mL HNO_3, 3 mL HF, 67 mL H_2O (slow) to 10 mL HNO_3, 8 mL HF, 82 mL H_2O (fast)	Used at room temperature to 55°C (130°F) for 3-5 minutes. Reveals grain size and surface defects
15 mL HNO_3, 10 mL HF, 75 mL H_2O	Etch about 2 minutes. Reveals flow lines and defects
Microetchants	
1-3 mL HF, 10 mL HNO_3, 30 mL lactic acid	Reveals hydrides in unalloyed titanium
Kroll's reagent: 1-3 mL HF, 2-6 mL HNO_3, H_2O to 1000 mL	General-purpose etch for most alloys
10 mL HF, 5 mL HNO_3, 85 mL H_2O	General-purpose etch for most alloys
1 mL HF, 2 mL HNO_3, 50 mL H_2O_2, 47 mL H_2O	Removes etchant stains for most alloys
2 mL HF, 98 mL H_2O	Reveals α case for most alloys
6 g NaOH, 60 mL H_2O, heat to 80°C (180°F), add 10 mL H_2O_2	Good α+β contrast, general microstructures for most alloys
10 mL KOH (40%), 5 mL H_2O_2, 20 mL H_2O	Stains α, transformed β
50 mL 10% oxalic acid, 50 mL 0.5% HF with H_2O	Etch 12-20 seconds. General-purpose etch for β alloys

5.2.2 Optical microscopy

A Nikon/Optiphot[5] was used for the examination of microstructural features of the welded samples and heat treated samples. Objective lenses from 5× up to 40× were employed.

5.2.3 Scanning electron microscopy (SEM)

In order to get good quality images for analysis of fracture surfaces, scanning electron microscopy (SEM) was used in the work. In the SEM, the sample surface is scanned with a high-energy electron beam; the electrons interact with the atoms in the sample, producing signals that include: secondary electrons (SE), back scattered electrons (BSE) and characteristic x-rays which can be used in energy dispersive x-ray analysis (EDX). The SE provide the information about the topography and surface structure; the BSE provide the information about the distribution of different elements via average atomic number; the EDX is used to identify and quantify the composition of the materials with a resolution of about 2 μm. Samples for analysis in the SEM were mounted in 'Conductive' Bakelite. The same polishing regime as used in optical microscopy was employed. For use in the SEM, conducting aluminium tape was used to eliminate any build up of charge on the samples. A Philips XL30 tungsten filament Scanning Electron Microscope[6] was used to image and characterize the samples. An Oxford Instruments 6650 energy dispersive X-ray analysis system[7] was used to determine the chemical composition of the parent materials and weld materials. All samples were examined using 20 kV voltage, with a working distance of 10 mm. The counting time for EDX analysis was 200 seconds. Image analysis software (Image J, National Institutes for Health, Maryland, USA) was used to measure the area of the molten zone from cross-sectional images of the weld, and β-phase area fraction of samples heat treated at 950 °C for 1 hour, 8 hours and 20 hours.

---

[5] Nippon Kogaku KK

[6] FEI, North America NanoPort 5350 NE Dawson Creek Drive Hillsboro, Oregon 97124 USA

[7] Oxford Instruments, X-ray Technology, Inc. 360 El Pueblo Road Scotts Valley, CA 95066

5.3 Mechanical property characterization

5.3.1 Hardness testing

Micro-hardness of the samples was measured using the Vickers Hardness testing with a Leco M-400 tester[8], using a 15 seconds indentation time. The hardness values were recorded by measuring the length of diagonals of the hardness indents and converting to Vickers Hardness reading. The conversion equation showed below:

$$H_V = \frac{2F\sin\frac{\theta}{2}}{d^2} \approx \frac{1.854F}{d^2}$$ **Equation 5.1**

Where F is the load in gf, $\theta = 136°$, d is arithmetic mean of the two diagonals of the hardness indents in mm. H_V is the Vickers hardness in gf/mm^2. The 200 gf load was used for all hardness measurements. Hardness traces (line of hardness indentations) were made across the welded samples; All hardness indents were placed along the centreline of the test pieces.

5.3.2 Tensile testing

The tensile test experiments were carried out on Instron 5569 Tensile and Compression Test Machine[9] at room temperature with a load cell of 50 kN and a cross head speed of 1 mm min^{-1}, with tests being carried out to tensile failure. Two strain gauges were used for measurement of strain;

- A strain gauge was attached to the gauge section of the sample and was used to measure tensile strains lower than 0.2%.
- At higher strains, the cross-head movement was used to calculate the strains in the gauge section of the sample.

---

[8] Leco® Corporation, 3000 Lakeview Ave. St. Joseph, MI 49085-2396, USA

[9] Instron, Coronation Road, High Wycombe, Bucks, HP12 3SY, UK

All the tensile test coupons (Figure 5.3) were machined using a vertical milling cutter from parent material and weld samples. The width and thickness of the tensile gauge section was checked with a micrometer before tensile testing.

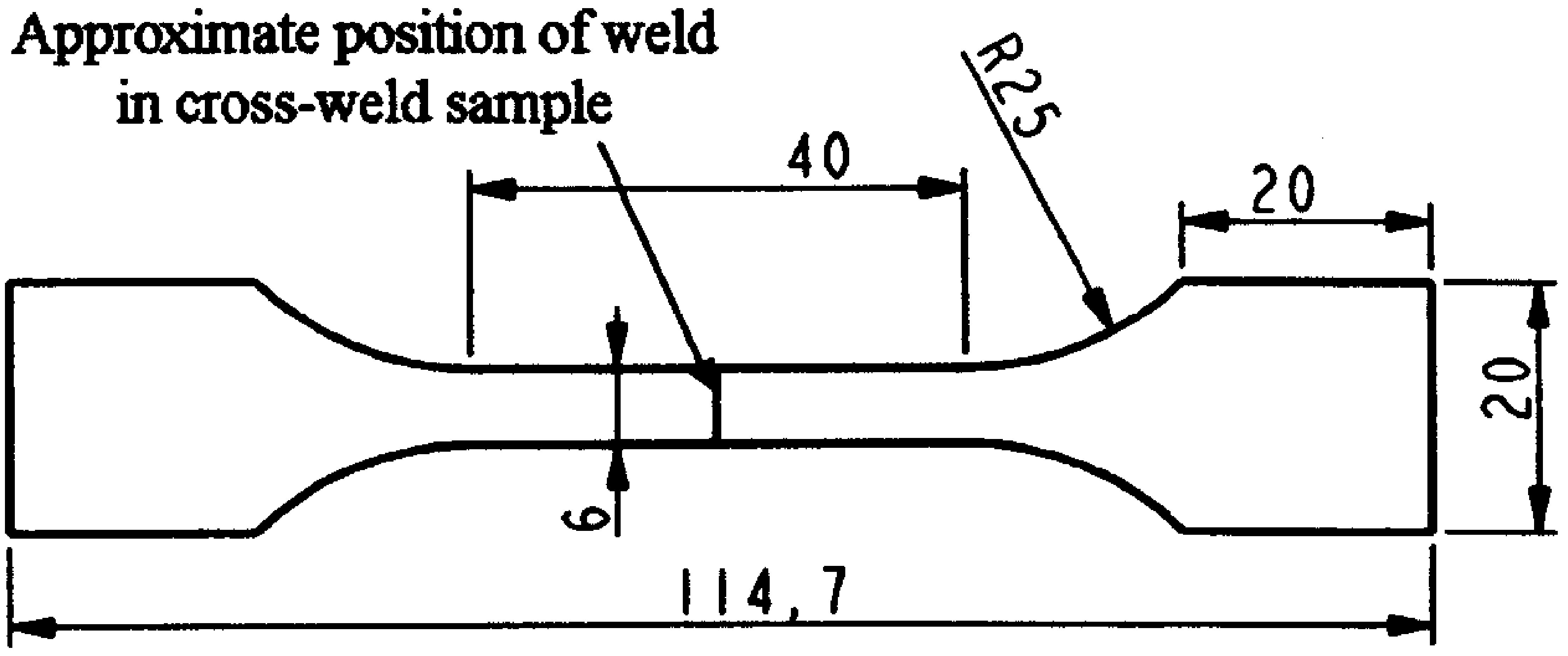

Figure 5.3 Geometry of tensile test sample

To provide data for the FEA modelling of the weld, both the Young's modulus and yield strength of all the material types in the weld were required (parent, HAZ and FZ). To simulate the FZ, samples were heated to 1050°C and water quenched. In order to eliminate any α-case formed in the heat treatment, 100 μm was ground from the top and bottom surface. The HAZ properties were assumed to be those of the parent. In order to measure the nominal stress-nominal strain behaviour of both parent materials and water quenched materials, the strain gauge method was used until just before tensile failure.

5.4 Heat treatment

Two types of furnaces were used for heat treatment respectively with water quenching and furnace cooling.

- A Rapid Heat Furnace[10] (RHF 16/3) from Carbolite was adopted for water quenching process. The samples were heat treated for 8 minutes when the Carbolite rapid heating furnace reached required temperature, then water quenched.
- A Lenton Argon Furnace[11] was used for annealing process. Argon was used as shielding gas along with a Cussons rare gas purifier-4[12]. The samples were kept in the furnace for 1 hour, 8 hours and 20 hours followed the requirement at certain temperatures, then furnace cooled to room temperature. As mentioned in chapter 3, cooling rate affects the microstructure significantly, hence the cooling speed of furnace was recorded manually during the furnace cooling process.

There is no surrounding gas protection in the Rapid Heat Furnace and an oxidation layer was generated during heat treatment. Although there is covering gas in Lenton Argon Furnace, there was very thin oxidation layer existed after heat treatment. Covering Ti6Al4V plates were used to protect the top and bottom surfaces.

---

[10] ELITE thermal systems, 6 Stuart Road, Market Harborough, LE16 9PQ, Leicestershire, UK

[11] Lenton Furnaces and ovens, P.O Box 2031, Hope, Hope Valley, Derbyshire, S33 6BW, UK

[12] Cussons Technology, 102 Great Clowes Street, Manchester M7 1RH, UK

5.5 Tensile fatigue test

Before tensile fatigue testing commenced, the prediction of life cycle was calculated using the 'stress-life approach developed by Basquin (1910) with the observation of a log-log relationship between the stress amplitude and life cycles' as shown in Equation 5.2 [2, 3]:

$$\frac{\Delta\sigma}{2} = \sigma_f^{'}(2N_f)^b \qquad \textbf{Equation 5.2}$$

Where $\Delta\sigma$ is the stress range, $\sigma_f^{'}$ is the fatigue strength coefficient, b is the fatigue strength exponent, N_f is the life cycle. In Ti6Al4V grade 5, $\sigma_f^{'}$ is equal to 2030, b is equal to -0.104 [2].

A Denison Mayes 250kN capacity servohydraulic machine[13] was used for tensile fatigue testing. Figure 5.4 is a schematic diagram of the tensile fatigue test setup:

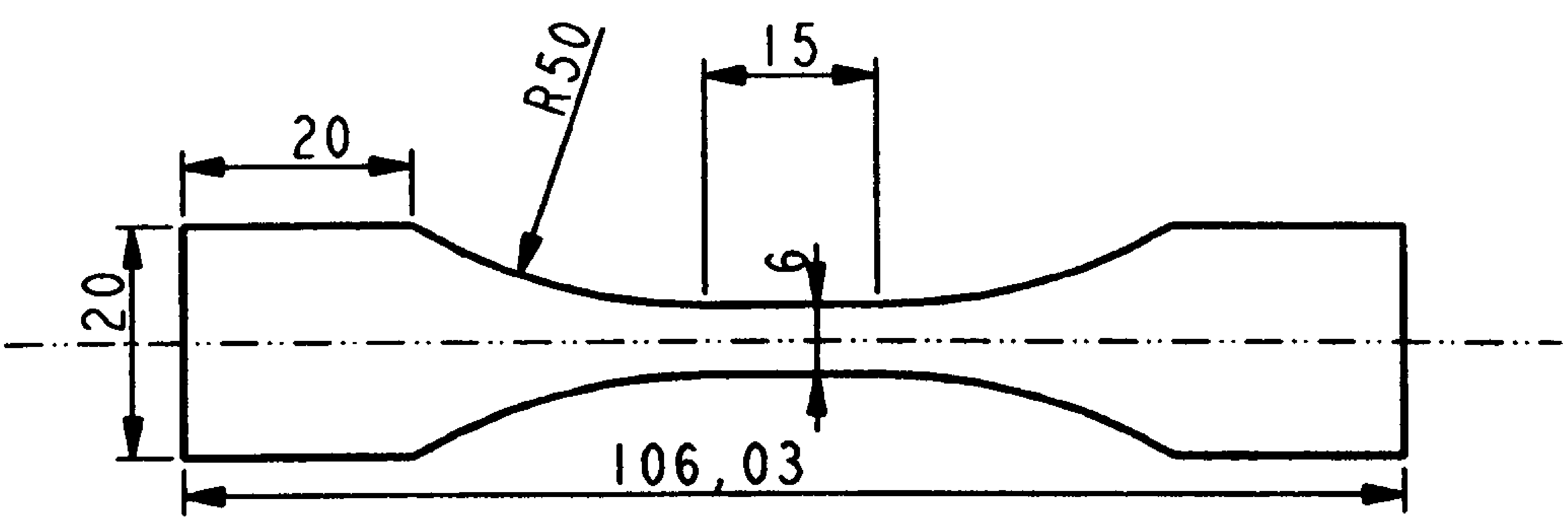

Figure 5.4 Schematic diagram of tensile fatigue test sample

The employed maximum stresses for parent materials were 600 MPa, 500 MPa, 450 MPa and 400 MPa. The employed maximum stresses for welded materials were 450 MPa, 350 MPa, 325 MPa and 300 MPa. The stress ratio used for all samples was 0.1 and the cycling frequency was 7 Hz.

---

[13] Denison Mayes Group, Moor Road, Leeds, West Yorkshire LS10 2DE, UK

5.6 Finite element analysis

Finite element analysis (FEA) is commonly employed in engineering applications which include structure analysis, electro-magnetics, geo-mechanics, biomechanics etc [4, 5]. An overview of the procedure of FEA implementation is shown in Figure 5.5. Generally, the main FEA procedural steps include: generation of an appropriate sub-geometry to represent the application, mesh generation (density, element type, size and number), applying boundary conditions, applying displacement conditions, applying displacement steps (displacement sequence), computer calculation and post-processing (extracting results and preparing graphics).

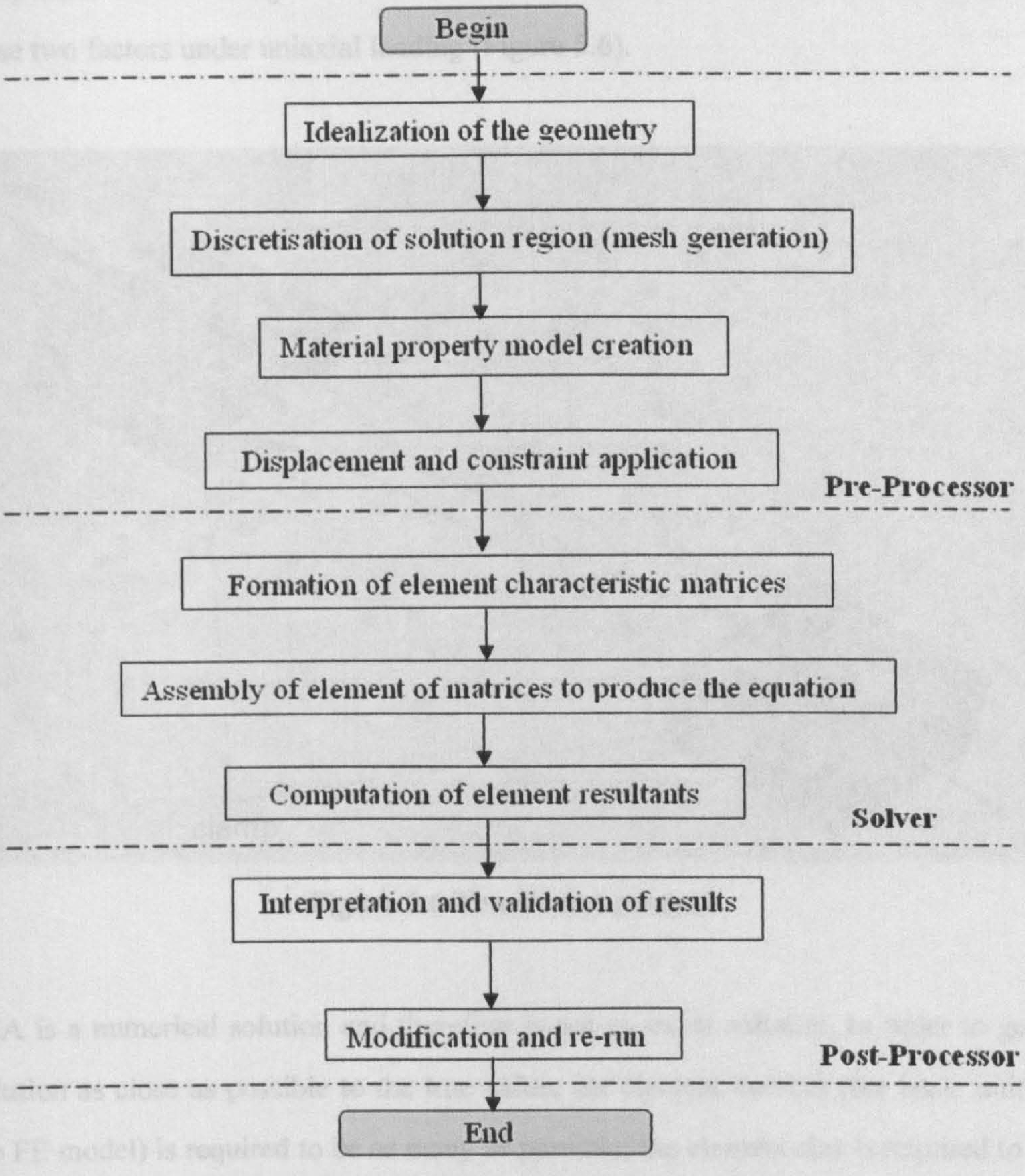

Figure 5.5 Procedure of FEA implementation [6]

There are a very large number of comprehensive commercially available FEA packages which are suitable to be run on PCs and workstations. Abaqus6.7 was employed here for simulated structural analysis of the laser welded Ti6Al4V samples.

5.6.1 Simplification of distortion phenomenon

As mentioned in chapter 4, distortion was one kind of defect in laser beam welding. At the same time, different types of lasers produced welds with different cross-sectional geometries. Both of these features can affect the stress distributions in a component under loading. FEA was used to understand and evaluate the influences of these two factors under uniaxial loading (Figure 5.6).

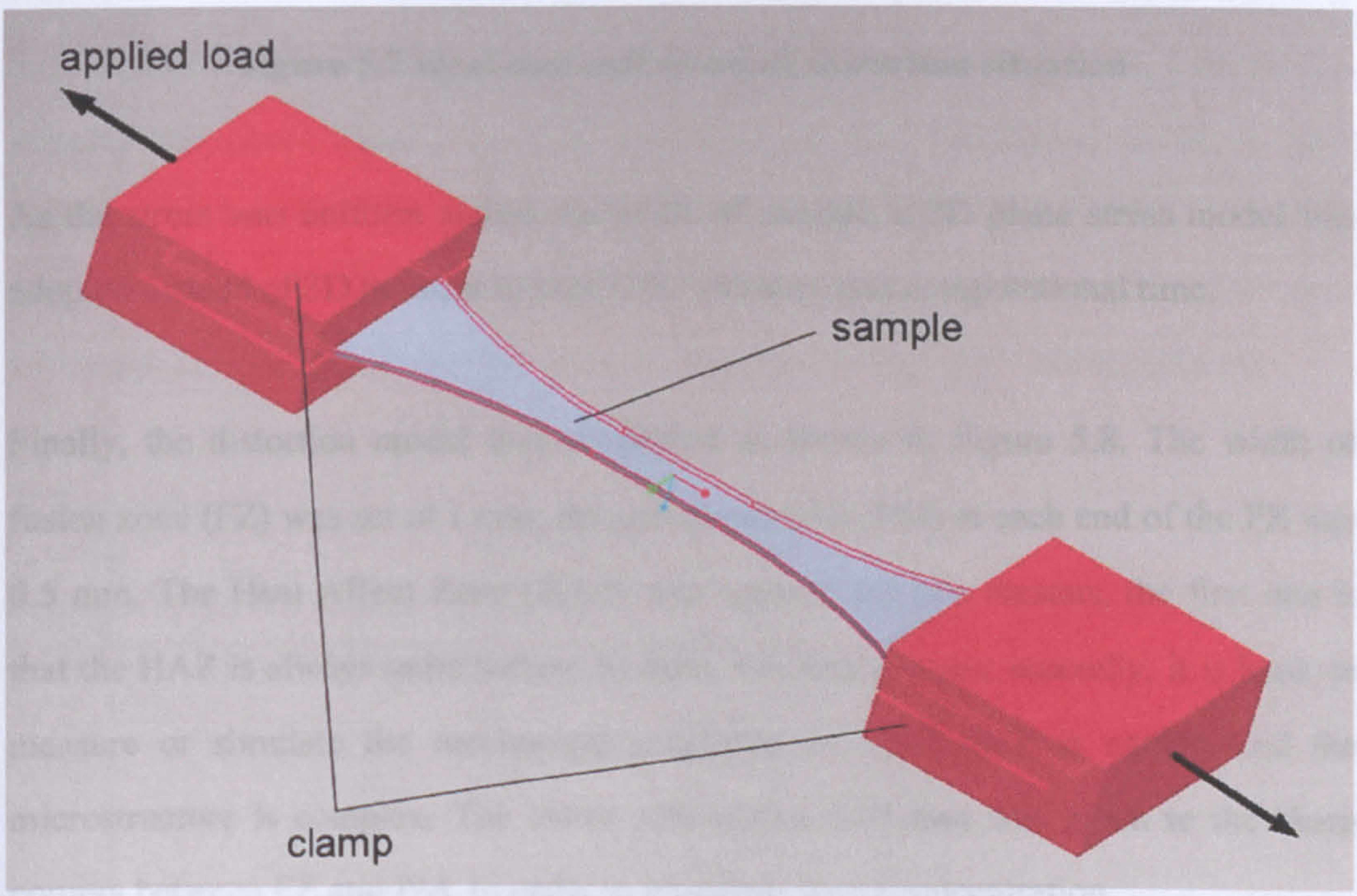

Figure 5.6 Tensile test process

FEA is a numerical solution and therefore is not an exact solution. In order to get a solution as close as possible to the true value, the element number (the basic unit of the FE model) is required to be as many as possible; the element size is required to be as fine as possible. However, an increase in element number and refinement in element size will significantly increase the computation time. Sometimes, it will exceed the working capability of the CPU and memory of the PC.

Figure 5.6 illustrates the tensile fatigue test sample. As the test sample is a long thin component, it is impossible to simulate the whole structure with very fine elements. It may be initially assumed that the distortion results in a misalignment as shown in a 2D cross-sectional view in Figure 5.7:

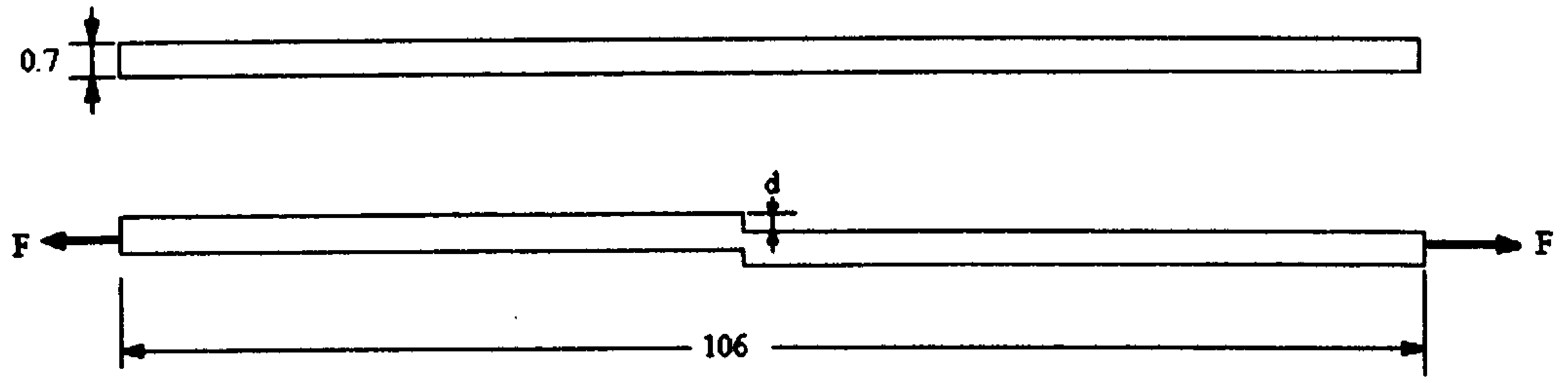

Figure 5.7 ideal case and assumed distortion situation

As the stress was uniform across the width of sample, a 2D plane stress model was adopted instead of 3D in order to save CPU memory and computational time.

Finally, the distortion model was simplified as shown in Figure 5.8. The width of fusion zone (FZ) was set at 1 mm; the parent material (PM) at each end of the FZ was 0.5 mm. The Heat Affect Zone (HAZ) was ignored for two reasons, the first one is that the HAZ is always quite narrow by laser welding process; secondly, it is hard to measure or simulate the mechanical properties of HAZ as it is narrow and the microstructure is complex. The curve with radius 0.05 mm was given to the sharp corners between FZ and PM, in order to eliminate stress concentration.

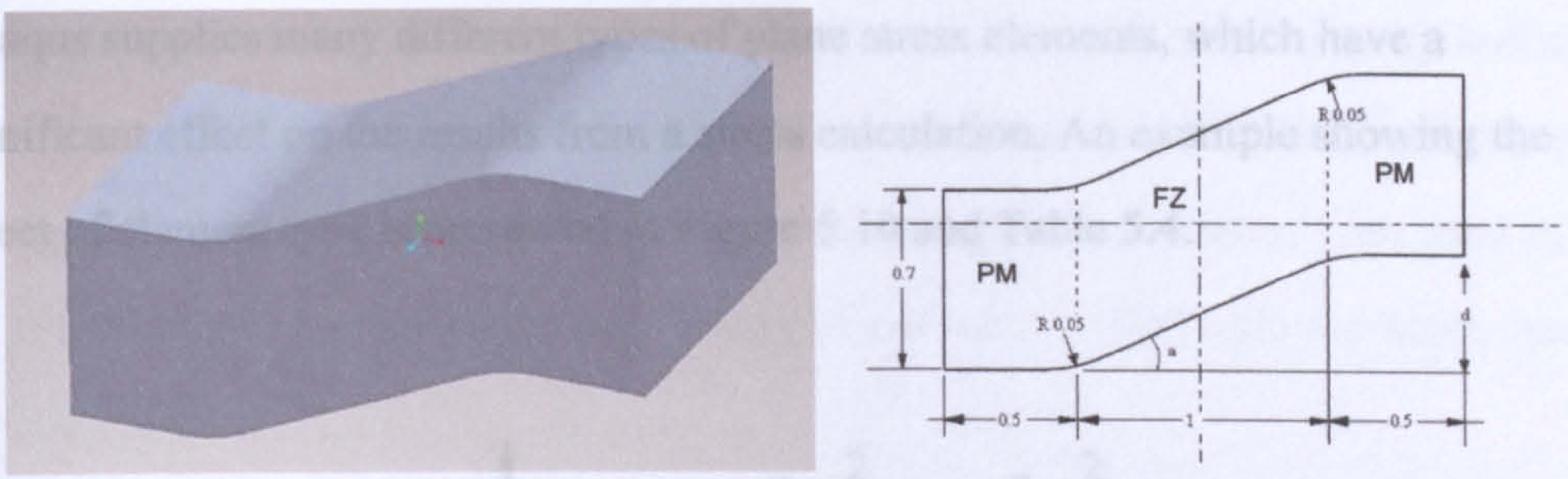

Figure 5.8 Geometry of distortion FE model

5.6.2 Mesh generation of model

Meshing means the selection of right type and size of elements. The common way to verify that the element size is suitable in a given model is to run the same analysis with smaller size of finite elements and to look at the variation in the model output as the element size is reduced. As the element size is reduced, the FE results tend towards the exact results. In Figure 5.9, f(n1) was considered to be a good approximation to the exact result, and f(n2) was 90-95% of f(n1). In this case, f(n2) was seen to be a reasonable approximate to the exact result, whilst achieving the need for computational efficiency. The element size corresponding to n2 was selected.

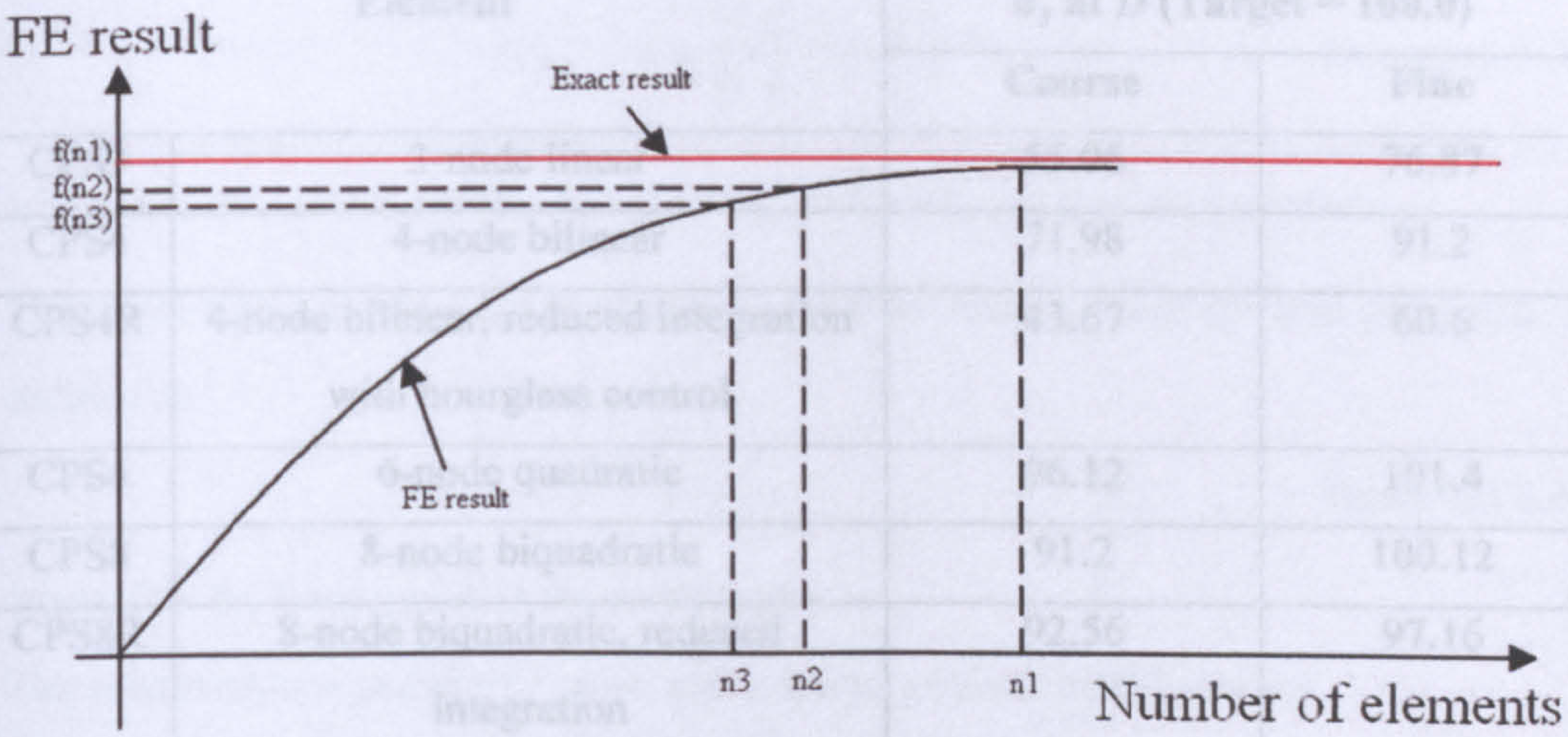

Figure 5.9 FE result compared with exact result [6]

Abaqus supplies many different types of plane stress elements, which have a significant effect on the results from a stress calculation. An example showing the effect of element type is presented in Figure 5.10 and Table 5.4.

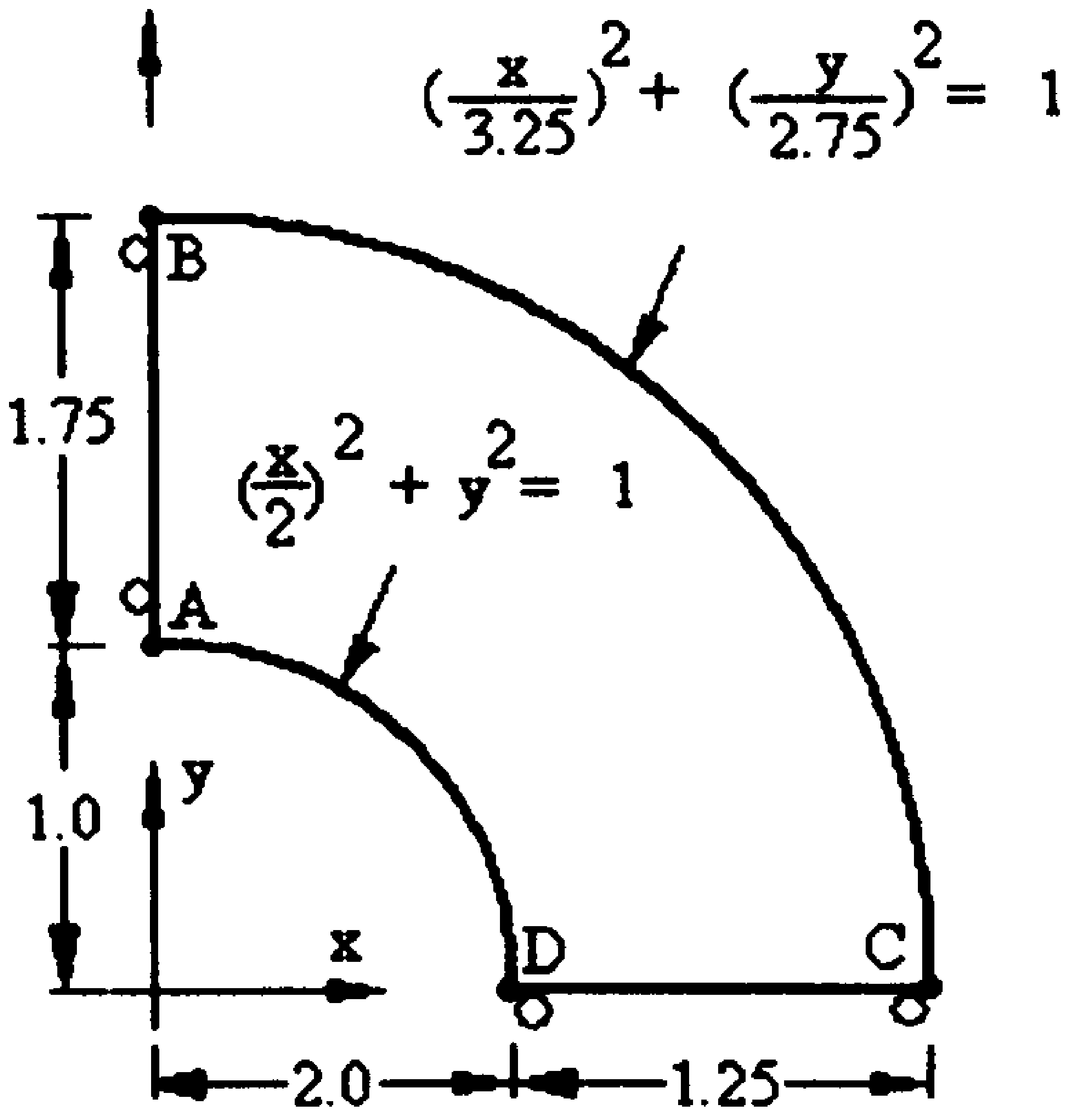

Figure 5.10 example model used to show the effect of different mesh element and density on the results of an FE model [7]

Table 5.4 showed the FE results with different plane stress elements [7]

Element		**σ_y at D (Target = 100.0)**	
		Coarse	**Fine**
CPS3	3-node linear	55.06	76.87
CPS4	4-node bilinear	71.98	91.2
CPS4R	4-node bilinear, reduced integration with hourglass control	43.67	60.6
CPS6	6-node quadratic	96.12	101.4
CPS8	8-node biquadratic	91.2	100.12
CPS8R	8-node biquadratic, reduced integration	92.56	97.16

The results are shown in Table 5.4, showing the effect of both mesh density and mesh type. The maximum error would be 56.33% using course size CPS4R. The best result was gained from fine size CPS8 element. Accordingly, the element type used in the FE model of this current study was 8-node biquadratic (CPS8) with the mesh density of 0.003 mm.

5.6.3 Materials properties for the FEA

For modelling, the material properties including FZ properties, HAZ properties and PM properties are required. The properties required include Young's modules, tensile yield stress, and Poisson ratio. Beside these, characteristics of plasticity in FZ and PM were needed, because the stress level may exceed the linear elastic behaviour of the materials.

When defining plasticity data in Abaqus, true stress and true strain were required. The data from tensile yield tests are values of nominal stress and strain. And as such, the nominal stress/strain values needed to be converted to true stress/stain values. True strains in compression and tension are the same only if considered in the limit as $\Delta l \to dl \to 0$

$$\varepsilon = \int_{l_o}^{l} \frac{dl}{l} = \ln(\frac{l}{l_o}) \qquad \textbf{Equation 5.3}$$

where l is the current length, l_o is the original length, and ε is the true strain.

The stress measure that is the conjugate to the true strain is called the true stress and is defined as

$$\sigma = \frac{F}{A} \qquad \textbf{Equation 5.4}$$

where F is the force and A is the current area.

The relationship between true strain and nominal strain is established by

$$\varepsilon_{nom} = \frac{l - l_o}{l_o} = \frac{l}{l_o} - 1 \qquad \textbf{Equation 5.5}$$

Adding unity to both side of this equation and taking the natural log of both sides provides the relationship between the true strain and the nominal strain

$$\varepsilon = \ln(1+\varepsilon_{nom}) \qquad \textbf{Equation 5.6}$$

The relationship between true stress and nominal stress is gained by considering the incompressible nature of the plastic deformation and assuming the elasticity is also incompressible

$$l_o A_o = lA \qquad \textbf{Equation 5.7}$$

The current area is related to the original area by

$$A = A_o \frac{l_o}{l} \qquad \textbf{Equation 5.8}$$

Substituting this definition of A into the definition of true stress gives

$$\sigma = \frac{F}{A} = \frac{F}{A_o}\frac{l}{l_o} = \sigma_{nom}(\frac{l}{l_o}) \qquad \textbf{Equation 5.9}$$

where $\frac{l}{l_o}$ can be written as $1+\varepsilon_{nom}$

Hence, the relationship between true stress and nominal stress and strain is

$$\sigma = \sigma_{nom}(1+\varepsilon_{nom}) \qquad \textbf{Equation 5.10}$$

Definition of plasticity strain in Abaqus will be the total strains in the material. The total strain values were decomposed into the elastic and plastic strain components. The plastic strain is obtained by subtracting the elastic strain, defined as the value of true stress divided by the Young's modulus, from the value of the total strain (see Figure 5.11).

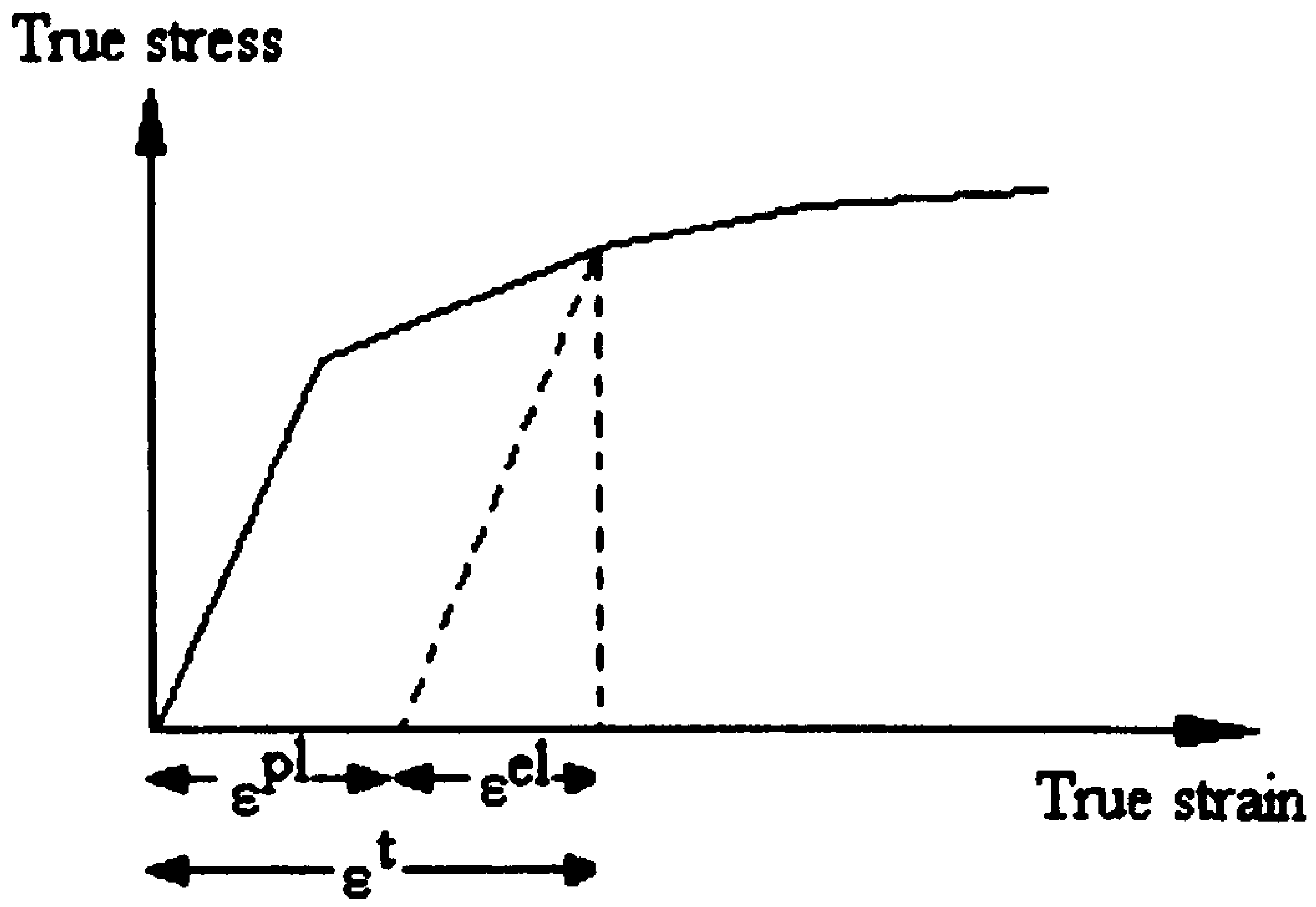

Figure 5.11 decomposition of the total strain into elastic and plastic components

$$\varepsilon^{pl} = \varepsilon^{t} - \varepsilon^{el} = \varepsilon^{t} - \frac{\sigma}{E}$$ **Equation 5.11**

where ε^{pl} is true plastic strain, ε^{t} is true total strain, ε^{el} is true elastic strain, σ is true stress and E is Young's modulus.

The definition of a plasticity model in Abaqus is by use of a series of straight lines joining the given data points instead of a smooth stress-strain curve.

The nominal stress - nominal strain behaviour of the PM were gained from uniaxial tensile testing. As mentioned before, in order to measure the real nominal stress and nominal strain of the PM, the attached strain gauge was used until just before tensile failure. It is difficult to test the properties of the FZ for such a thin and small weld zone. As shown in chapter 4, the microstructure of the FZ is quite similar to that of materials water quenched from 1050°C. Hence, the nominal stress - nominal strain behaviour of the FZ were simulated by water quenching PM from 1050°C. Before testing, all the heat treated samples had the thick oxidation layer removed by milling; a removal depth of 100 μm was measured from each side to ensure that only water quenched material was tested in the tensile test.

5.6.4 Boundary condition of FEA

During the tensile test as shown in the FE model (Figure 5.6), samples extend following application of a uniaxial load. The boundary conditions can be load or deformation (displacement). Displacement was selected as boundary condition of the model (Figure 5.12). The reason is that the quantity of nodes at the side of the FE model (where the boundary condition is employed) is variable due to the FE model and mesh densities. The displacement can be distributed uniformly at any set of nodes. If the force is used as the boundary condition, there is a need to calculate the average force for each node (total force divided by the number of nodes).

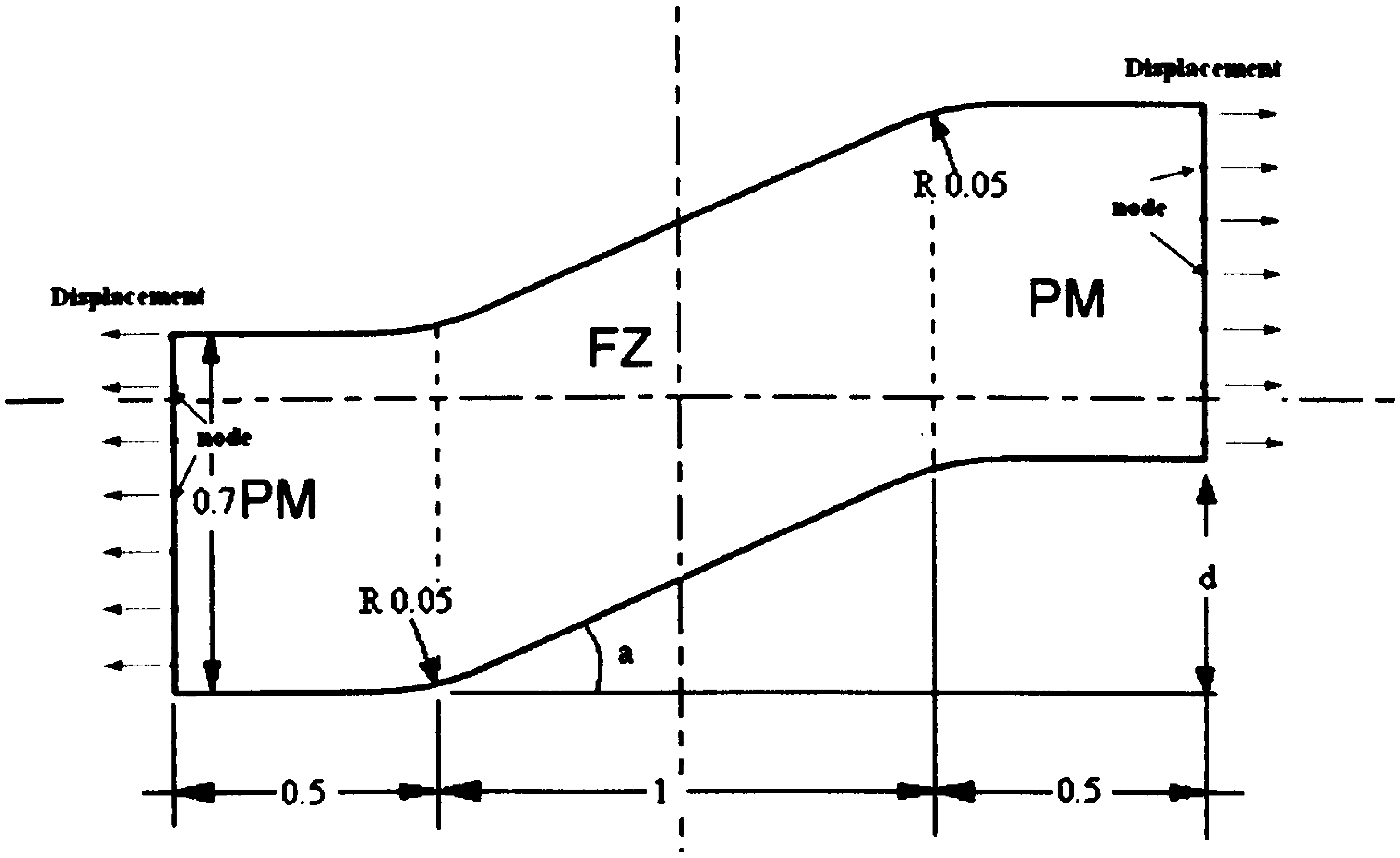

Figure 5.12 Boundary condition of the model

By changing misalignment distance d from 0 μm to 100 μm, with 10 μm as the step, the maximum stress in the samples as a function of distortion could be found. In all cases, the Von Mises equivalent stress was used Equation 5.12

$$\sigma_v = \sqrt{\frac{(\sigma_1-\sigma_2)^2+(\sigma_2-\sigma_3)^2+(\sigma_3-\sigma_1)^2}{2}}$$ **Equation 5.12**

This stress could then be directly compared with the tensile yield stress.

5.6.5 FEA of real cross-sectional shape of weld

Real cross-sectional shapes of welds were recorded from light microscope cross-sectional images. A series of image analysis software packages (Paint.Net, IMG2CAD and Mastercam Mill v9.0) were used to convert the image into readable IGS files by Abaqus. As before, the element type used here was 8-node biquadratic (CPS8) with a mesh density of 0.003 mm. The boundary conditions (displacements) were increased from 0 mm to 0.018 mm, with 0.002 mm as the step.

References:

[1] ASM Handbook. Properties and Selection:Nonferrous alloy and special-purpose materials. 1996;2.

[2] S.Suresh. Fatigue of materials. 2nd ed: Cambridge university press 1998.

[3] British Standard. 3518-1:Methods of fatigue testing. 1993.

[4] Abaqus/standard User's Manual. Ver.6.2 ed. Pawtucket: Hibbit, Karlsson&Sorensen, Inc. 2001.

[5] R.D.Cook, D.S.Malkus, M.E.Plesha, R.J.Witt. Concepts and applications of Finite Element Analysis. 4th ed: Xi'an jiaotong university press 2007.

[6] Y.Wang. A methodology of Fixture Evaluation Analysis and Optimisation. PhD thesis, Nottingham: Nottingham University; 2004.

[7] L.Zhao. The application of Abaqus 6.6 in mechanism engneering; 2007.

[8] Y. Zhang. Changes in Microstructure and Mechanical Properties of P91 Weld Metal during Creep. PhD thesis, Nottingham: Nottingham University; 2009.

CHAPTER 6

Chapter 6 Results

6.1 Characterisation of parent material

6.1.1 Microstructure of parent materials

Figure 6.1 shows an SEM image of a polished cross-section of as-received 0.7mm Ti6Al4V parent material sheet (PM). The EDX analysis of the general area indicates that there are only three types of elements in the material which are 5.57 wt% Al, 3.38 wt% V and 91.05 w% Ti. In the light area of the microstructure, the vanadium content rises up sharply to 12.0 wt%. At the same time, the aluminium content drops off to 3.3 wt%. In contrast, in the dark area, the vanadium content decreases to 2.8 wt% and the aluminium content slightly increases to 6.1 wt%. (Table 6.1)

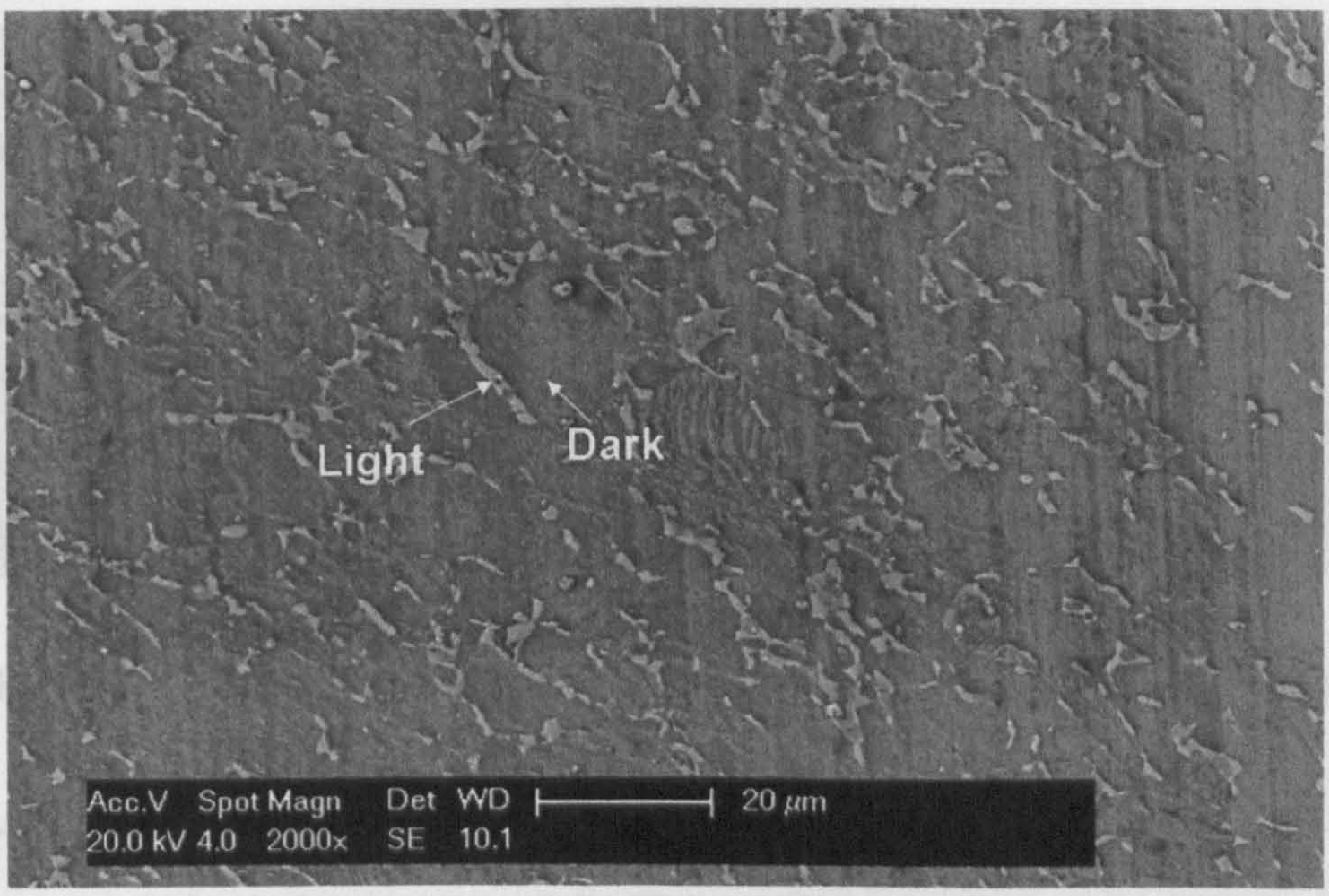

Figure 6.1 SEM image of parent material as-received Ti6Al4V

Table 6.1 Element distribution in parent material as-received Ti6Al4V

Position	Element	Element w%
Overall view	Al	5.57
	Ti	91.05
	V	3.38
Dark area	Al	6.09
	Ti	91.14
	V	2.77
Light area	Al	3.34
	Ti	84.62
	V	12.04

Figure 6.2 shows optical microscope images of PM from both cross-section and top surface view. There is no significant difference between cross-section view and top surface view. The images also indicate that an equiaxed fine grain structure (around 20 μm) exists in PM, which was formed by the recrystallisation and globularization process.

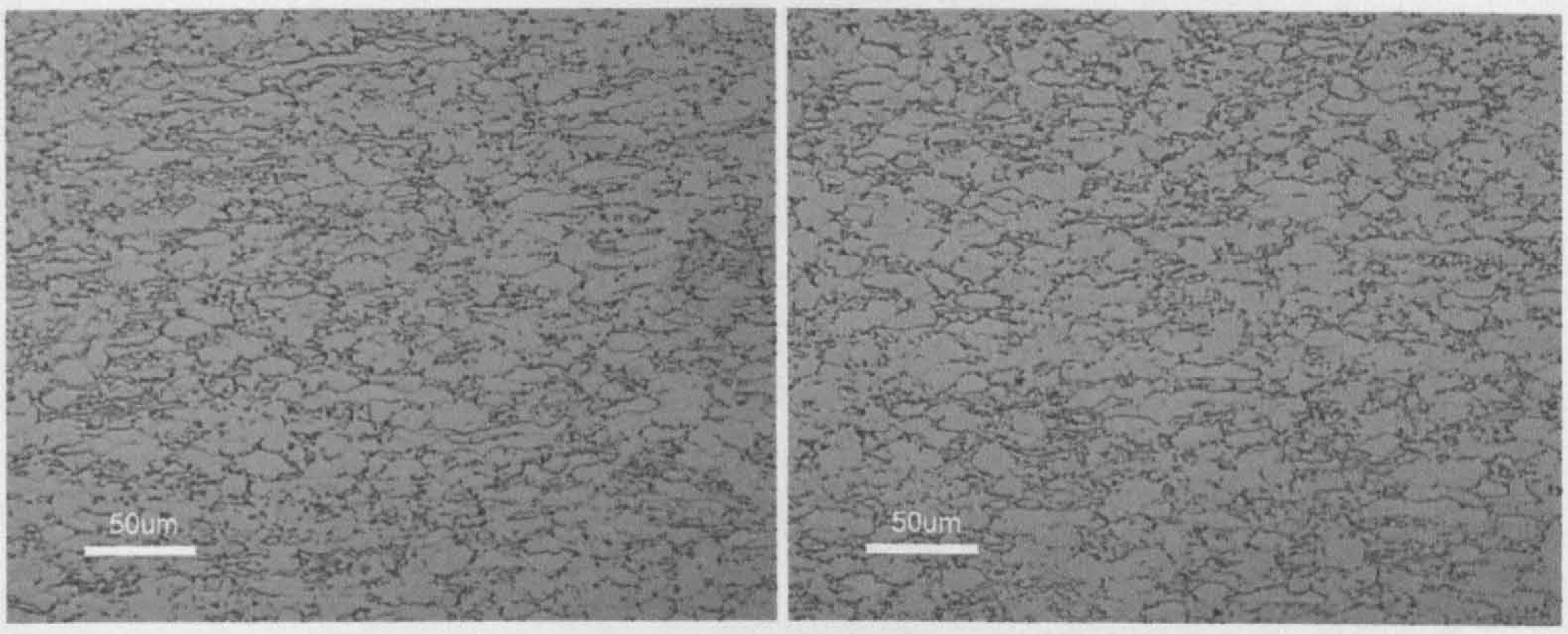

(a) Cross section (b) Top surface

Figure 6.2 Optical microscope images of parent material as-received Ti6Al4V

6.1.2 Mechanical properties of parent materials

The main mechanical properties of the PM are shown in Table 6.2 which includes microhardness (for both cross section and top surface), Young's modulus, 0.2% tensile stress and elongation to fatigue. There is no significant difference between the hardness value for both cross section and top surface.

Table 6.2 Mechanical properties of parent material as-received Ti6Al4V

Hardness (Cross section) / kgmm^{-2}	**Hardness (Top surface) / kgmm^{-2}**	**Young's Modulus / GPa**	**0.2% Tensile stress / MPa**	**Maximum stress / MPa**	**Elongation / %**
362.5 ± 5.3	367.4 ± 6.9	111.0 ± 3.1	978.2 ± 15.3	1054 ± 4.3	13.6 ± 1.7

*the error bar (±) is standard deviation

6.2 Heat treatment of parent material

6.2.1 Microstructure of heat treated Ti6Al4V

Figure 6.3 shows the cooling rate of the Lenton Argon furnace. The trend of the curve can be divided into three stages: the average cooling rate (0.476°Cs^{-1}) is high at temperatures above 650°C; from 650°C to 350°C, the average cooling rate (0.083°Cs^{-1}) tends to be slower; below 350°C, the cooling rate (0.029°Cs^{-1}) is nearly stable.

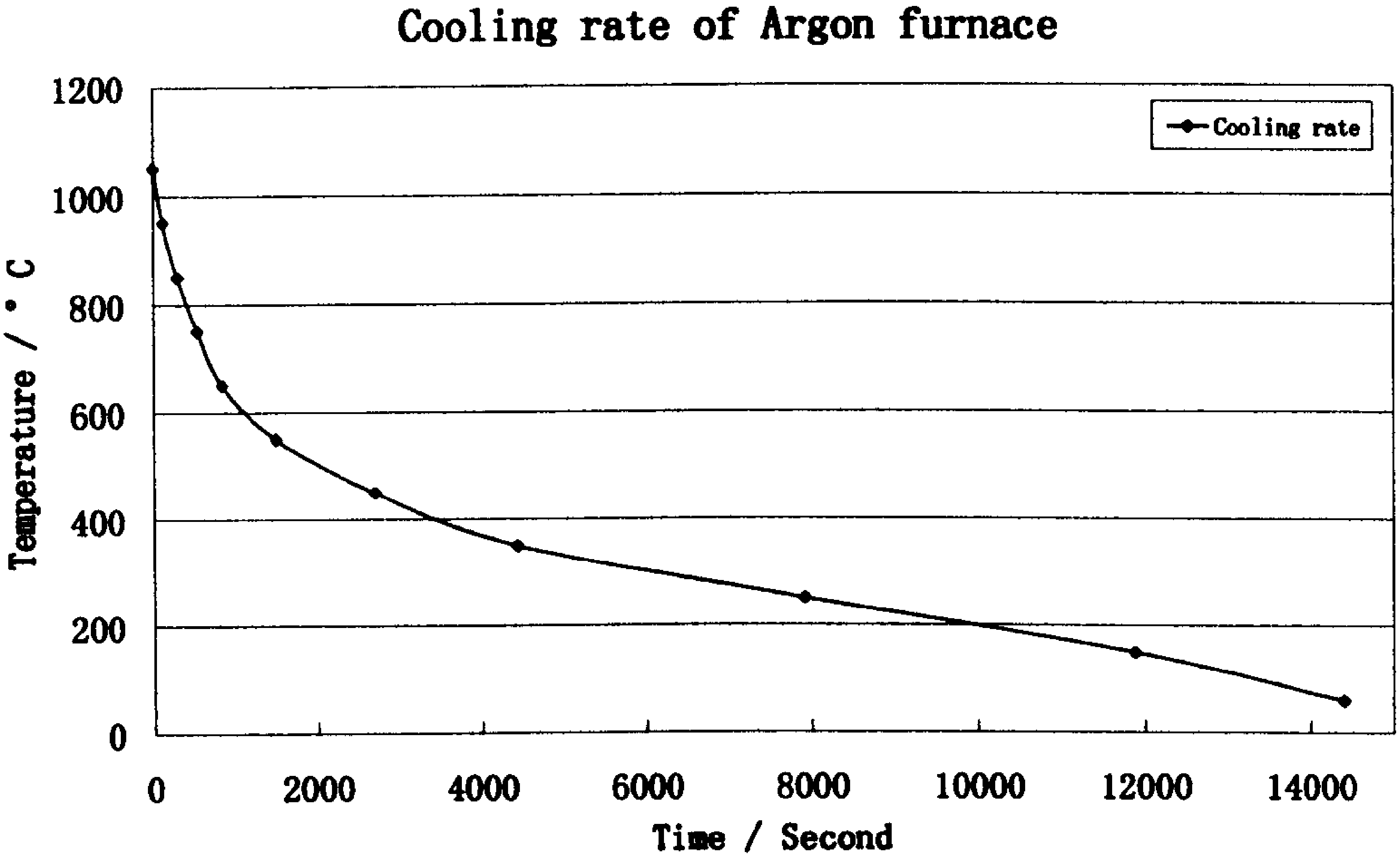

Figure 6.3 Cooling rate of Lenton Argon Furnace

The Ti6Al4V parent material was heat treated at 650°C, 750°C, 850°C, 950°C and 1050°C for 1 hours followed by furnace-cooling (A) or water-quenching (Q) to investigate the microstructural development. The optical images of PM with different heat treatment temperatures and cooling rates are shown in Figure 6.4. There is no significant difference from PM to 650A (Figure 6.4b), 750A (Figure 6.4d), 850A (Figure 6.4f), 650Q (Figure 6.4c), 750Q (Figure 6.4e). All of these images exhibit equiaxed α phase surrounded by β phase boundary. There is a slight difference between 850Q (Figure 6.4g) and others, where the β phase boundary seems to be thicker.

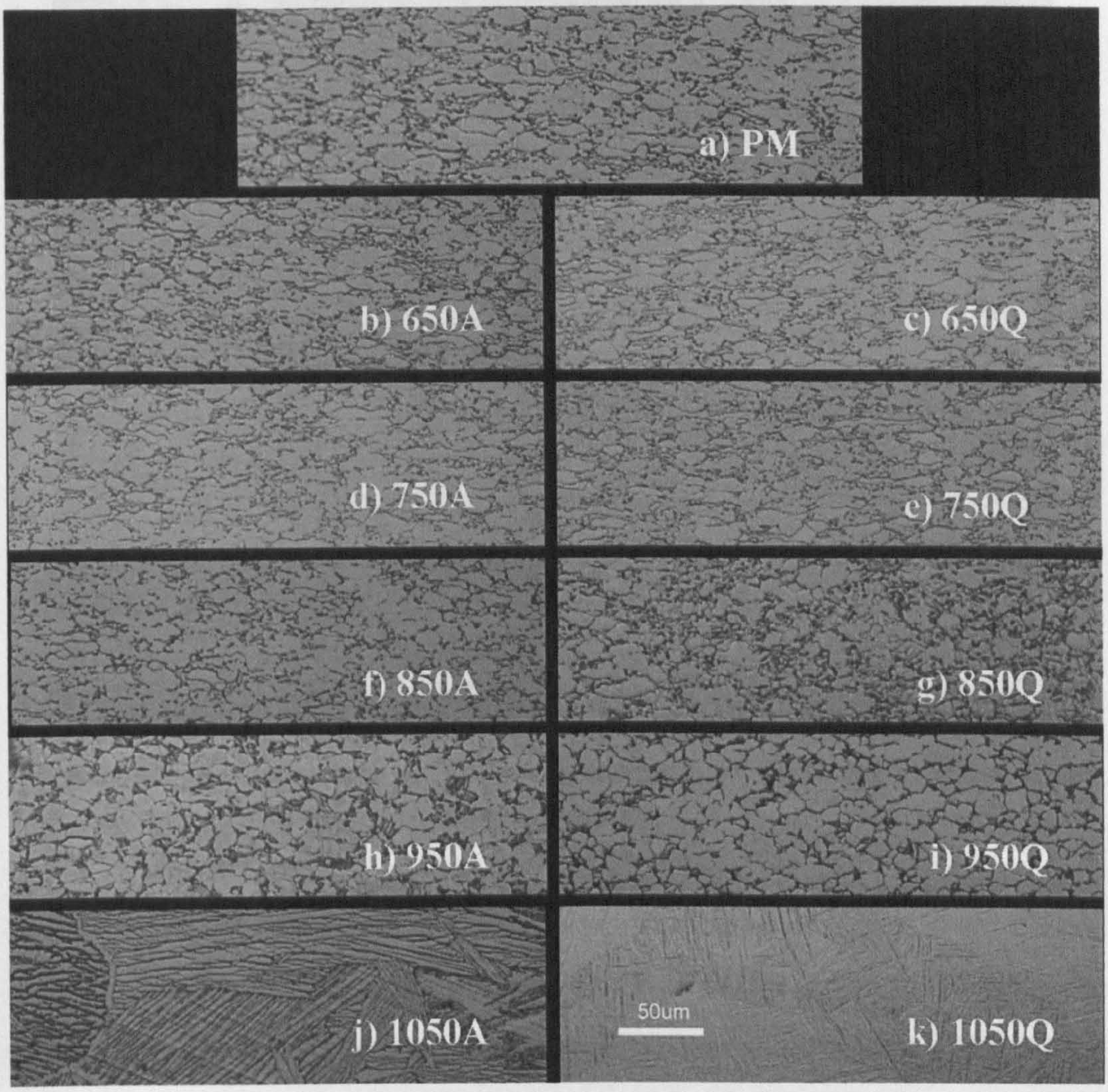

Figure 6.4 Optical microstructure of as-received and heat-treatment Ti6Al4V. The number indicates the heat treatment temperature. A indicates furnace cool and Q indicates a quench.

In Figure 6.5 (PM heat treated at 950A), an equiaxed structure with primary α phase and part of β phase boundary still exists, but some transformation from prior β phase boundary to lamellar α+β phase has occurred.

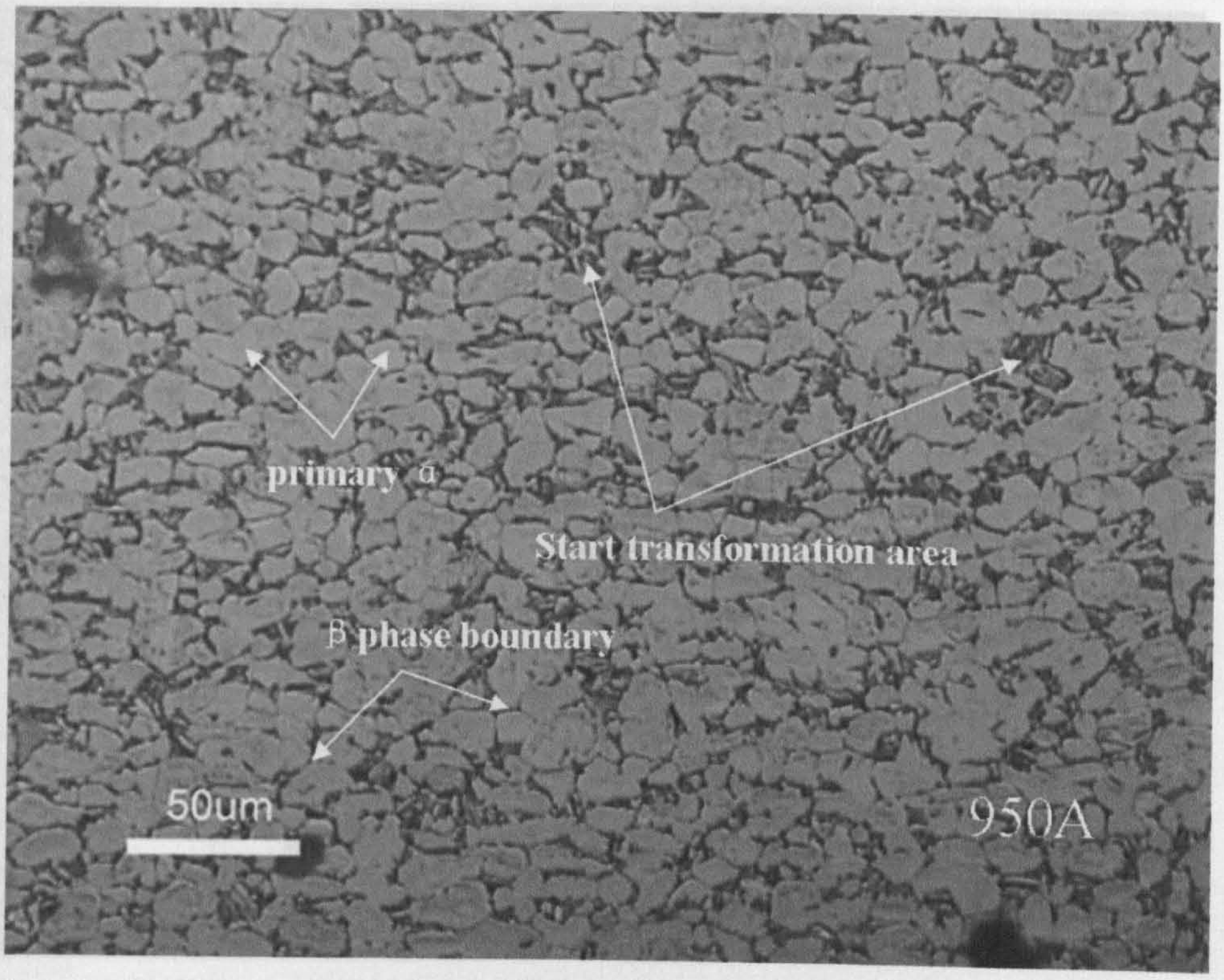

Figure 6.5 Microstructure of Ti6Al4V following heat treatment at 950°C with furnace cooling

In Figure 6.6 (PM heat treated at 950Q), an equiaxed structure with primary α phase and part of β phase boundary is observed which is as similar as 950A. The difference is that there is no lamellar α+β phase but instead a region of metastable β (dark region) which has been transformed from the β phase boundary regions is observed.

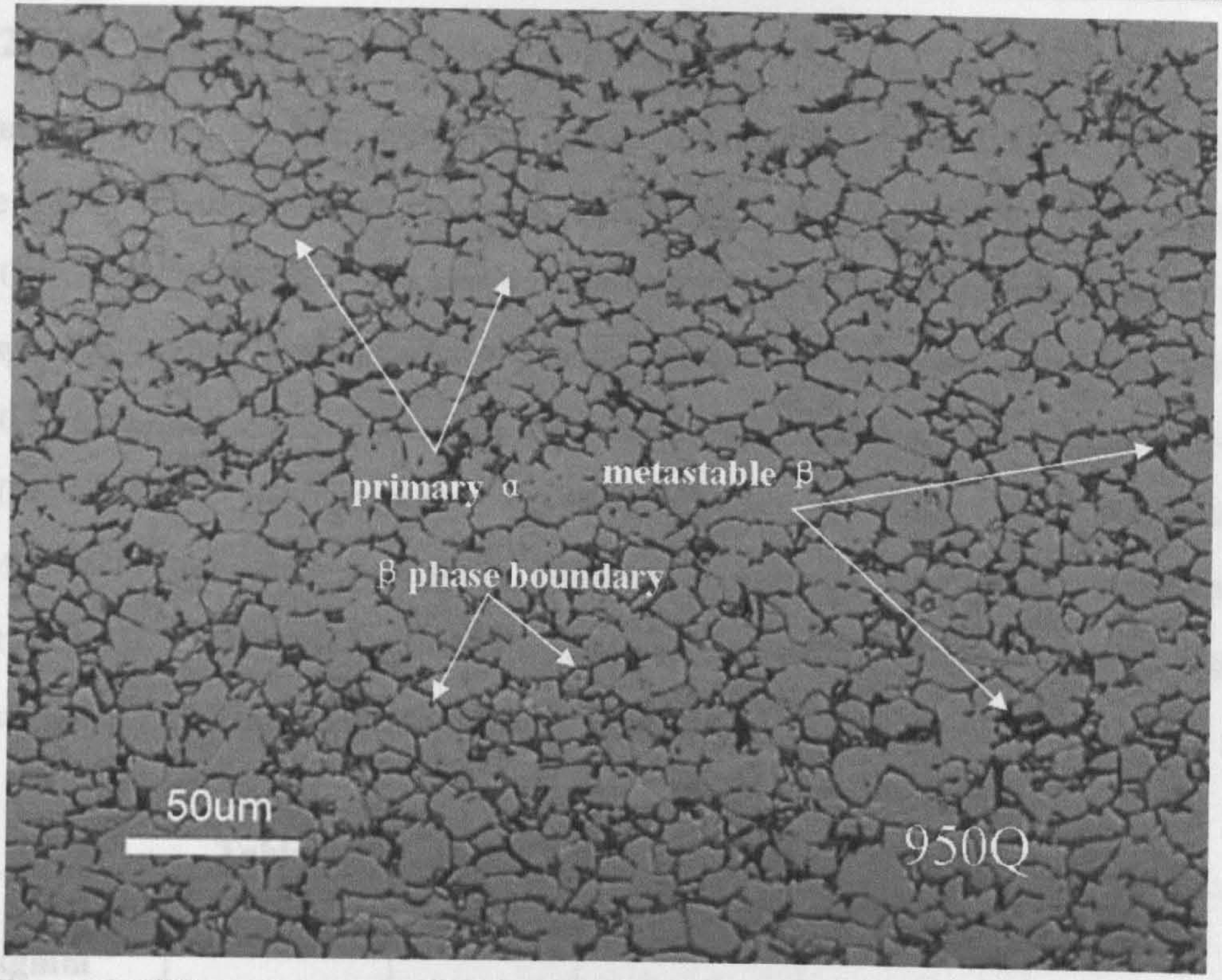

Figure 6.6 Microstructure of Ti6Al4V following heat treatment at 950°C with water quenching

Figure 6.7(a) shows a typical lamellar structure with α grain boundary in the prior β grains from 1050°C furnace cooling. Figure 6.7(b) shows acicular α′ martensite structure with β phase between martensitic laths. The grain size tends to be coarse.

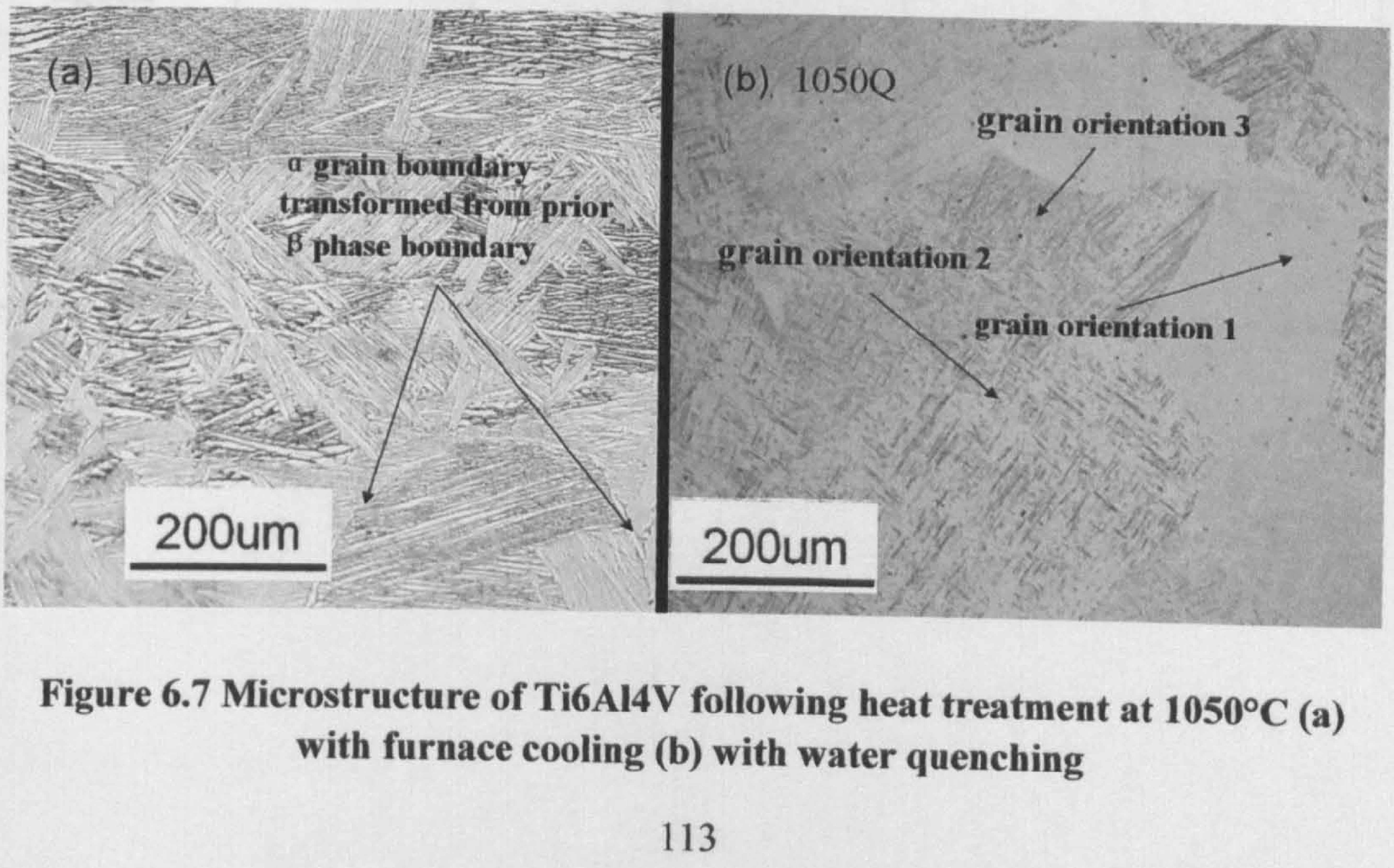

Figure 6.7 Microstructure of Ti6Al4V following heat treatment at 1050°C (a) with furnace cooling (b) with water quenching

6.2.2 Hardness of heat treated Ti6Al4V

Hardness testing has been conducted on heat treated Ti6Al4V PM. Figure 6.8 shows the results of hardness examination of Ti6Al4V heat treated at 650°C, 750°C, 850°C, 950°C and 1050°C for 1 hour with furnace-cooling (A) and water-quenching (Q) respectively. There is no significant change of hardness values between 650A, 750A, 850A, 650Q and 750Q. Following furnace-cooling, hardness values increase from 850°C to 1050°C; the highest hardness value appeared at 1050°C (7.41% bigger than PM). Following water-quenching, hardness values increased from somewhere between 750°C and 850°C to 1050°C; the highest hardness value is 15.58% bigger than that of PM. The results are shown graphically in Figure 6.8.

Table 6.3 Hardness data of heat treated Ti6Al4V

Unit: kgmm^{-2}	**650A**	**750A**	**850A**	**950A**	**1050A**
Furnace cool	361.0±3.4	360.0±2.0	365.2±2.3	378.2±4.1	389.4±5.9
PM (362.53 ± 5.32)	-0.42%	-0.70%	0.07%	4.32%	7.41%
Unit: kgmm^{-2}	**650Q**	**750Q**	**850Q**	**950Q**	**1050Q**
Water quench	361.6±3.3	362.0±2.0	370.8±3.4	394.6±4.8	419.0±9.1
PM (362.53 ± 5.32)	-0.26%	-0.15%	2.28%	8.85%	15.58%

*the error bar (±) is standard deviation

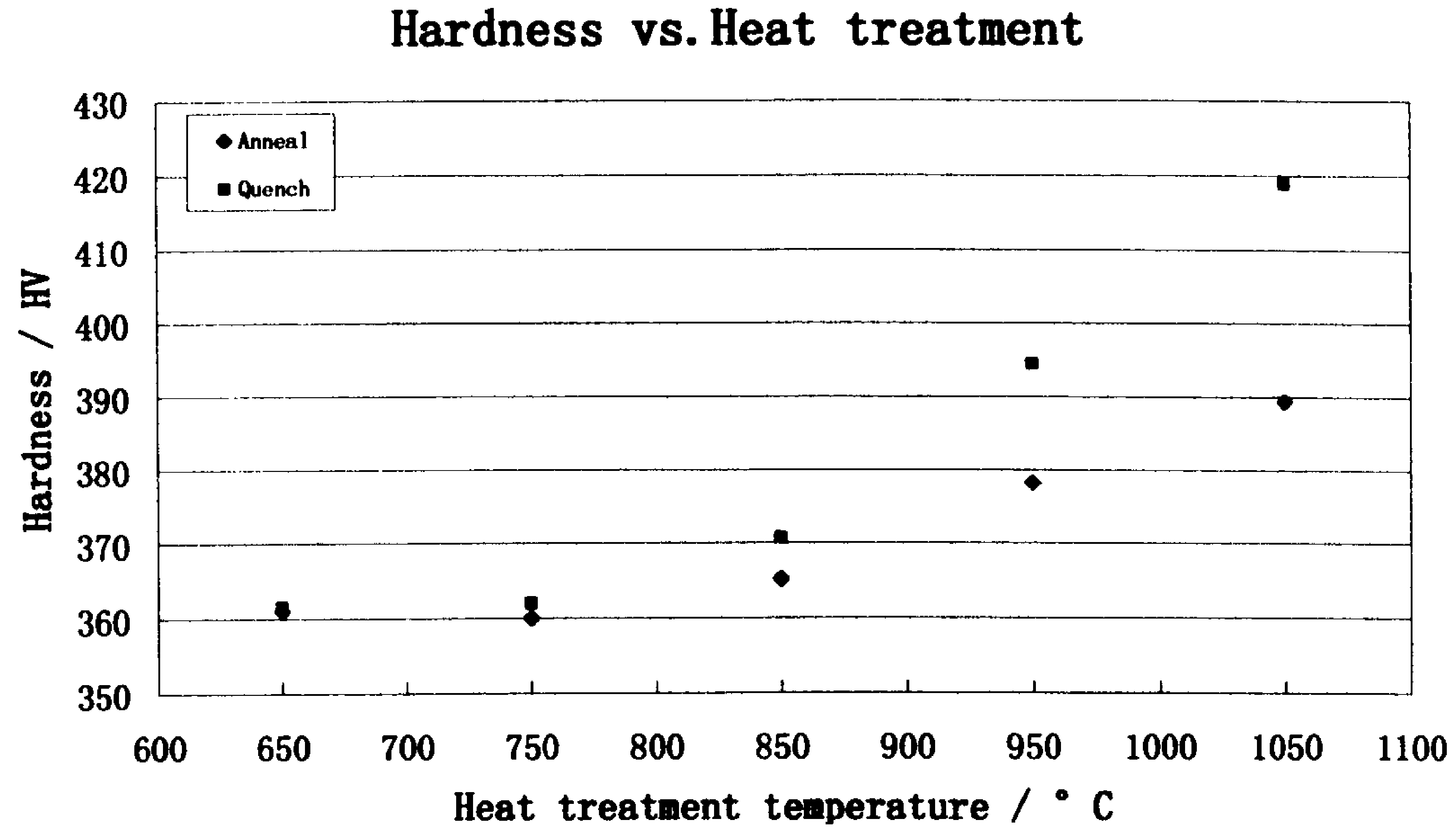

Figure 6.8 The effect of annealing temperatures and cooling schedules on hardness of Ti6Al4V

6.2.3 Tensile properties of heat treatment Ti6Al4V

The trend (Figure 6.9) of 0.2% proof stress values of heat treated Ti6Al4V following both furnace-cooling and water-quenching is very similar to that of the hardness values. The highest proof stress values appeared at 1050°C water-quenching condition, which is 13.78% higher than that of the PM. The data are shown in Table 6.4.

Table 6.4 0.2% proof tensile stress of heat treatment on Ti6Al4V

Unit: MPa	**650A**	**750A**	**850A**	**950A**	**1050A**
Furnace cool	980.7±22.1	979.7±11.5	987.0±15.5	1017.3±22.1	1041.0±32.0
PM (978.20)	0.25%	0.15%	0.90%	4.00%	6.42%
Unit: MPa	**650Q**	**750Q**	**850Q**	**950Q**	**1050Q**
Water quench	981.3±14.5	981.0±22.0	1008.3±13.1	1052.0±28.5	1113.7±31.5
PM (978.20)	0.32%	0.28%	3.08%	7.54%	13.78%

*the error bar (±) is standard deviation

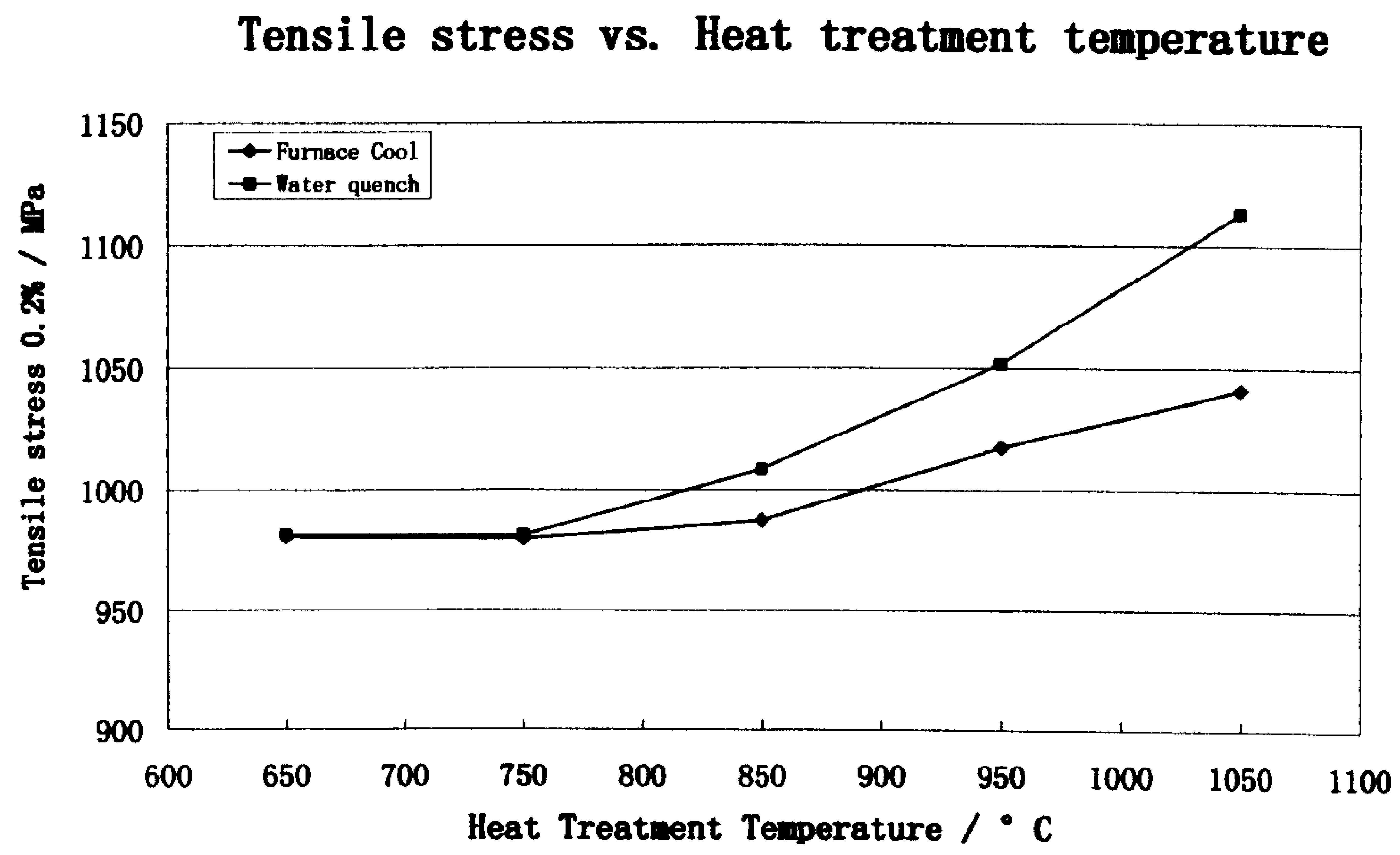

Figure 6.9 The effect of different heat treatment temperatures on tensile strength of Ti6Al4V

The value of elongation to failure of PM cannot be improved by furnace-cooling or water-quenching following heat treatment in the temperature range 650°C to 1050°C as seen in Figure 6.10. There is no significant change of elongation values between 650A, 750A, 850A, 650Q and 750Q. In annealing furnace-cooling condition, elongation values decrease from 850°C till 1050°C; the lowest elongation value is 24.38% smaller than that of the PM. In the water-quenched condition, elongation values drop off more quickly from somewhere between 750°C and 850°C till 1050°C. The lowest elongation value is 42.73% smaller than that of PM. The data are presented in Table 6.5.

Table 6.5 Percentage elongation as a function of heat treatment schedule for Ti6Al4V

Unit: %	**650A**	**750A**	**850A**	**950A**	**1050A**
Furnace cool	13.6±1.1	13.9±0.4	13.5±1.0	11.8±0.4	10.3±0.6
PM (13.62)	-0.15%	2.06%	0.88%	-13.61%	-24.38%
Unit: %	**650Q**	**750Q**	**850Q**	**950Q**	**1050Q**
Water quench	13.5±0.7	13.7±0.2	11.7±0.5	9.9±0.2	7.8±0.5
PM (13.62)	-0.63%	0.58%	-13.85%	-27.31%	-42.73%

*the error bar (±) is standard deviation

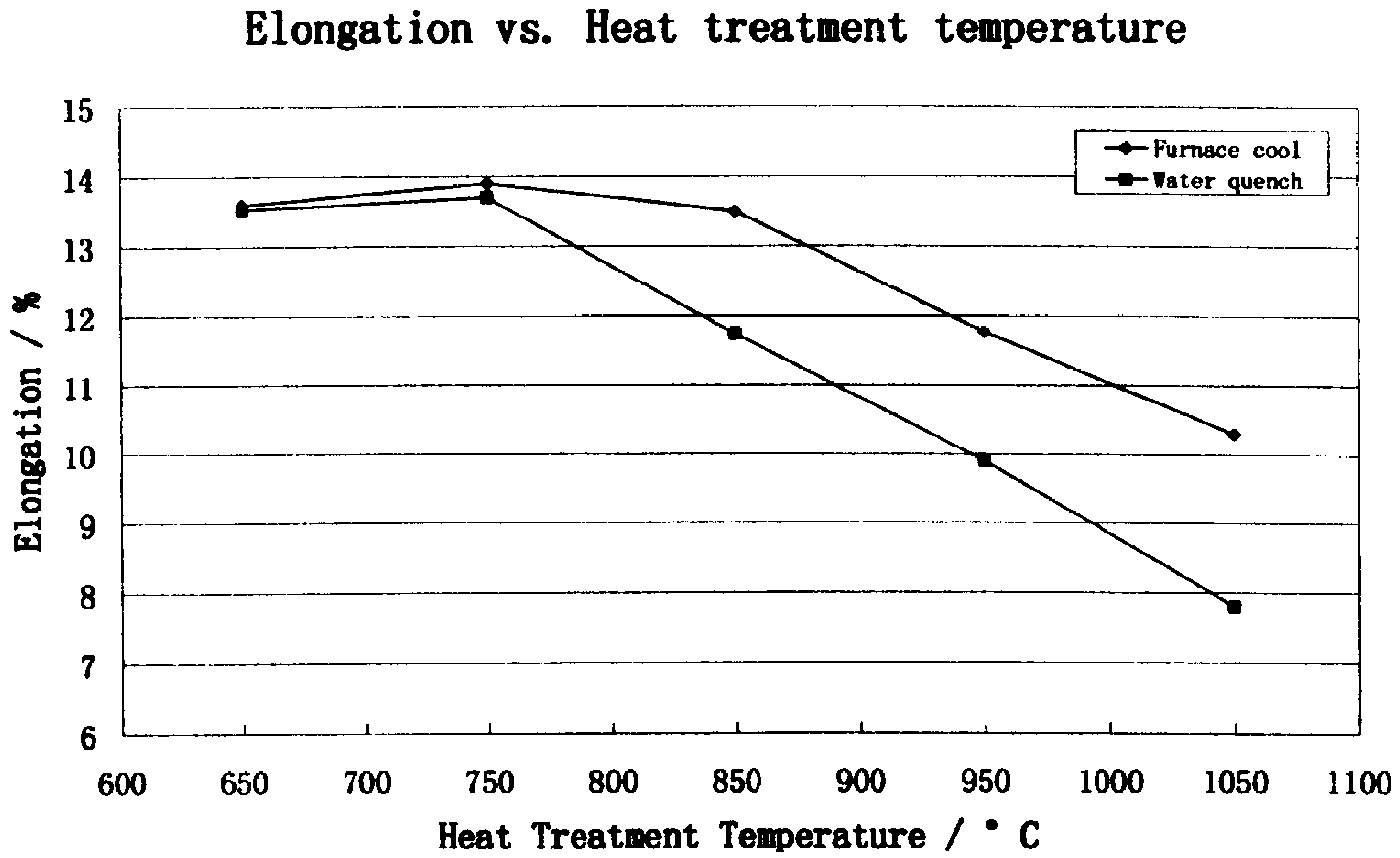

Figure 6.10 The effect of different temperature heat treatment schedules on percentage elongation in tensile testing

6.3 Characterisation of laser welded Ti6Al4V

6.3.1 Cross-sectional shapes of various lasers welding

Figure 6.11 (a) shows the cross section of PM sheet which is used for welding. Figure 6.11 (b)-(e) show typical cross-sectional photographs of the weld geometries produced by the various welding methods. The structures of all the welds show that the grains sizes are quite coarse. The average size of grains by diode laser welding (DLW) is the largest (245 μm), while the average sizes by fibre laser welding (FLW) (123 μm) and Nd:YAG Welding (137 μm) can be nearly half of that of DLW. The top width of FZ by DLW (Figure 6.11e) is the largest (can be more than 4 mm). The top width of FZ by FLW (Figure 6.11b) is around 1 mm. The top width of FZ by Nd:YAG (6.11d) is around 0.94 mm. For all three types of LBW, the HAZ width is narrow compared with the width of their FZs, (DLW is less than 2 mm, FLW is around 0.18 mm, Nd:YAG is around 0.25 mm).

The cross-sectional shapes of CW and Pulsed LBW are significantly different. Figure 6.11(b) shows four grooves occur at both the entry and exit sides near the HAZ of the FLW, the biggest thickness appeared at the centre line of the weld. The groove in the pulsed Nd:YAG LBW appeared toward the centre of the FZ (Figure 6.11(d)). There are two types of cross-sectional shapes associated with fibre laser welding. 40% of the cross-sectional shapes are according with Figure 6.11(b), and 60% of the welded samples exhibit cross-sectional shapes as shown in Figure 6.11(c).

Figure 6.11 (f-i) shows the 3D profiled images of four types of laser welding. The geometries of the each of the weld types are almost uniform along the welding direction. In that case, the 2D optical microscope images of cross sections can stand for the 3D geometries of the welds.

The melting area of FLW (Figure 6.11(b)) is around 0.49 mm^2. The melting area of DLW (Figure 6.11(e)) is around 3.06 mm^2. The melting area of Nd:YAG (Figure 6.11(d)) is around 0.37 mm^2.

The distortion of the weld geometries produced by the various weld methods is identified as misalignment by comparing with two parallel lines. The misalignment of DLW (Figure 6.11(e)) is the most significant. The misalignment of Nd:YAG (Figure 6.11(d)) is smaller than that of the FLW (Figure 6.11(b)).

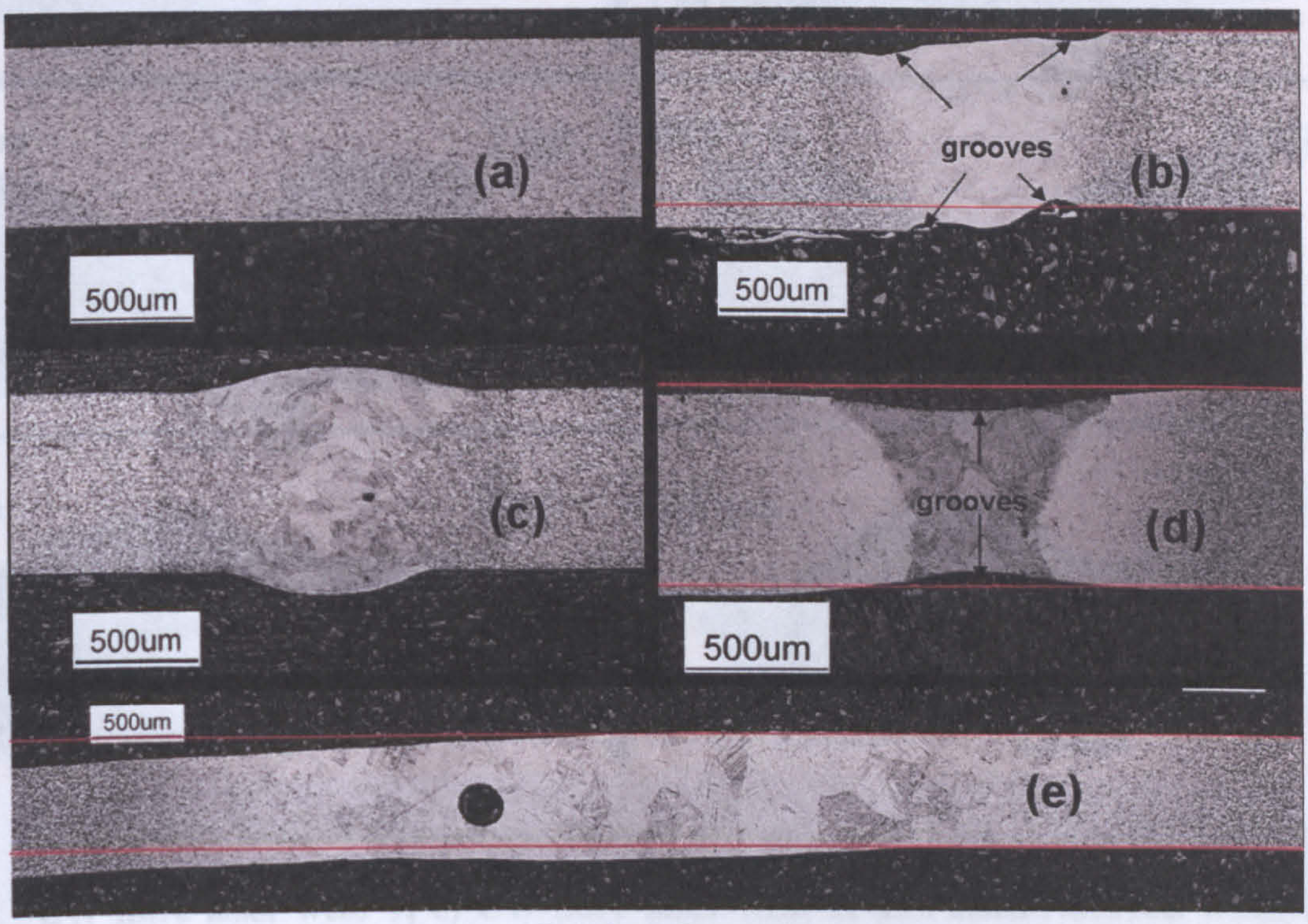

Continued

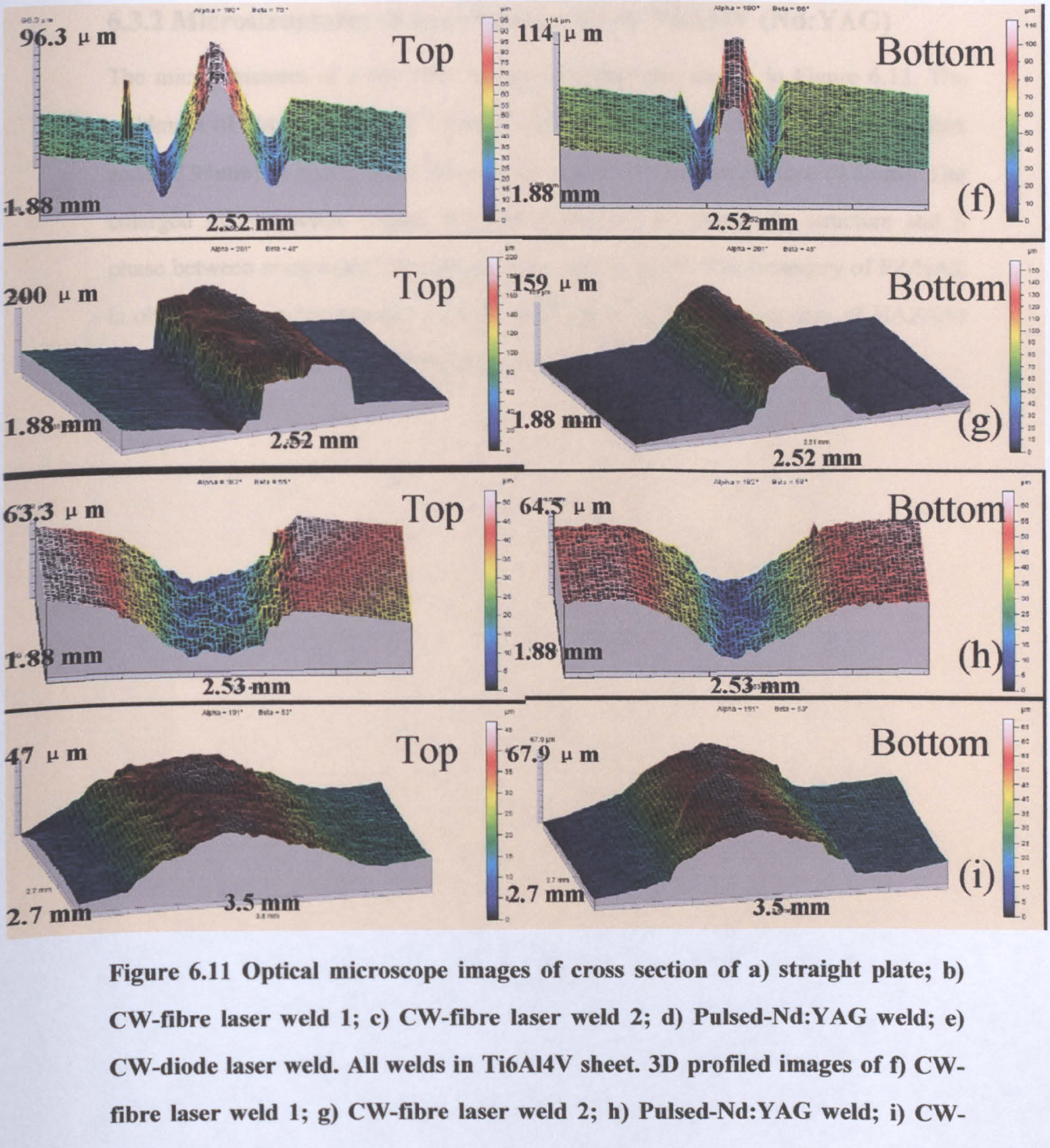

Figure 6.11 Optical microscope images of cross section of a) straight plate; b) CW-fibre laser weld 1; c) CW-fibre laser weld 2; d) Pulsed-Nd:YAG weld; e) CW-diode laser weld. All welds in Ti6Al4V sheet. 3D profiled images of f) CW-fibre laser weld 1; g) CW-fibre laser weld 2; h) Pulsed-Nd:YAG weld; i) CW-diode laser weld

* Top surface and bottom surface

6.3.2 Microstructures of laser beam welded Ti6Al4V (Nd:YAG)

The microstructures of a Nd:YAG welded Ti6Al4V are shown in Figure 6.12. The weldment of Nd:YAG welded Ti6Al4V shows the top surface width of the molten zone (0.94mm) is nearly twice the size of that of the bottom surface (0.5mm). The enlarged microstructure (Figure 6.12(a)) shows the α′ martensite structure and β phase between martensitic laths inside of the grains in FZ. The boundary of FZ/HAZ is obvious. The microstructure of HAZ in Figures 6.12b and boundary of HAZ/PM 6.12c include a mixture of martensite α′, acicular α, and primary α.

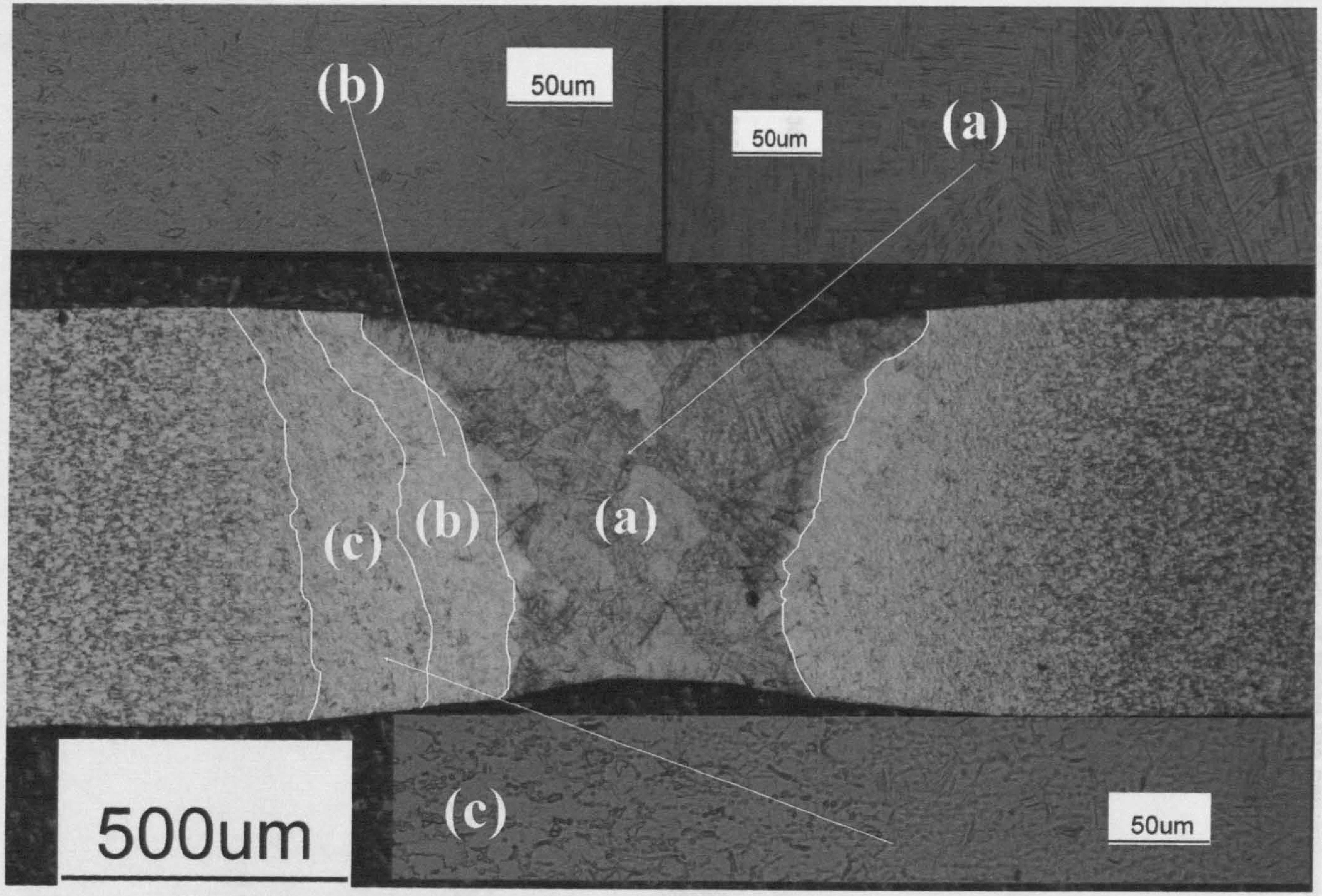

Figure 6.12 Microstructure of Nd:YAG welded Ti6Al4V (a) Microstructure of the FZ (b) Microstructure of the HAZ (c) Microstructure of boundary of the HAZ/PM

6.3.3 Mechanical properties of laser beam welded Ti6Al4V

In the Nd:YAG, FLW and DLW Ti6Al4V (Figure 6.13-6.15), hardness values increase when proceeding from the PM across the HAZ towards the FZ. Table 6.6 shows the mean values found in the FZ, HAZ and PM for FLW, DLW, Nd:YAG welds. Standard deviation values were derived from six groups of data randomly from three samples cross sections for each weld type. It listed the percentage increase from Δ% FZ-PM and Δ% HAZ-PM. It can be noted that the increase Δ% FZ-PM is much larger than Δ% HAZ-PM.

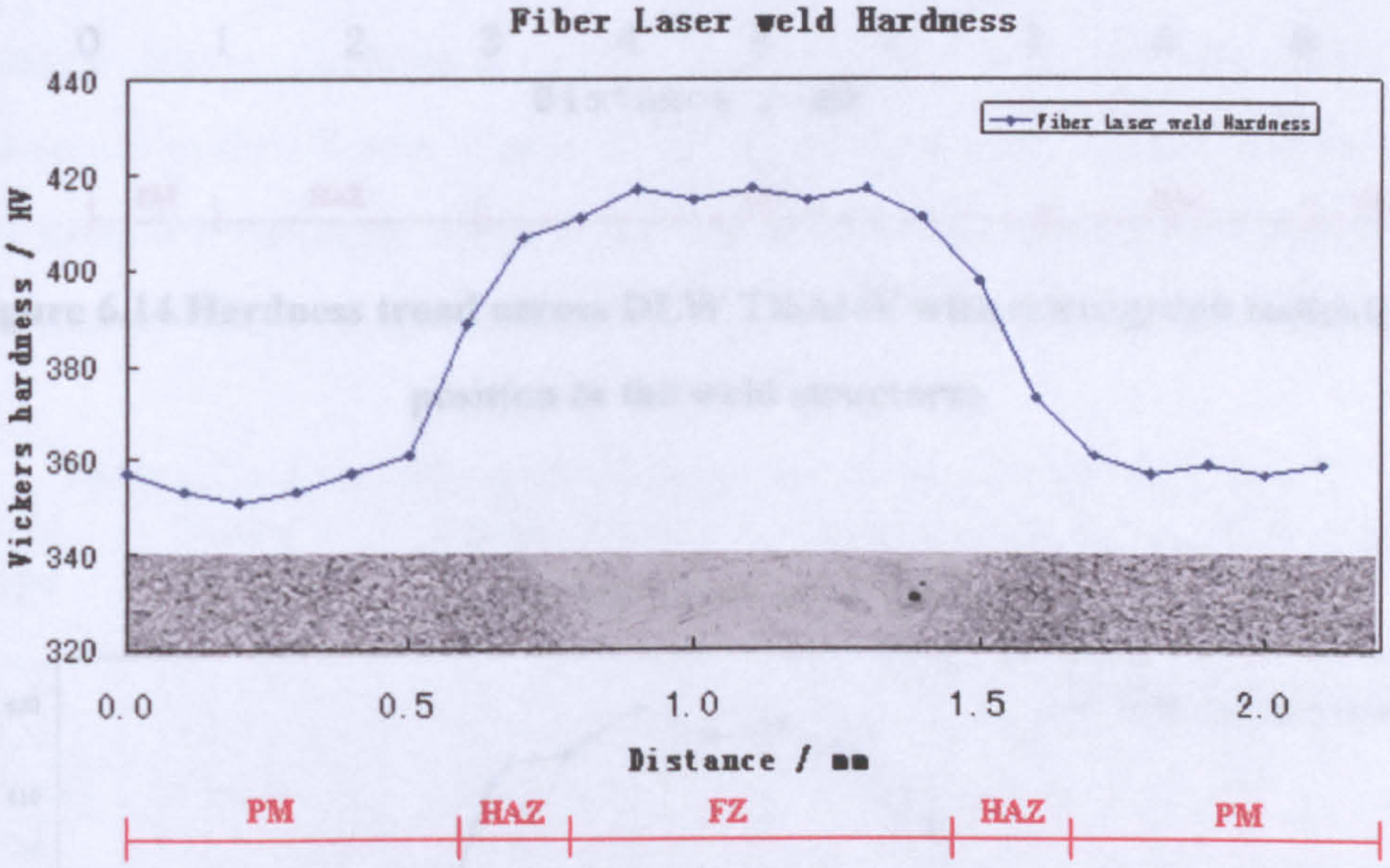

Figure 6.13 Hardness trend across FLW Ti6Al4V with micrograph indicating position in the weld structures

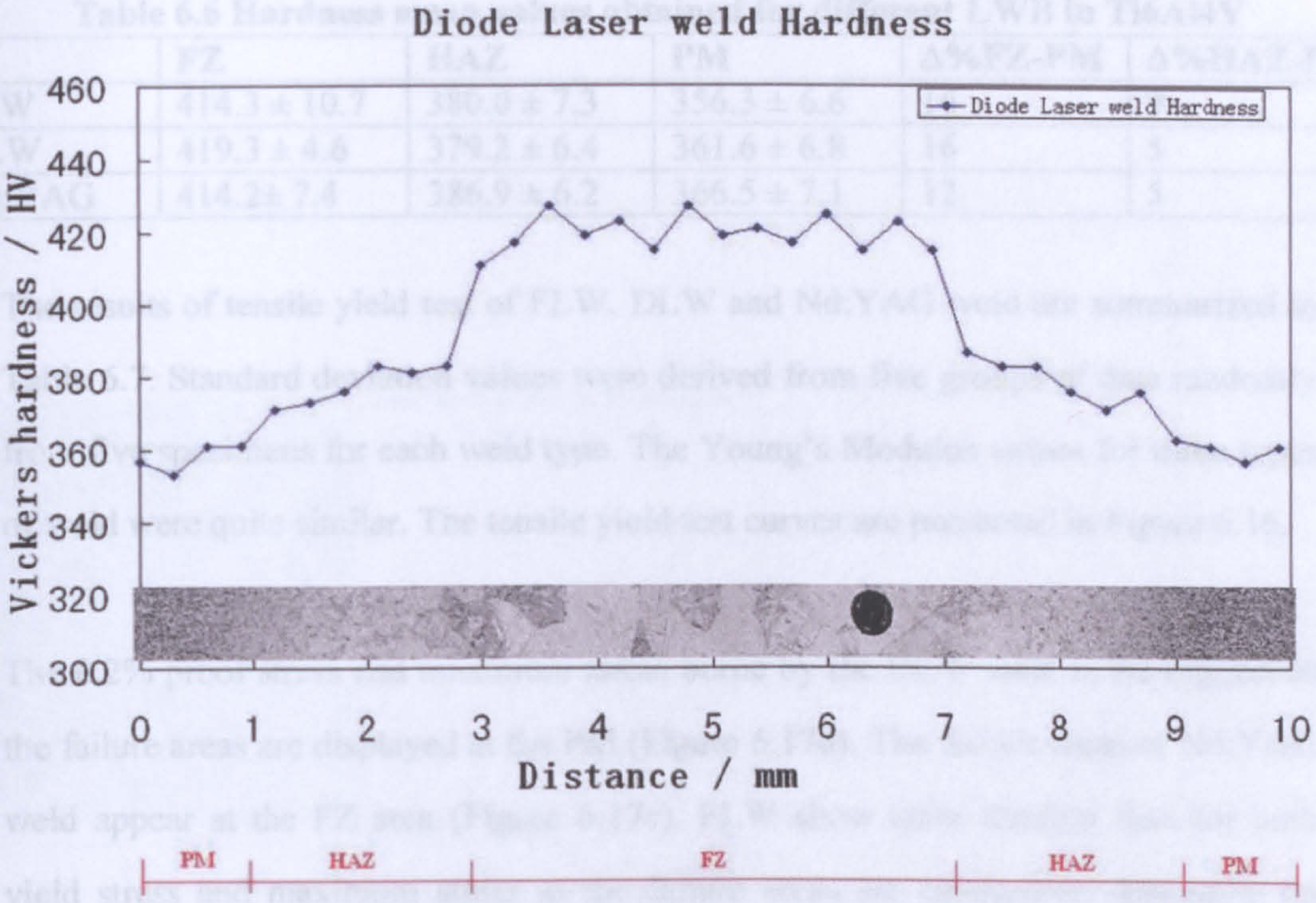

Figure 6.14 Hardness trend across DLW Ti6Al4V with micrograph indicating position in the weld structures

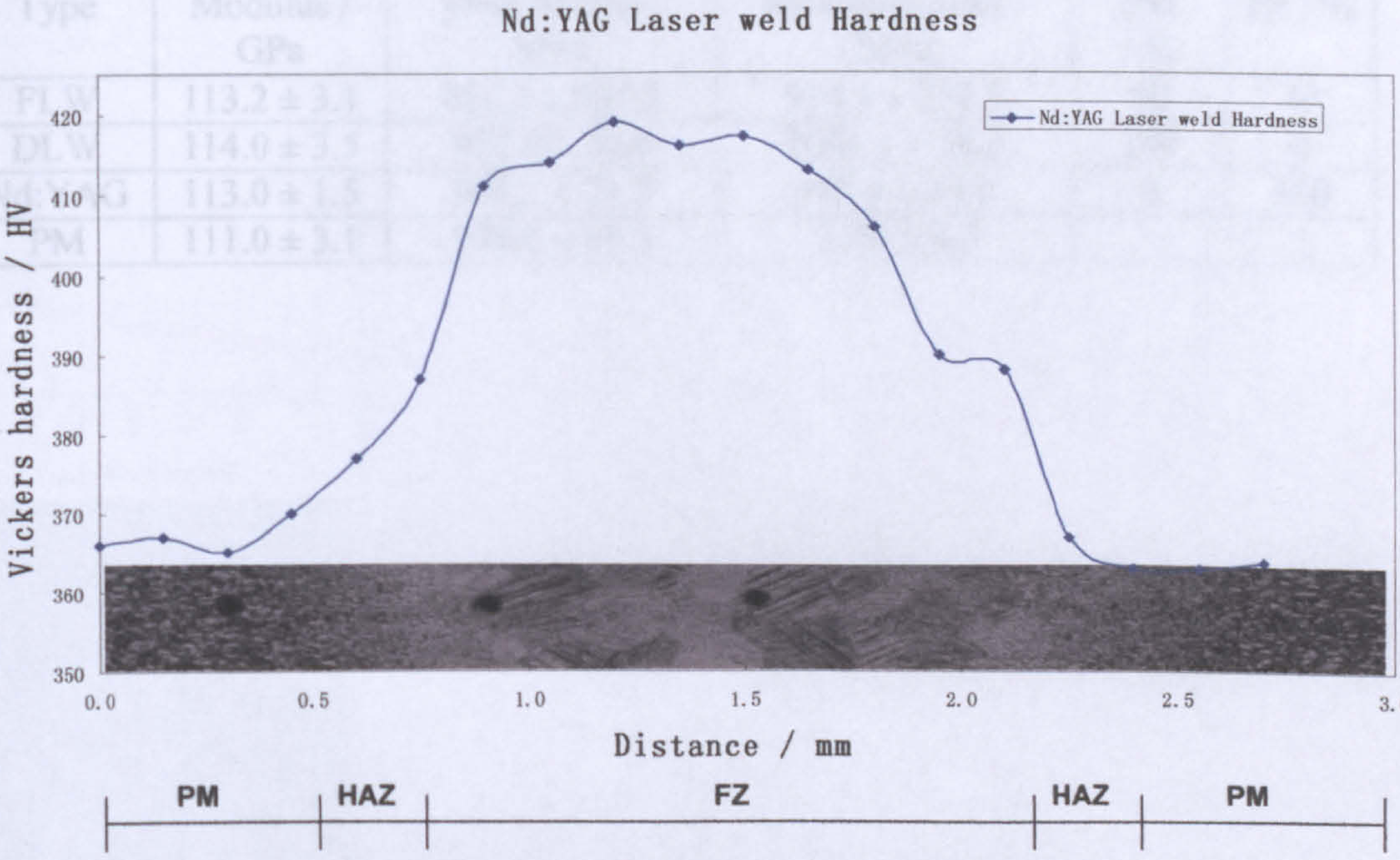

Figure 6.15 Hardness trend across Nd:YAG Ti6Al4V with micrograph indicating position in the weld structures

Table 6.6 Hardness mean values obtained for different LWB in Ti6Al4V

	FZ	HAZ	PM	Δ%FZ-PM	Δ%HAZ-PM
FLW	414.3 ± 10.7	380.0 ± 7.3	356.3 ± 6.6	16	7
DLW	419.3 ± 4.6	379.2 ± 6.4	361.6 ± 6.8	16	5
Nd:YAG	414.2± 7.4	386.9 ± 6.2	366.5 ± 7.1	12	5

The results of tensile yield test of FLW, DLW and Nd:YAG weld are summarized in Table 6.7. Standard deviation values were derived from five groups of data randomly from five specimens for each weld type. The Young's Modulus values for three types of weld were quite similar. The tensile yield test curves are presented in Figure 6.16.

The 0.2% proof stress and maximum stress borne by the DLW weld is the biggest as the failure areas are displayed at the PM (Figure 6.17d). The failure areas of Nd:YAG weld appear at the FZ area (Figure 6.17c). FLW show quite random data for both yield stress and maximum stress as the failure areas are changeable depending on cross-sectional shapes (Figure 6.17a-b).

Table 6.7 tensile test results obtained for different LWB in Ti6Al4V

Weld Type	Young's Modulus / GPa	Tensile stress at yield (0.2%) / MPa	Tensile stress at maximum load / MPa	Failure area	
				PM / %	FZ / %
FLW	113.2 ± 3.1	832.3 ± 267.2	914.1 ± 251.5	60	40
DLW	114.0 ± 3.5	977.0 ± 36.6	1084.1 ± 16.3	100	0
Nd:YAG	113.0 ± 1.5	963.3 ± 21.7	989.4 ± 34.6	0	100
PM	111.0 ± 3.1	978.2 ± 15.3	1054 ± 4.3		

[redacted]

[redacted]

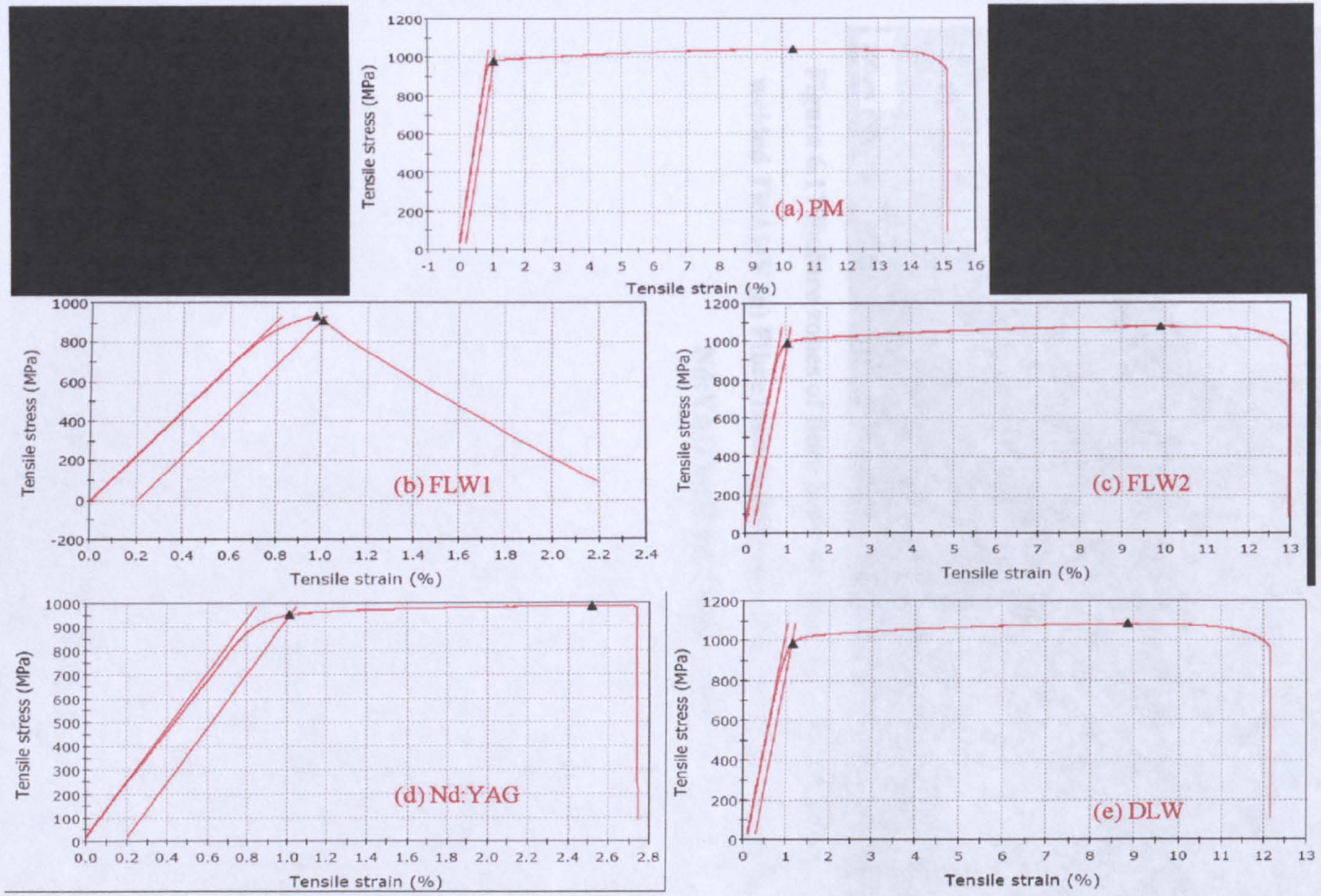

Figure 6.16 Tensile yield test curve of Ti6Al4V in various conditions (a) parent material (b) fibre laser welding type 1 (c) fibre laser welding type 2 (d) Nd:YAG welding (e) diode laser welding

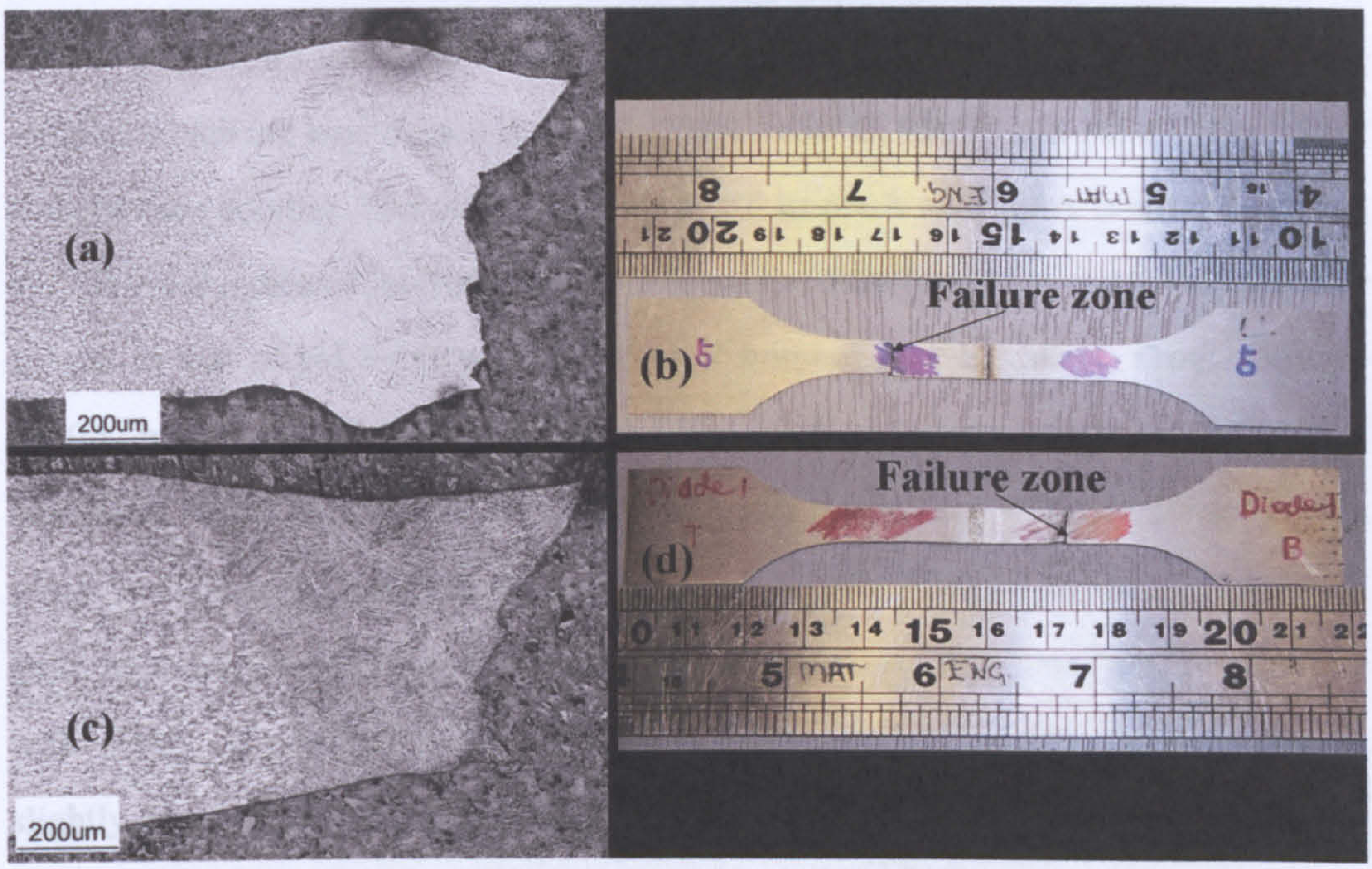

Figure 6.17 Failure zones of fibre laser welded, Nd:YAG welded and Diode welded Ti6Al4V (a) Fibre laser weld type 1 (b) Fibre laser weld type 2 (c) Nd:YAG weld (d) Diode weld

6.4 Characterisation of heat treatment on Nd:YAG welded Ti6Al4V

Figure 6.18 shows the cross-sectional microstructures of Nd:YAG welded Ti6Al4V samples which are heat treated at 650°C, 750°C, 850°C, 950°C and 1050°C for 1 hour with furnace cooling. The microstructure of FZ in 650A and 750A is still martensite α′. Table 6.8 indicates hardness values of these two heat treatment conditions are very similar to that of Nd:YAG welded Ti6Al4V without heat treatment. From 850A to 1050A, martensite α′ starts to transform into α colony microstructure with β phase boundary. As the temperature increases, the width of α colony becomes thicker. From 950A to 1050A, α grain boundary in the prior β grain starts to appear. In 1050A, α grain boundary tends to be very coarse; and the PM transforms into lamellar structure with plenty of oriented α colonies and β phase boundaries. The hardness values slightly drop off from 950A to 1050A (Table 6.8).

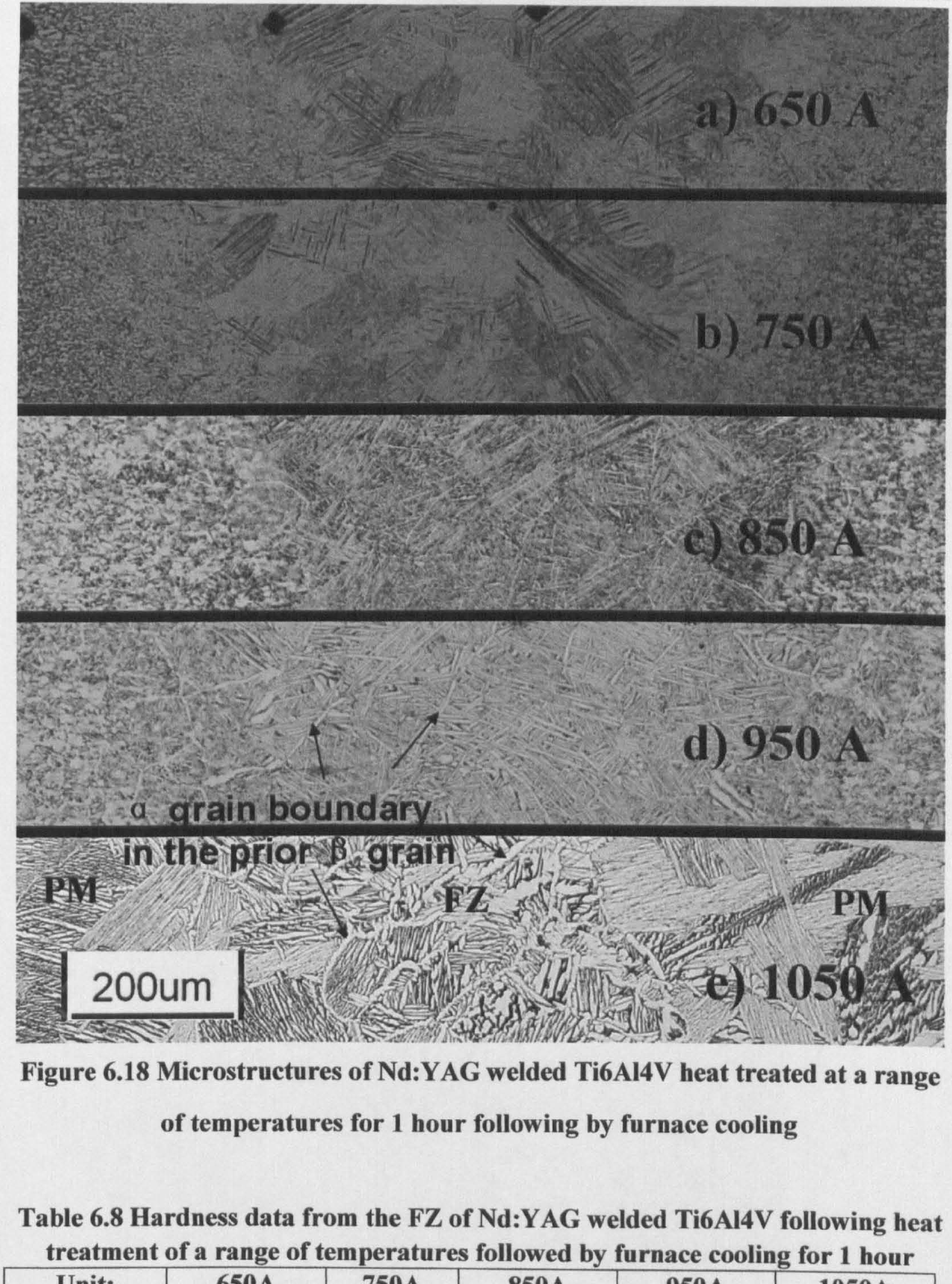

Figure 6.18 Microstructures of Nd:YAG welded Ti6Al4V heat treated at a range of temperatures for 1 hour following by furnace cooling

Table 6.8 Hardness data from the FZ of Nd:YAG welded Ti6Al4V following heat treatment of a range of temperatures followed by furnace cooling for 1 hour

Unit: kgmm^{-2}	650A	750A	850A	950A	1050A
Furnace cool	416.0±6.4	413.3±9.0	408.1±8.6	404.2±7.1	403.2±6.6
Nd:YAG (414.2± 7.4)	0.48%	-0.24%	-1.45%	-2.42%	-2.66%

Figure 6.19 shows cross-sectional microstructures FZ of Nd:YAG welded and heat treated Ti6Al4V samples which are annealed at the temperature of 950°C with the same furnace and cooling but with different heat treatment times (1 hour, 8 hours and 20 hours). All of these heat treatment conditions transform martensite α′ (Figure 6.19a) into α colony microstructure. As shown in Table 6.9, the β-phases area fractions of 8 hours and 20 hours heat treated samples are very similar and slightly higher than that of 1 hour heat treated sample. As the time increases, the width of α colony tends to be thicker and the hardness values decrease (Table 6.9). In Figure 6.19(b), there is α grain boundary which can be possibly transformed from prior β grain boundary. In Figure 6.19(c), more metastable β phases are formed.

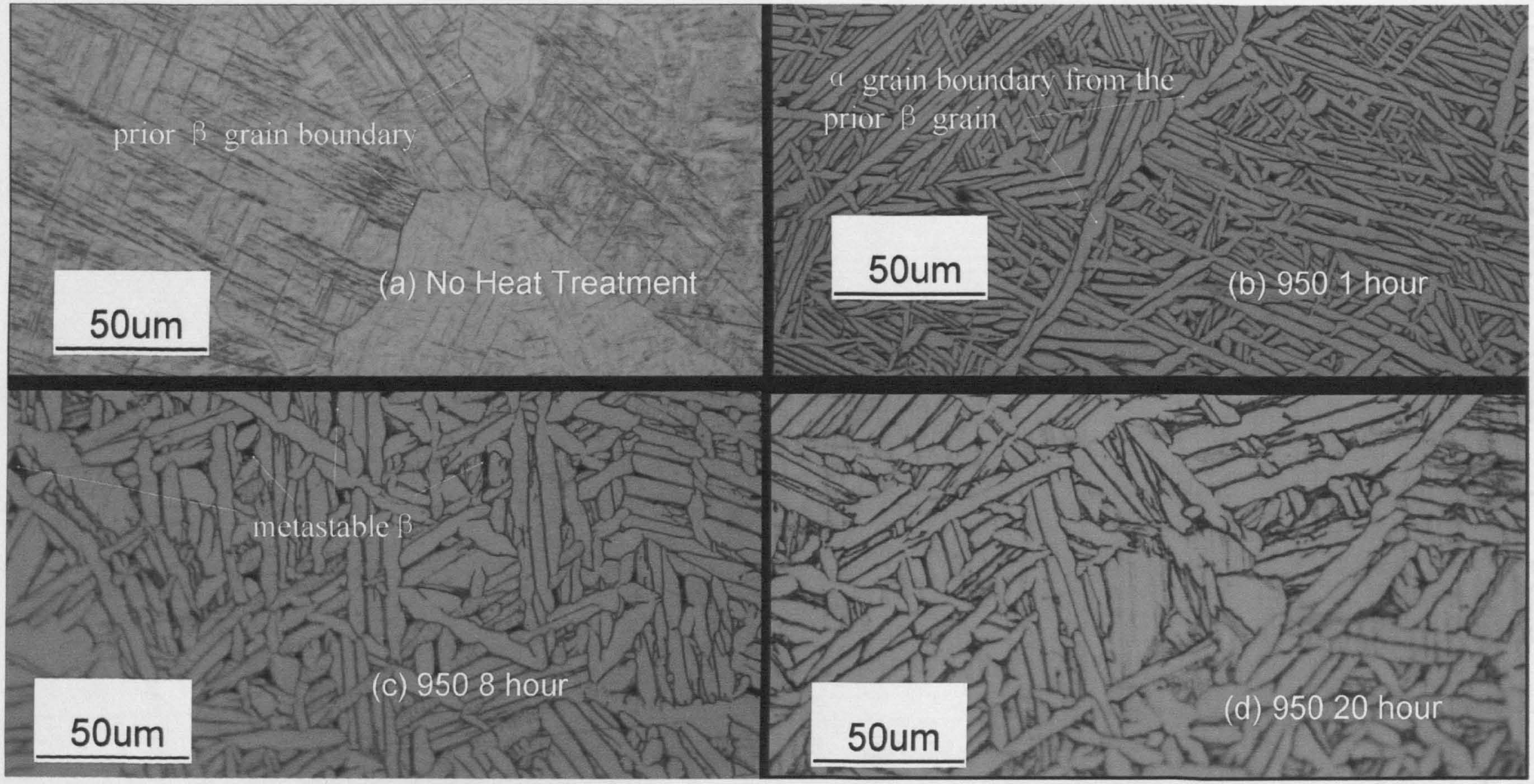

Figure 6.19 Microstructures FZ of Nd:YAG welded and heat treated Ti6Al4V. a) No heat treatment; b) 950°C 1 hour; c) 950°C 8 hour; d) 950°C 20 hour. All samples furnace cooled.

Table 6.9 Hardness data, Grain size and Phase content of 950°C heat treatment on Fusion Zone of Nd:YAG Ti6Al4V for 1 hour, 8 hours and 20 hours followed by furnace cooling

Hardness / kgmm^{-2}	**1 hour**	**8 hours**	**20 hours**
950°C Furnace cool	404.2±7.1	398.0±6.9	384.6±4.9
Average α colony width / μm	**1 hour**	**8 hours**	**20 hours**
950°C Furnace cool	3.25	5.06	7.99
β-Phase Area Fraction / %	**1 hour**	**8 hours**	**20 hours**
950°C Furnace cool	7.6	8.8	8.6

6.5 Fatigue behaviour of laser beam welding Ti6Al4V

6.5.1 S-N curve

Figure 6.20 shows the fatigue fracture lives of PM, fibre laser welded samples, Nd:YAG welded samples and Nd:YAG welded with different heat treatment conditions (Nd:YAG No treatment, Nd:YAG heat treatment for 1hr, Nd:YAG heat treatment for 8hrs and Nd:YAG heat treatment for 20hrs) as a function of stress amplitude. Figure 6.21 are zoom-in S-N curves of experimental data. Predicted values (using Equation 5.2 and the values of the constants derived from the literature) are shown alongside. The results can be summarized as:

1. The predicted fatigue life of prediction is much higher than that of PM. The reason is that predicted values were derived from the experiment for fully reversed loading ($R = -1$). This will be discussed in the next chapter.

2. Failure areas of all the welded samples are in FZ of the weld. Fatigue fracture lives of these welded samples are much lower than that of PM. The fatigue fracture lives of fibre laser welded samples are lowest at both high stress level and low stress level. The fatigue fracture lives of Nd:YAG welded samples are much larger than that of fibre laser welded samples. Especially, the life is increased from 15,667 to 89,500 at high stress level (202.5MPa), this improvement is about 471%. At 157.5MPa, the improvement in life is only 193%.

3. In Nd:YAG weld, at a high stress level 202.5MPa, 1 hour heat treated samples exhibit nearly no increase in fatigue life; The improvement rates of 20 hours heat treated samples and 8 hours heat treated samples are respectively 72%, 110%. At a low stress level of 157.5MPa, the improvement rates of 1 hour heat treated samples, 20 hours heat treated samples and 8 hours heat treated samples are respectively 10%, 41% and 54%. At a stress level 146.25MPa, the improvement rates of 1 hour heat treated samples, 20 hours heat treated samples and 8 hours heat treated samples are

respectively 31%, 28% and 41%. Nd:YAG welded samples with heat treatment for 8 hours show the largest fatigue lives at both high stress level and low stress level.

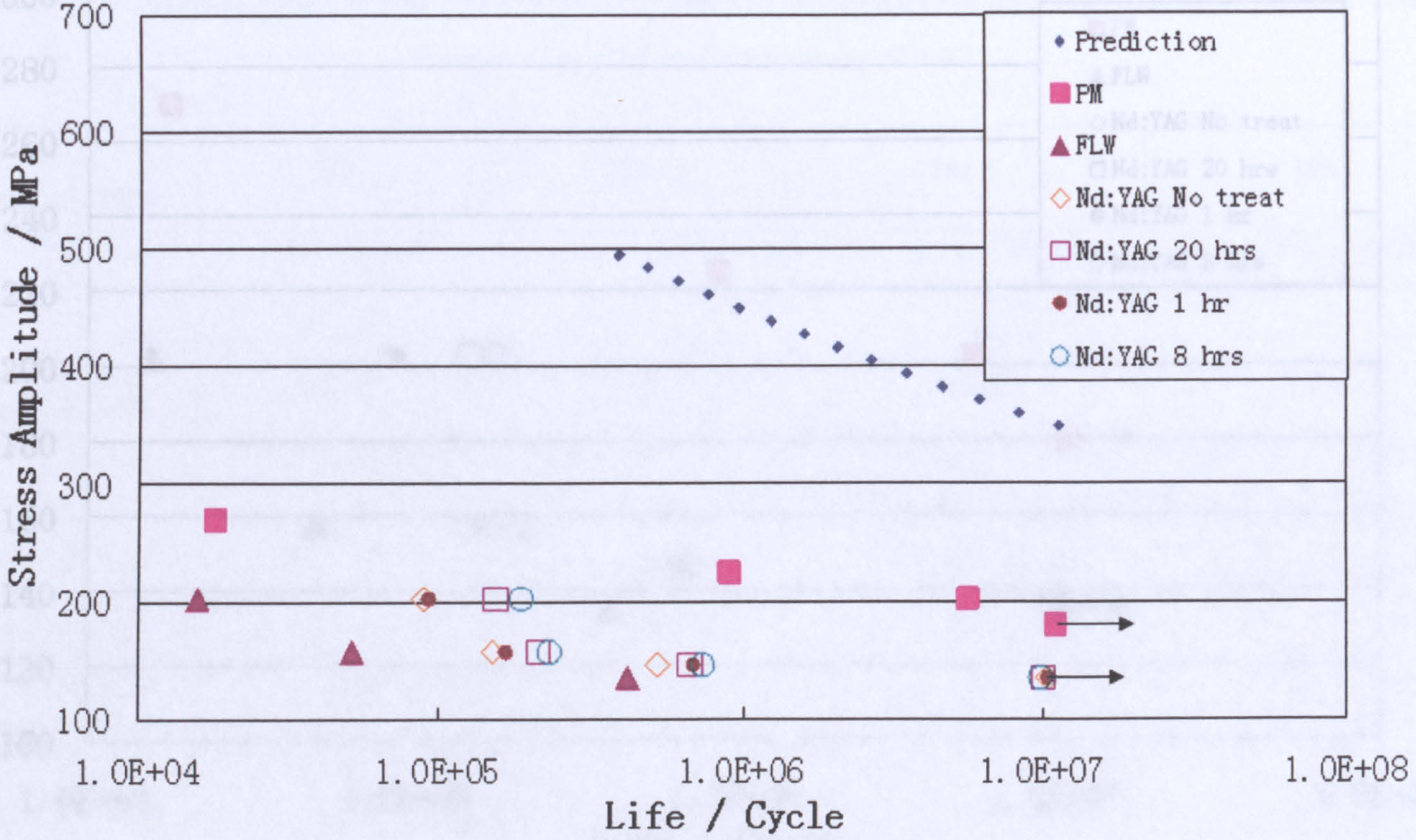

Figure 6.20 S-N curve of prediction, parent material, fibre laser welded material, Nd:YAG welded material, Nd:YAG welded material heat treated for 1 hour, Nd:YAG welded material heat treated for 8 hours and Nd:YAG welded material heat treated for 20 hours

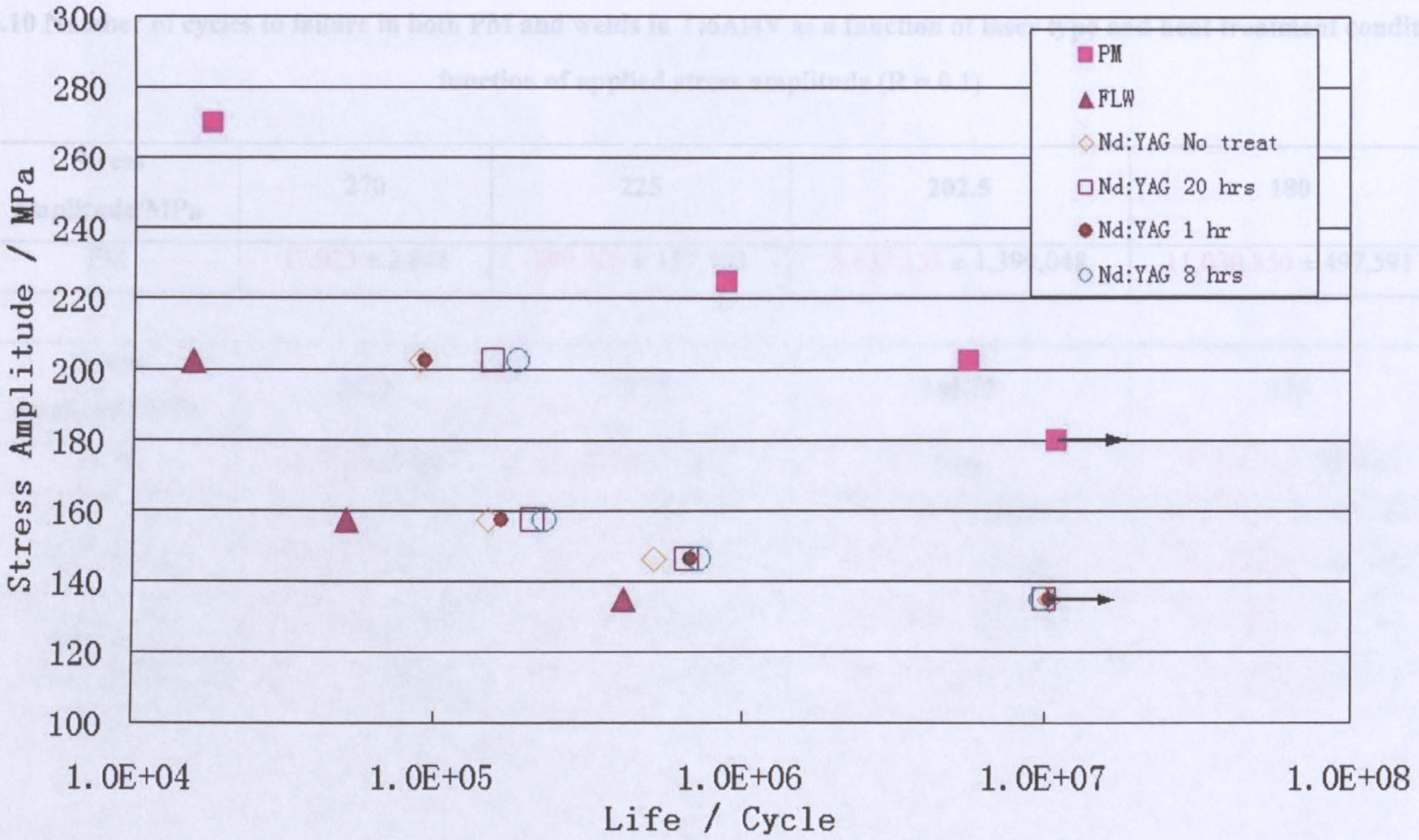

Figure 6.21 Zoom-in S-N curve of parent material, fibre laser welded material, Nd:YAG welded material, Nd:YAG welded material heat treated for 1 hour, Nd:YAG welded material heat treated for 8 hours and Nd:YAG welded material heat treated for 20 hours

Table 6.10 Number of cycles to failure in both PM and welds in Ti6Al4V as a function of laser type and heat treatment condition as a function of applied stress amplitude (R = 0.1)

Stress amplitude/MPa	**270**	**225**	**202.5**	**180**
PM	17,925 ± 2,848	899,400 ± 157,503	5,633,133 ± 1,399,048	11,030,850 ± 497,591
Stress amplitude/MPa	**202.5**	**157.5**	**146.25**	**135**
FLW	15,667 ± 1,450	51,500 ± 17,088	N/A	415,967 ± 156,424
Nd:YAG	89,500 ± 17,067	150,900 ± 48,476	523,267 ± 218,703	10,330,400 ± 508,551
Nd:YAG-1hr	92,467 ± 12,815	166,633 ± 11,851	684,667 ± 164,850	10,364,800 ± 90,368
Nd:YAG-8hr	187,600 ± 48,772	232,100 ± 35,527	736,300 ± 168,250	9,830,550 ± 311,763
Nd:YAG-20hr	154,167 ± 66,385	212,827 ± 31,971	667,323 ± 104,729	10,037,500 ± 10,607

6.5.2 Fractograph of Fatigue Tested Ti6Al4V

Figure 6.22 (a-f) are SEM fractographs of failed fatigue samples of PM, fibre laser weld, Nd:YAG welds and Nd:YAG welds with different heat treatment conditions. Fatigue life depends on the initiation and propagation of fatigue cracks. All SEM fractographs show the initiation area (left) and propagation area (right). Porosity is detected in all the welded samples (Figure 6.22b-f). The fibre laser welded sample shows the most serious porosity (Figure 6.22b), and a microcrack is found as well.

Fractographs of PM (Figure 6.22a) shows the propagation area (Figure 6.22 a(iii)) is flat and uniform. Fractograph of Nd:YAG weld (Figure 6.22c) shows mountain-shape surface in propagation area, which is possibly caused by the coarse grain size. Nd:YAG weld after heat treatment (Figure 6.22d-f), tends to be flat and uniform again. Following long time heat treatment (Figure 6.22f), basket-weave α colony is found.

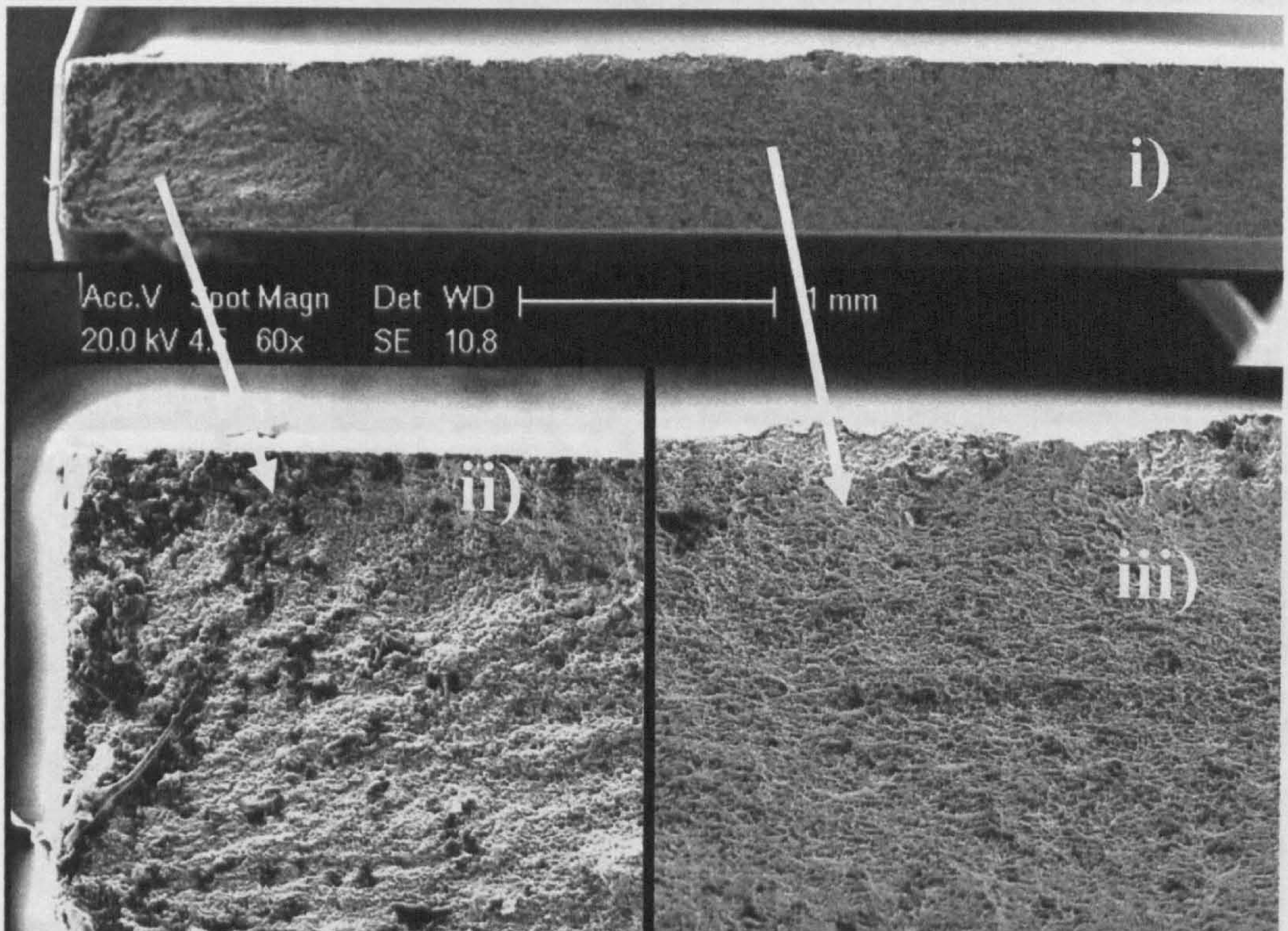

(a) PM

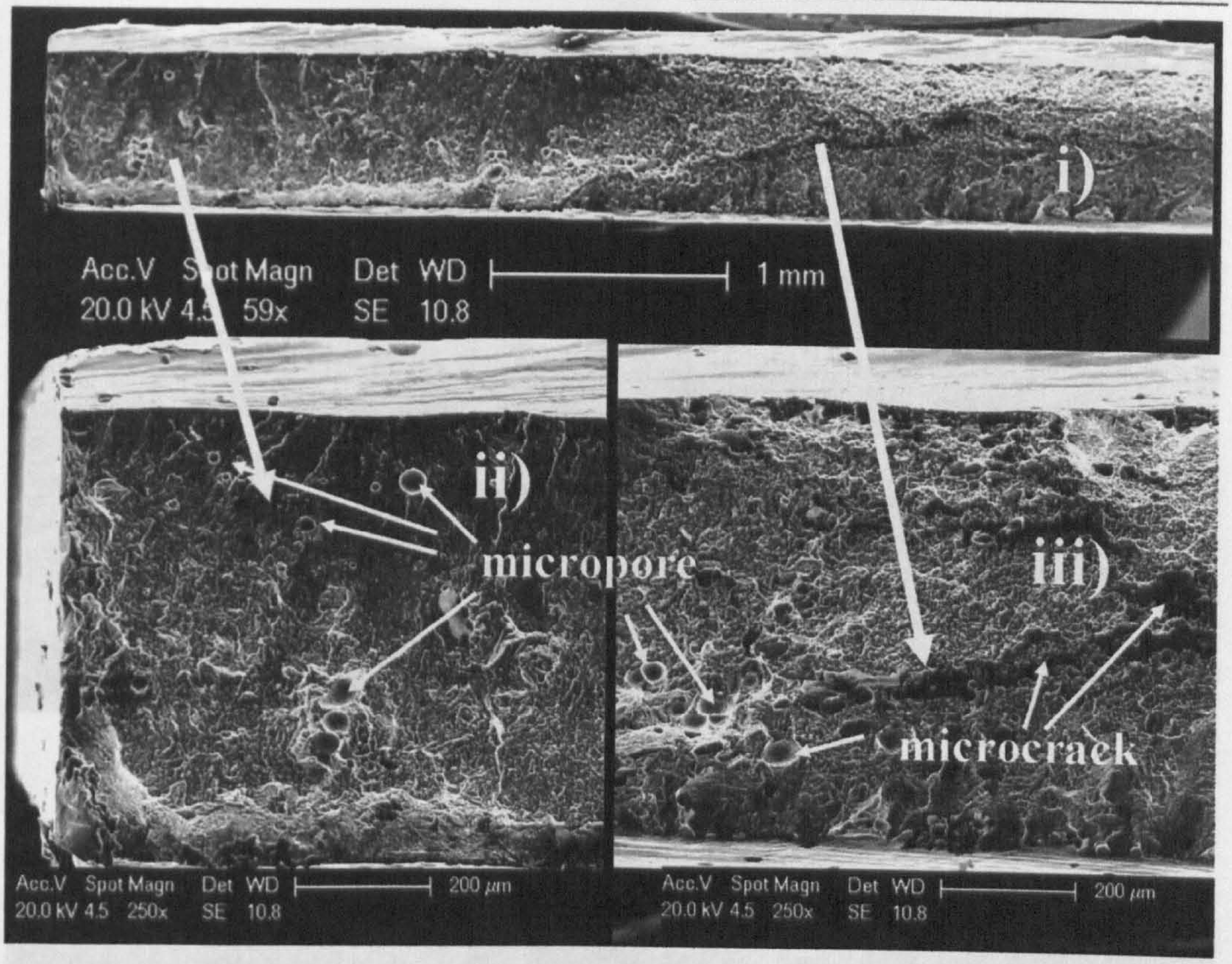

(b) FLW

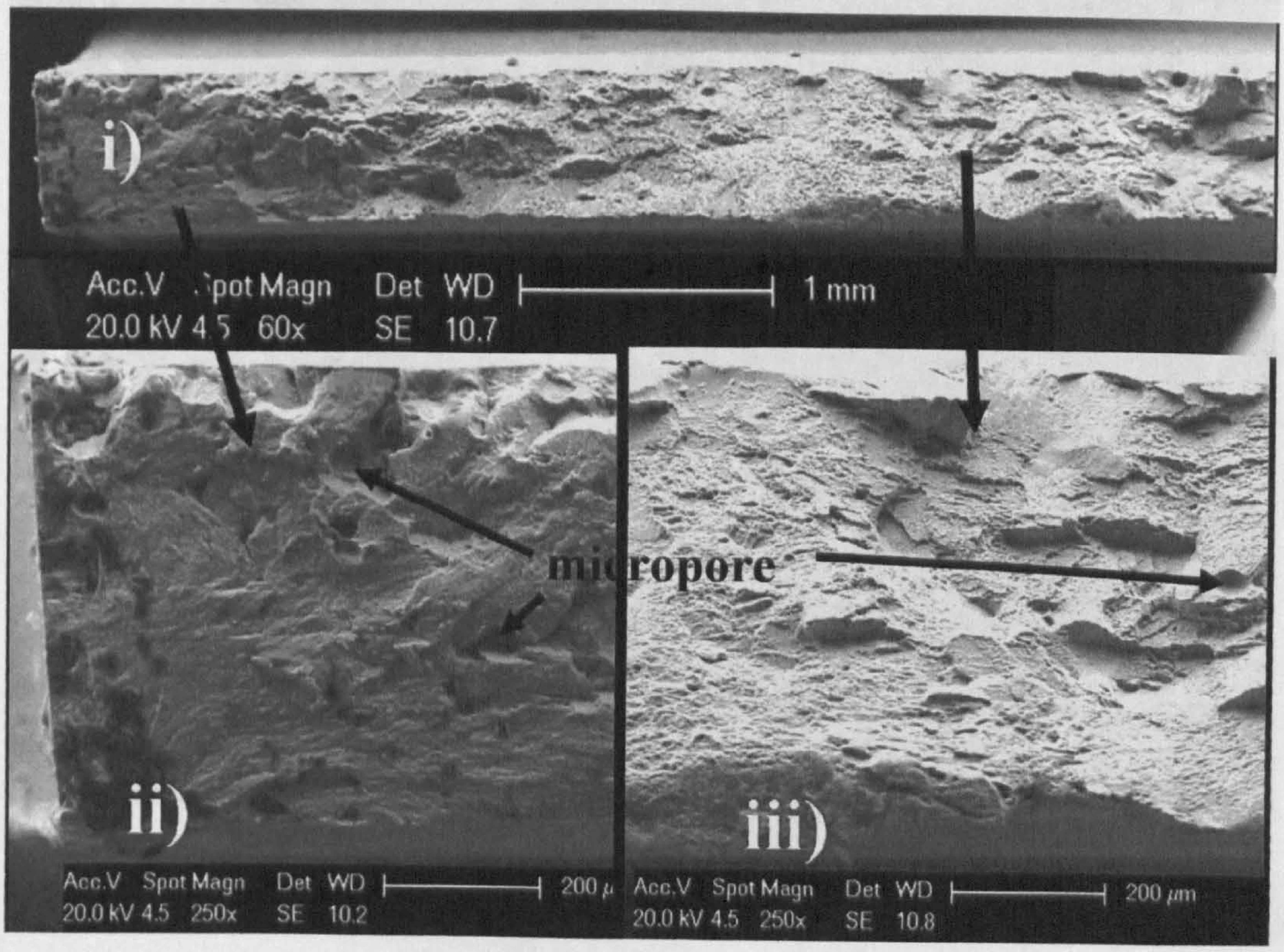

(c) Nd:YAG No heat treatment

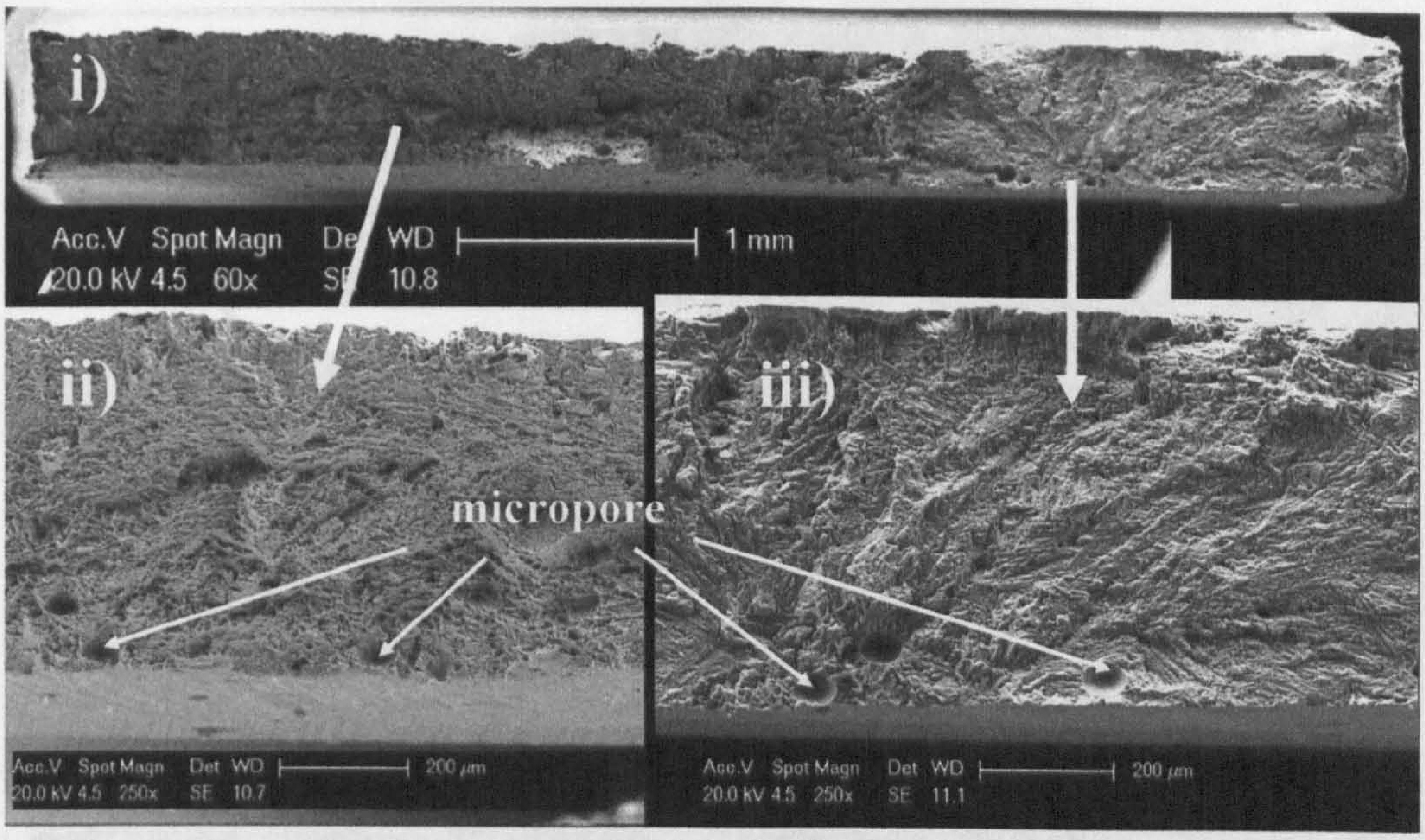

(d) Nd:YAG 1 hour

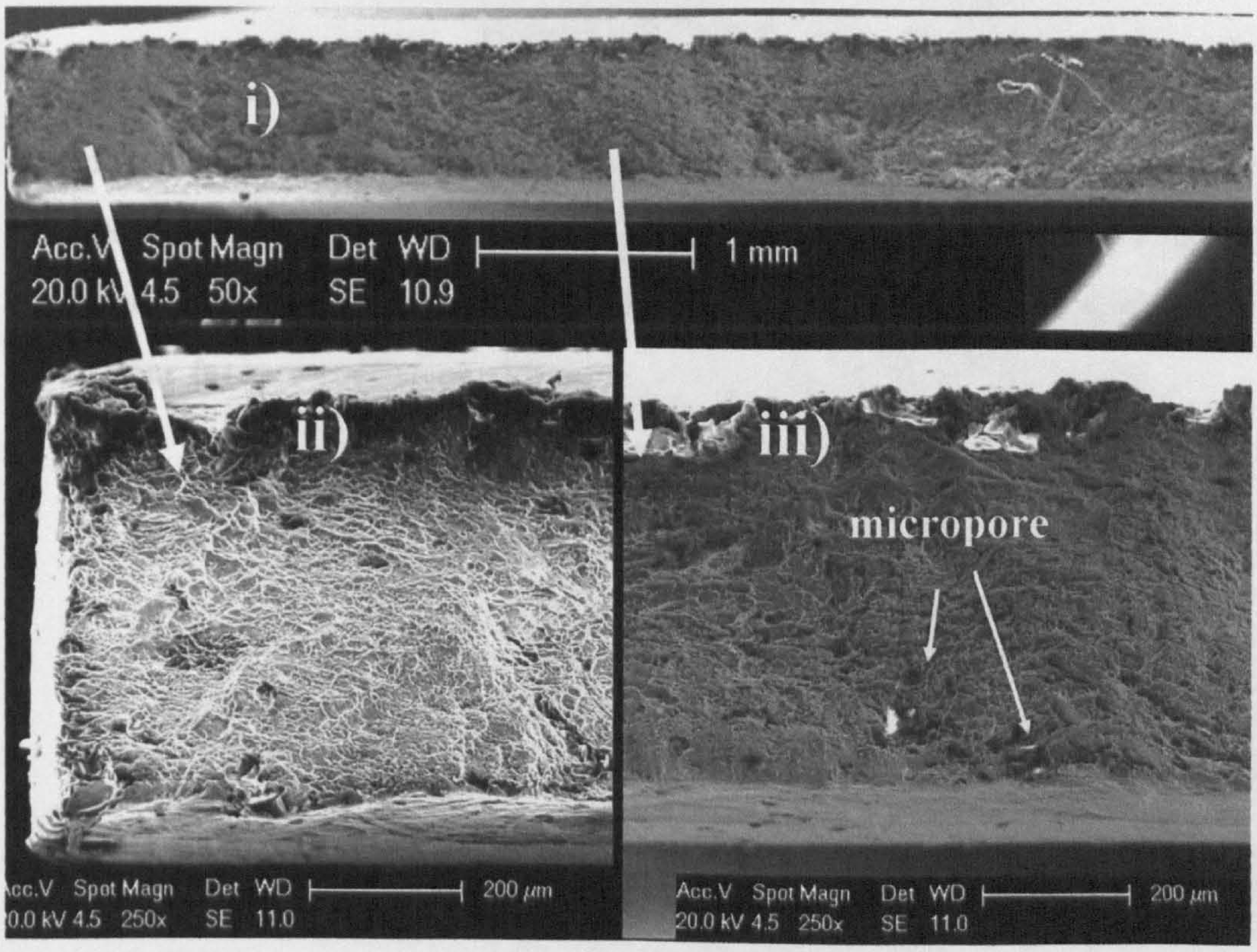

(e) Nd:YAG 8 hour

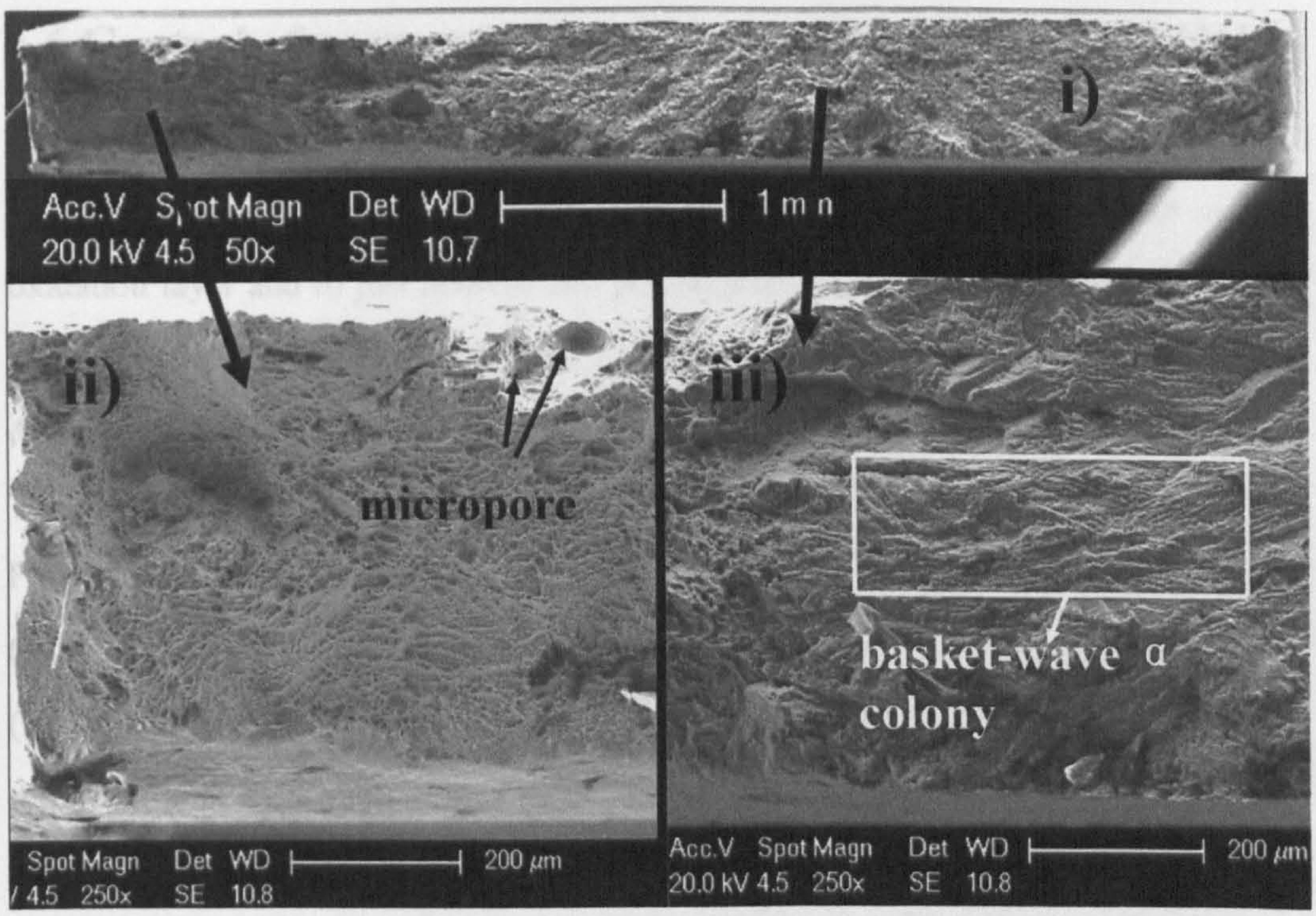

(f) Nd:YAG 20 hour

Figure 6.22 SEM fractographs of fatigue samples of (a) PM, (b) fibre laser weld, (c) Nd:YAG weld no heat treatment, (d) Nd:YAG weld heat treatment at 950°C for 1 hour furnace-cooling condition, (e) Nd:YAG weld heat treatment at 950°C for 8 hour furnace-cooling condition, (f) Nd:YAG weld heat treatment at 950°C for 20 hour furnace-cooling condition

6.6 Control of parameters on laser beam welding Ti6Al4V

There are several risks for welding thin metal as it is easy to be penetrated and oxidized. Bead-on-plate process was used to choose the right P and V to get reduced oxidation layer and to just achieve full penetration butt weld specimens. The control of weld width in continuous wave and pulsed laser is controlled respectively by power & travel speed and power only.

Figure 6.23 illustrates the width of top surface (WT) and width of bottom surface (WB) of the molten zones versus specific input energy (which is equal to laser power (P) divided by traverse speed (V)) in CW FLW process. It is clear that by decreasing the linear heat input (PV^{-1}), both parameters (WT and WB) decrease. The WT values are always higher than the WB values.

Once a power level was established, the increase in traverse speed value corresponds to a decrease in WT and WB value, thus implying that the melting area become lower. On the other hand, once a V was established, with an increase the laser power, the width of the weld increased as there is more input energy which causes more melting.

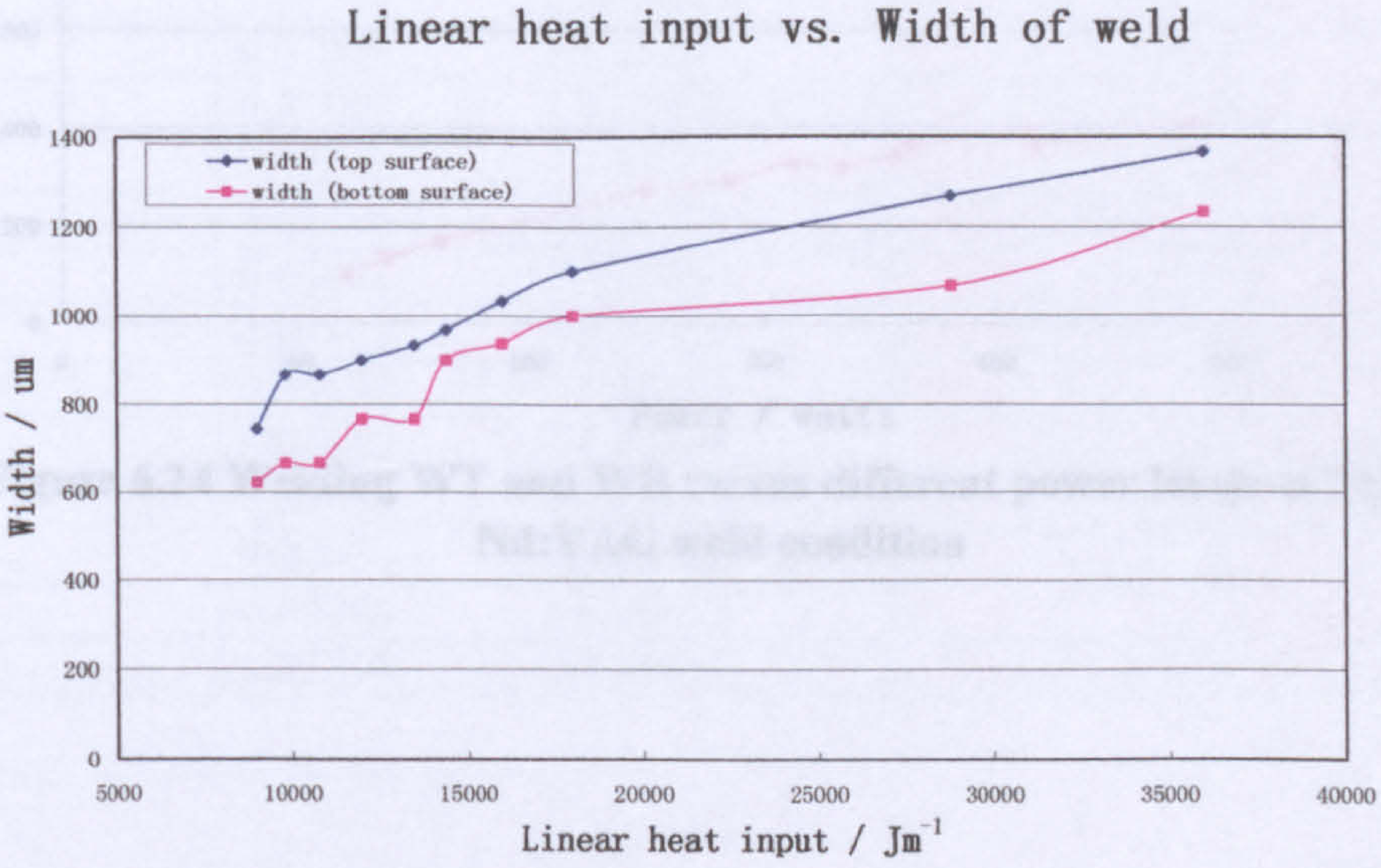

Figure 6.23 Trend of WT and WB vs. Linear heat input at CW-FLW condition

Figure 6.24 illustrates the width of top surface (WT) and width of bottom surface (WB) versus peak power in Pulsed Nd:YAG process. Once a pulse time was established, the increase in energy value corresponds to an increase in WT and WB value. On the other hand, once an energy per pulse was established, with an increase in the pulsed time, the width of weld decreases as there is lower peak power density which causes less melting.

The difference of control parameters between CW LBW and Pulsed LBW is that the melting efficiency is primarily determined by the power density in pulsed LBW. In pulsed LBW, travel speed can be decided after determination of optimum spot size, pulse energy and pulse duration. Travel speed is used to obtain the required pulse overlap. It is notable that the WB values are much less than the WT values in pulsed LBW (Figure 6.24) but very similar in FLW (Figure 6.23).

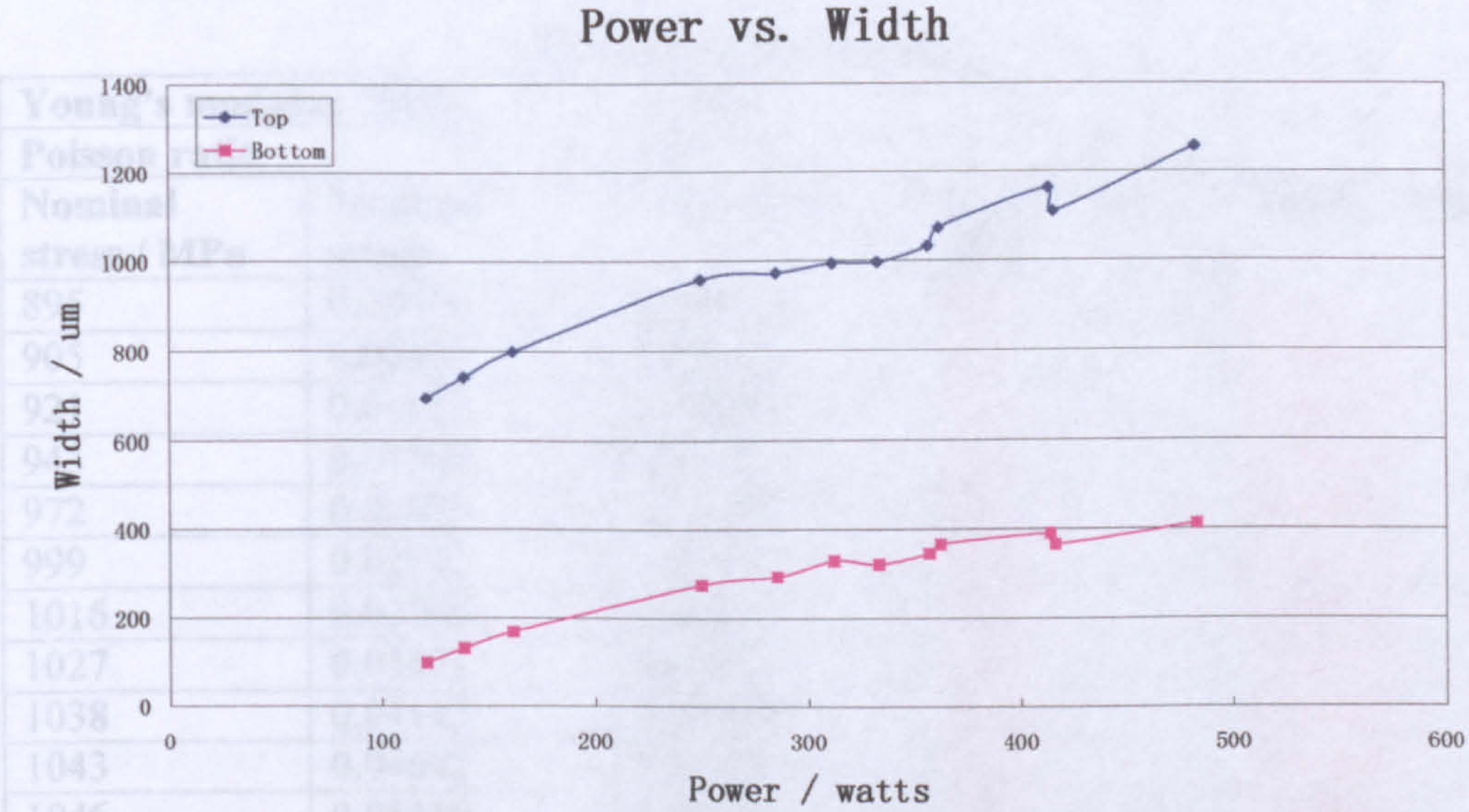

Figure 6.24 Welding WT and WB versus different power levels at Pulsed Nd:YAG weld condition

6.7 FEA of influence of distortion and cross-sectional shape on stress Level

Figure 6.11 has already shown that distortion existed in all types of laser welds, and that different cross-sectional weld shapes were generated by the different types of lasers. The aim of the FEA was to study the influence of weld geometry on the stress level for its various weld types.

6.7.1 Definition of material properties

Table 6.11 and Table 6.12 show the main mechanical properties of PM and simulated FZ (water quenched PM) from tensile yield test, which include Young's modulus, and the measured (nominal) stress-strain data and the true stress-true stain data which is used in the FE models. Data of Poisson ratio is adopted from handbook.

Table 6.11 PM properties

Young's modulus / MPa		111000		
Poisson ratio		0.342		
Nominal stress / MPa	**Nominal strain**	**True strain**	**True stress / MPa**	**Plastic strain**
895	0.00816	0.00813	902	0
905	0.00904	0.00900	913	0.00035
921	0.01013	0.01008	930	0.00114
943	0.01304	0.01296	955	0.00383
972	0.01805	0.01789	989	0.00863
999	0.02242	0.02217	1021	0.01281
1016	0.02769	0.02731	1044	0.01785
1027	0.03471	0.03412	1062	0.02452
1038	0.04143	0.04059	1081	0.03087
1043	0.04692	0.04585	1091	0.03603
1046	0.05110	0.04984	1099	0.03994
1049	0.05798	0.05636	1110	0.04636
1054	0.06622	0.06412	1124	0.05400
1053	0.07056	0.06818	1128	0.05803
1050	0.07214	0.06966	1126	0.05951

Table 6.12 Simulated FZ properties (PM water quenched from 1050°C)

Young's modulus / MPa		117580		
Poisson ratio		0.342		
Nominal stress / MPa	**Nominal strain**	**True strain**	**True stress / MPa**	**Plastic strain**
1017	0.0078	0.00777	1025	0
1031	0.0083	0.00827	1040	0.00047
1062	0.0091	0.00906	1072	0.00126
1110	0.0102	0.01015	1121	0.00235
1114	0.0215	0.02127	1138	0.01347
1116	0.0298	0.02936	1149	0.02157
1117	0.0345	0.03392	1156	0.02612

6.7.2 Calculation of ideal situation

In the FE model, the samples were deformed by application of a displacement, from which stresses were measured. The applied nominal tensile stress at 0.008 mm displacement was:

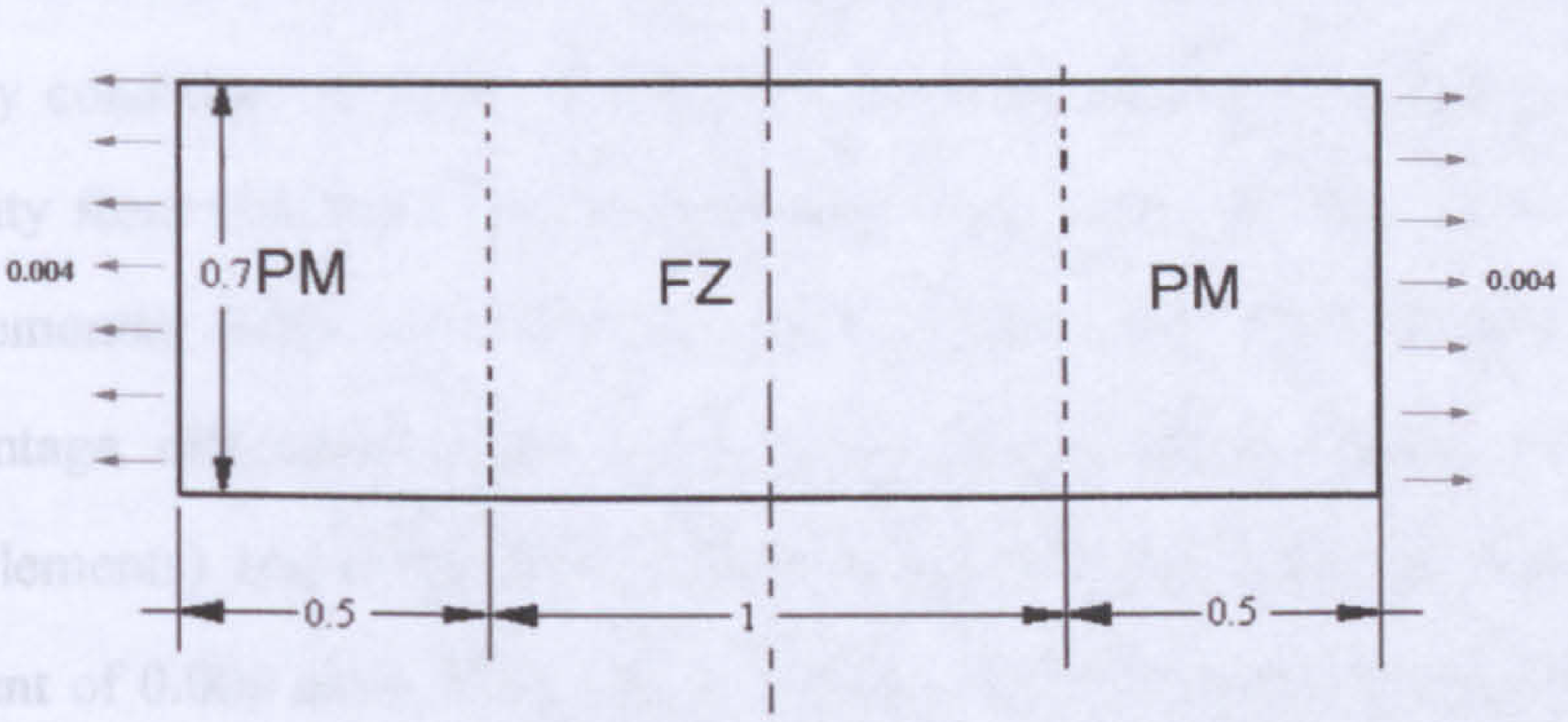

Figure 6.25 **No distortion situation**

$$\varepsilon = \frac{l_d}{l_o} = \frac{0.008}{2} = 0.004$$

$$\sigma = E \times \varepsilon = 111000 \times 0.004 = 444 MPa$$

where l_d is displacement, l_o is original length, E is Young's module, σ is stress.

When a displacement (0.004 mm for both sides) was selected and PM properties were assumed, the stress equals to 444 MPa.

$$\sigma = E \times \varepsilon = 117580 \times 0.004 = 470.32 MPa$$

When a displacement (0.004 mm for both sides) was selected and FZ properties are assumed, the stress equals to 470.32 MPa. These simple calculations will be compared to the FE results

6.7.3 Convergence for mesh density

Meshing means the selection of right type and size of elements. The common way to verify the element size is to run one test analysis with smaller size of finite elements. As the smaller the element size is, the closer the FE results tend to the exact results. It will tend to be convergent at the end. From such an analysis, test analysis mesh type selected was finally decide as 8-node biquadratic (CPS8) 0.003 mm, for 155,411 elements. The mesh technique is quad-dominant structural style. The element size was defined as 0.003 mm. Figure 6.26 shows the stress levels at node coordinate 0.5, 0.7, at boundary condition of 0.006, 0.008, 0.01 mm displacement, with increase of the mesh density from 0.05 mm (588 elements), 0.01 mm (14,140 elements), 0.005 mm (56,280 elements), 0.003 mm (155,411 elements) to 0.002 mm (349,650 elements). The percentage differences between the Von Mises stress values of 0.003 mm (155,411 elements) and 0.002 mm (349,650 elements) are respectively 0.5% (for a displacement of 0.006 mm), 0.3% (for a displacement of 0.008 mm) and 0.5% (for a displacement of 0.01 mm).

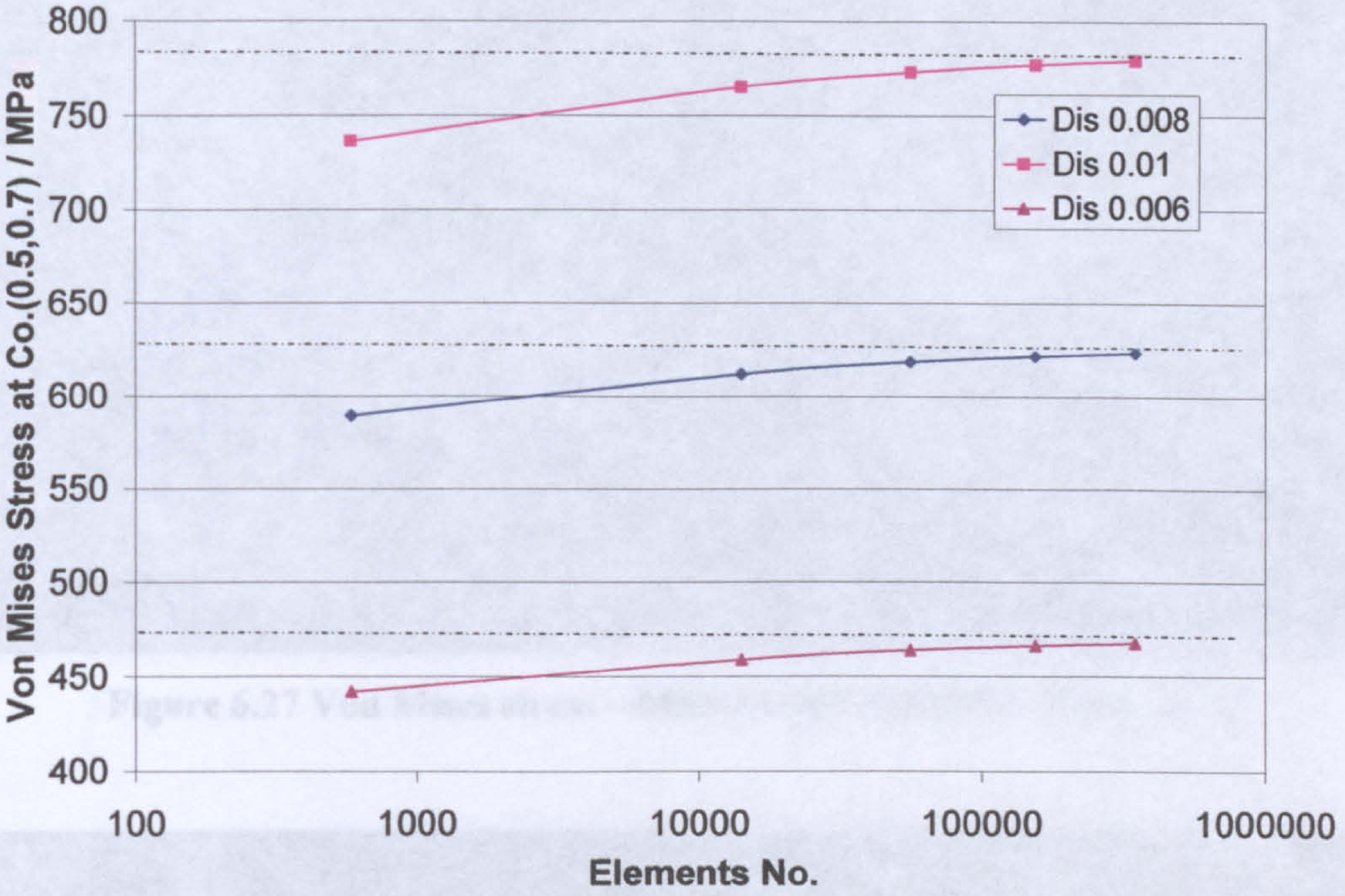

Figure 6.26 convergence with mesh density at coordinate (0.5, 0.7) for d value (misalignment level) equal to 0.05 mm at three displacement boundary conditions (0.006, 0.008 and 0.01 mm)

6.7.4 FEA results with material properties definition

Figure 6.27 shows an FE model defined as PM properties, misalignment level (Mis) is 0μm, mesh density (Md) is 0.003mm, and boundary displacement condition (Dis) is 0.008mm. FEA shows Von Mises stress equal to 444MPa which is as same as calculation results. When define the material with FZ properties (Figure 6.28), FEA shows Von Mises stress equal to 470.3MPa which again is the same as the theoretical result. When define the material with both FZ and PM properties as shown in Figure 6.29, the maximum stress exists at the boundary between the FZ and PM, and is 461.5MPa.

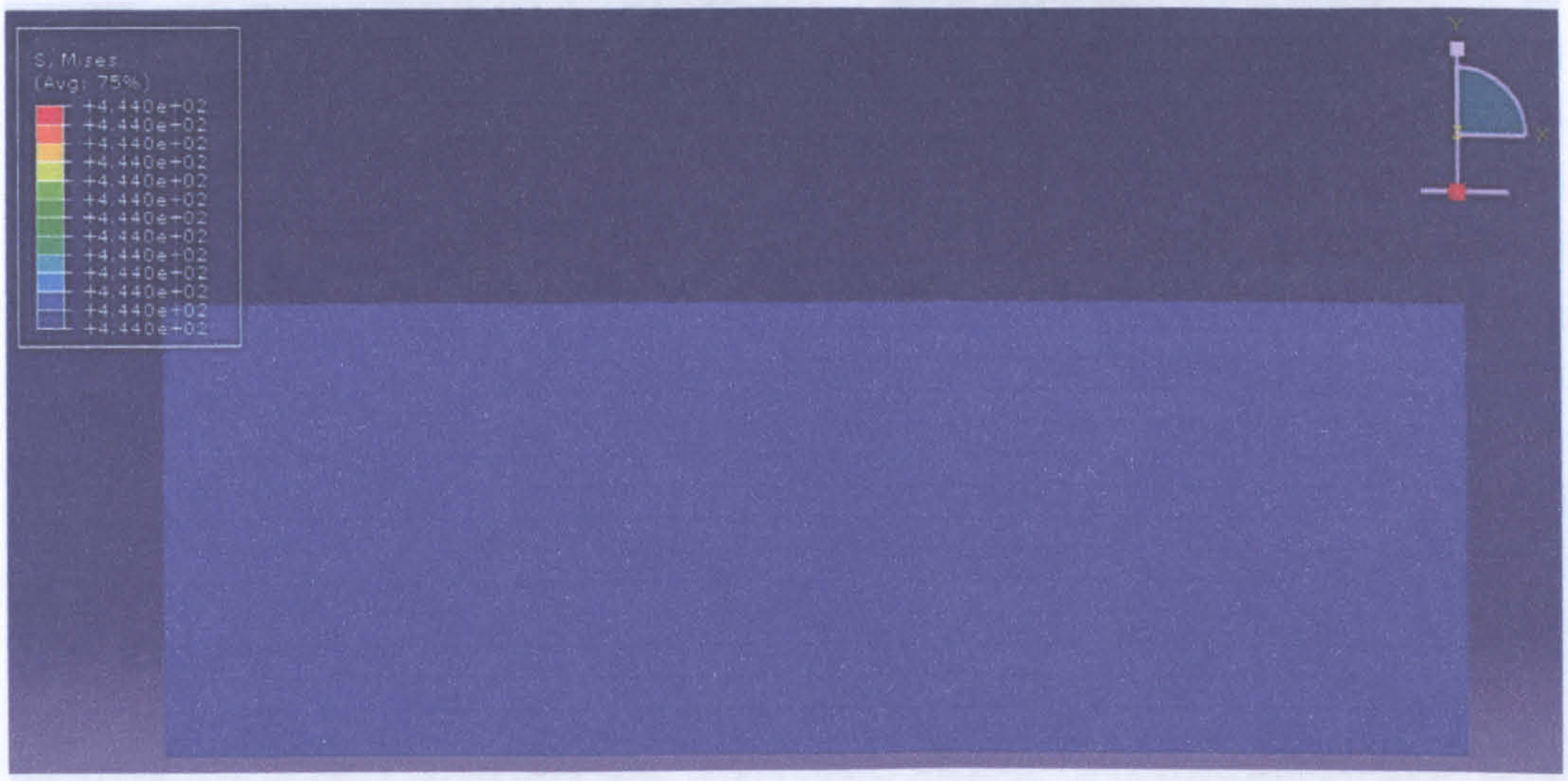

Figure 6.27 Von Mises stress – Mis0-Md0003-Dis0008-PMproperty

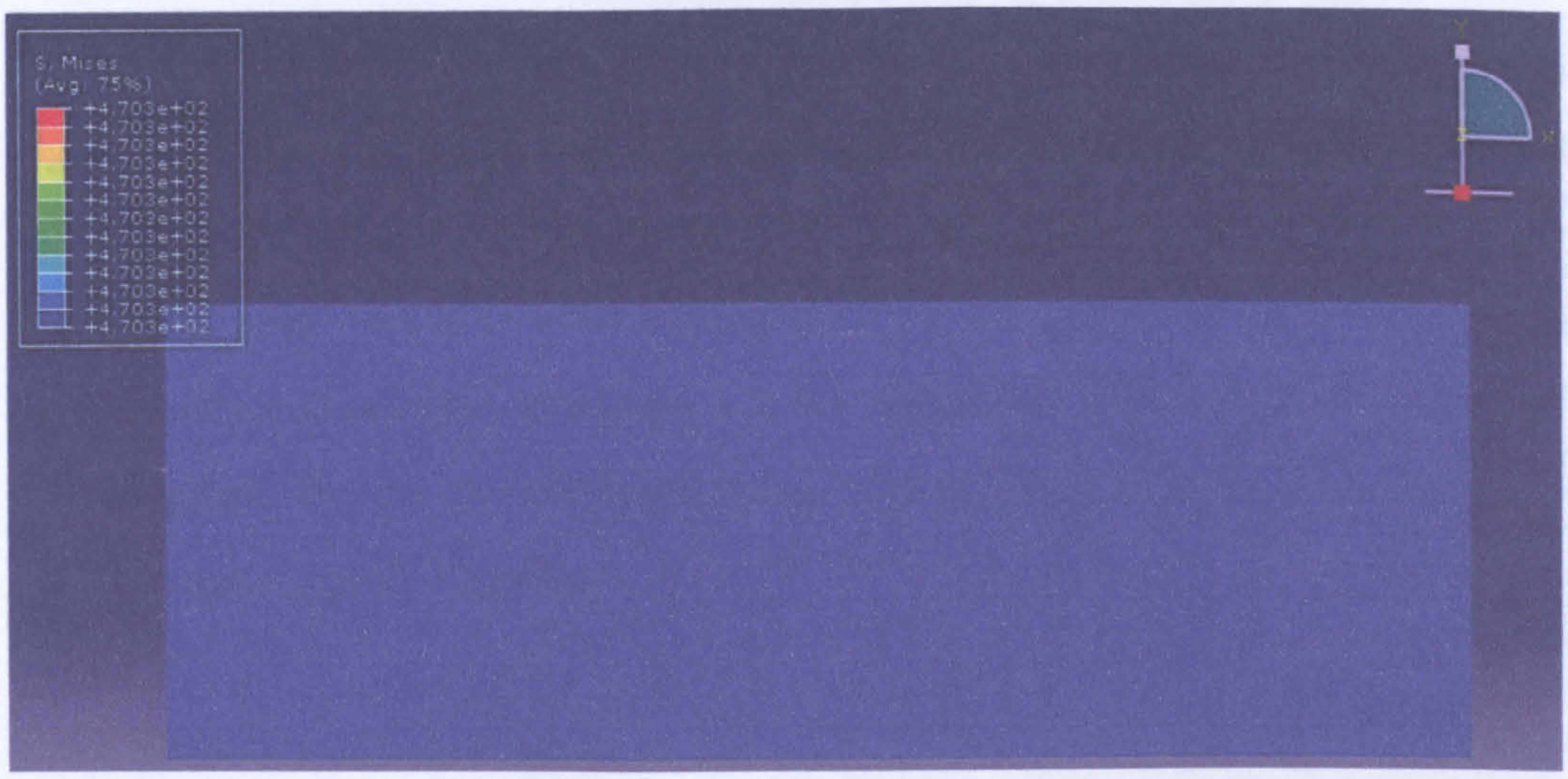

Figure 6.28 Von Mises stress – Mis0-Md0003-Dis0008-FZproperty

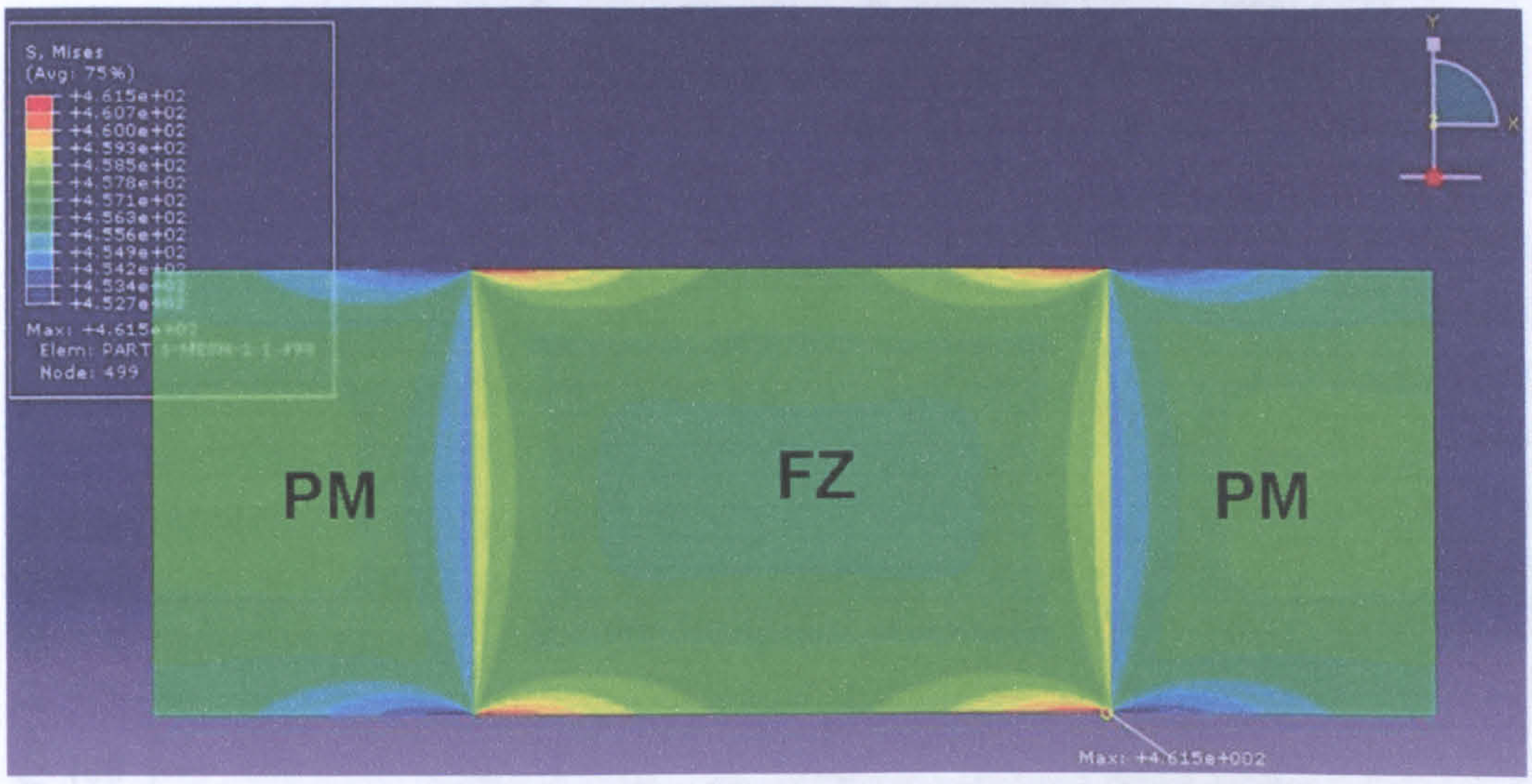

Figure 6.29 Von Mises stress – Mis0-Md0003-Dis0008-PMFZproperty

6.7.5 FEA results with increase of misalignment level d value

Figure 6.30 shows results of maximum stress point in the model with increase in the d value (misalignment value – see Figure 5.12) to a maximum value of 100 μm (using PM and FZ properties as indicated in Figure 5.12). The maximum stress appeared at the boundary corner, node coordinate 1.5, 0.1 (Figure 6.31). When the misalignment level reached 100 μm, the maximum stress level is nearly twice as large as that in ideal (non-misaligned) situation.

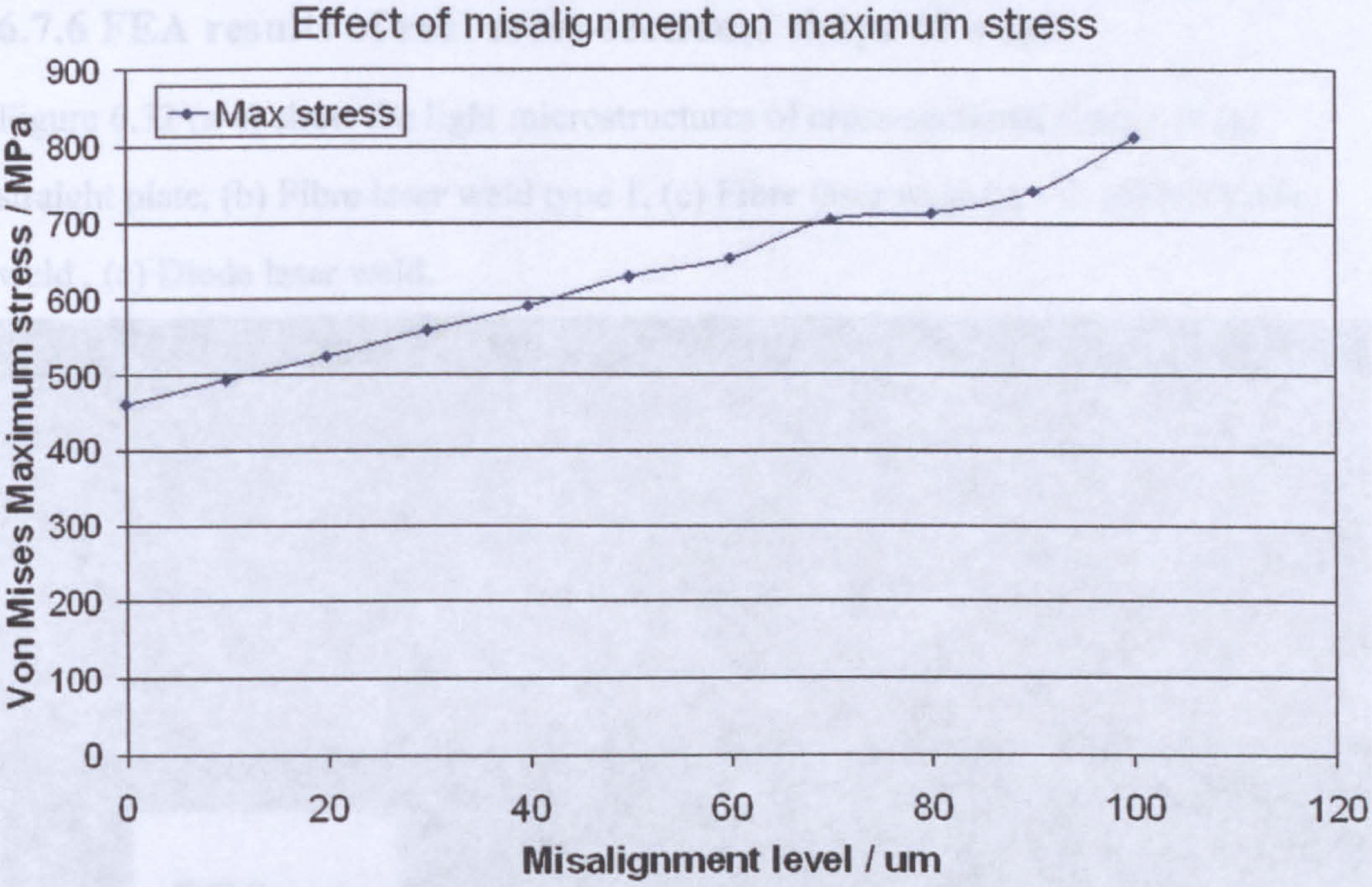

Figure 6.30 Maximum Von Mises stress versus misalignment value for a displacement of 0.008 mm using a model as defined in Figure 5.12

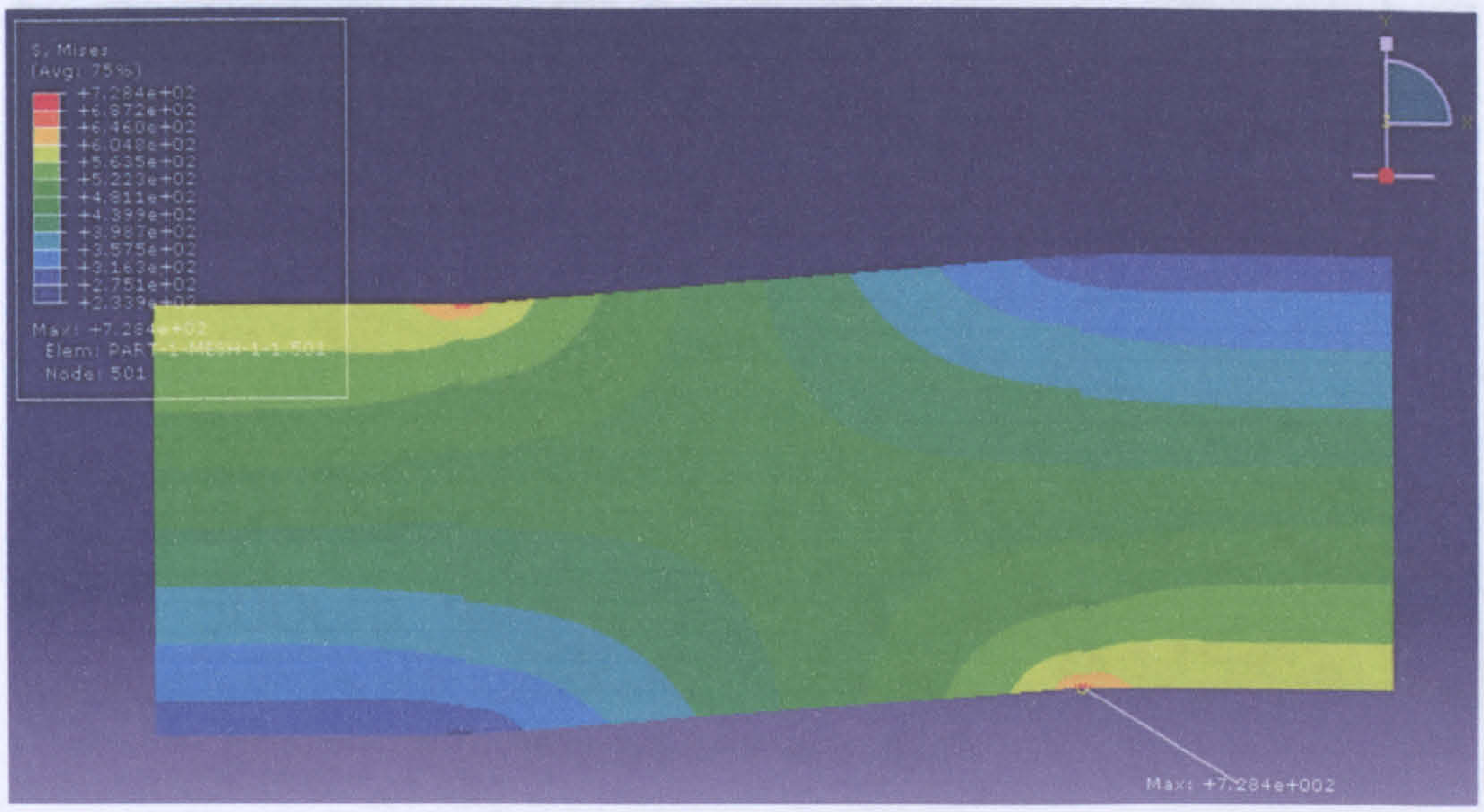

Figure 6.31 Maximum Von Mises stress in FEM: Mis80-md0003-dis0008

6.7.6 FEA results of real cross-sectional shape of welds

Figure 6.32 (a-e) show the light microstructures of cross-sectional shapes of (a) straight plate, (b) Fibre laser weld type 1, (c) Fibre laser weld type 2, (d) Nd:YAG weld , (e) Diode laser weld.

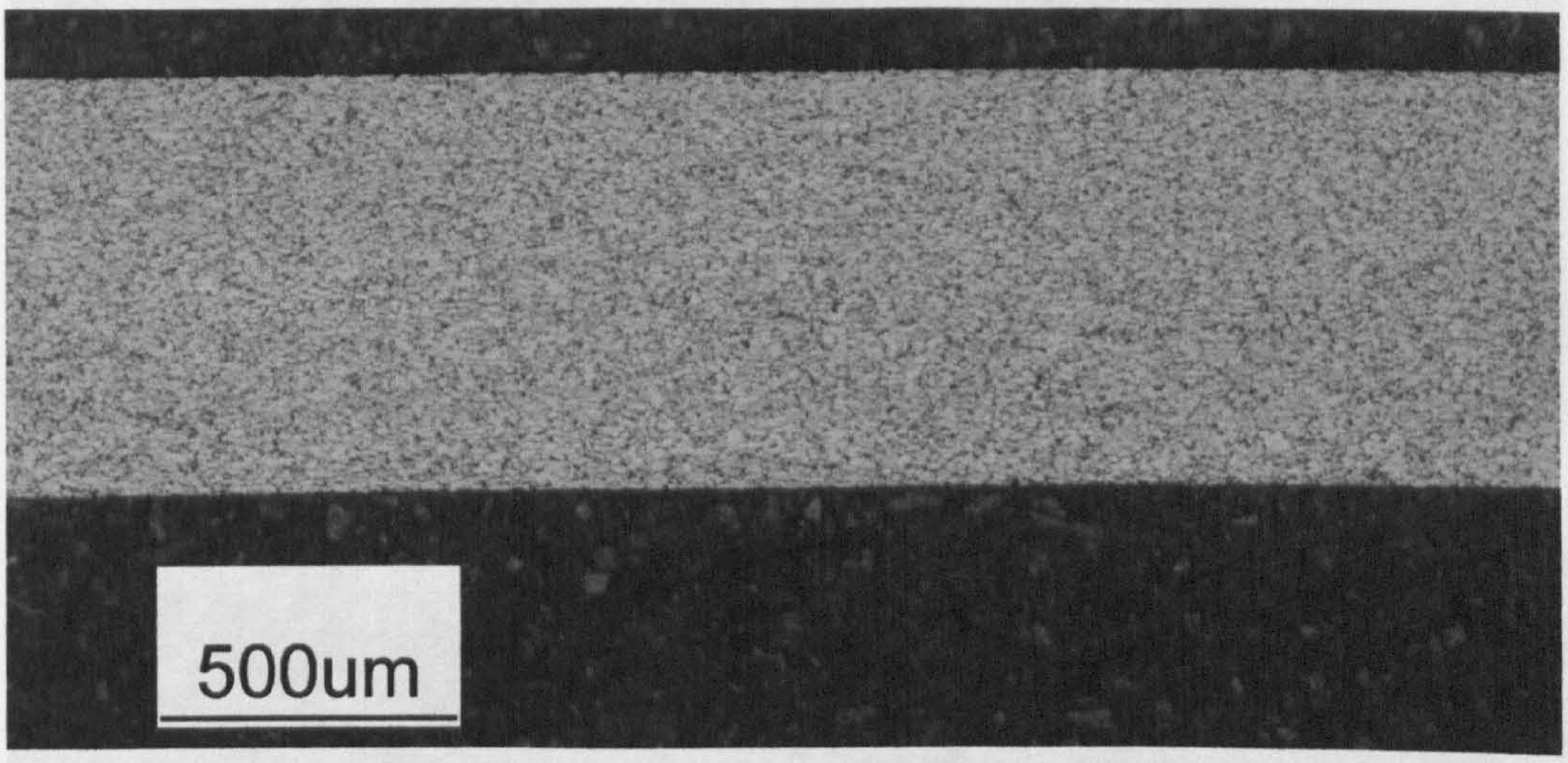

(a) Flat PM plate

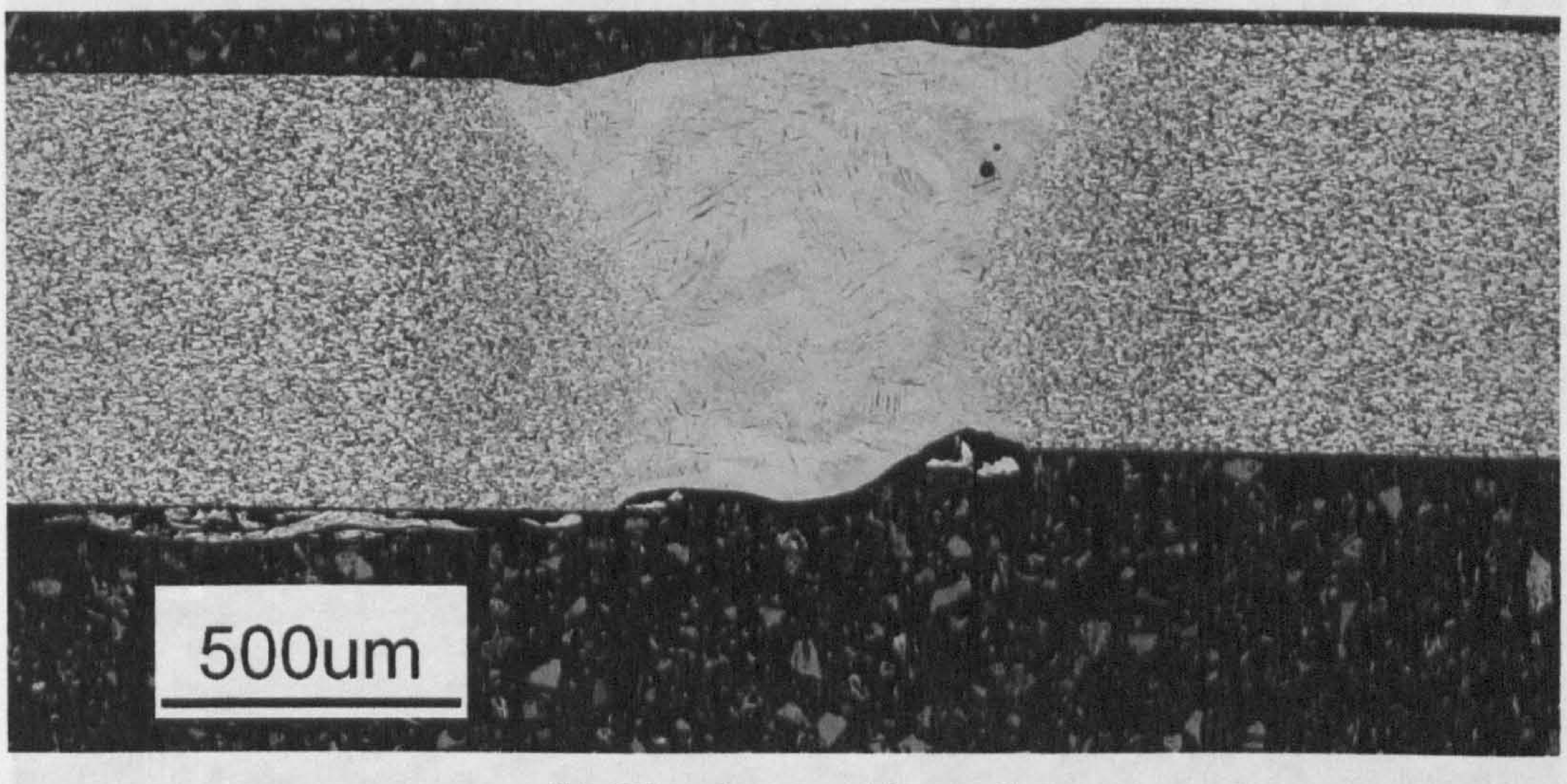

(b) Fibre laser weld type 1

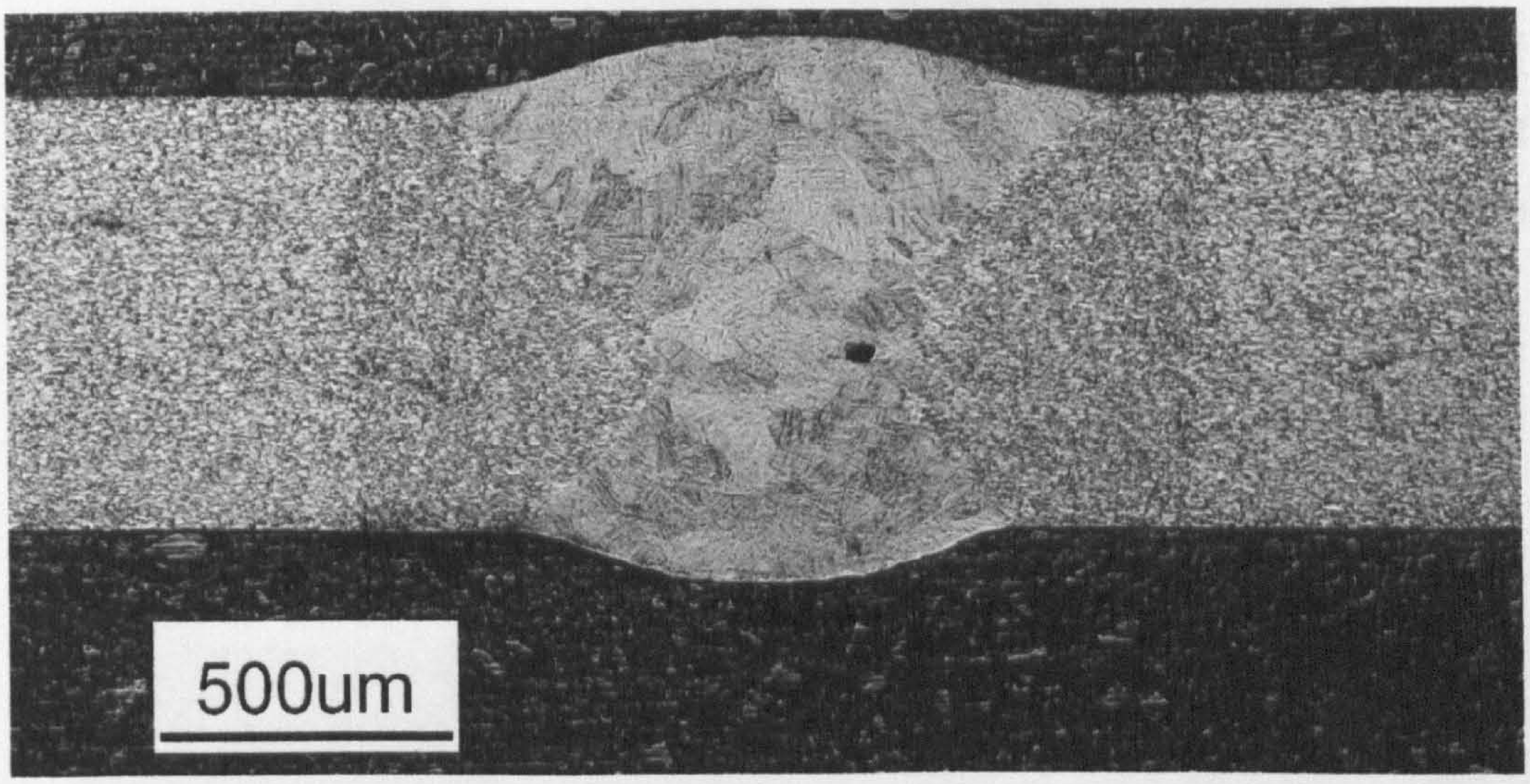

(c) Fibre laser weld type 2

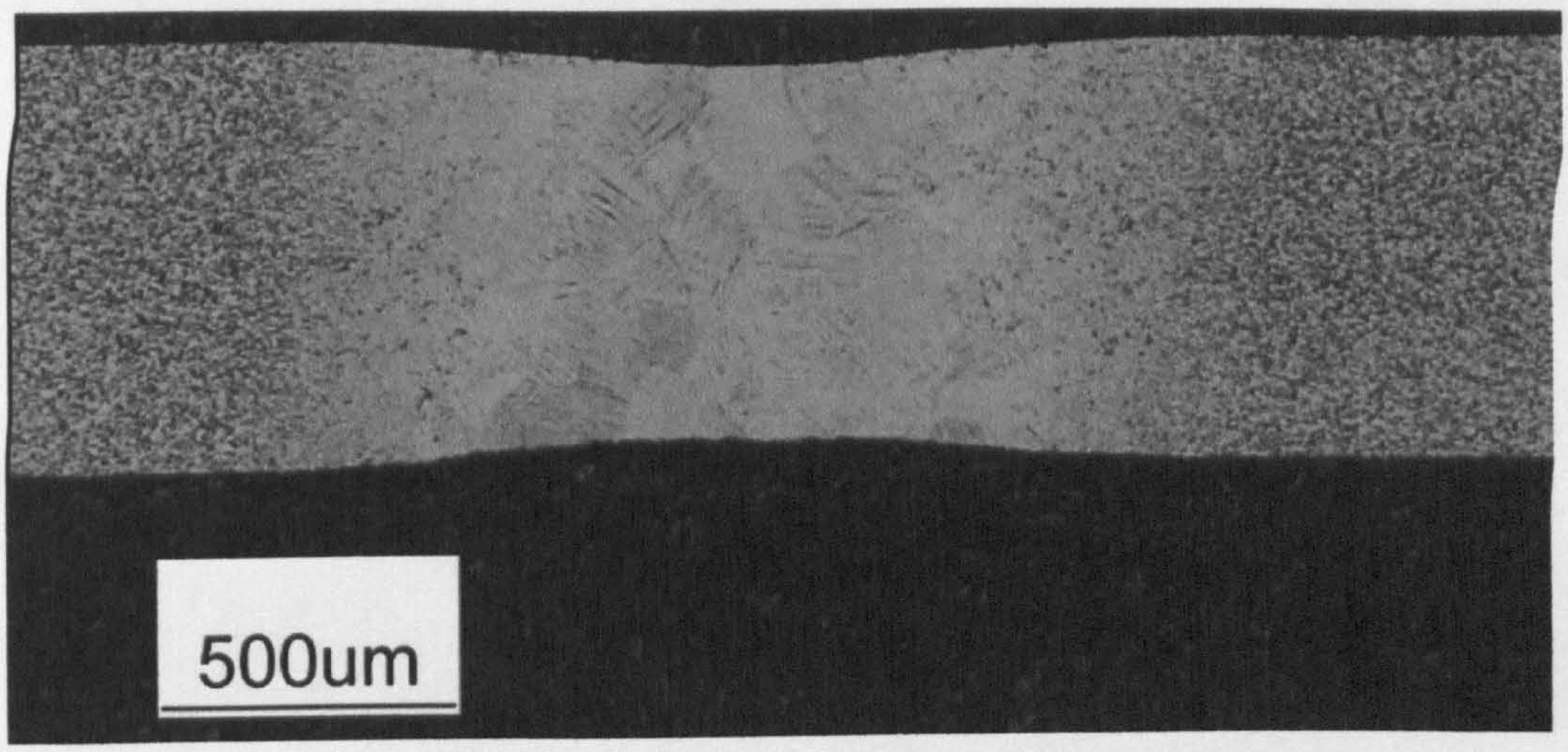

(d) Nd:YAG weld

(e) Diode weld

Figure 6.32 Light microstructures of weld cross-sectional shapes

Figure 6.33 shows the procedure of one example to transfer the cross-sectional shape image into a readable surface file by Abaqus using image treatment softwares Paint.Net, IMG2CAD and Mastercam Mill v9.0. All the FE Models of real cross-sectional shapes are scanned into JPEG line (Figure 6.33b) by paint.net; IMG2CAD is used to convert the image file to be readable DXF file by Mastercam Mill v9.0; then Mastercam Mill v9.0 creates surface file and convert it to be readable IGS file (Figure 6.33c) by Abaqus.

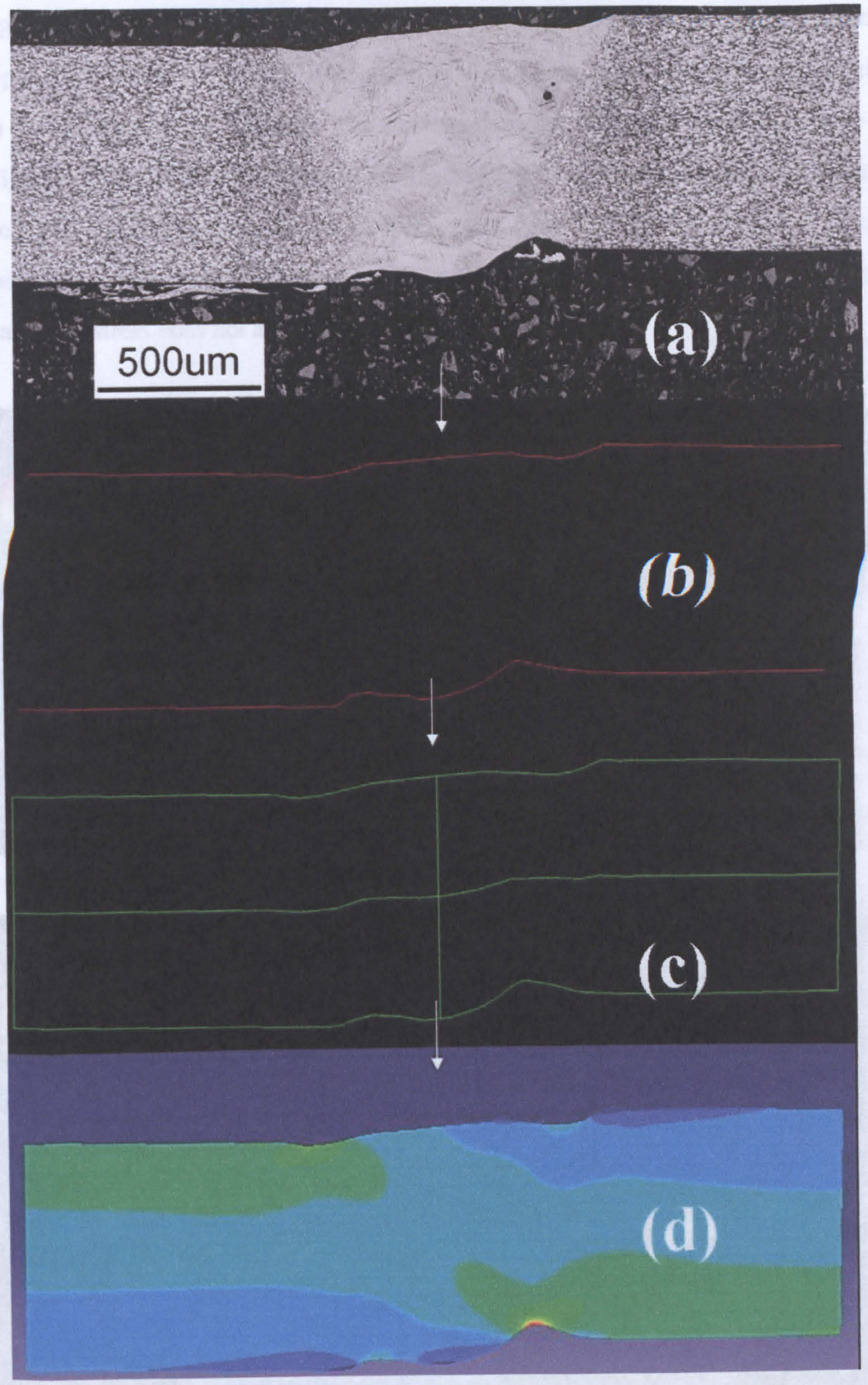

Figure 6.33 a) Light microstructure of cross-sectional shape; b) Image of JPEG line; c) Image of IGS surface; d) FE model

Figure 6.34 (a-e) shows the FEA results of real cross-sectional shape welds when the applied nominal stress is 333MPa. As can be seen, all the maximum stress points exist on the surface of the material. The maximum stress points of Fibre laser type 1 (Figure 6.25b) and Nd:YAG laser (Figure 6.25d) weld exist at the round corner of FZ area, the maximum stress points of Fibre laser type 2 (Figure 6.25c) exist at the connection point between FZ and HAZ. In the diode laser weld (Figure 6.25e), the maximum stress does not appear at FZ or HAZ.

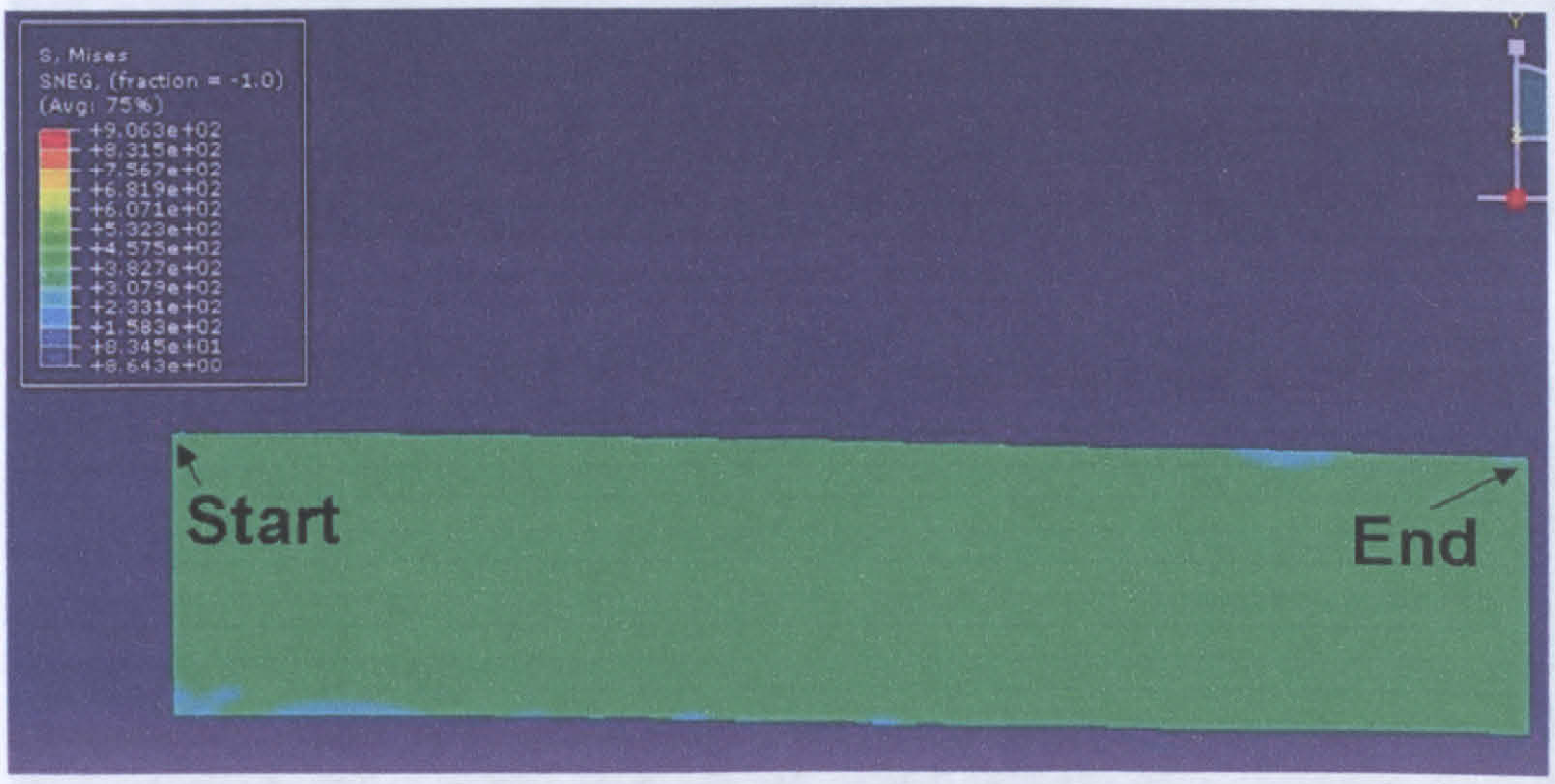

(a) Flat PM plate

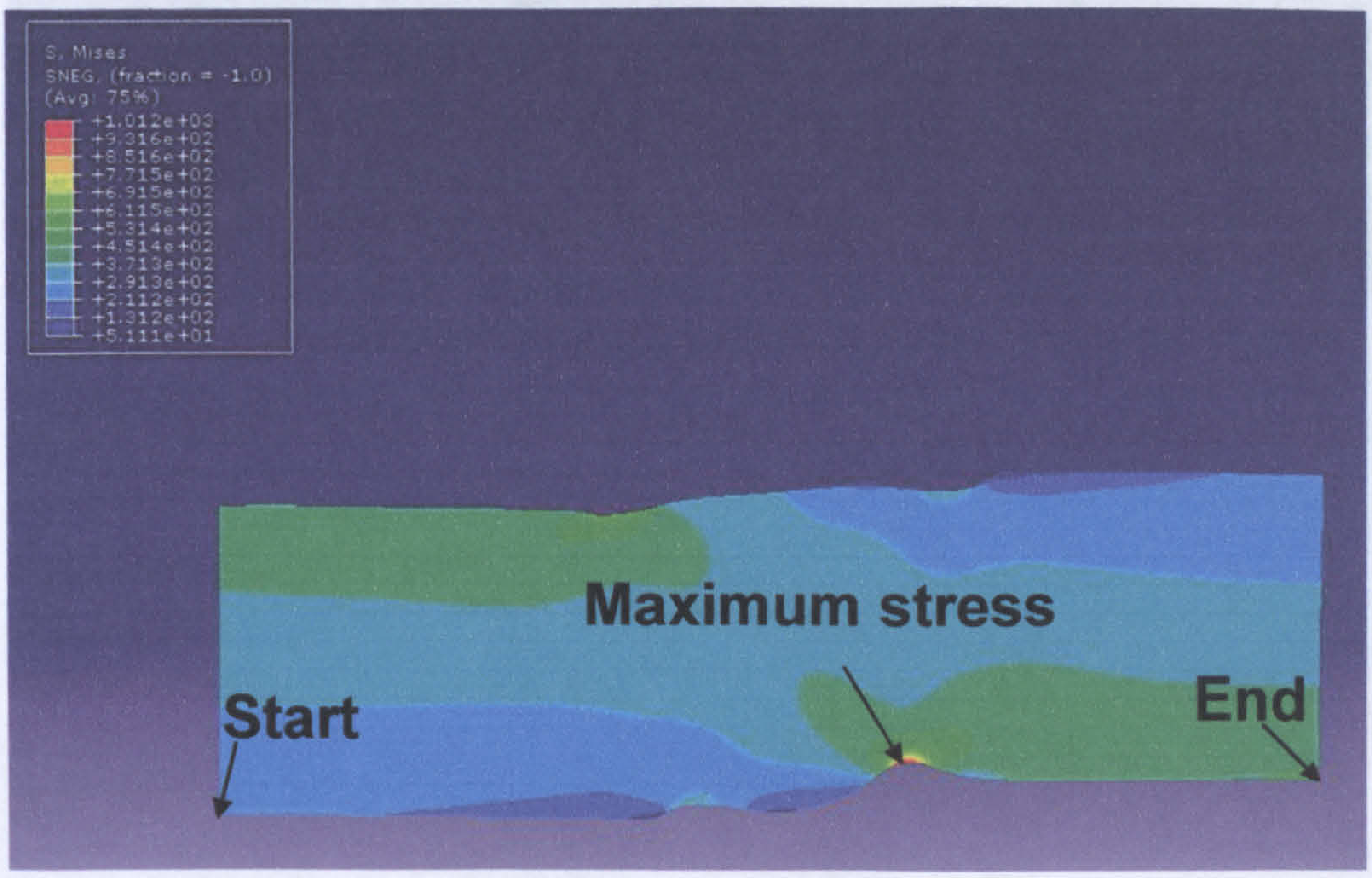

(b) Fibre laser weld type 1

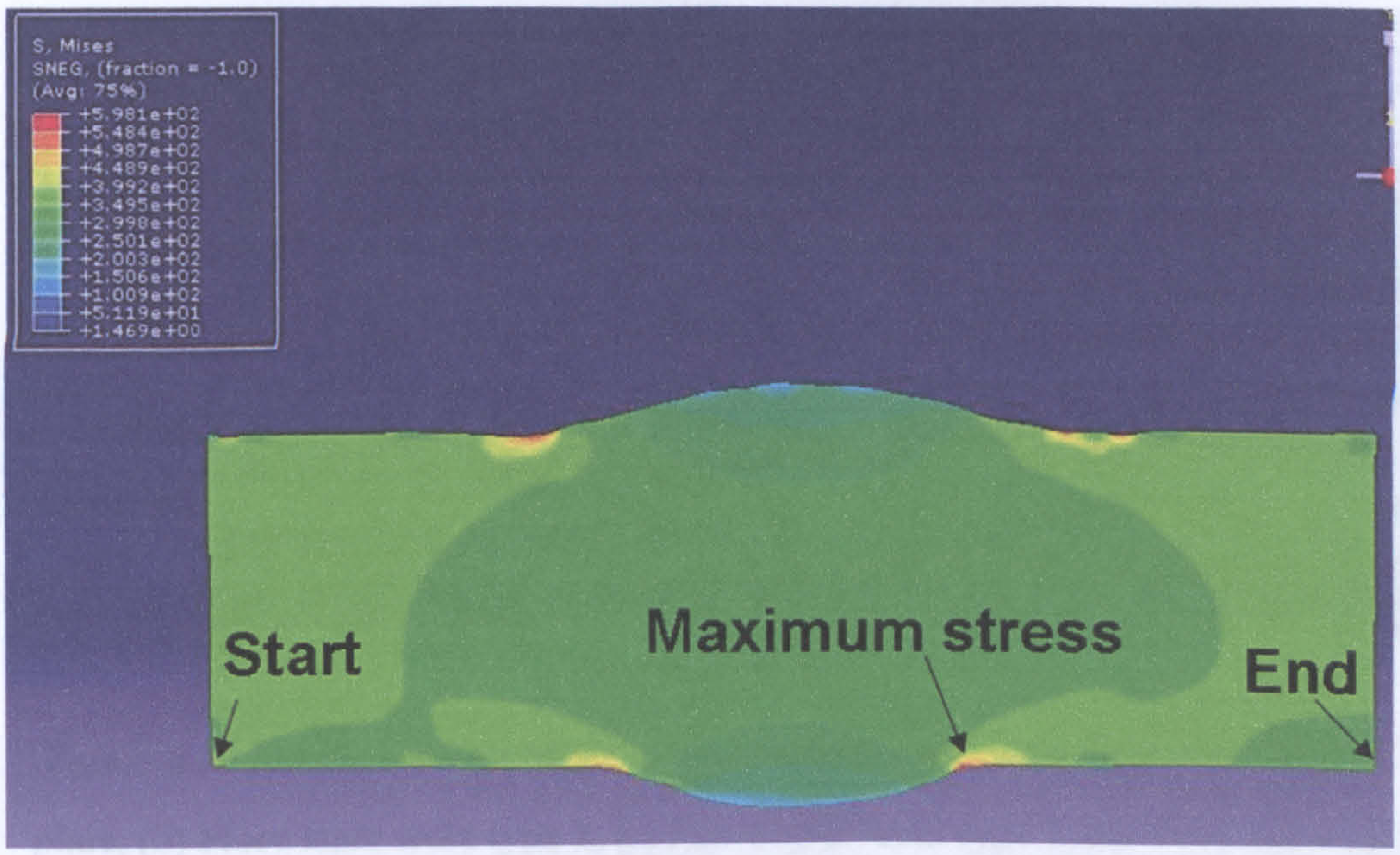

(c) Fibre laser weld type 2

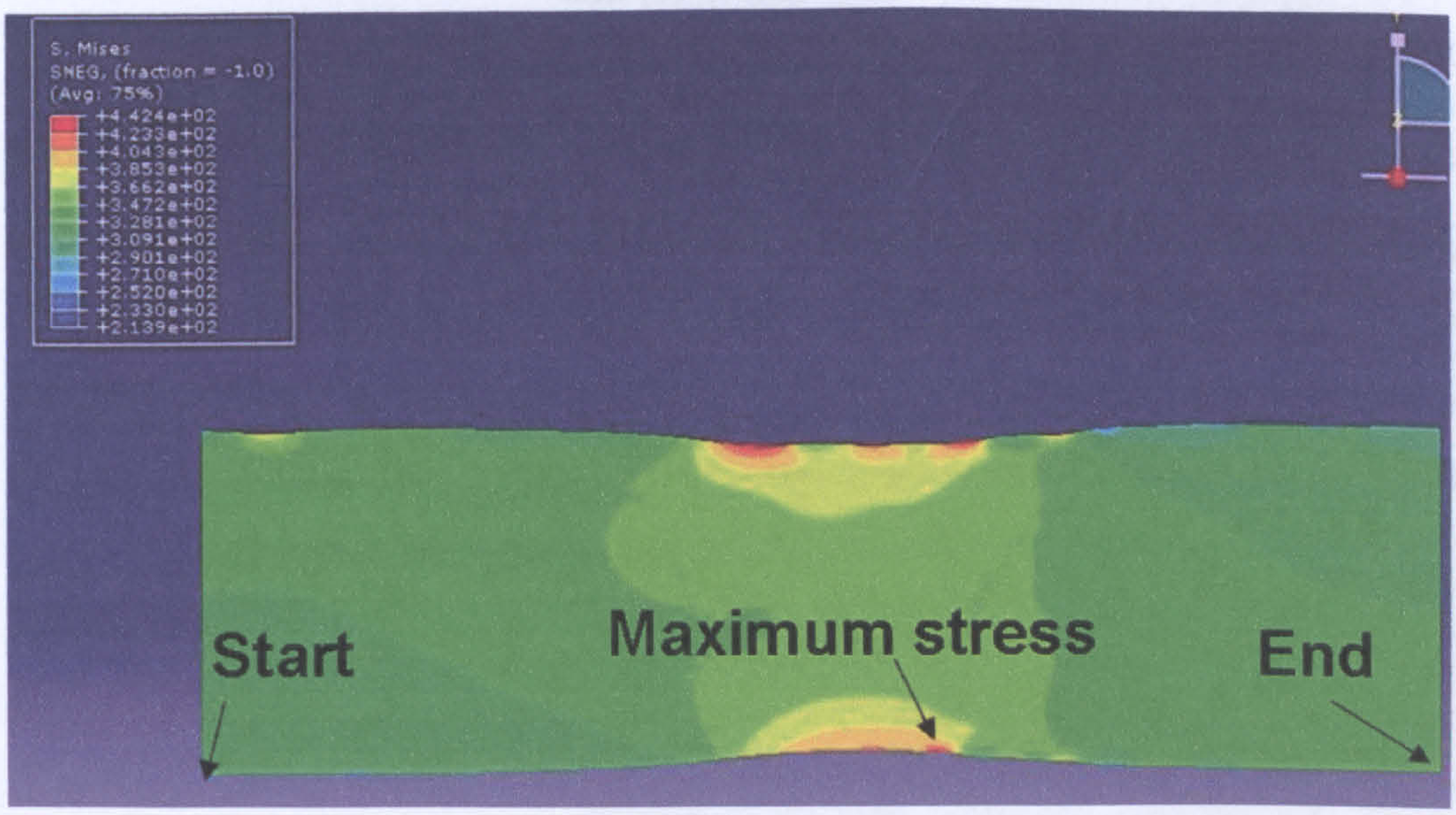

(d) Nd:YAG weld

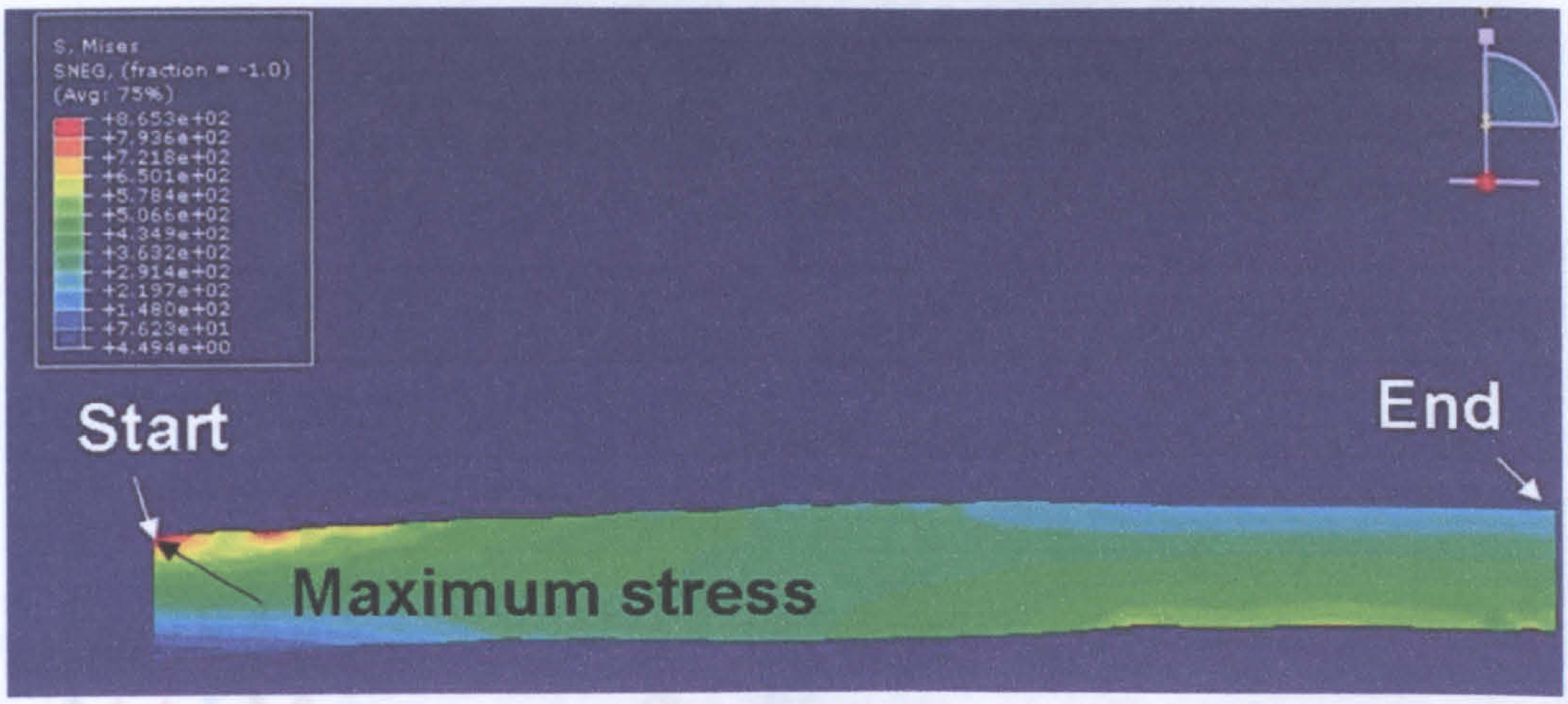

(e) Diode weld

Figure 6.34 Maximum Von Mises stress points shown in the FEA (a) Flat PM plate, (b) Fibre laser weld type 1, (c) Fibre laser weld type 2, (d) Nd:YAG weld and (e) Diode weld

In order to under stand where the weakest point is, Von Mises stress data at each node along the maximum stress located surface were collected, as shown in Figure 6.34 (a-e), from the start point to the end point. From results shown in Figure 6.35, all the maximum stress values have exceeded not only the PM limitation (pink square) but the also FZ limitation (red triangle). In that case, no matter where the maximum stress point exists, it could be the failure point.

.

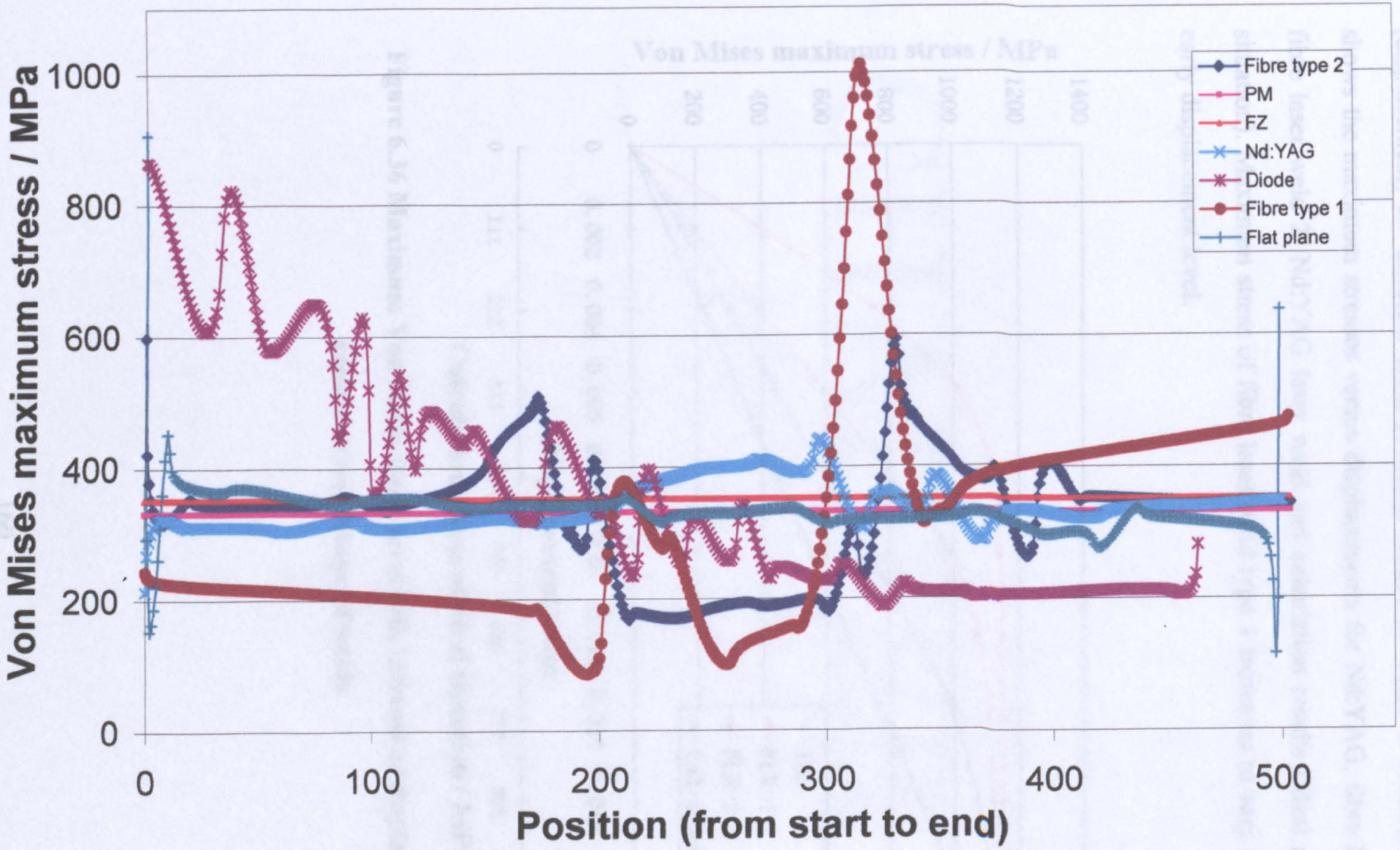

Figure 6.35 Von Mises stress data at node along the maximum stress located surface

As shown above, different types of cross-sectional shape can cause very high maximum stresses. In tensile yield test and fatigue test, the stress level can be much higher than the nominal stress level. In order to understand and modify the stress level in S-N curve, the maximum stress level with increase of boundary condition (displacement) for different cross-sectional shapes of welds is studied. Figure 6.36 shows the maximum stresses versus displacements for Nd:YAG, fibre laser weld 1, fibre laser weld 2, Nd:YAG laser weld and calculation results (ideal no distortion situation). Maximum stress of fibre laser weld type 1 increases to very high level at early displacement level.

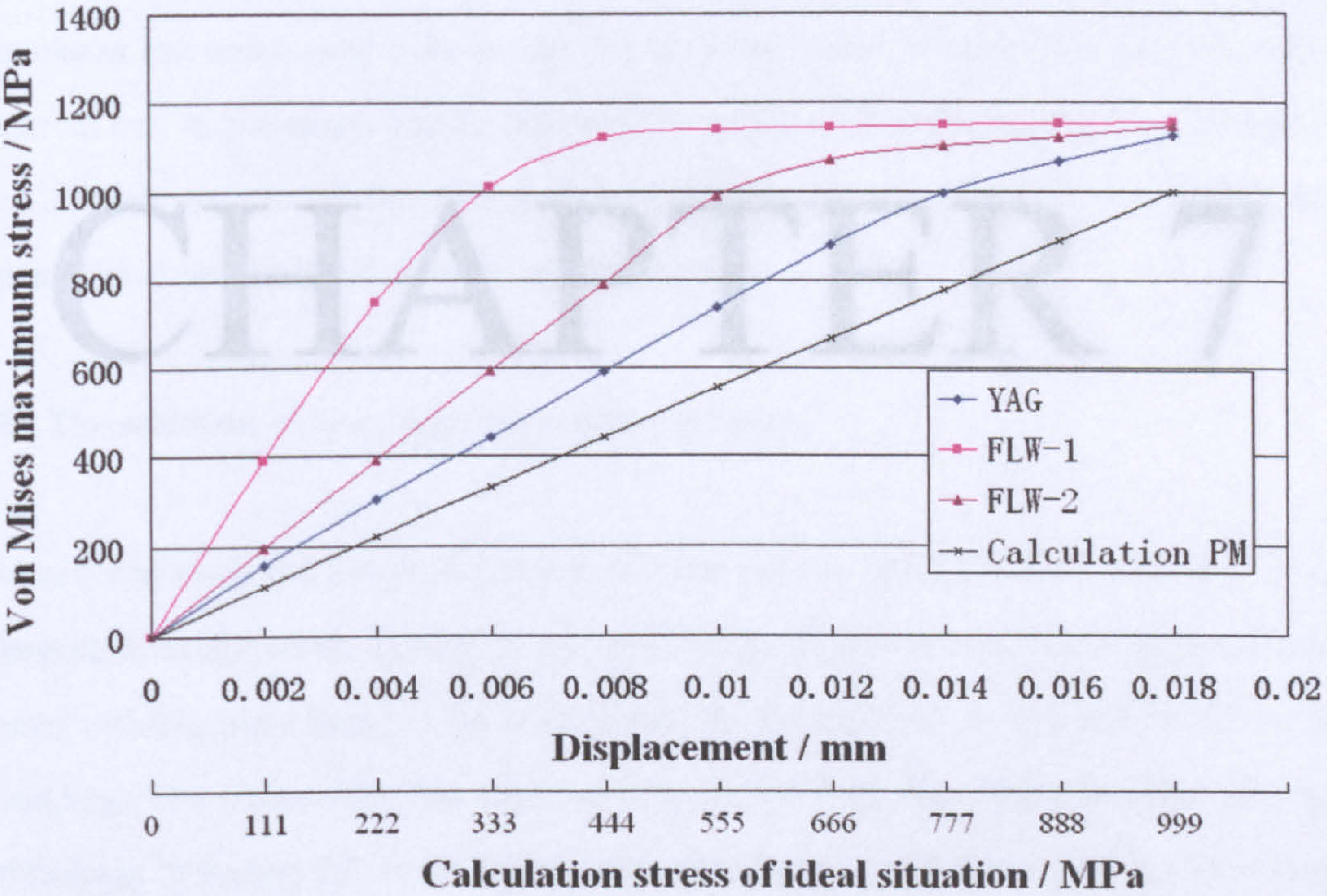

Figure 6.36 Maximum Von Mises stress level with increase of displacement for cross-sectional shape of welds

CHAPTER 7

Chapter 7 Discussion

This Chapter is divided into four major themes of discussion as follows, based on the experimental results and FEA results in chapter 6:

I. Microstructure and mechanical properties of laser beam welded Ti6Al4V

Microstructures in Ti6Al4V alloy include equaixed, lamellar, bimodal, Widmanstätten and martensite. The mechanical properties are significantly affected by these structures. The structure in the fusion zone of laser beam welded Ti6Al4V is primarily martensite which has the lowest ductility. In this work, heat treatment, hardness test and tensile tests on the PM and laser beam welded Ti6Al4V have been carried out. A discussion will be conducted in section 7.1 regarding the transformation of microstructures of the PM and laser beam welded Ti6Al4V, and effect on mechanical properties of these microstructures.

II. The selection of laser type for welding process

In order to study the fatigue behaviour of laser beam welded Ti6Al4V thin sheet, it is important to notice the quality of the weld itself. The fibre laser welding and diode laser welding were found to be less suitable for the application than pulsed Nd:YAG welding. The reasons for this (such as defects and unpredictable geometies) will be discussed in section 7.2. In addition, the porosity generated during laser beam welding was also discussed in terms of control by the laser welding parameters.

III. Fatigue behaviour of laser beam welded Ti6Al4V

A fatigue fracture life is the combination of fatigue initiation and fatigue propagation. The fatigue fracture lives of the laser welded Ti6Al4V were significantly affected by the structure, phase content and grain size. Section 7.3 focuses on understanding the

S-N curve of the laser welded Ti6Al4V thin sheet and the influence of those factors mentioned above.

IV. The effect of geometries on the stress level for the various laser welds

The details of the geometries of the welds themselves were variable depending on the types of lasers. FEA can be used to analyse and understand these complex geometries. The challenge of FEA is to understand how close the FEA results compare with the real results. In section 7.4, a methodology of using FEA for analysis of the geometry the laser welded Ti6Al4V is discussed. In addition, a further understanding and modification of results from the tensile and fatigue tests were also discussed. The significance of the geometry in controlling mechanical failure of the welds was outlined.

7.1 Microstructure and mechanical properties of parent material and laser beam welded Ti6Al4V

7.1.1 Feature of Ti6Al4V parent materials

The microstructures of Ti6Al4V parent materials (figure 7.1) are strongly dependent upon production procedure and following heat treatments. The parent materials used by Pinke et al. were defined as fine lamellar structure [1] which exhibits lower strength and lower ductility than that observed for an equiaxed structure (Table 3.5). The lower strength level of the lamellar structure often results in low fatigue crack initiation resistance. However, the lamellar structure has high fatigue crack propagation resistance as the propagating cracks are readily deflected along differently oriented lamella packets [2]. It is important to notice that this so-called lamellar structure (Figure 7.1a) may in fact be a Widmanstätten structure. It will be discussed in section 7.1.2. The parent materials used by Jovanović et al. were coarse lamellar structures with massive β phase boundary. It is difficult to judge the strength of Jovanović et al.'s PM. Although a coarse grain size structure generally shows lower strength and lower ductility than that of fine grain size structures (Table 3.5), massive β phase boundary can increase the strength level. The parent materials used in this project are fine equiaxed structures, which exhibit higher strength and higher ductility than lamellar structures. The microstructures transformed from these three types of PMs following heat treatment were significantly different (Figure 3.4, Figure 3.5, Figure 3.6 and Figure 6.4).

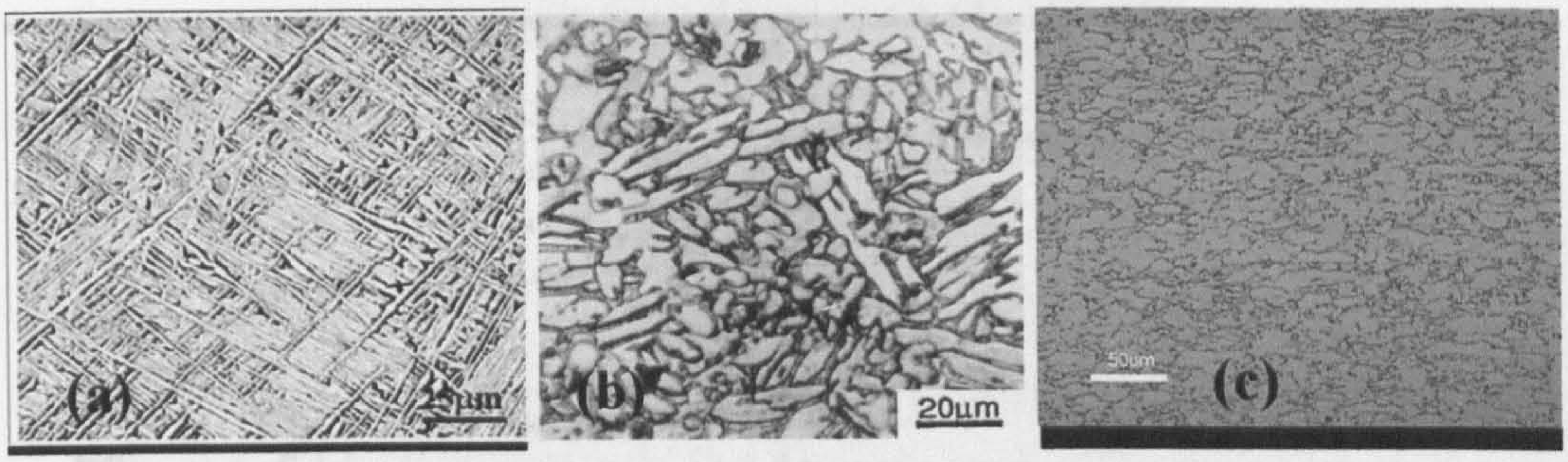

Figure 7.1 The parent materials of (a) Pinke et al.'s precision cast Ti6Al4V[1] (b) Jovanović et al.'s investment cast Ti6Al4V[3] (c) author's as-received Ti6Al4V

Figure 6.1 and EDX results show the vanadium content tends to be higher in β phase. The combination of titanium and vanadium promotes the β phase. At the same time, as the Ti-Al binary phase diagram shows (Figure 7.2), Ti6Al transforms into β phase Ti (A2) at temperatures above around 1000°C. The beta transus temperature for Ti6Al4V is 980°C which is very similar to the transus temperature of β phase Ti to α phase Ti in Ti-Al binary phase diagram. Hence, above beta transus temperature, both the combination of titanium and vanadium and the combination of titanium and aluminium exhibit β phase. Once the temperature goes below the transus temperature, the combination of titanium and aluminium start to transform into α phase Ti which forms α phase in Ti6Al4V alloy. The combination of titanium and vanadium may become the β phase boundary surrounding α phase.

All the structures of PM above show β phase boundary surrounding α phase nucleus. The β phase exhibits high strength but low ductility; on the other hand, the α phase shows high ductility but low strength. This combination results in the desirable mechanical properties of Ti6Al4V.

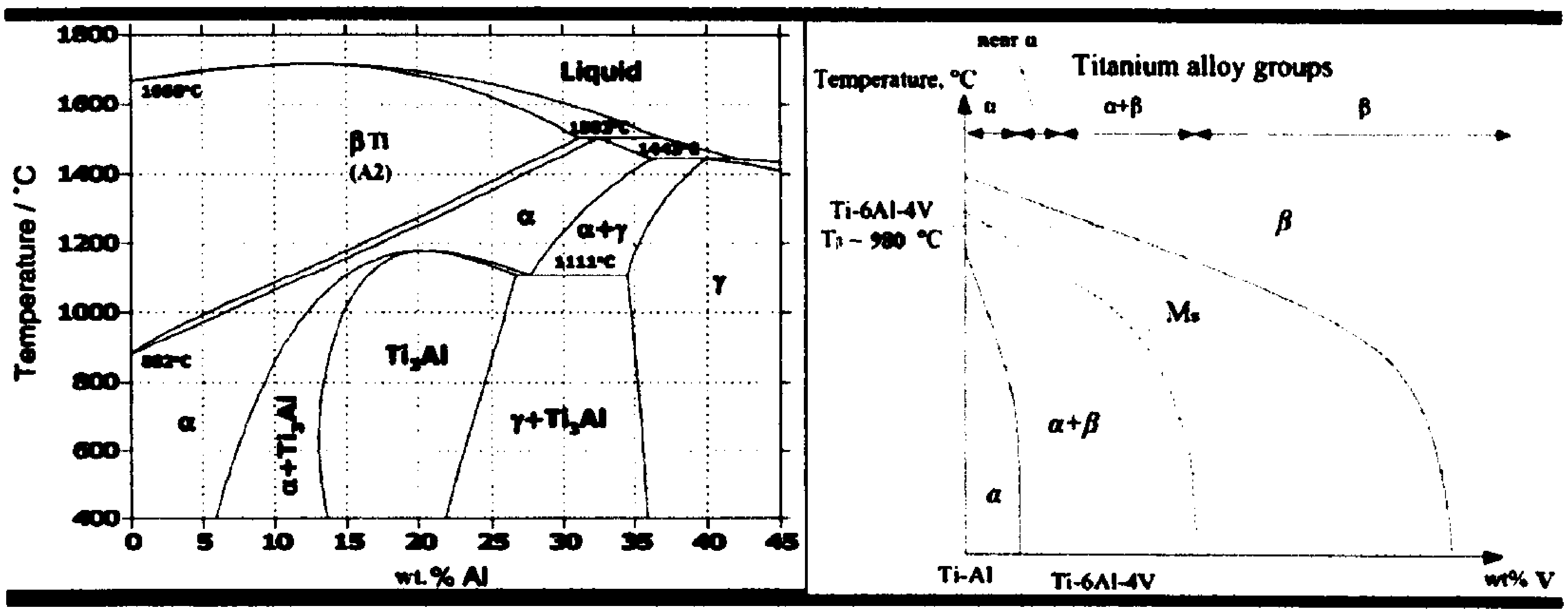

(a) (b)

Figure 7.2 (a) Ti-Al binary phase diagrams [4] (b) Ti6Al-V Schematic ternary phase equilibrium diagram [5]

7.1.2 The selection of heat treatment methods for laser beam welded Ti6Al4V

The different microstructures are generated by heat treatment of the PM. Generally, most of the commercially used Ti6Al4V has been heat treated via a complex sequence of solution heat treatment, deformation, aging and annealing for stress relief, recrystallization and globularization. Temperatures of 650-850°C are normally used for these. As shown in figure 6.4 (b) to figure 6.4 (f), the microstructures were not modified. There is no significant difference in the mechanical properties (hardness, tensile stress and elongation) associated with heat treatment of these temperatures. In industrial application, stress relief, recrystallization and globularization can be realized by annealing at from 650°C to 850°C; however, the associated oxidation layer thickness increases at the same time [6]. Water quenching from 850°C to 1050°C tends to increase the strength due to higher and higher β phase content. Water quenching at 1050°C transformed the equiaxed structure into acicular α′ martensite structure, and the strength showed the highest values (13.8% increase in the 0.2% proof stress compared to the PM) but with a reduction in ductility (42.7% lower elongation compared to the PM). Unlike martensite in steel, martensite in Ti6Al4V is not significantly strong but it is more brittle than the PM. Ti6Al4V heat treated at 950°C followed by furnace cooling shows slight lamellar structure at prior β phase boundary (Figure 6.5). It is termed a bimodal microstructure (consisting partly of equiaxed primary α and a lamellar α+β matrix) which results from heat treatment just below the β transus temperature [2, 7]. Bimodal microstructures can be considered as a combination of lamellar and equiaxed microstructure, and exhibit well-balanced properties [2] between fatigue initiation resistance and fatigue propagation resistance.

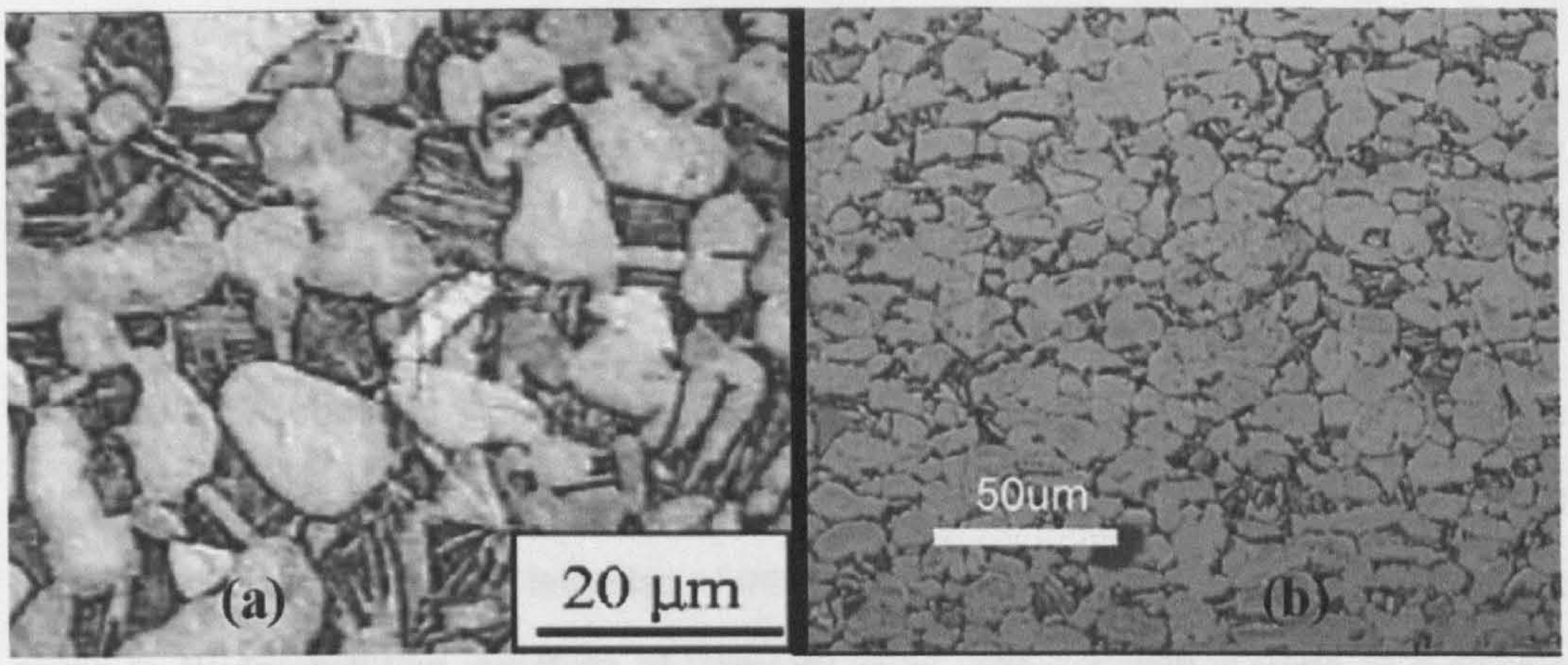

Figure 7.3 (a) bimodal structure[7] (b) author's microstructure heat treated at 950°C for 1 hour followed by furnace cooling

It is hard to identify the structure of Ti6Al4V heat treated at 1050°C followed by furnace cooling. In Ahmed's [8] work, an as-received 31.8 mm diameter bar was used to study the phase transformations in Ti6Al4V. He indicated that for a heat treatment at 1050°C for 30 min, Widmanstätten is formed when the cooling rate is below 20 $°Cs^{-1}$.

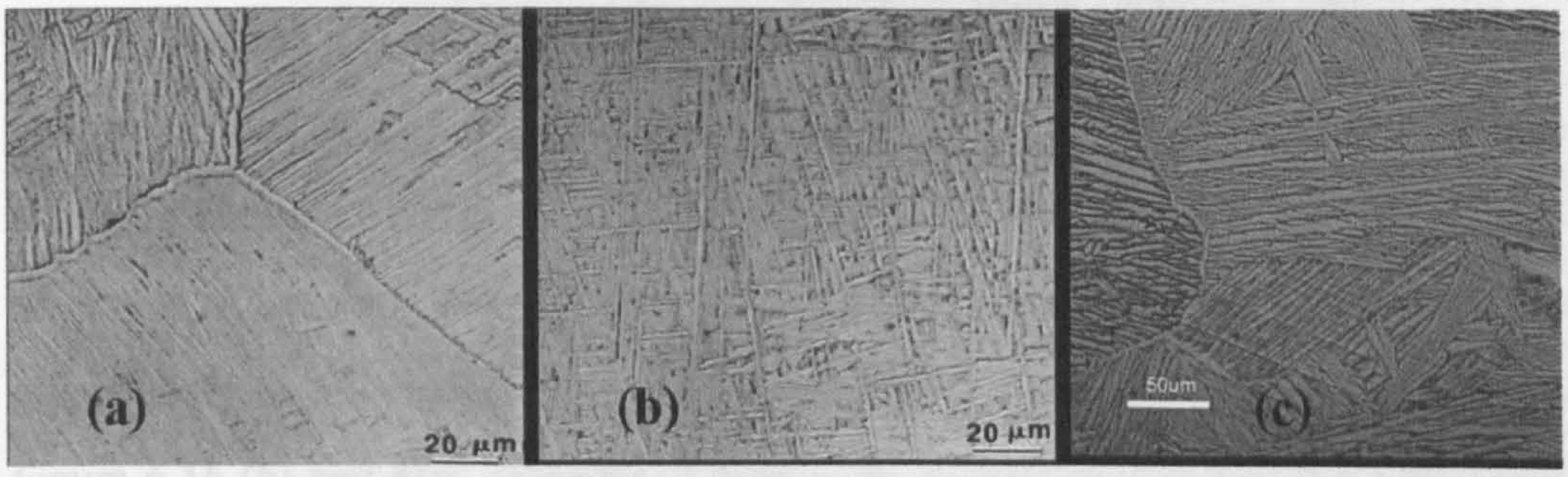

Figure 7.4 (a) as-called Widmanstätten type 1 cooled at 15 °Cs^{-1} from 1050°C [8] (b) as-called Widmanstätten type 2 cooled at 15 °Cs^{-1} from 1050°C [8] (c) author's microstructure cooled below 0.5 °Cs^{-1} from 1050°C

There are two type of structures cooled at 15°Cs^{-1} from 1050°C for 30 min in Ahmed's [8] work. Type 1 has 'zig-zagged' (α grain boundary) appearance; type 2 shows more 'normal' appearance. Both of them were defined as Widmanstätten structure by Ahmed. In the current study, the microstructure in material cooled at a rate below 0.5°Cs^{-1} from 1050°C (Figure 7.3 c) is more similar to the type 1 structure but with differences in the lamellar width. Actually, people have no full definition given to Widmanstätten structure of titanium alloy, but it is only named as a classic basket weave structure. The Widmanstätten structure may be considered as a special type of lamellar structure (with smaller lamellar width and greater orientation).

It should be noticed that the structure heat treated at 1050°C followed by furnace cooling exhibits a slightly higher strength (6.4% higher 0.2% proof stress compared to the PM) but with much lower ductility (24.4% reduction in elongation compared to that of the PM). A lamellar structure is generally observed to have both lower strength and ductility as shown in Table 3.5. Thus, Figure 7.3 (c) should be considered as Widmanstätten structure. At the same time, a smaller lamellar (about 5 µm) width results in increasing the strength (Table 3.5).

A laser beam generally has an extremely high power density due to its high directionality and high brightness. This can generate temperatures more than 3000°C

[9]. The thermal conductivity of metal is always higher than that of water and thus, cold metal acts as a very effective quenching medium. Thus, the microstructures shown in Figure 6.11 indicate that α′ martensite structures exist in the FZ no matter what type of laser adopted. As mentioned above, the microstructures of α′ martensite give slightly higher strength but exhibit significantly reduced ductility (as shown in Figure 6.16 (b) and (d)). The prior β grain size is coarse in the FZ due to its rapid growth on cooling from the liquid. These large grain sizes can result in decreased fatigue lives. Annealing treatment was used to modify the microstructures in the FZ. Annealing temperatures from 650°C to 850°C were not high enough to change the α′ martensite. The temperature of 1050°C was too high, so that not only the structures in the FZ but also those in the PM were changed. At the end, the temperature of 950°C was selected as annealing temperature. In order to study on the effect of phase content and grain size on the fatigue behaviour, Laser Beam Welded Ti6Al4V were annealed at the temperature of 950°C with different heat treatment times (1 hour, 8 hours and 20 hours). The microstructures (Figure 6.19) and Image J analysis (Table 6.9) show that 8 hours heat treatment gave a good-balance of hardness (strength) and grain size and a relatively higher β-phase area fraction. In addition, the microstructures annealed at the temperature of 950°C for 1 hour, 8 hours and 20 hours can be classified as Widmanstätten structure by comparing with that of PM heat treated at the temperature of 1050°C for 1 hour (Figure 7.4c).

7.1.3 Summary

The microstructures transformed from different PMs by heat treatment depend strongly on the original PM microstructures. The beta transus temperature for Ti6Al4V is the transition temperature of the β phase Ti to α phase Ti in Ti-Al alloy. The combination of titanium and vanadium may become the β phase boundary surrounding the α phase. The structure with the best combination of mechanical properties is a bimodal structure which can be formed from the PM following 950°C heat treatment with a furnace cool. A heat treatment temperature of 950°C was used to modify the martensite structure in FZ of laser welded Ti6Al4V; the transformed structures are thought be Widmanstätten structures.

7.2 The selection of laser type for welding process

The weld geometries were significantly different depending on the welding method used to produce them. As mentioned in chapter 2, linear heat input is a key parameter to control the melting area of a given weld type (Figure 2.4). This is the reason that diode laser weld has the largest melting area (Table 7.1).

Table 7.1 The relationship between linear heat input and spot area on melting zone

Type of LBW	Linear heat input / kJ m^{-1}	Melting area / mm^2	Spot area / μm^2	Beam quality
CW-Fibre 1	9.0	0.49	31400	1[10]
CW-Diode	130.0	3.06	12000000	4 [11]
Pulsed-YAG	9.7*	0.37	70650	1-2 [10]

* Average power and traverse speed were used in pulsed model welding

In Pulsed-YAG welding, the linear heat input was calculated by the product of the average power and the traverse speed as shown in Figure 7.5 (assuming it is a rectangular gated pulse):

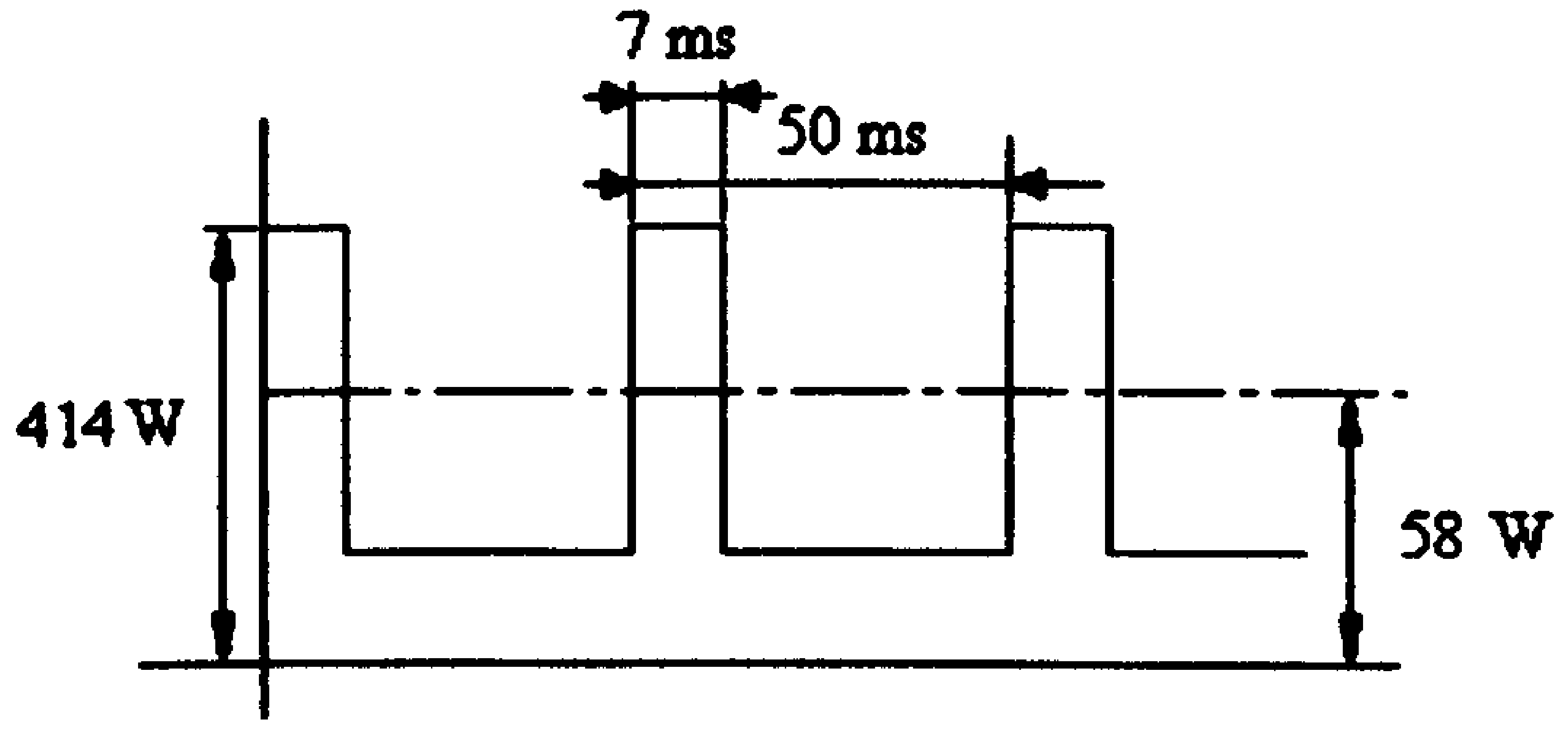

Pulse width 7 ms
Pulse frequency: 20 Hz
Pulse energy: 2.9 J
Traverse speed: 360 mm/min

Average power = pulse frequency × pulse energy

Linear heat input = average power × traverse speed
= 58 W × 360 mm/min

Figure 7.5 Calculation process of linear heat input for the pulsed Nd:YAG welding

The diode laser has the widest spot area (Table 7.1) due to the poor beam quality. Laser beam quality is used to evaluate how close the output of a laser beam is to the ideal diffraction limited output. The diode laser has the poorest directionality compared with solid lasers and gas lasers [9], which results in the highest M^2 value (a key parameter to measure beam quality) as shown in Figure 7.6.

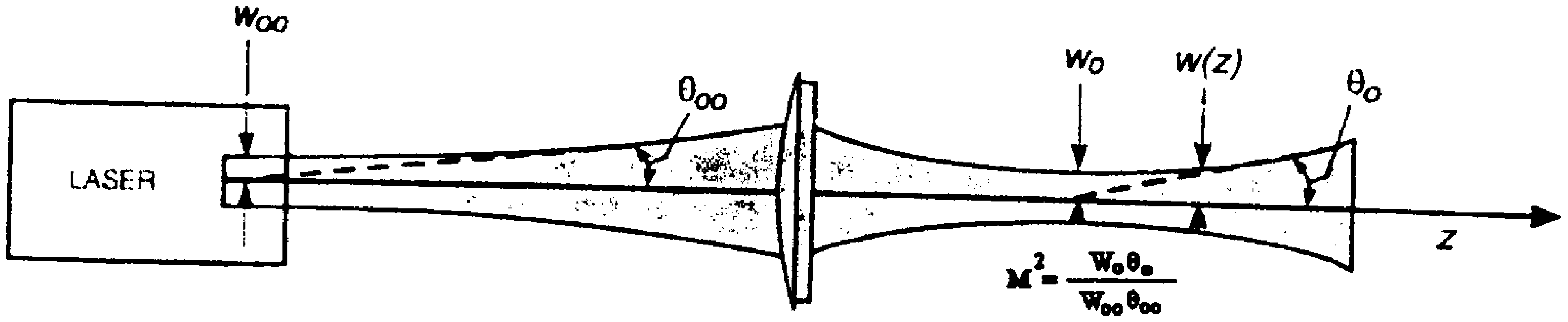

Figure 7.6 The equation for propagation of a laser beam through a focusing lens [10]

High linear heat input and poor beam quality (big spot size) promote a large melting zone and more heat generation during the welding process, which has resulted in the most serious distortion or misalignment level (Figure 6.11) occuring in the diode laser welding. In addition, there will be more chance to damage the fragile component inside of the micro packaging if it is a heat sensitive component. Thus, the CW diode laser welding is not suitable as a hermetic welding technique for sealing the micro packaging.

The fibre laser is well-known for its good beam quality and high welding speed which can create a very thin weld within a short time. However, fibre laser was eliminated in this project as a hermetic welding technique for the micro packaging. There are two reasons:

1. The geometries produced by the fibre laser welding are quite variable as shown in Figure 6.11(b) and Figure 6.11(c). The tensile yield test results (Figure 6.16 (b) and (c)) and the FEA results (6.34 (b) and (c)) showed the failure zones and maximum stress locations are also quite variable, since they are affected by the geometries significantly. The fibre laser type 1 weld (Figure 6.11 (b)) failed at the right hand side

of the FZ which accorded with the maximum stress location displayed in the FE model as shown in Figure 7.7. Figure 6.35 showed the stress concentration at this yield stress point. It has reached the maximum stress of Ti6Al4V when the applied stress is about 444 MPa (Figure 6.36). This is the reason that the failure of fibre laser welding occurred under such low applied stresses (Figure 6.16 (b)).

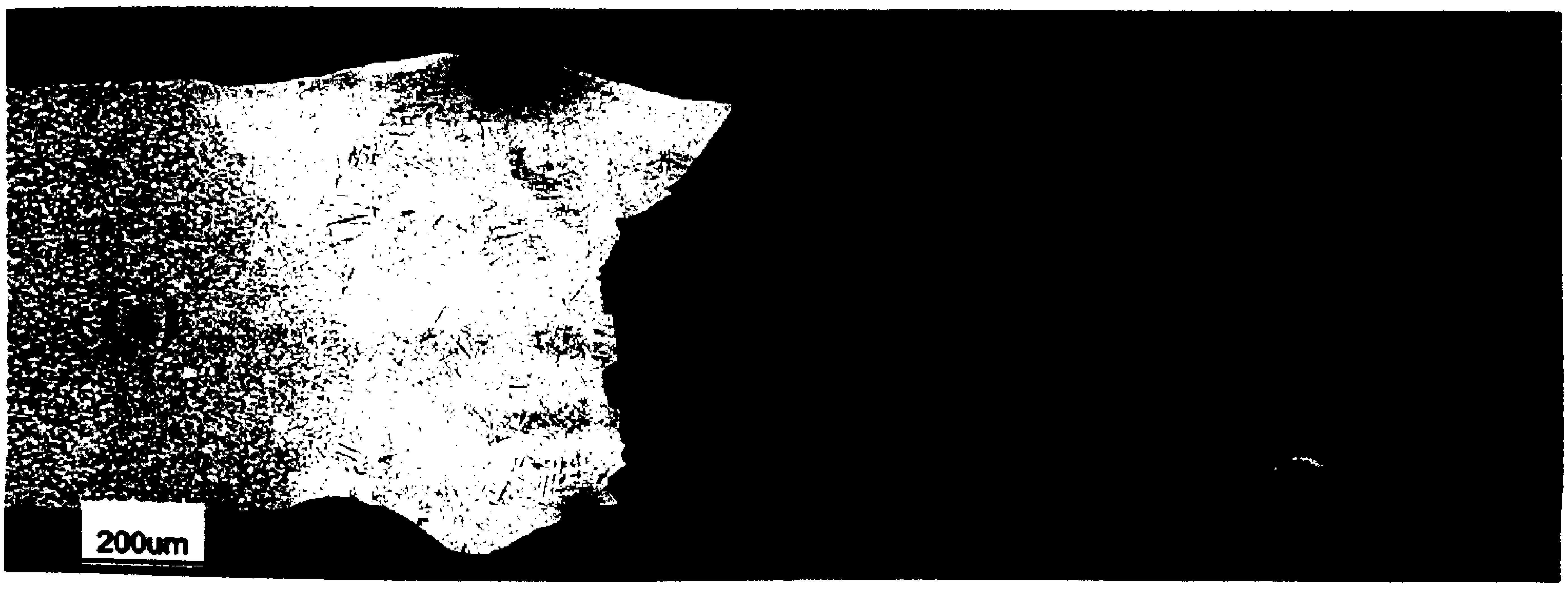

Figure 7.7 (a) Cross sectional microstructure of failure zone in fibre laser type 1

(b) Maximum stress location of FE model of fibre laser type 1

The cross-sectional shape of fibre laser type 1 welds are very similar to those observed in Wang et al.'s [12] and Tsay et al.'s [13] research as shown in Figure 7.8. Both of them used a continuous wave (CW) CO_2 laser for welding on Ti6Al4V plate with thickness around 4 mm. Aalderink et al.'s [14] research indicated that the grooves were generated during the process whereby the molten materials fill the keyhole as shown in Figure 4.3 in CW keyhole welding mode. The longer the filling distance is, the more chance the generation of grooves will be. The fibre laser type 1 welds have the largest ratio between weld top width and the thickness as shown in Table 7.2.

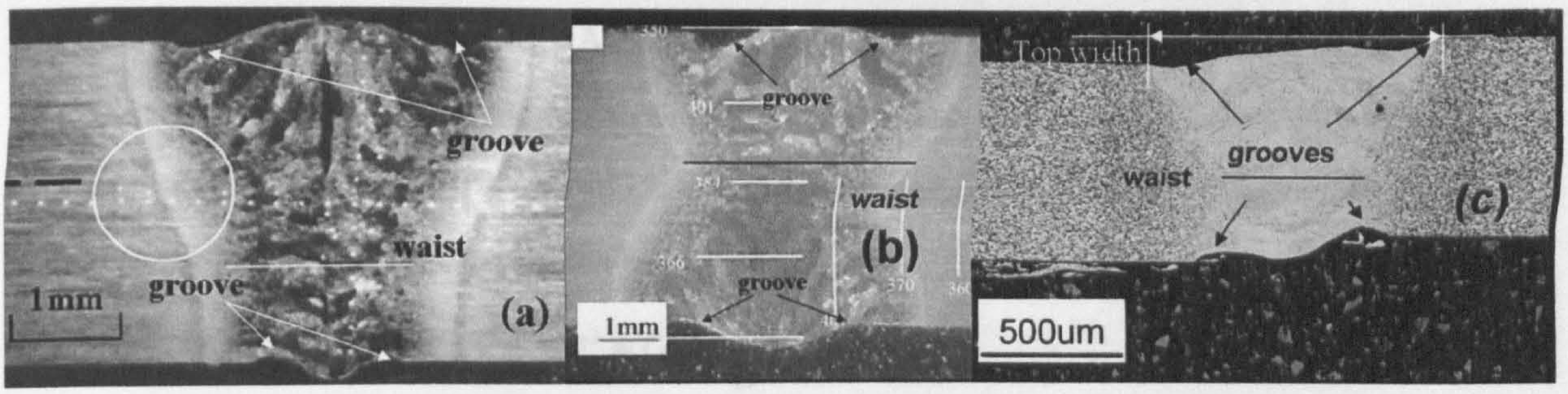

Figure 7.8 Cross-sectional shapes of (a) Wang et al.'s research (b) Tsay et al.'s research (c) author's type 1 fibre laser weld

Table 7.2 The R_{tt} (top width to thickness of the plant) ratio of different welds.

	Top width / mm	Thickness / mm	R_{tt}
Wang	3.08	3.08	1
Tsay	5.25	5.375	0.98
Fibre laser type 1 (current work)	1	0.7	1.43

A completely different cross-sectional shape which has been termed fibre laser type 2 weld was generated with the same welding parameters. The cross-sectional shape of the fibre laser welding type 2 indicated that there was some additional material which made a large weld bead.

2. The phenomenon of porosity in the fibre laser welds is serious (Figure 6.22(b)). The traverse speed 4000 mm min^{-1} was used in the experimental welding process. Faster traverse speed provides less heat input which results in less chance for distortion and damage of the heat sensitive components inside of the micro packaging. However, faster traverse speed also increases the possibility of porosity generation as there is less time for the bubbles come out from the melt pool. As mentioned in chapter 4, porosity significantly affects the strength and the reliability of welded joints.

The diode laser and fibre laser have been identified as having serious short comings for welding of thin Ti6Al4V sheet due to their disadvantages which were mentioned above. In addition to the Nd:YAG laser, CO_2 lasers may also be suitable for such a weld situation. However, the longer wavelength (10.6 μm) of the CO_2 laser compared with that (1.06 μm) of Nd:YAG laser gives lower directionality (higher plane divergence angle values) as shown in Equation 7.1 [9]:

$$\theta^2 \approx (2.44\frac{\lambda}{D})^2 \qquad \textbf{Equation 7.1}$$

where θ is plane divergence angle, λ is wavelength of laser, D is diameter of cross section of laser beam. Lower directionality results in poorer beam quality. At the same time, the brightness tends to be lower due to higher θ value (Equation 7.2 [9]):

$$B = \frac{P}{S\theta^2} \qquad \textbf{Equation 7.2}$$

where B is brightness, P is power of laser, S is surface area of laser beam.

1.06 μm light from the Nd:YAG is transmitted easily through a fibre but 10.6μm light from the CO_2 cannot [10], hence the Nd:YAG laser system is more flexible.

The porosity of Pulsed Nd:YAG welding is lower than that of the CW fibre laser welding. There are two reasons:

1. Pulsed welding agitates the molten pool, promotes a periodic molten metal flow, and thus causes bubbles to float to the surface [15]. In CW welding, the melt pool is much more stable, there is no pulsing, and thus more bubbles remain in the weld pool during the solidification.
2. Zhou and Tsai's research [16] indicated the formation of porosity is caused by two competing factors: solidification rate of the molten metal and the backfilling speed of the molten metal. The solidification rate is primarily affected by heat transfer (the energy transfer takes place between material bodies as a result of a temperature difference). Heat transfer in a welding process is complex, but is primarily made up of conductive heat transfer into the cold Ti6Al4V itself and convection heat transfer between the Ti6Al4V and the surrounding gas environment.

The backfilling speed of the molten metal during the keyhole collapse process is dominated by the speed of the keyhole movement. The faster the keyhole moves, the faster the molten metal is required to fill into the previous locations.

Comparing porosity formation in the FLW and Nd:YAG weld, there is same thermal conductivity, a very similar melting area and depth-to-width ratio. The only significant difference between two of them is the traverse speed as shown in Table 7.3. The 4000 mm min^{-1} traverse speed of the fibre laser welding required a higher backfilling speed of the molten metal during the keyhole collapse process, which caused serious generation of the porosity.

Table 7.3 Compare of main parameters between fibre laser weld 1 and Nd:YAG weld

	Power / watt	**Traverse speed / mm min^{-1}**	**Melting area / mm^2**	**Top width / mm**
Fibre laser 1	600	4000	0.49	1
Nd:YAG	414*	360**	0.37	0.94

*** The peak power is 414 W**
**** The real traverse speed is 108 mmmin^{-1} due to 70% overlap rate**

As mentioned in chapter 4, previous research [15-17] has proposed several methods to prevent and reduce porosity, such as welding in vacuum environment, using dissolved shielding gas. The purpose of those methods is to improve the surrounding gas environment. Beside these, the weld geometry which is controlled by the various laser types and parameters can affect the porosity as well. The bigger the melt area is, the slower the solidification rate is. The wider the weld zone is, the more chance the bubble has to float to the surface. As shown in Figure 6.23, the top widths and bottom widths of CW fibre laser welds increase with increase of linear heat input. Towards pulsed Nd:YAG welds as shown in Figure 6.24, the top widths and bottom widths increase with increase of pulsed power. Hence, in CW mode welding, the porosity can be reduced by increasing the power or decreasing the traverse speed; in pulse mode welding, the porosity can be reduced by increasing the pulsed energy or decreasing the pulsed width.

In conclusion, under the condition of small weld zone and less heat input (faster traverses speed, smaller power), there is a need to balance the generation of the porosity (slower traverse speed, bigger power). In this project, the pulsed Nd:YAG welding resulted in less porosity, uniform geometry, and a reasonably narrow weld zone. Hence it is suggested as the hermetic laser welding technique for sealing micro package.

7.3 Fatigue behaviour of laser beam welded Ti6Al4V

The fatigue fracture life of a material is the number of cycles to crack initiation plus the number of cycles of crack propagation to failure [18]. Leyens and Peters [2] indicated that, on titanium alloy, for high stress amplitudes (low-cycle fatigue) condition, the crack initiation life can be a small portion compared with the crack propagation life (sometimes, the ratio of N_I to N_F can be 0.01). The portion of the crack initiation life tends to increase with decreasing the stress amplitudes. The high-cycle fatigue strength can be considered a good measure of resistance to fatigue crack initiation. In summary of the above statement, the contributions of the fatigue crack initiation and the crack propagation to the fatigue fracture life can be expressed as in Figure 7.9:

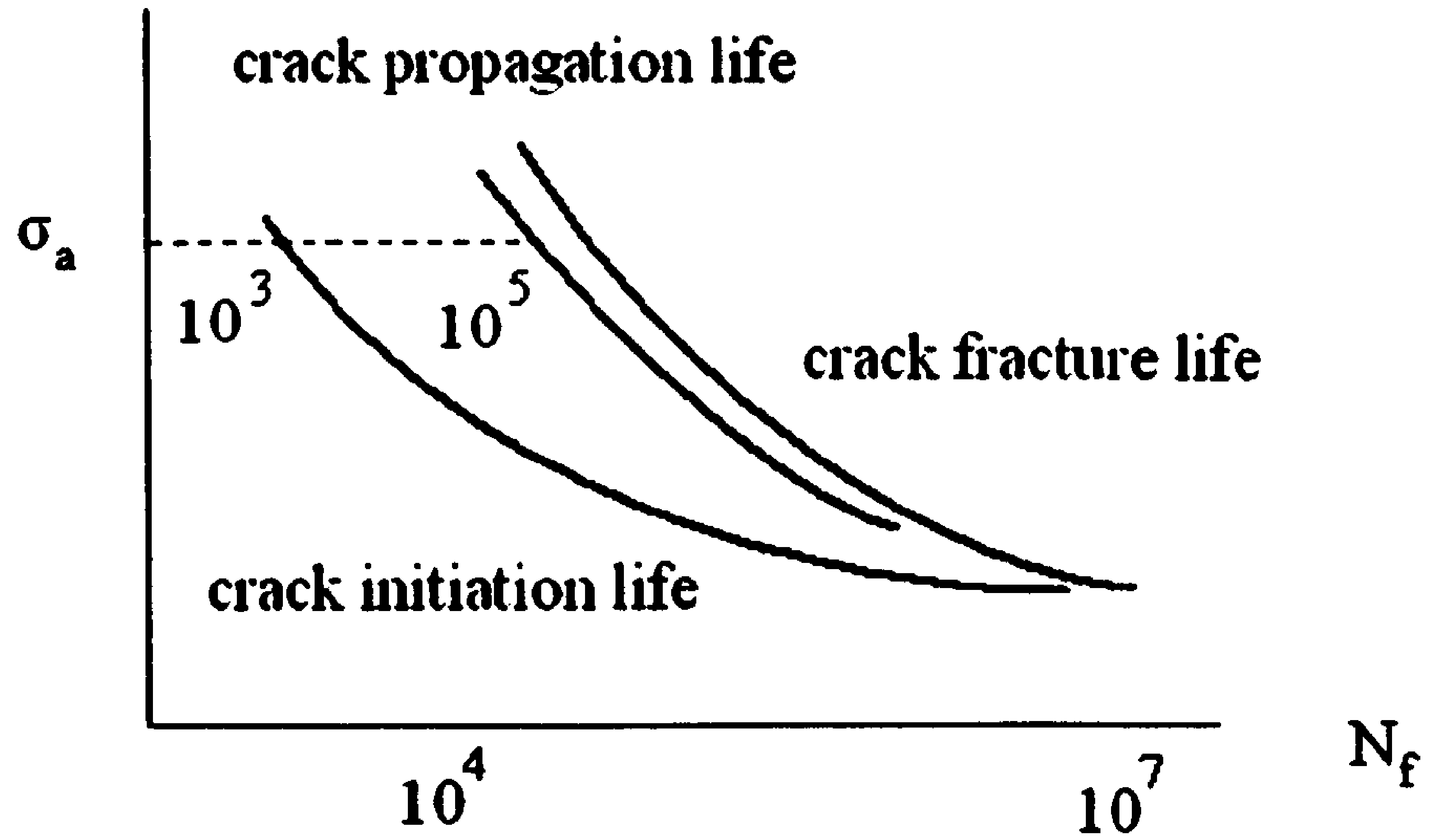

Figure 7.9 Contribution of crack initiation and crack propagation processes to fracture behaviour

There are several experimental methods to derive S-N curve of a material, which include plane bending, rotating bending, uniaxial compression-tension (push-pull) and tension-tension loading. Out of those, the stress amplitude σ_a for fully reversed loading (R = -1) is the most popular experimental method. By summarizing of previous [2, 6, 7, 19] S-N curve data for Ti6Al4V with R=-1, the range of the stress amplitudes to the fracture lives are shown in Table 7.4:

Table 7.4 Stress amplitude range of previous experimental data and prediction at life cycles of $10^{5,}$ 10^6 and 10^7 with R = -1

	10^5	10^6	10^7
Range of previous experimental data/ MPa	520 – 760	500 - 750	490 - 730
Prediction* / MPa	562	440	348

*The prediction was calculated using Basquin approach (Equation 5.2) with R = -1

In order to compare with previous data, the fatigue lives of the PM of R=0.1 were modified into that of R=-1 with Goodman relation Equation 7.5:

$$\sigma_a = \sigma_{fs}\left\{1 - \frac{\sigma_m}{\sigma_{UTS}}\right\} \qquad \textbf{Equation 7.5}$$

where σ_a is the stress amplitude denoting the fatigue strength for a nonzero mean stress, σ_{fs} is the fatigue strength for 10^7 cycle at fully reversed loading and zero mean stress, σ_m is the mean stress value, σ_{UTS} is the ultimate tensile strength of the material

Table 7.5 the modification process of experimental fatigue lives for the PM

σ_{UTS} = 1054 MPa			
	10^5	10^6	10^7
σ_a / MPa	248	225	180
Measured σ_m (R=0.1) / MPa	303	275	220
Transformed σ_a (R=-1) / MPa	>347*	>304*	227

*The stress amplitudes at R=-1 for 10^5 and 10^6 are above these values

The modified fatigue strength (227 MPa) is lower than both the other data and the predicted value. Besides the microstructure, stress ratio and mean stress, there are other parameters or factors which can affect the fatigue behaviour of materials, such as loading frequency, sample size, surface treatment, service environment (e.g. temperature and humidity). Morrissey [20] indicated that the fatigue strength increased with increasing frequency. The reason is that with lower frequency there is a greater possibility that other factors (e.g. service environment) will affect the micro-crack (where the fracture starts from), leading to increased propagation speed, so that the fatigue strength decreases. Most of fatigue data collected from titanium alloys were at frequencies of 20-50 Hz. Most of titanium alloy components served in engine of aircraft at frequencies much higher than 1 kHz. In this study, the frequency used was 7 Hz. This could be the reason that the fatigue strength of this study is lower than the other's studies and prediction value.

As shown in Figure 6.21, the fatigue fracture lives of the fibre laser welded samples are lowest at both high stress amplitudes and low stress amplitudes. The reason is due to the high porosity levels in the welds (Figure 6.22(b)) and geometries of the weldment themselves. All the heat treated Nd:YAG weld samples exhibited improved life cycle over that of the original Nd:YAG weld. However, the increase rates are variable depending on heat treatment times and stress amplitude as shown in Figure 7.10:

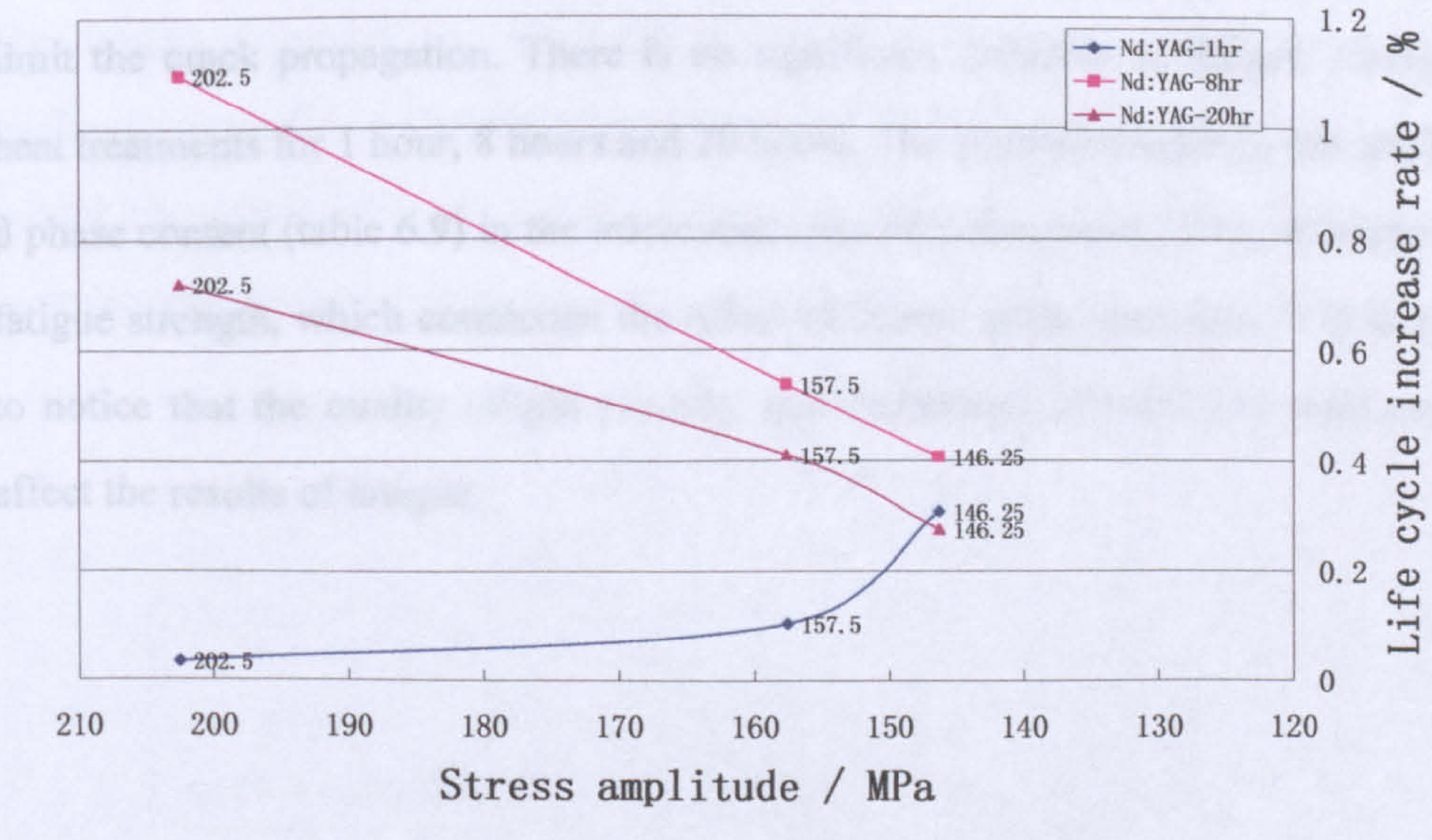

Figure 7.10 Increase in life cycles versus Stress amplitude for Nd:YAG weld of heat treatment at 950°C for 1 hour, 8 hours and 20 hours to compared original Nd:YAG weld

The microstructures of the laser welded Ti6Al4V annealed at the temperature of 950°C for 1 hour, 8 hours and 20 hours should be Widmanstätten structure. Compared with martensite structures, Widmanstätten structure has a distinct improvement in ductility with a slight decrease in strength. At higher stress amplitudes (202.5 MPa), the increase in fatigue resistance for heat treatments for 8 hours and 20 hours is much higher than that of heat treatment for 1 hour. This is because the coarse grain size has higher fatigue propagation resistance than the fine grain size material (table 3.5). At higher stress amplitude, the propagation life takes a large proportion of the fracture life. The portion of the propagation life tends to decrease with decrease in the stress amplitudes (Figure 7.10). These could be the reasons that, from higher stress amplitude (202.5 MPa) to lower stress amplitude (146.25 MPa), the increase rates of heat treatments for 8 hours and 20 hours kept decreasing. The increase in fatigue life associated with heat treatments for 8 hours is always higher than that for 20 hours. The reason is possibly due to the metastable β which exists in the microstructure of samples heat treated for 8 hours of 950°C (Figure 6.19(c)). The crack propagation follows along the grain boundary [2]. The dispersion of stronger metastable β tends to limit the crack propagation. There is no significant different in fatigue strength for heat treatments for 1 hour, 8 hours and 20 hours. The possible reason is that the higher β phase content (table 6.9) in the microstructures of 8 hours and 20 hours improve the fatigue strength, which counteract the effect of coarse grain structures. It is important to notice that the quality (slight porosity and distortion) of Nd:YAG weld can also affect the results of fatigue.

7.4 The effect of geometries on the stress level for the various laser welds

As shown in Figure 6.11, the geometries of welds were variable depending on the types of lasers, which can affect the stress level during tensile test and fatigue test. FEA was used here to understand the influence of misalignments and geometrical features on stress level.

The challenge of FEA is to understand how close the FEA results compare with the real results. These are strongly affected by the definition of material properties, mesh density and boundary condition. Under a given mesh density (0.003 mm) and boundary condition (0.008 mm), the FE models without misalignment defined as PM property (Figure 6.27) and FZ property (Figure 6.28) showed no error compared with calculation results (Section 6.7.2), as both of them were simple regular shapes. When given the properties of FZ and PM (Figure 6.29), the maximum stress was predicted to occur at the joint between the FZ and the PM, and the value was between 444 MPa (PM property's model) and 470.3 MPa (FZ property's model). The reason is that, the stiffness of the FZ is slightly higher than that of PM, when applied a force on the model, the deformation of the PM part is higher than that of the FZ. Thus, the stress concentration occurred at the joint area as shown in Figure 7.11.

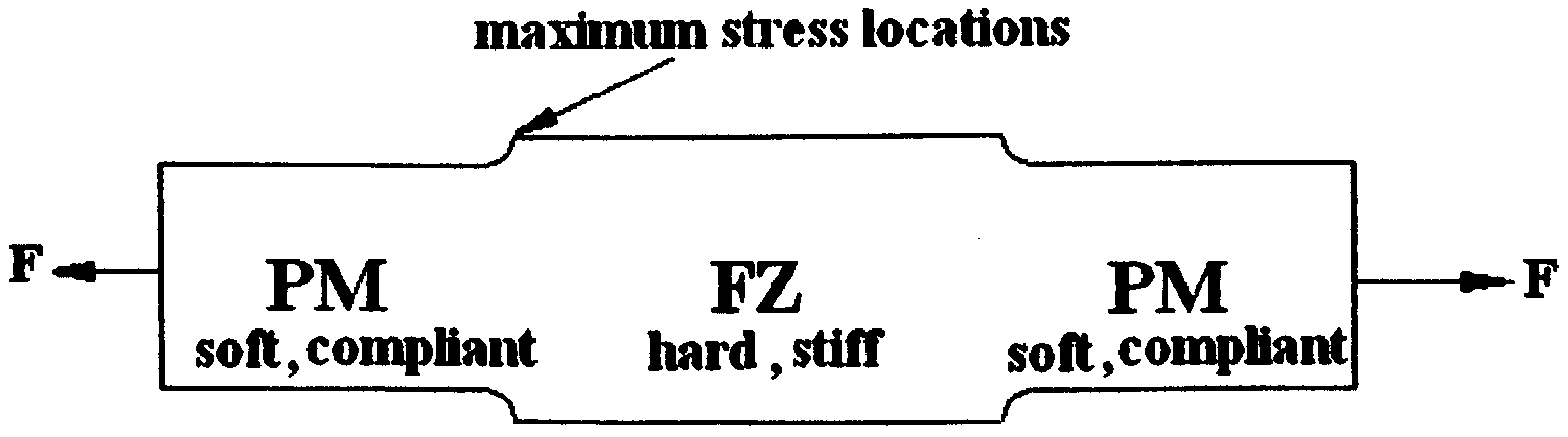

Figure 7.11 Schematic diagram of deformation of the FE model applied a force

The effect of misalignment level on stress was serious for such thin (0.7 mm) material as shown in section 6.7.5. When the misalignment level reached 100 μm (1/7 of the thickness), the maximum stress level is nearly twice as large as that in the non-misaligned situation with a given boundary condition of 0.008 mm displacement. The maximum stress points were still located at the joint between the FZ and the PM. Hence, the joint area should be the weakest part of the whole structure. As mentioned before, the misalignment level in the diode laser weld is the most serious. However, the failure areas of all the diode laser welds were at the PM far away from the FZ and the HAZ. Hence, it can be observed that misalignment level is just one factor effect on the stress level.

It was found that the stress levels were affected significantly by the geometries of the welds. But the maximum stress location may not necessarily be in the failure zone, because the strength of the FZ is higher than that of the PM. In order to understand this, the relationships between the maximum stress locations for each of the welds and stress levels of the non-misaligned situations were plotted in Figure 6.35. In this case, no matter where maximum stress point exists, it should be the failure point. It has been showed in Figure 7.7 that the failure area is generally in according with the maximum stress location. The Nd:YAG weld failed at right hand side of the FZ which accorded with the maximum stress location displayed in the FE model as shown in Figure 7.12.

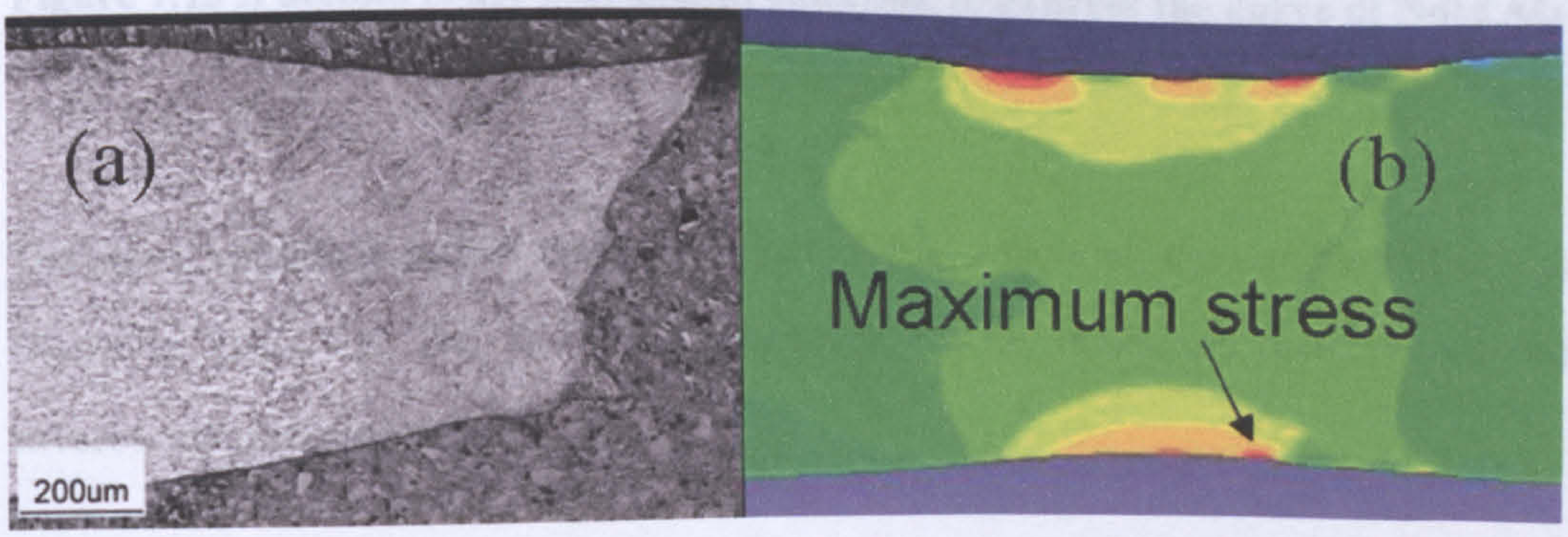

Figure 7.12 (a) Cross sectional microstructure of failure zone in Nd:YAG weld (b) Maximum stress location of FE model of Nd:YAG weld

The results of the tensile testing of the diode laser welds and the type 2 fibre laser welds showed that the failure areas occured in the PM (Figure 6.17 b and d). The maximum stress location in the diode laser weld did not exist in the FZ (Figure 6.34). However, the maximum stress location of the fibre laser welding type 2 existed in the joint.

Figure 6.36 showed the maximum stress levels with increase of displacement for the various cross-sectional shapes of welds. The second order polynomial equation can be used to express the correlation of displacements and maximum stress levels as shown in Figure 7.13.

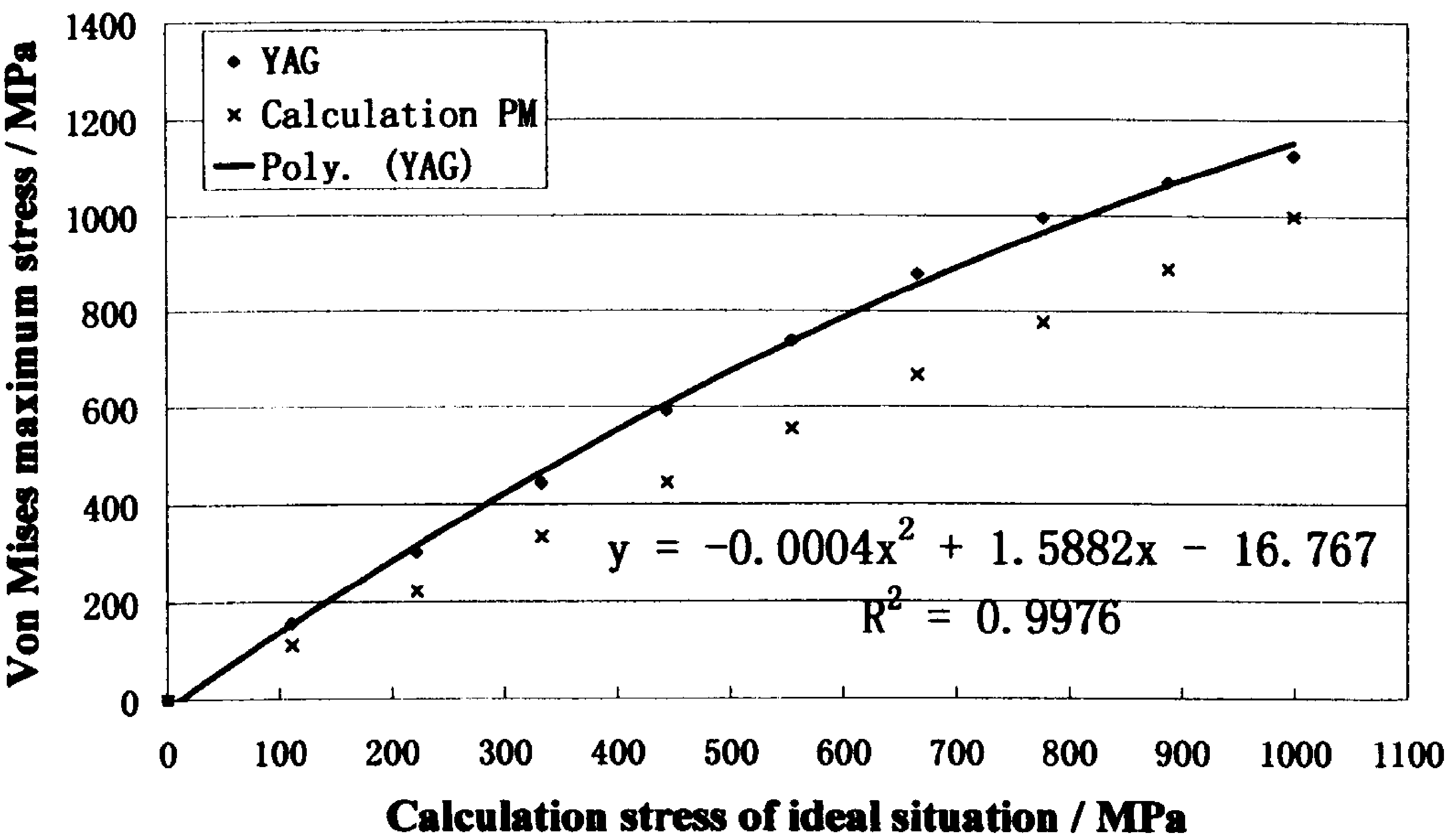

Figure 7.13 A second order polynomial equation to express the curve of Nd:YAG welding

The stress amplitude in S-N curve can be modified following the equation above as shown in Table 7.6. The real stress amplitude values should be between original stresses and modified stresses.

Table 7.6 Original stress amplitude versus Modified stress amplitude

Original stress amplitude / MPa	Modified stress amplitude / MPa	Increase rate / %
202.5	288.4	42.4%
157.5	223.5	41.9%
146.3	207.0	41.5%
135	190.4	41.0%

Reference:

[1] P.Pinke, L.Čaplovič and T.Kovács. The influence of heat treatment on the microstructure of the casted Ti6Al4V Titanium alloy. *Materials World*. 2007; 2:1-6.

[2] C.Leyens and M.Peter. Titanium and titanium alloy: fundamentals and applications: WILEY-VCH GmbH & Co. KGaA 2003.

[3] M.T.Jovanović, S.Tadić, S.Zec, Z.Mišković and I.Bobić. The effect of annealing temperatures and cooling rates on microstructure and mechanical properties of investment cast Ti-6Al-4V alloy. *Materials and design*. 2006; 27:192-9.

[4] I.Ohnuma, Y.Fujita, H.Mitsui, K.Ishikawa, R.Kainuma and K.Ishida. Phase equilibria in the Ti-Al binary system. *Acta Materialia*. 2000; 48(12):3113-23.

[5] A.B.Short. Gas tungsten arc welding α+β Titanium alloy: a review. *Material Science and Technology*. 2009; 25:309-24.

[6] IMI titanium. Titanium alloy IMI318. 2006.

[7] J.H.Zuo, Z.G.Wang and E.H.Han. Effect of microstructure on ultra-high cycle fatigue behavior of Ti-6Al-4V. *Materials Science and Engineering: A*. 2008; 473(1-2):147-52.

[8] T.Ahmed and H.J.Rack. Phase transformations during cooling in alpha + beta titanium alloys. *Materials Science and Engineering A*. 1998; 243(1-2):206-11.

[9] L.Q.Zhu, J.C.Niu, S.L.Zhu and Z.J.Xue. Application of Modern Laser Engineering. 1st ed. Beijing: National Defense Industry Press 2008.

[10] American Welding Society. Recommended Practices for Laser Beam Welding, Cutting, and Drilling: ANSI/AWS 1998.

[11] K.Maeda, M.Kumagai and K.Namba. Application of diode laser to welding of aluminium alloys. *Welding international*. 2003; 17(11):860-3.

[12] S.H.Wang, M.D.Wei and L.W.Tsay. Tensile properties of LBW welds in Ti-6Al-4V alloy at evaluated temperatures below 450°C. *Materials Letters*. 2003; 57(12):1815-23.

[13] L.W.Tsay, Y.P.Shan, Y.H.Chao and W.Y.Shu. The influence of porosity on the fatigue crack growth behavior of Ti-6Al-4V laser welds. *Materials Science*. 2006; 41:7498-505.

[14] B.J.Aalderink, D.F.de.Lange, R.G.K.M.Aarts and J.Meijer. Keyhole shapes during laser welding of thin metal sheets. *J Phys D: Appl Phys*. 2007; 40:5388-93.

[15] T.Y.Kuo and S.L.Jeng. Porosity reduction in Nd-YAG laser welding of stainless steel and inconel alloy by using a pulsed wave. *Journal of physics D: applied physics*. 2005; 38:722-8.

[16] J.Zhou and H.Tsai. Porosity formation and prevention in pulsed laser welding. *ASME*. 2007; 129:1014-24.

[17] S.Katayama, Y.Kobayashi, N.Seto, M.Mizutani and A.Matsunawa. Effect of vacuum on penetration and defects in laser welding. proceeding of ICALEO; 2000; 2000. p. 182-91.

[18] S.Suresh. Fatigue of materials. 2nd ed: Cambridge university press 1998.

[19] A.J.McEvily, T.Nakamura, H.Oguma, K.Yamashita, H.Matsunaga and M.Endo. On the mechanism of very high cycle fatigue in Ti-6Al-4V. *Scripta Materialia*. 2008; 59(11):1207-9.

[20] R.J.Morrissey, D.L.McDowell and T.Nicholas. Frequency and stress ratio effects in high cycle fatigue of Ti-6Al-4V. *International Journal of Fatigue*. 1999; 21(7):679-85.

CHAPTER 8

Chapter 8 Conclusions

This work has concentrated on the investigation of microstructures, mechanical properties and fatigue behaviours of thin (0.7 mm) Ti6Al4V sheet following welding, both in the as-welded state and following heat treatment with the welding being conducted with three types of lasers, namely Nd:YAG, diode and fibre lasers. The major conclusions drawn can be summarized as follows,

1. The rank of the strength from high to low for all types of the microstructures of Ti6Al4V observed in this study is: α′ martensite, metastable β, Widmanstätten, bimodal and equiaxed microstructure (see Figure 8.1). The rank of the ductility from high to low for all types the microstructures of Ti6Al4V observed in this study is: equiaxed, bimodal, Widmanstätten, metastable β and α′ martensite microstructure (see Figure 8.2).

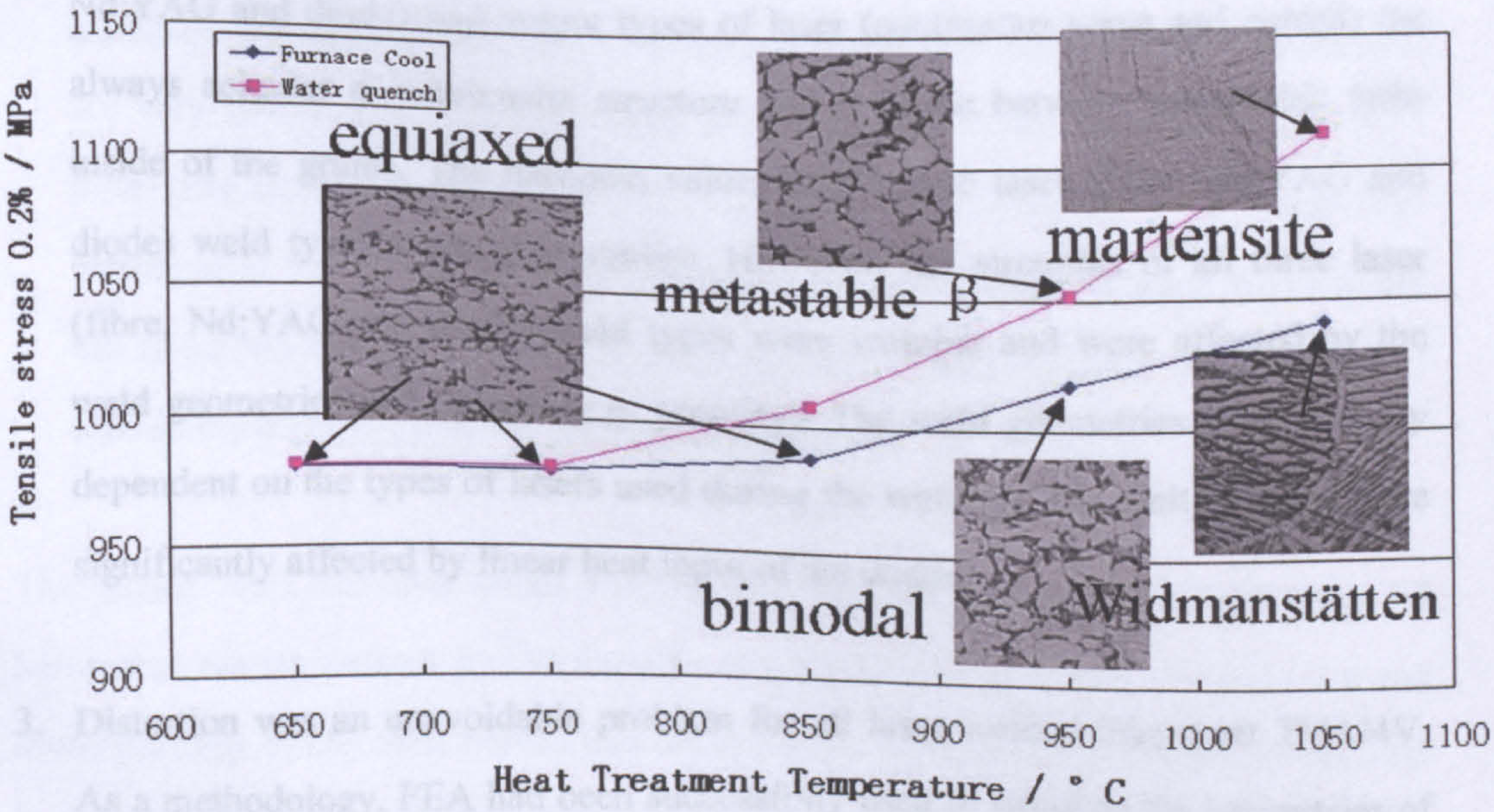

Figure 8.1 The rank of the strength of the microstructures in Ti6Al4V

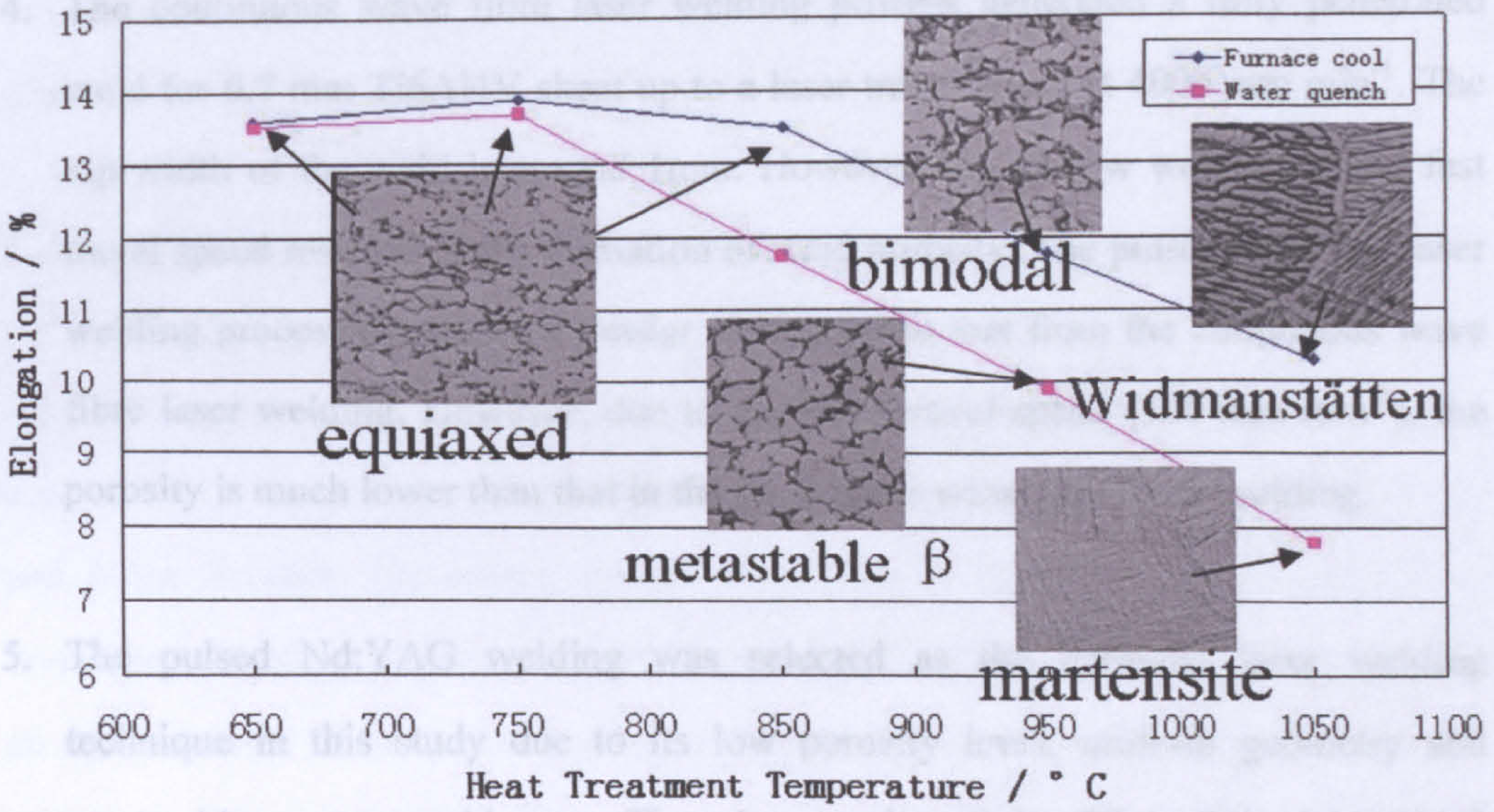

Figure 8.2 The rank of the ductility of the microstructures in Ti6Al4V

2. The microstructures of the FZ generated by all three types of lasers (fibre, Nd:YAG and diode) and output types of laser (continuous wave and pulsed) are always acicular α′ martensite structure and β phase between martensitic laths inside of the grains. The hardness values of all three laser (fibre, Nd:YAG and diode) weld types were very similar. However, the strengths of all three laser (fibre, Nd:YAG and diode) weld types were variable and were affected by the weld geometries and defects (e.g. porosity). The weld geometries were strongly dependent on the types of lasers used during the welding. The melting areas were significantly affected by linear heat input of the welds.

3. Distortion was an unavoidable problem for all laser welded thin sheet Ti6Al4V. As a methodology, FEA had been successfully used to simulate the geometries of the welds and evaluate the influence of the weld geometries on stress level. The results of FEA showed that small misalignment levels significantly affected the stress level for thin sheet Ti6Al4V.

4. The continuous wave fibre laser welding process generated a fully penetrated weld for 0.7 mm Ti6Al4V sheet up to a laser travel speed at 4000 mm min^{-1}. The top width of the weld is around 1mm. However, the narrow weld zone and fast travel speed resulted in the formation of weld porosity. The pulsed Nd:YAG laser welding process generated a similar weld zone to that from the continuous wave fibre laser welding. However, due to the slow travel speed (360 mm min^{-1}), the porosity is much lower than that in the continuous wave fibre laser welding.

5. The pulsed Nd:YAG welding was selected as the hermetic laser welding technique in this study due to its low porosity level, uniform geometry and reasonably narrow weld zone. The α′martensite of the FZ in Pulsed Nd:YAG welded Ti6Al4V can be transformed into basket-wave Widmanstätten microstructure with β phase boundary with heat treatment at above 950°C with furnace cooling. The longer the heat treatment temperature, the wider the width of α colony. β-phase area fractions following 8 hours and 20 hours of heat treatment are very similar but higher than that in the original welded condition and the 1 hour heat treated condition. Pulsed Nd:YAG weld followed by 8 hours heat treatment at 950°C and furnace cooling showed the highest fatigue fracture life due to a good-balance between the grain size and β-phase content; the existence of metastable β limits the crack propagation as well.

The pulsed Nd:YAG laser beam welding was recommended for the application of hermetical sealing process for the impeller of a LVAD due to narrower weld zone and lower porosity. It has been proved that the existence of Widmanstätten and metastable β showed the highest fatigue fracture life, which can be transformed by a heat treatment at 950°C for 8 hours followed by furnace cooling. Unfortunately, such a heat treatment process can not be adapted to the impeller of a LVAD, as the electronic and magnetic devices inside the impeller are heat-sensitive components. Long time and high temperature heat treatment can cause demagnetization. However, this heat treatment process can still be used for the application of the other micro packages which have not such a magnetic device or the other heat-sensitive components.

Porosity can be a significant defect in laser beam welding. Based on the literature survey of reduction of the porosity in the welding, the increase of the melting area can reduce the porosity. In this study, it has been verified that the melting areas were controllable by power and traverse speed (in continuous wave mode) and pulse energy and pulse duration (in pulsed mode). One part of further work is required to investigate the effect of laser parameters (for both continuous wave and pulsed mode) on the formation of the porosity using a high power X-ray microtomograph (Micro-CT) to detect the porosity in the welds. Another part of further work is required to try to find a method with short time and low temperature heat input which still can get Widmanstätten and metastable β (or similar microstructures) instead of a heat treatment at 950°C for 8 hours followed by furnace cooling. A tentative laser peening process is suggested to reach this target.